University of Udine
Department of Mathematics, Informatics and Physics

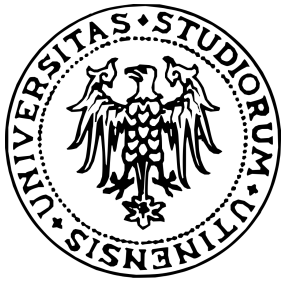

Doctoral Thesis

Spectral Energy Distribution Modeling of Markarian 501 through a non-linear least square minimization

Advisor: Prof. ALESSANDRO DE ANGELIS
Tutor : Prof. MASSIMO PERSIC

Candidate: BARBARA BIASUZZI

Academic Year 2015-2016

To what is most precious to me,

my Family.

Abstract

So far the Spectral Energy Distribution (SED) of Active Galactic Nuclei (AGN), in particular blazars, have been obtained in a heuristics way. This is mainly due to both the many free parameters of the emission model and the severe lack of simultaneous multi-frequency data. This leads to non-rigorous and possibly biased analyses, and makes it difficult to compare results coming from different analyses. However, recent simultaneous multi-frequency campaigns are providing long-term broad-band coverages of source activity, and large multi-frequency data sets are becoming available. So emission model fitting may be attempted with better profit now.

The main aim of this thesis is to develop a statistical approach that fits AGN SEDs in a rigorous way. Such an approach consists in a χ^2-minimization, based on the Levenberg-Marquardt algorithm, that returns the most likely values of the SED parameters, plus a method devised to obtain the related uncertaintes. The whole minimization process is implemented in a C++ code. However, this approach may reveal unexpected features of the χ^2-manifold that might affect convergence, due to spurious correlations between model parameters and/or inadequacy of the currently available datasets. For these reasons, a statistical analysis will be carried out on the solutions obtained from several minimizations, each starting from different points of the parameter space.

This approach is applied to different activity states of the blazar Markarian 501, in a Synchrotron Self Compton (SSC) framework. In particular, starting from available observations of this source taken with the ground-based Major Atmospheric Gamma-ray Imaging Cherenkov telescopes (MAGIC) in 2011, 7 multi-frequency datasets were obtained. Based on multi-frequency and simultaneity requirements, all datasets include also data provided by the Swift UVOT, Swift XRT, and Fermi LAT orbiting telescopes. The SED modelling of each dataset will be performed through a non-linear χ^2-minimization in order to obtain the most likely values of the parameters describing the SSC model.

Finally, it is worth remarking that this approach is not only a rigorous statistical method to find the most likely source parameters for different scenarios, but it also represents a powerful tool to efficiently discriminate between different emission models (once they have been implemented in the code).

The contents of this thesis is divided as follows. A brief introduction on γ-ray astrophysics and the main properties of the AGN are reviewed in Chapter 1. In Chapter 2 the MAGIC telescopes are presented. In Chapter 3 both the minimization approach and its implementation in a C++ code are described and discussed in detail. In Chapter 4 all steps to collect Markarian 501 simultaneous and multi-frequency data (focussing in particular on MAGIC and FERMI-LAT analyses) are reported. In Chapter 5 the minimization process is applied on seven broad-band simultaneous datasets, and, finally in Chapter 6 the obtained results are

discussed, together with the future outlooks.

Contents

Chapter 1

Introduction

This thesis concerns the modeling of the γ-ray emission of blazars. In this chapter I give a brief overview on their origin, the physical processes generating them, and on the detection tecniques is carried out. Since the γ-ray are a small percentage of the cosmic-rays, the latter are introduced in Section 1.1. In Section 1.2 and 1.3 the γ-ray production mechanisms and the way they propagate through the Universe are presented. Finally, in Section 1.4 the ground-based and the space detection tecniques are described. For an exhaustive intoduction on the astroparticle physics, see [1], while for the compleate treatment of the high energy processes described in this chapter, refer to [2].

1.1 Cosmic-rays

Studying the γ-rays coming from the sky, allows the most powerful non-thermal processes of the Universe to be investigated. The γ-ray emissions are correlated to the presence of charged particles, accelerated up to very high energies. Relativistic particles reach such energies in celestial sources that act as particles accelerators. These particles, by interacting with the low energy photons or the ambient sorrounding the source, generate the γ-ray emission.

All the time Earth is bombarded by a flux of high energy particles coming from the Universe. Such particles, called cosmic-rays, were discovered to be of extraterrestrial origin by Victor Hess and Domenico Pacini. They are are mainly composed by protons (90%), helium nuclei ($< 10\%$), heavier nuclei ($< 1\%$), electrons ($< 1\%$), and γ-rays ($0.1 - 1\%$). γ-rays, togheter with neutrons and neutrinos, are the neutral component of cosmic-rays. They are particularly interesting because they mantain their arrival direction information, since they are not deflected by the magnetic fields permeating the Universe and surrounding the Earth. Neutrons and neutrinos, unllike *gamma*-rays, are difficult to detect because the former are characterized by a very short lifetime, while the latter interact very weakly with matter. So, even if γ-rays represent only a very small percentage of the cosmic-rays, they are the best candidate to study the emitting sources, the underlying acceleration mechanisms, and the propagation of cosmic-rays through the interstellar medium. Since they cover a large region of the electromagnetic spectrum, they are arbitrarily divided and classified into subclasses, according to their energy: the low energy (LE) in the 0.1-1 MeV reange; the medium energy (ME) in the 10-20 MeV range; the high energy (HE) in the 20 MeV - 30 GeV range; the very high energy (VHE) in the 30 GeV - 30 TeV; the ultra high energy (UHE) in the 30 TV - 30 PeV range; and the extremely high energy (EHE) above 30 PeV.

1.1.1 Cosmic-rays Spectrum

As shown in Figure 1.1[1], the domain of the cosmic-rays is very wide: its energy extends over more than 13 decades in energy, approximately from $10^9 - 10^{21}$ eV, and its fluxs for 32 order of magnitudes, from $10^{-28} - 10^4$ (m^2 sr s GeV)$^{-1}$. The flux as a function of energy is described by a power-law:

$$\frac{dN}{dE} \propto E^{-\alpha} \tag{1.1}$$

where the spectral index, α, slighly varies between 2.5-3, depending on the energy range. In particular:

- $\alpha \simeq 2.7$ for energies $E \leq 10^{15.5}$ eV;
- $\alpha \simeq 3.0$ for energies $10^{15.5} < E < 10^{18}$ eV;
- $\alpha \simeq 2.6$ for energies $E \geq 10^{18}$ eV.

The energies corresponding to the changes of the index α are called *knee* and *ankle*, respectively. The cosmic-rays characterized by energies below $10^15.5$ are supposed to be of galactic origin, while the particles with energies above 10^{17} eV are supposed to be of extragalactic origin because the galactic magnetic field would be too weak to trap and confine them. There is a theoretical upper limit to the maximum energy of the cosmic-rays, called *GZK cutoff* [3], [4]. This is due to pion photon-production when a proton with energy above 10^{20} eV interacts with the photons of the cosmic microwave background (CMB) radiation:

$$\begin{aligned} p + \gamma_{CMB} &\longrightarrow \Delta^+ \longrightarrow p + \pi^0 \\ p + \gamma_{CMB} &\longrightarrow \Delta^+ \longrightarrow n + \pi^+ \end{aligned} \tag{1.2}$$

generating a less energetic proton and a neutral pion, or a neutral and a positively charged pion.

1.1.2 Air Particle Showers

The atmosphere is generally opaque to electromagnetic radiations, with the exception of the optical band, the radio band, and some narrow infrared bad (at higher altitude). Instead, at X- and γ-ray energy the atmosphere is completely opaque, this radiation can not be detected directly.

When cosmic-rays enter the Earth's atmosphere, they interact with its atoms through different processes that depend on energy. Cosmic-rays with energy up to 20 MeV interact by Compton and photoelectric effect, between 20 and 50 MeV by e^+e^+ couple production, and above 50 GeV they initiates cascades of secondary particles, called *air particle showers*. These showers can be distinguished in electromagnetic and hadronic, depending on the nature of their generating particle, called *primary particle*. Electromagnetic showers are generated mainly by electrons, positrons, and photons, while the hadronic ones by protons, neutrons, pions, kaons, and exotic barions.

[1] http://astroparticle.uchicago.edu

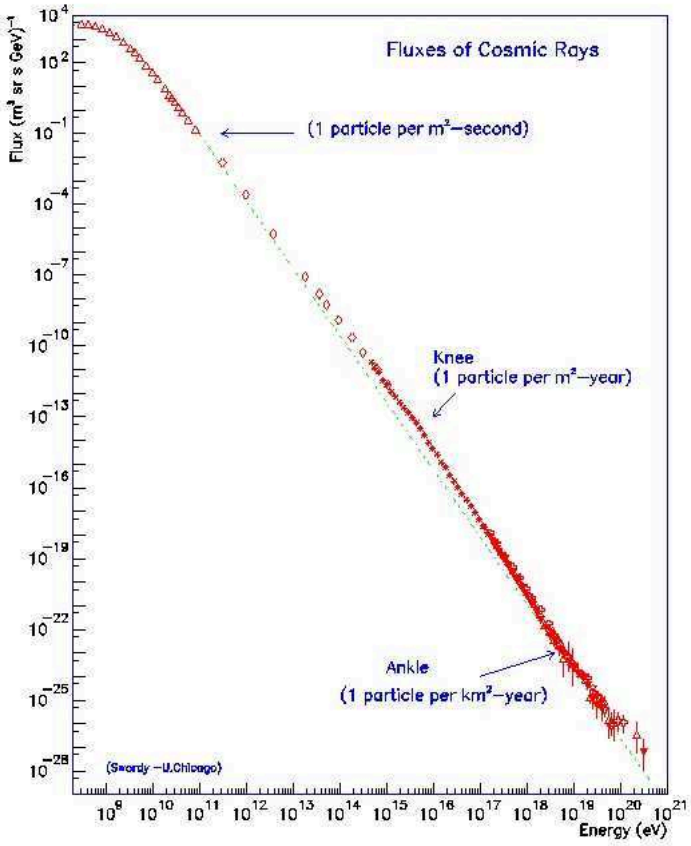

Figure 1.1: Energy spectrum of the cosmic rays.

Electromagnetic Air Showers

Let's consider that the primary particle originating an electromagnetic air shower is a γ-ray with energy E_0. When it enters the atmosphere, it interacts with the electromagnetic field of the atoms, and after travelling an X_0 lenght, produces an e^+e^- pair or, more rarely, a $\mu^+\mu^-$ couple since muons have a smaller cross-section. After the pair production, the electron and positron will have an energy of $E_0/2$ each. They, in turn, will cover an X_0 lengh before producing a γ photon of energy $E_0/4$ by Bremsstrahlung. These secondary γ can produce further e^+e^- couples and the process keep going on - doubling its particles at each X_0 - until a threshold energy is reached. A γ-ray photon can produce a couple e^+e^- down to an energy of 83 MeV, below this energy the process ends.

In Figure 1.2, the develope of an electromagnetic shower is shown. The shower reaches its maximum when the energy of the single particles e^+ and e^- assumes the critical value of $E_c = 83$ MeV. At this energy, the energy losses by ionization and Bremsstrahlun are balanced. The photons generated by these particles are approximately characterized by an energy of few MeV, and photoelectric absorption and the Compton scattering become the dominant processes, and the shower stops developing. The maximum distance X_{max} reached by the shower corresponds to $X_0 \ln(E_0/E_c)$, where $X_0 \sim 37$ g cm^{-2} is the typical atmosphere radiation length in the ultra-relativistic regime for pair production and the ensuing emission of a γ photon by Bremsstrahlung. At each step n of the process the number of the particles is given

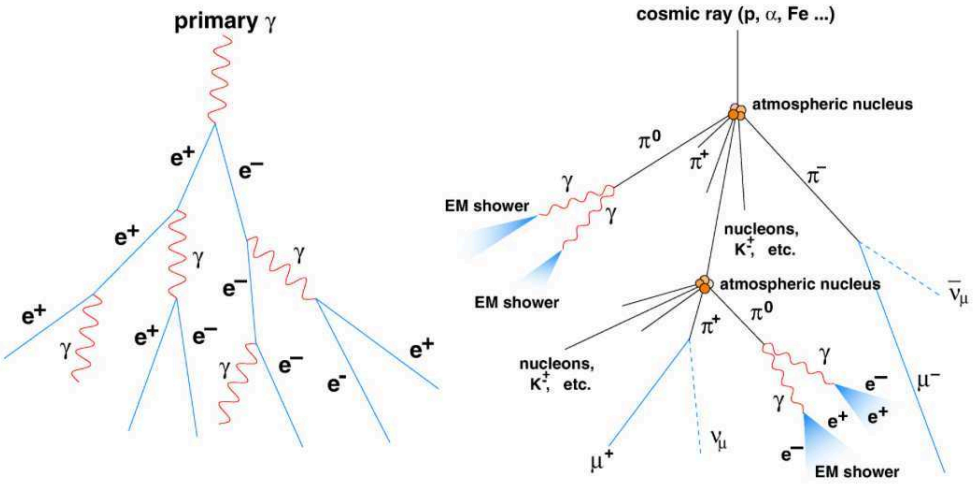

Figure 1.2: Left: a typical electromagnetic shower developement. Right: an example of hadronic shower [5].

by 2^2, and at the end the total number contained in the shower is $N_{max} = \ln(E_0/E_c)/\ln(2)$.

The longitudinal development of the shower, i.e., the variation of the total number of e^+e^+ is given by

$$N_e^{\pm}(t) = \frac{0.31}{\sqrt{\ln(E_0/E_c)}} e^{t(1-1.5\ln(s))}$$

where $t = X/X_0$ is the optical depth, and s the age of the shower defined by:

$$s = \frac{3t}{t + 2\ln(E_0/E_c)} \ .$$

Figure 1.3 shows the relations between some quantities characterizing the showers. The parameter s indicates the evolution status of the shower: $s < 1$ before reaching the maximum, $s = 1$ at its maximum, $s > 1$ after the maximum, $s = 2$ end of the shower. From the Figure is quite easy to see that a shower generated by a primary particle of $E = 10^{17}$ GeV reachs their maximum at 3000 m above the sea level, particle of $E = 10^{15}$ GeV at 5000 m, particle of $E = 10^{13}$ GeV at 7000 m, and so on. This means that a large number of particles can reach the ground, especially if we consider high altitude sites.

The trasversal development of the shower is due to the coulombian scattering and to the particle interactions with the Earth magnetic field. However, due to the relativistic velocity of the particles, the latter effect is quite negligible, making the electromagnetic shower compact and strongly collimated along the incident direction of the primary γ-ray.

Hadronic Air Showers

These kind of shower are produced mainly protons, since they form the most of cosmic-rays. When they entering the atmosphere, they interact with their atoms to create secondary particles as pions, kaons, nucleons that, in turn, can generate other particle. The formation of secondary particles keeps going on until the pion production threshold is reached, corresponding to 1 GeV. When the energy of the particles reaches this critical value, the shower stops

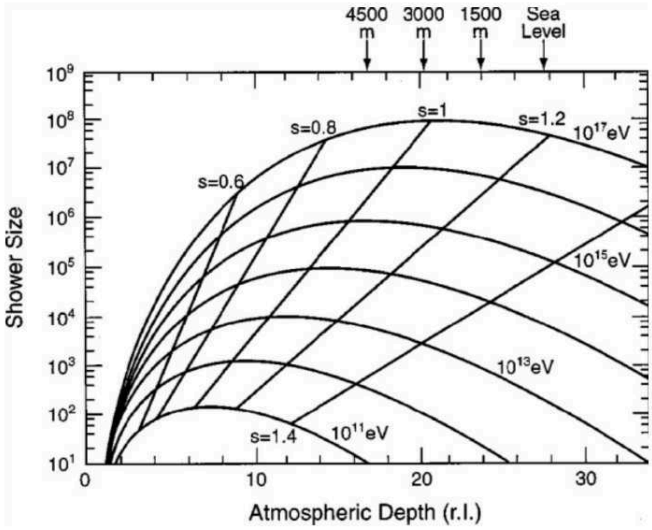

Figure 1.3: Longitudinal shower development [6] as a function of the energy of the primary particle. Parameter s refers to the the developement of the shower: $s = 1$ corresponds to its maximum developement [6].

developing. The proton atmospheric radiation lenght is $X_0 = 67$ g cm^{-2}, higher than the lenght characterizing the electromagnetic shower due to the higher mass. The development of an hadronic shower is more complicate than that of an the electromagnetic one, because many more reaction channels are involved. In fact, protons interacting with the atmospheric atoms can produce kaons, pions and nucleons that in turn can split into other different reaction. In particular kaons can decay in muons, pions and neutrinos; charged pions can decay in muons and neutrinos; some muons can decay in electrons; and neutral pions can decay in γ-photons. Due to all these different channels, the transversal development of the hadronic showers is generally much larger than the electromagnetic ones.

A typical hadronic shower, shown in Figure 1.2, is formed by three different components:

- a hadronic core, made by high-energy nucleons and mesons that decay in muons and neutrinos following the reaction $k^{\pm} \rightarrow \mu^{\pm}\,\nu_{\mu}(\bar{\nu_{\mu}})$, $k^{\pm} \rightarrow \pi^{\pm}\,\pi^{0}$, $\pi^{\pm} \rightarrow \mu^{\pm}\,\nu_{\mu}(\bar{\nu_{\mu}})$;
- a muonic component, deriving by the kaon and pion decays. Due to the long lifetime, they can even reach the ground, carring on a significative fraction of the energy of the primary particle. Nevertheless, a small fraction of muons decay into electros according to the reaction $\mu^{\pm} \rightarrow e^{\pm}\,\nu\bar{\nu}$;
- an electromagnetic component, due to the neutral pions decay. Neutral pions are about 30% of the total pions producted in the shower, and can generate two γ-photons, $\pi^{0} \rightarrow \gamma\gamma$. The γ-ray photons in the hadronic showers are indistinguishable from those of the electromagnetic ones. So, they represent the main source of background in ground-based γ astronomy.

By assuming that any particle of atomic mass A and energy E_0, able to generate a hadronic shower, can be considered as formed by several protons - each with energy E_0/A, the longitudinal developement of the hadronic showers can be expressed as:

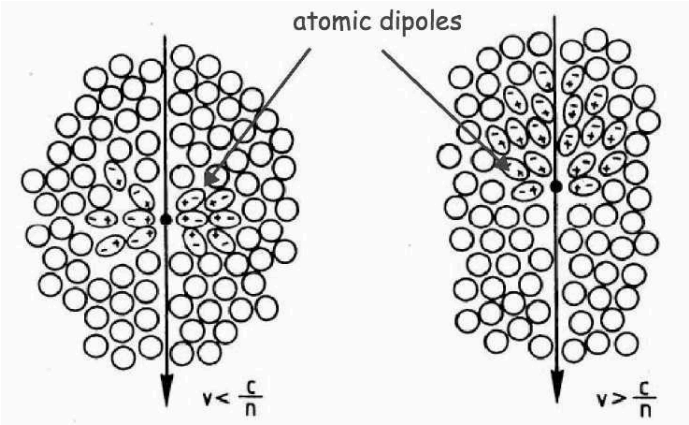

Figure 1.4: Polarization of the atoms in the atmosphere due to the motion of a non-relativist (left) and relaticistic (right) charged particle.

$$X_{max} \propto \ln\left(\frac{E_0}{A\,E_c}\right)\epsilon_N$$

where $\epsilon_n \sim 100$ g cm^{-2} is the nuclear absorption length in the atmosphere. This means that heavier nuclei are not able to penetrate deeply into the atmosphere and produce more extensive and larger showers.

1.1.3 Cherenkov Effect

When a charged particle passes through a dense medium with a velocity exceeding the light velocity in that medium, electromagnetic radiation is emitted, propagating with a conic wave front. This effect is known as *Cherenkov effect*. Such emission occurs since the charched particle polarizes the atoms lying along its path, transforming them into electric dipoles. The time variation of the charge results in the emission of electromagnetic radiation.

If the particle has a velocity $v < c/n$ (where $n > 1$ is the refraction index of a transparent medium) - i.e., in non-relativistic condition - the polarization created by the particle is characterized by spheric simmetry, as shown in Figure 1.4(left). In this case, the photons emitted by the polarized atoms, interfer destructively to one another, with no resulting radiation. On the contrary, if $v > c/n$, the superluminal particle generates an asymmetric polarization, as shown in Figure 1.4(right), that resluts in a radiative contribution. Such radiation, called *Cherenkov radiation* is emetted by the atoms of the medium surrounding the particle, and not by the particle itself. The relativistic particle loses part of its energy by polarizing the medium, that returns such energy in terms of radiation. In particular, the particle during its motion modify the atoms'configuration, giving them a dipole moment that disappears, once the relativistic particle has flown by. So the charges that constitutes the dipole moment are istantaneously accelerated to re-establish their previous equilibrium configuration, and emit radiation.

The radiation praopagates in a conic wave front, analogous to the Mach cone for the mechanic waves. The angle, θ, between the particle path and the Cherenkov photons, can be obtained by simple geometric consideration and is given by:

$$\theta = \arccos\left(\frac{1}{n\beta}\right) \tag{1.3}$$

where n is the refraction index of the medium, and $\beta = v/c$. The Cherenkov light is emitted only if the condition $\beta > 1/n$ is satisfied, i.e., if the particle is relativistic and if its velocity is $v > c/n$. Since the velocity of the particle cannot exceed the light velocity, ther e is a maximum limit on the angle emission cone:

$$\theta_{max} = \arccos\left(\frac{1}{n}\right)$$

obtained for $\beta = 1$. It is also possible to obtain the minimun velocity for a particle to emit Cherenkov light $v = c/n$, that corresponds to the light velocity propagation in the medium crossed by the particle. Anothe important quatity is the energy threshold for a given particle to produce Cherenkov light:

$$E_{th} = \frac{mc^2}{\sqrt{1 - \frac{1}{n^2}}} .$$

Indeed, the energy threshols is a function of the altitude, since it dependes on the refraction index that decreases according to the relation $n = 1 + \eta_h = 1 + \eta_0 e^{(-h/h_o)}$, where h is the altitude, $h_0 \sim 7.1$ km the altitude scale, and η_0 the refraction index at the sea level. The energy threshold as a function of altitude becomes:

$$E_{th} = \frac{mc^2}{\sqrt{2\eta_0 e^{(-h/h_o)}}} .$$

At sea level, the electron energy threshold correspond to $E_{th}(e^-) = 21.3$ MeV, for protons $E_{th}(p) = 39.1$ GeV, and for muons $E_{th}(\mu) = 4.4$ GeV. Since η_h decreases with the altitude, the energy threshold increases: at 10 km altitude, the electron energy threshold is $E_{th}(e^-) = 42$ MeV. From equation 1.3, also the Cherenkov angle descreses with increasing altitude. The Cherenkov photons produced at higher energy have to travel longer distances before reaching the ground, so they distribute on a larger surface than photons emitted at lower quotes. This causes a spread of the signal and a descreasing in the surface energy density of the Cherenkov photons. The area that hold the Cherenkov photons reaching the ground is called *Cherenkov pool*, and it has a radius of about 120 m.

The Cherenkov intensity scales as λ^-3. Its spectrum is limited for low λ -i.e. in the X-ray region - where the refraction index is < 1, and the condition for the emission are not satisfied anymore. The Cherenkov spectrum, i.e., the number of emitted photons, per unit of path lenght, and in the range $[\lambda_1, \lambda_2]$ is given by:

$$\frac{dN}{dx} = 2\pi\alpha\left(\frac{1}{\lambda_1} - \frac{1}{\lambda_2}\right)\left(1 - \frac{1}{\beta^2 n^2}\right) \simeq 44 e^{(-h_0/h)}$$

where here $\alpha = e^2/\hbar c$. The Cherenkov light is emitted between 290 and 600 nm, in the UV-VIS range. By considering that the number of the emitted photons is proportional to λ^{-2}, the most of the Cherenkov emission is concentrated in the blue band. An electromagnetic shower generated by a 1 TeV primary particle, the number of Cherenkov photons, $N_\gamma = 8.2 \times 10^3$ per unit of wavelenght. This implies a flux at the ground level of 30-50 photon/m^2 in an 100

m-radius area. Finally, the Cherenkov cone is affected by the geomagnetic field that, acting on the charged particles, causes a widening in the West-East direction.

The Cherenkov light is produced in the atmosphere, so there are several attenuation process to be taken into account:

- Rayleigh scattering. A photn of wavelenght λ is diffused by air particles, whose dimension is $< \lambda$. The diffusion coefficient is proprotional to λ^{-4}, so photons characterized by lower λ are much more diffused. This kind of scattering dominates at an altitude between 2 and 15 km.
- Mie scattering. The particles responsible of this scattering are mainly dust, and drop of water. This process does not depend strongly on the wavelenght, but it difficult to be modelled due to the motion of the diffusive particles.
- Molecolar absorption. This is due to H_2O and CO_2 molecules and affect mainly photons characterized by $\lambda > 800$ nm. It is important because it determines the upper frequency limit of the Cherenkov spectrum.
- Ozon absorption. The O_3 layer is responsible of the absorption of photon characterized by $\lambda < 290$ nm, $O_3 + \gamma \rightarrow O_2 + O$.

1.2 γ-ray Production

In the Universe, γ-rays are produced in presence of high-energy charged particles. So the presence of γ-sources are strictly related to regions permeated by high-energy hadrons end leptons. The processes originating γ-rays can be distinguished into two main classes: (i) the leptonic processes, in which relativist electrons generate radiation that, in turn, can produce γ-photons through inverse Compton; and (ii) hadronic processes where the γ-emission is generated by the interaction between ultra-relativistic protons and the photon field or the matter sorrounding the source. So, the presence of both relativistic particles and their emission are the building blocks to understand how γ-ray emission originate. For this reason, it is necessary to understand which mechanisms are able to accelerate particles up to relativistic energies, and which are the radiative processes involving such charged particles. In what follows, the main processes at the base of the γ-ray origin are described, however a full treatment can be found in [2].

1.2.1 Synchrotron Radiation

Relativistic electrons travelling through a magnetic field generated by a celestial object, follow helical paths around the magnetic field lines, and - since they are subjected to a centripetal acceleration - emit synchrotron radiation. The emission spectrum of a particle distribution can range from radio to γ, and is a function of the magnetic field intensity and the electron density.

A charged relativistic particle in a magnetic field is subjected to the Lorentz force, and its motion equation are:

$$\frac{d}{dt}(\gamma m \bar{v}) = \frac{e}{c}\bar{v} \wedge \bar{B} \tag{1.4}$$

$$\frac{d}{dt}(\gamma mc) = e\bar{E}\vec{v} \ . \tag{1.5}$$

If the electric field is $E = 0$, from Equation 1.5 it results that the energy γ is constant, and therefore also the velocity $\bar{v}$. So, Equation 1.4 can be re-written as:

$$\gamma m \frac{d\bar{v}}{dt} = \frac{e}{c}\bar{v} \wedge \bar{B} \; . \tag{1.6}$$

This last equation can be written by recurring to the parallel and perpendicular components of the velocity, $v_{\parallel}$ and $v_{\perp}$, with respect to the magnetic field direction. For the parallel component it results:

$$\frac{v_{\parallel}}{dt} = 0$$

that implies $v_{\parallel} = const$, while the solution of the motion equation in the perpendicular direction results in an uniform circular motion with frequency:

$$\omega = \frac{eB}{\gamma mc} = \frac{\omega_L}{\gamma} \tag{1.7}$$

where ω_L is the so-called Larmor frequency. So the motion of the relativistic electrons is an elicoidal path - with constant pass - along the lines of the magnetic field.

The synchrotron radiation is strongly collimated in a cone characterized by an angle $\alpha \sim m_e/E \sim 1/\gamma$, along the particle motion direction. For this reason, an hypotetical observer is reached by the radiation only when such cone is pointing towards its direction. In particular he can observe a series of pulses with a duration $1/\gamma^3\omega$ with a frequency of $2\pi/\omega$. The higher is the energy particle, the smaller is the aperture α of the emission cone. This has a direct implication on the frequency of the emitted radiation: the smaller is α, the smaller is the emission time, and higher is the characteristic frequency ω_c:

$$\omega_c = \frac{3}{2}\gamma^2 \omega_{cicl} \tag{1.8}$$

where $\omega_c = (2\pi qB)/(mc)$ is the cyclotron frequency. The spectrum of the emission given by a single particle results peaked around the characteristic frequency. Since its motion is periodic, the spectrum is composed by a serie of spectral lines at the characteristic frequency and by all their harmonics. However, the separation between the emission lines becames smaller and smaller with increasing enegy particle, up to form a continuum spectrum. In Figure 1.5(a) the normalized emission spectrum by a single particle is shown. The flux is given by

$$F(\omega) \propto \begin{cases} \left(\frac{\omega}{\omega_c}\right)^{1/3} & \text{if } \omega/\omega_c \ll 1 \\ \left(\frac{\omega}{\omega_c}\right)^{1/2} e^{\frac{-2\omega}{\omega_c}} & \text{if } \omega/\omega_c \gg 1 \end{cases}$$

However, the observed radiation is given by the all the contributions resulting from an ensemble of particles, characterized by a given energy distribution. The most common function for a distribution of high energy particle is given by:

$$N(E)dE = C_0 E^{-s} dE \tag{1.9}$$

that is equivalent to:

$$N(\gamma)d\gamma = C_1 \gamma^{-s} d\gamma \tag{1.10}$$

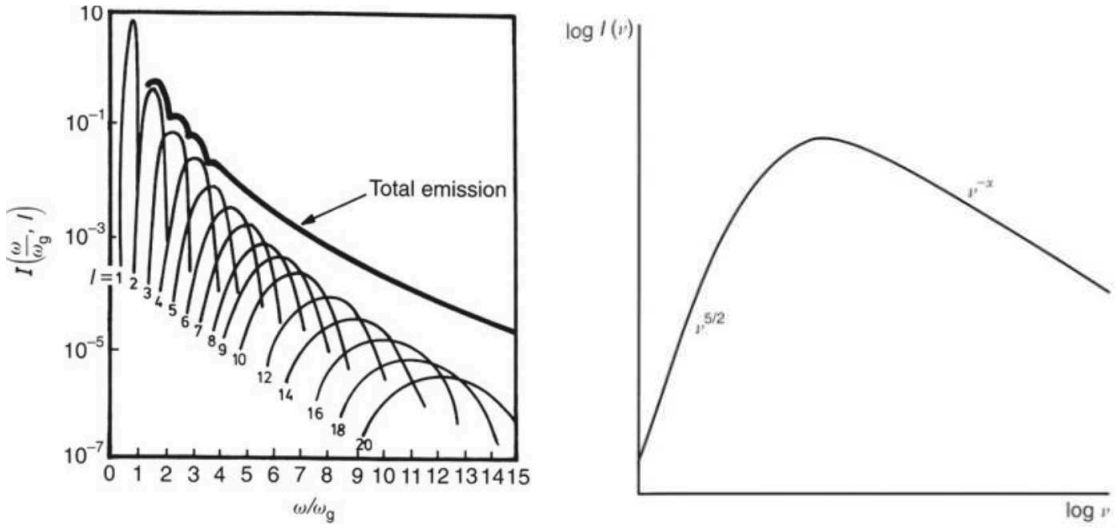

(a) (b)

Figure 1.5: (a): the synchrotron emission spectrum formed by the first 20 harmonics of mildly relativistic cyclotron radiation for an electrons with $v = 0.4c$. (b): the synchrotron spectrum which shows the phenomenon of synchrotron self-absorption. From [2].

with $\gamma_1 < \gamma < \gamma_2$. So, the radiated power is given by integrating the emission of a single particle over all the particle distribution:

$$F(\omega)_{tot} = C_1 \int_{\gamma_1}^{\gamma_2} F(\omega)\gamma^{-s} d\gamma \tag{1.11}$$

that, by placing $x = \omega/\omega_c$ and $\omega_c = \gamma^2 \omega_{cycl}$, results:

$$F(\omega)_{tot} = \frac{C_1}{2} \left(\frac{\omega}{\omega_{cycl}}\right)^{\frac{-(s-1)}{2}} \int_{x_1}^{x_2} F(x) x^{\frac{s-3}{2}} dx \ . \tag{1.12}$$

From the last equation, it is clear that if the particle energy distribution follow a power-law function characterized by an index $-s$, the emission spectrum is still described by a power-law function, but with index $-(s-1)/2$. In Figure 1.5(b) a generic synchrotron emission spectrum is shown. In the optically thin part, the spectrum is characterized by a trend $I(\nu)d\nu \propto \nu^{(1-s)/2}$, while at low frequencies by $I(\nu) \propto \nu^{5/2}$. Since the electrons are emitting radiation, they lose their energy. So, the synchrotron procees is a cooling process. The energy loss rate is $dE/dt \propto B^2 E^2$.

1.2.2 Bremsstrahlung Radiation

This process involves mainly free electrons immersed in ionized gas. These electrons, by interacting with the electric field of heavy nuclei, are decelerated and emit radiation. Such an emission is the so-called Bremsstrahlung radiation. Every charged particles emit through this mechanism, however - since the emitted power is proportional to m^{-4} (where m is the particle mass) - the process is more efficient for lighter particles. In Figure 1.6 the Bremsstrahlung spectrum is shown. It is a continuum spectrum with an increasing intensity with the increasing

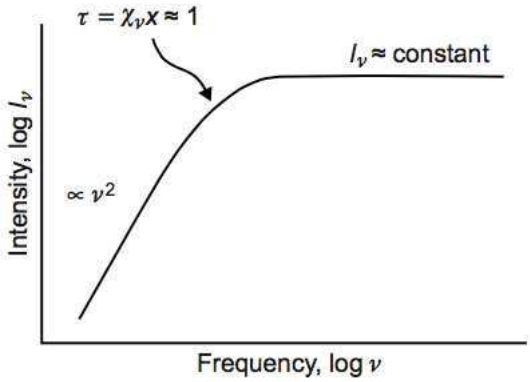

Figure 1.6: An example of thermal Bremsstrahlung spectrum that shows self-absorption at low radio frequencies [2].

frequencies and the particle energy. It can be divided into (i) an optically thin part, and (ii) an optically thick part. In the optically thin part the intensity is porportional to ν^α (where $\alpha \sim -0.1$), while in the thick part it is proportional to $(2KT\nu^2)/c^2$.

In case of relativistic electrons, the Bremsstrahlung emission is strongly collimated along the motion of the particle, inside a cone characterized by an angle $\theta \sim 1/\gamma$. The Bremsstrahlung emission is dominant with respect to the ionization process if the energy of the free particles travelling in the medium exdeed an energy threshold, E_0, given by:

$$E_0 =\simeq \frac{1600mc^2}{Z}$$

where m is the mass of the particles, and Z the atomic number of the atoms of the medium. The particle energy losses are given by the formula of Bethe-Heitler:

$$E(X) = E_0 e^{-X/X_0}$$

that represent the fraction of energy loss for Bremsstrahlung emission when the particle has travelled for a distance X. X_0, the so-called radiation length - represent the traveled path at the end of which the loss of energy is $1/e$, and is expressed through the relation:

$$X_0 \propto \frac{A}{Z^2\rho}$$

where A is the atomic mass, and ρ the density medium. Since X_0 is proportional to the medium density, cosmic-rays penetrate more efficiently less dense media.

The Bremsstrahlung radiation is observed above all in ionized gas region, and its spectrum typically ranges from the radio band (e.g., the planetary nebulae) to the X-band (e.g., the clusters' hot medium). However, if the relativistic particles are accelerated up to TeV energies, Bremmstrhalung radiation can reach the γ-band.

1.2.3 Inverse Compton Scattering

The Compton scattering is a process related to the collisions between an electron and a photon, with the ensuing energy transfer from the photon to the electron. However, when

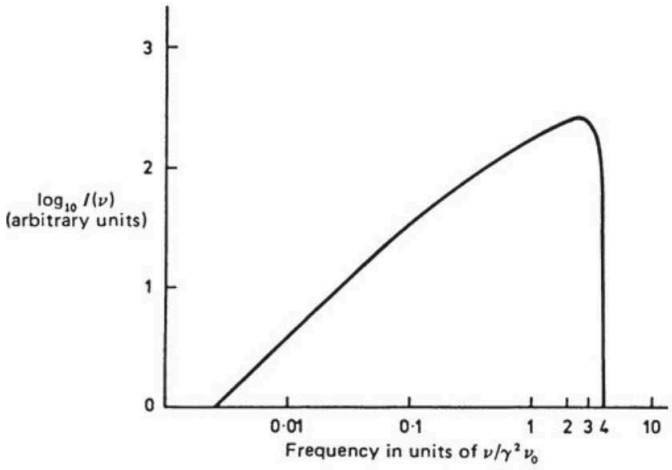

Figure 1.7: A typical spectrum due inverse Compton scattering [7].

the energy of the electron is much greater than that of the photon, the collision can transfer energy from the electron to the photon. Such process is called inverse Compton scattering. In particular, when relativistic electrons interact with low energy photons, the energy of the latter can be increased up to the X- and γ-bands. In other words, the inverse Compton is a cooling process that transfers part of the energy of the electrons to the photon field.

Given an energy-density electron distribution and a photon field distribution, it is possible to compute the inverse Compton contribute in two regimes: (i) in the Thomson limit, and (ii) in the Klein-Nishina limit. In the Thomson regime, the photon energy - in the electron frame - satisfies the relation $E_\gamma \ll m_e c^2$. In this case the cross-section of the process - the Thomson cross-section - is independent from the energy of the photon and it is given by:

$$\sigma_T = \frac{8}{3}\pi r_e^2 \, . \tag{1.13}$$

The Thomson cross-section is used to compute the energy losses - i.e., the radiated power - that are given by:

$$\frac{dE}{dt} = \frac{4}{3}\sigma_T \, c \, \gamma^2 \, \beta^2 \, U_{rad} \, . \tag{1.14}$$

In Figure 1.7 the inverse Compton spectrum given by a mono-energetic electron population is shown. Some features characterize such spectrum: (i) the collision kinematics put an upper limit on the maximum energy that the photon can reach: $E_{max} \sim 4\gamma^2\epsilon$, where ϵ is the energy of the photon; (ii) at low energy the spectrum tends to zero; and (iii) the maximum emission is located at $E \sim 3\gamma^2\omega$.

When the electron population is described by a power-law, with a spectral index q, and the photon field is characterized by a temperature T, the photon energy distribution is given by:

$$\frac{dN_\gamma}{dE_\gamma} \propto E_\gamma^{-\frac{q+1}{2}} \, . \tag{1.15}$$

The (extreme) Klein-Nishina regime occurs when $E_\gamma \gg m_e c^2$ in the electrons rest of frame. In this case the cross-section to be used is the Klein-Nishina one, given by:

$$\sigma_{KN} = \frac{3}{8}\sigma_T \frac{mc^2}{E_\gamma}\left[\frac{1}{2} + \ln\left(\frac{2E_\gamma}{mc^2}\right)\right] . \tag{1.16}$$

In this case the energy loss rate is:

$$\frac{dE}{dt} \sim \frac{4}{3} c\sigma_t \, \gamma^2 \, T^4 \tag{1.17}$$

and, when the injection electron distribution is described by a power-law with index q, the steady state electron distribution is:

$$\frac{dN_\gamma}{dE_\gamma} \propto E_\gamma^{-(q+1)} \ln(E_\gamma) . \tag{1.18}$$

While in the Thomson limit the total emitted power depends on the square of the electron energy, in the Klein-Nishina regime it shows only a logarithmic dependence.

1.2.4 Particle Acceleration: Fermi I and II Mechanism

So far, the effects of relativistic charged particles traveling thorugh magnetic fields, photons fields, and matter have been discussed. Let's now consider the mechanisms that can accelerated particles up to these energies.

Fermi proposed a stochastic model - now called second-order Fermi mechanism (Fermi II) - where particles can gradually increase their energy due to collisions with the dishomogeneities of the local magnetic field, or with the particles of a moving plasma. This mechanism is slower than the standard acceleration ones, but it can increase the energy particles over several orders of magnitude. Let's consider a region containing a number of particles $N_0 \gg 1$, with initial energy E_0. Let's consider also a test particle that after the local collision increases its energy according to:

$$E_{fin} = E_{init}(1 + \psi)$$

where $\psi = \Delta E/E \ll 1$ is the energy increment. After k collisions the energy of the test particle is given by:

$$E_k = E_0(1 + \psi)^k$$

The probability, P_k, for the particle to escape the acceleration region is given by considering the probability $(1 - p)$ that such particle remains confined in the region, and the probability to escape after $(k + 1)$ collisions:

$$P_k = \underbrace{(1-p)\ldots(1-p)p}_{k \text{ times}} . = p(1-p)^k$$

So, the number of particles, n_k, escaping the acceleration region with energy E_k is given by:

$$n_k = N_0 P_k = N_0 p(1-p)^k = N_0 P \left(\frac{E_k}{E_0}\right)^{\frac{\ln(1-p)}{\ln(1+\psi)}} .$$

The particle energy spectrum becomes:

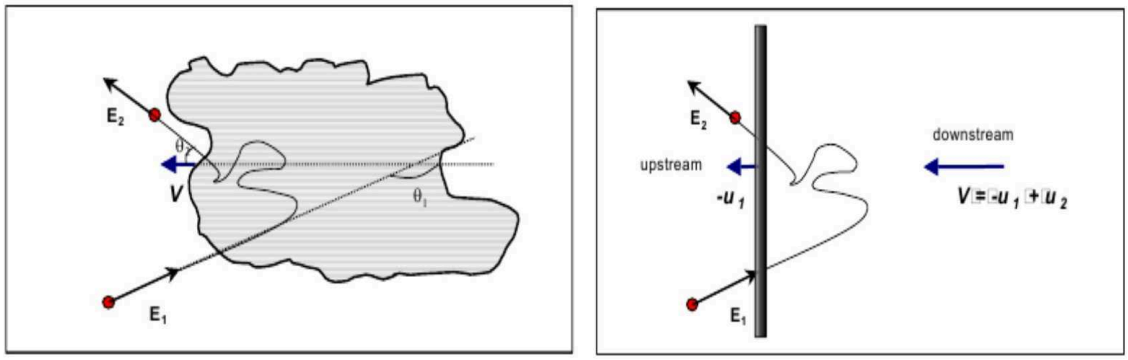

(a) (b)

Figure 1.8: (a) Fermi II acceleration mechanism: charged particle collisions with a magnetic cloud. (b) Fermi I acceleration mechanism: charged particles crossing a front shock.

$$\frac{dn}{dE} \propto E^{\frac{\ln(1-p)}{\ln(1+\psi)}-1} .$$

In the laboratory reference system the particle has an energy given by:

$$E_1^{'} = \gamma E_1(1 - \beta\cos(\theta_1))$$

where E_1 and θ_1 are the energy and the entrance angle of the particle entering the region, respectively, γ is the Lorentz factor of the region, and $\beta = vc$ (with v velocity of the region). When the particle leaves the acceleration region has an energy $E_2^{'}$ that in the laboratory referens system is given by:

$$E_2 = \gamma E_2^{'}(1 + \beta\cos(\theta_2^{'}))$$

where $\theta_2^{'}$ is the exit angle of the particle as seen from the laboratory system of reference. Since inside the acceleration region there are elastic collisions, for the energy conservation $E_2^{'} = E_1^{'}$. The energy gain, ϵ, in the laboratory reference system is given by:

$$\begin{aligned}
\epsilon &= \frac{E_2 - E_1}{E_1} \\
&= \frac{\gamma E_2^{'}}{(}1\beta\cos\theta\theta_2^{'})\frac{E_1^{'}}{\gamma(1 - \beta\cos(\theta_1))} - 1 \\
&= \frac{1 - \beta\cos(\theta_1) + \beta\cos(\theta_2^{'}) - \beta^2\cos(\theta_2^{'})\cos(\theta_1)}{1 - \beta^2} - 1 .
\end{aligned}$$

If $\beta \sim 1$ and the region is big enough, $\langle\cos|\,(\theta_2^{'})\,|=\rangle\, 0$ and the average on the exit angle results $\theta_1 = \beta/3$. So, the average of the energy, $\bar{\epsilon}$, is:

$$\bar{\epsilon} = \frac{1 + \beta^3/3}{1 - \beta^2} \simeq \frac{4}{3}\beta^2 .$$

Even if the energy gain is proportional to β^2, such regions are characterized by small velocity that translates into a low energy gain. For $\beta \sim 10^{-5}$ each single scattering contributes only

with $10^{-10}E_1$. The main weak point of the Fermi II mechanism is that it is not able to reach acceleration up to the observed high energies.

In order to explain particle acceleration up to TeV energies, a similar mechanism was proposed (in the 1970s) based on plane parallel shock waves - such as those approximately encountered in SN explosions. This mechanism is called Fermi I mechanism, for obvious reasons that will be evident below. A shock wave corresponds to a discontinuity of the thermodynamic properties of a fluid, whose velocity varies in a thin fluid layer. Moreover the velocity of such a discontinuity exceeds the sound speed in the medium. This model involves a shock wave propagating in a diffuse medium, e.g., shock waves generated in supernovae explosions. A high-enegy particle flux is supposed to be on both side of the shock. The fluid part not yet reached by the shock is called *upstream*, while the remaining part is called *downstream* . The shock velocity is lower than those of the relativistic particles, so such particles - due to scatterings - can cross the shock in both directions (i.e., the upstream toward the downstream and viceversa). The matter ejected by a supernova reachs velocities up to 10^4 km/s that are much higher than the shock velocity $\sim$ 10 km/s. In the shock reference system the upstream particles reache the wave front with velocity $v_1 = U$ (where U is the shock front velocity), and once passed through it, are characterized by a downstream velocity v_2. The continuity equation imposes the mass conservation through the shock front: $\rho_1 v_1 = \rho_1 U = \rho_2 v_2$ (where ρ_1 and ρ_2 are the upstream and downstream particle density, respectively). In case of strong shocks:

$$\frac{\rho_1 v_1}{\rho_2 v_2} = \frac{\gamma + 1}{\gamma - 1} = 4 \, .$$

For a monoatomic or completely ionized gas $\gamma = 5/3$, that leads to $v_2 = 1/4 v_1$. So, the downstream particle flux travels with $v_2 = 3/4U$ with respect to the upstream one. When a particle crosses the shock front gains an energy $\Delta E/E \sim U/c$. The particles are scattered behind the shock front and their velocity distribution becomes isotropic.

Let's consider now the inverse process, i.e., when a particle passes from the downstream to the upstream region. Such particles meet particles moving towards the shock front with a velocity $v = 3/4U$. So, as in the previous case, they still receive an energy gain equal to ΔE. This means than particles gain energy indipendently from the crossing direction.

The energy of a particle passing from the upstream to the downstream region is:

$$E^{'} = \gamma(E + p_x v) \tag{1.19}$$

where p_x is the perpendicular momentum component to the shock front; $\gamma \sim 1$ since the shock is moving with velocity $U \ll c$. The relativistic particles have energy $E \sim pc$, and the momentum perpendicular component to the shock front is $p_x = p\cos(\theta) = (E/c)\cos(\theta)$. By inserting the latter relation in the Equation 1.19, the energy gain at each crossing results:

$$\frac{\Delta E}{E} = \frac{v}{c}\cos(\theta)$$

By taking into account that the probability that a crossing particle approaches the shock front with an angle in the range $[\theta, \theta + d\theta]$ is proportional to $\sin(\theta d\theta)$, and that the approaching rate - depending on the perpendicular component v_x - is proportional to $c\cos(\theta)$, it is possible to compute the probability that a particle crosses the front:

$$p(\theta) = 2\sin(\theta)\cos(\theta)d\theta \, .$$

The averaged energy gain is given by:

$$\langle \frac{\Delta E}{E} \rangle = \frac{2v}{c} \int_0^{\pi/2} \sin(\theta) \cos^2(\theta) d\theta$$

that lead to

$$\frac{\Delta E}{E} \sim \frac{4}{3}\frac{v}{c} = \frac{4}{3}\beta \, .$$

The Fermi I mechanism, compared to the Fermi II one, leads to an energy gain proportional to β and results more efficient. However, this process requires long time to bring a considerable total energy gain. For example, the acceleration process of a supernova takes 10^5 years, that can lead to a maximum particle energy of 10^{14} eV.

1.2.5 Hillas Diagram

Indipendently from the acceleration mechanism, Hillas [8] proposed a way to describe the source capabilty of accelerating particles at high energy by focussing on their extension. Basically, two requirements are needed: (i) a magnetic field able to confine particles in the acceleration region, and (ii) the dimension R of such a region must be larger than the particle orbital diameter by two Larmor radius, where the latter is defined as:

$$R_L = \frac{E}{BZe} \sim 0.1\mathrm{Mpc}(Ze)^{-1} \left(\frac{E}{10^{20}\mathrm{eV}}\right) \left(\frac{B}{10^{-6}\mathrm{G}}\right)^{-1} \, .$$

By taking into account that the effect of the velocity β on the scattering magnetic centers, it results:

$$\left(\frac{B}{\mu\mathrm{G}}\right) \left(\frac{R}{\mathrm{Kpc}}\right) > \frac{2}{Z\beta} \left(\frac{E}{\mathrm{eV}}\right)$$

where Z and E are the charge and the energy of the particle, respectively. The expression above can be visualized in Figure 1.9 that shows the capability of the source of accelerating particles as a function of their dimensions and magnetic field. There are many potential sites for particles to be accelerated up to 10^{20} eV: pulsar magnetospheres, active galactic nuclei, gamma ray bursts, and relativistic jets. The relation between the maximum energy E_{max} that a cosmic-ray can reach and the source properties can be written as:

$$\frac{E_{max}}{z\beta} = eBcR \, .$$

1.2.6 Hadronic Mechanisms

Unlike leptonic processes, hadronic mechanisms producing γ-rays involve only particles. There are three main precesses: (i) pion decay, (ii) pair annihilation, and (iii) annihilation of dark matter particles.

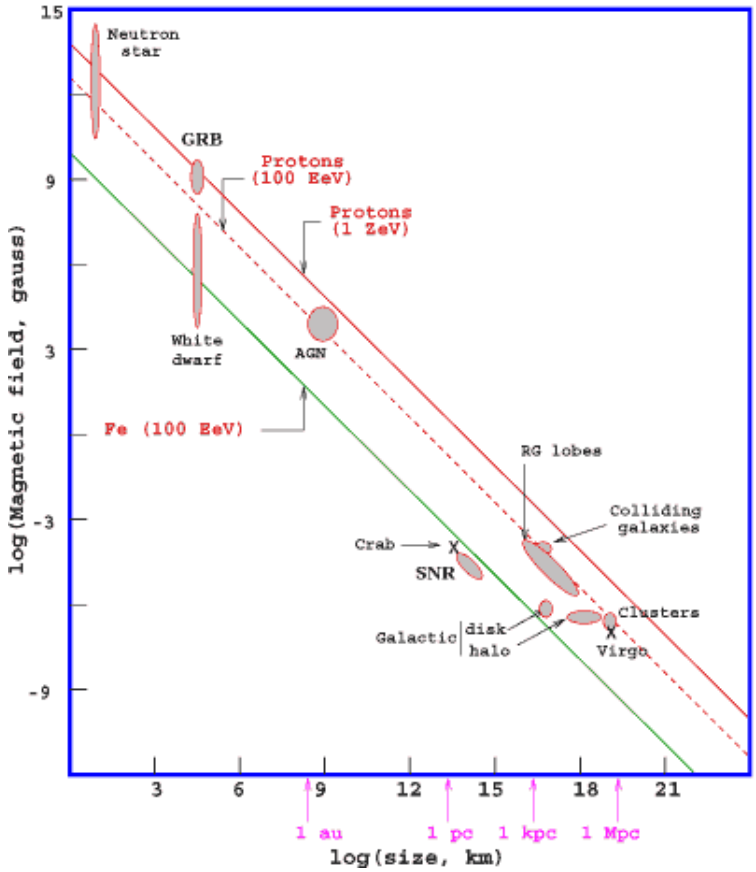

Figure 1.9: Source magnetic field versus source size. All objects lying below the dotted line are not able to accelerate protons above 10^{20} eV. From [8].

Neutral Pion decay

The γ-ray production can occur when ultra-relativistic protons interact with the matter sorrounding a given source. This interactions occur through anelastic collisions that generate basically mesons and kaons. The reaction characterized by the higher cross-section is the proton-proton interaction. The collision between two protons:

$$p + p \longrightarrow p + p + \pi^+ + \pi^- + \pi^0 \tag{1.20}$$

can lead to two less energetic protons, whose missing energy goes in favour to the creaction of charged and neutral pions. Both charged and neutral pions have the same probability to be created. In turn, the charged pions decay following the standard channels:

$$\begin{aligned} \pi^+ &\longrightarrow \mu^+ + \nu_{mu} \\ \pi^- &\longrightarrow \mu^- + \nu_{mu}^- \end{aligned} \tag{1.21}$$

where, in turn the mouns decay into:

$$\mu^+ \longrightarrow e^+ + \nu_{mu} + \bar{\nu_e}$$
$$\mu^- \longrightarrow e^- + \bar{\nu_{mu}} + \nu_e \ . \tag{1.22}$$

The neutral pion dacays are the key for generating γ-ray photons:

$$\pi^0 \longrightarrow \gamma + \gamma \ . \tag{1.23}$$

The decays of charged pions are characterized by a $\tau_{\pi^\pm} = 2.6 \times 10^{-8}$ s, while those of the neutral pion by $\tau_{\pi^0} = 10^{-16}$ s. The energy of each photon, generated by a pion is $E_\gamma = \frac{m_{\pi^0}}{2} \sim 67.5$ MeV, but if the pion has a velocity $v = \beta c$, the energy of each photon in the laboratory rest frame is given by:

$$E_\gamma = \gamma m_{\pi^0}(1 + \beta \cos(\theta_\gamma)) \tag{1.24}$$

where θ_γ is the angle between the pion velocity and the photon emission direction. In such a way, the obtained γ-ray spectrum is characterized by a power-law function with index ~ 2.5. The γ-rays of hadronic origin can be distinguished by the electromagnetic ones thanks to their spectrum. Finally, neutral pions can also be created through interaction between protons and photons of the cosmic microwave background radiation:

$$p + \gamma_{CMB} \longrightarrow \Delta^+ \longrightarrow p + \pi^0 \ . \tag{1.25}$$

Pair Annihilation

Pair annihilations can occur when a particle and its antiparticle approach each other. The annihilation process returns the energy associated with the rest masses in electromagnetic form. This process occurs when the two particles are almost at rest in such a way that their momentum $p = p_1 + p_2 \sim 0$. For momentum conservation, two photons - at least - must be generated. Moreover, for the energy conservation, the wavelenghts associated to the photon are related to the particle mass through the relation $2m_0c^2 = 2hc/\lambda$.

Dark Matter Annihilation

There are several particles candidated to be the building block of the dark matter. These particles are predicted by different models: some particles can interact only gravitationally, but others - such as the Weakly Interacting Massive Particles (WIMPs) - can be involved in annihilation processes or decays that result in γ-ray production. Without entering the details of the nature and the physics of the particle models, the neutralino χ is currently considered the best dark matter candidate. It should be a very stable particle, with a small cros-section, and that can interact only by annihilation processes. Some of this processes lead to the generation of γ-photons. The possible interactions are: (i) decay into two photons, $\chi\,\chi \longrightarrow \gamma\,\gamma$; (ii) decay into a Gauge-boson and a photon, $\chi\,\chi \longrightarrow Z^0\,\gamma$, and (iii) dacay into a Higgs-boson and a photon, $\chi\,\chi \longrightarrow H^0\,\gamma$.

1.3 γ-ray Propagation

When a γ-ray is emitted from a distant source, it has to travel distances before reaching the observer. During their path they can be asbsorbed or they can interact with other particles or photons that cause a flux decrease. Two reactions that involve γ-rays:

1. a pair production due to photon-matter interactions $\gamma(\gamma) \rightarrow e^+ e^-$;
2. a pair production due to photon-photon interactions $\gamma + \gamma_{background} \rightarrow e^+ e^-$.

In the first case the γ-ray escaping from galactic or extragalactic sources interacts with the electromacgnetic field of an atomic nuclei or a cosmic electrons, generating an e^+e^- pair. The second photon represents a virtual photon of the electromagnetic field. However the Universe is quite transparent to this process. The second one is the dominant process and it is particularly relevant because it causes a relevant absorption of the γ-photons, with the ensuing significative decreasing of their flux. This happens when a traveling γ-ray interacts with a photon of the background radiation ligh (see Section 1.3.1). The cross-section of this process is given by the Bethe-Heitler formula [9]:

$$\sigma(E,\epsilon) = 1.25 \times 10^{25}(1-\beta^2)\left[2\beta(\beta^2-2) + (3-\beta^4)\ln\left(\frac{1+\beta}{1-\beta}\right)\right] \tag{1.26}$$

where $\beta = \sqrt{[1-(m_e c^2)^2/(E\epsilon)]}$, m_e electron mass, E energy of the γ photon, and ϵ energy of the background photon. This cross-section is maximized when the energy of the background photon corresponds to $\epsilon = 500GeV/E$ eV, that means that for TeV γ-ray is mostly relevant the interaction with the optical-infrared background, while for the UHE photns ($>$ 1 PeV) the interaction occurs mainly with the photons of the cosmic background radiation.

Pair production is a source of opacity for γ-rays when the mean free path is shorter than the distance of their generating source. The main free path is inversely proportional to the energy of the γ-ray, so photons with energies higher than 100 TeV - coming from distant extragalactic sources - are completely absorbed. The detectability of photons with lower energies depends basically to the source distance. For photons with energies $<$ 10 GeV the Universe is, in practice, totally transparent. Figure 1.10 shows the main free path length as a function of photon energy.
The probability for a photon to survive in their path from the source to the observer is expressed by:

$$\frac{F_{ob}}{F_{em}} = e^{-\tau(E,z)} \tag{1.27}$$

where F_{ob} is the observed flux, F_{em} the emitted one, and $\tau(E,z)$ the optical depth. The latter is a function of photon energy, and the redshift of the source since it is related to its distance. The optical depth is obtained by convolving the numerical density of the background photon field, n_ϵ, with the cross-section expressed by the Equation 1.26, and afterward by integrating over the distance $l(z)$, the scattering angle, θ, and the corrected energy of the background photons according to their redshift:

$$\tau(E,z) = \int_0^z dl(z) \int_{-1}^{1} d\cos(\theta) \int_{\frac{2(m_e c^2)^2}{E(1-\cos\theta)}} d\epsilon(z) n_\epsilon(\epsilon(z),z)\sigma(E(z),\epsilon(z),\theta) \tag{1.28}$$

where the distance is a function of the cosmological parameters and given by [11]:

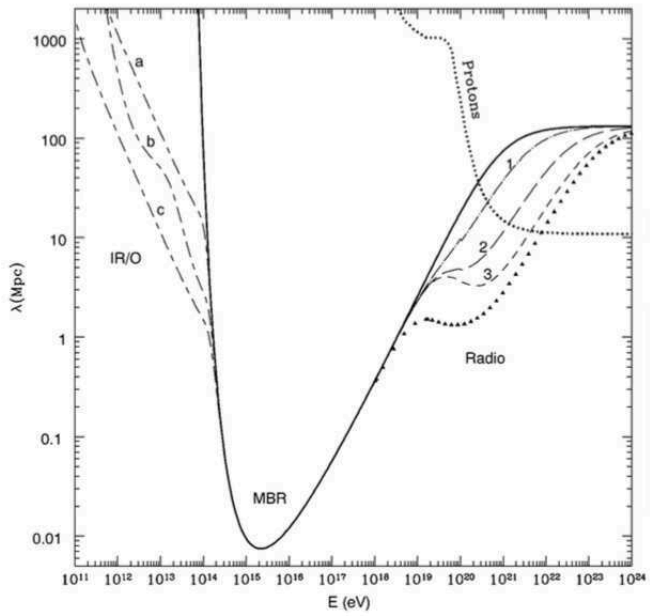

Figure 1.10: Local pair-production mean free path for VHE photons of energy, as a function of the energy photon [10].

$$\frac{d\Omega}{dz} = \frac{c}{H_0} \frac{1}{(1+z)\left[(1+z^2)^2(\Omega_M z+1) - \Omega_\Lambda z(z+2)\right]^{1/2}} \tag{1.29}$$

with Ω_M matter density, and Ω_Λ dark energy density. This absorption makes the observed source flux steeper at the high energies. So, the observed energy spectrum of distant source has to be corrected by EBL absorption.

1.3.1 Extragalactic Background Light

At the beginning of this section, the role of the photon of the Extragalactic Background Light (EBL), in aborbing the γ-ray flux has been pointed out. Nevertheless, its origin and nature have not been clarified. The EBL is formed by the total contribution of the ligh emitted by the stars, and the Active Galactic Nuclei (AGN) during the whole life of the Universe. In other words, it is formed by all the light modified by the redshift, and by the expansion of the Universe - emitted at every cosmic epoch. The spectral distribution of the EBL ranges from the near UV up to the far IR and shows two distinct peaks, as shown in Figure 1.11. The first bump, located at 1 μm, is due to the contribution of the stars and AGN, even less significant. The latter is due to the the star light reprocessed by dusts, and includes both the thermal continuum and the emission lines of the PHA molecules. At higher wavelengths the EBL is dominated by the CMB, while at lower wavelenghts the flux decreases rapidly because of the attenuation due to the molecular hydrogen in the stellar atmospheres, and in the interstellar and intergalactic medium.

Since the EBL is directly related with the star formation history of the Universe, some limits calculated on the EBL can used to put some constraints on the formation and the evolution of the galaxies. There are several approaches focused in estimating the EBL spectrum:

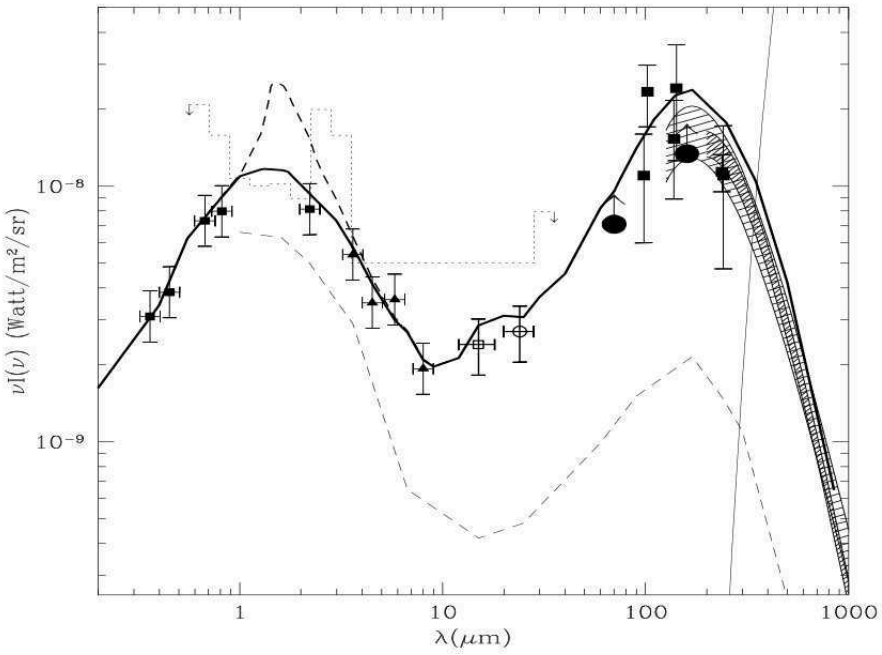

Figure 1.11: The Cosmic Infrared Background (CIRB) spectrum measured by [14], and the estimates of the optical extragalactic background by [15]. Figure from [13].

1. observations of the extragalactic sky brightness. They can provide constraints only on the local background, but not on its redshift evolution;
2. integration of discrete sources observed in large galaxy surveys. However this approach can give only a lower limit because of to the presence of sources not detected due the limit magnitude of the surveys;
3. by reconstructing the modified observed flux of the γ-ray sources. If the γ-ray emission of distant sources were physically known, it would be possible to obtain the EBL by reconstructing the original flux, starting from the observed one. So, the EBL cosmological history could be then reconstructed by comparing the observed fluxes - of source at different redshifts - to their intrinsic spectrum. Although some important constraint obtained with this method in [12], it requires that the knowlwdge of the emission mechanisms and the intrinsic sources' spectra. Unfortunatelly, up to now this is a still opened question;
4. by forward evolution models. In this approach the evolution of the emissivity of the galaxies is computed by starting from the conditions in the early Universe. The process of galaxy formation are then simulated to obtain the actual observable and the spectrum of the EBL;
5. by background evolution models. Here the EBL is computed by starting from the galaxy luminosity functions and trying to reconstructing its evolution with the redshift, once an evolution function has been assumed. The most popular and used EBL model is that obtained in [13].

1.4 γ-ray Detection

As seen in the previous sections, the γ-ray spectrum covers a very wide range of energy, and usually its flux decreases with the increasing energy. For these reasons only one kind of detector is not sufficient to explore all the γ-ray spectrum, and to have a complete panoramic of the high energy phenomena. There are two main categories of detectors: the ground-based, and the space ones. They are complementary because they detect the γ-ray emission in different part of the spectrum. The space telescopes detect LE, ME, and HE photons (i.e., in the MeV - GeV range), since the athmosphere is completely opaque at these energies due to the absorptions processes. On the other side, the ground based telescopes with their big detection area can detect the γ-ray photons at VHE and above, by cathing the Cherenkov light produced in thier interaction with the atmosphere.

1.4.1 Ground-based Detectors

All the ground-based telescopes built to detect the γ-rays do not detect directly the γ-photons, but the products of their interactions with the atmosphere, in particular they detect the Cherenkov light of the atmospheric showers (see Section 1.1.3) produced when a γ-ray enters the atmosphere. The ground-based detectors work basically at energies between 100 GeV and 100 TeV. There are two types of detectors: the Cherenkov telescopes operating from $\sim$100 GeV to 50 TeV, and the EAS (Electromagnetic Air-Shower) detectors operating from $\sim$400 GeV to 100 TeV.

Cherenkov telescopes

The Cherenkov telescopes, by recurring to the IACT tecnique (see Section 1.4.2), detect the Cherenkov light produced by the motion of relativistic particles in the atmosphere. These big telescopes are made by a very large collector, usually a parabolic reflective dish, that reflect the Cherenkov light on a camera. Such camera, located on the telescope focal plane, is composed by an array of photomultiplier tubes[2] with a tipic quantum efficiency of 30%. The signal collected in the camera is then transferred to a trigger system, responsable of the selection of the events generated by the air shower. The events outcoming from the trigger are then sent to a data aquisition system, ready to be analyzed.

The duration of the ligh generated by an air shower is typically around 3-4 ns, and the typical time resolution on the arrival time is $\sim$ 1 ns. These telescopes are characterized by a high sensitivity, a low energy threshold, but a small field of view (few squared degrees) that allow only observation of single sources. Since these telescope are sensitive the the visible light, there are two main sources of light interesting them: (i) the Cherenkov light of the air-showers, and (ii) the night sky background light. The latter represents the main source of noise, and generally it decreases with increasing galactic longitudes. It comprehends: (i), the light pollution; (ii) bright stars (especially those located in the field of view); (iii) the zodiacal light, caused by scattering due to the interplanetary dust; and (iv) the Moon light. The latter is so strong to do not allow observations during the full-Moon phase.

The main operating ground-based telescopes are:

- MAGIC (Major Atmospheric Gamma-ray Imaging Cherenkov) telescopes [16]. It is a system of 2 telescopes of 17 m-diameter, operating in stereo mode, located at the Roque

[2] SiPm

de Los Muchachos site, in La Palma Canary Islands, (Spain) at an elevation of 2400 m. The MAGIC telescopes system will be described in detail in Chapter 2.

- HESS (High Energy Stereoscopic System) telescopes [17]. It is a system of 5 telescopes, located at Khomos highlands, in Namibia. 4 telescopes have a diameter of 12 m, while the 5th, added later on, has a diameter of 28 m. HESS is charachterized by an energy threshold of few 10-GeV.
- VERITAS (Very Energetic Radiation Imaging Telescope Array System) telescopes [18]. It is an array of four 12 m optical reflectors, with an energy threshold of $\sim$ 80 GeV.
- CTA (Cherenkov Telescope Array) [19]. The project and the commissioning are still in progress. CTA will consist in two big arrays of Cherenkov telescopes located in the Southern and Northern emisphere, respectively. The former will consist of 4 large-size telescopes, 24 medium-size telescopes and 72 small-size telescope, for a total covered area of $\sim$ 4 km^2. The latter will consist in 4 large-size telescopes and 15 medium-size telescopes. These big arrays have been designed to considerably improve the performances of the Cherenkov telescopes in current operation.

EAS detectors

EAS detectors consist in big arrays of single detectors sensitive to the secondary particles generated in the air-shower. They are characterized by a large field of view, but by a low sensitivity. Since the shower maximum induced by a 1 TeV photon occurs at $\sim$8000 m from the sea level (see Section 1.1.2), the energy threshold of these detectors (around 0.5-1 TeV) is higher than the Cherenkov telescope ones, and also depend on the altitude of the first interaction of the γ-ray with the atoms of the atmosphere. The EAS detectors are built to detect VHE, and UHE γ-photons. Since at these energies the γ-ray fluxes are rather low, a big surface (of the order of 10^4 m^2) is needed to ensure the detections. Some detectors are equipped with muon detectors to discriminate the hadronic air-shower from the electromagnetic ones. If this dispositive is not present the discrimination is based on the shape reconstruction of the shower.

Some of the major EAS detectors are:

- AUGER. The Pierre Auger Observatory [20] is located at Malargue, in Argentina. It detects high energy particles through two techniques: (i) by particle interaction with water placed in surface detector tanks, and (ii) by detecting the Cherenkov light they produce in the atmosphere. In the former case it uses 1660 water surface detector tanks, covering an area of $\sim$3.000 km^2. The latter uses 27 fluorescence detectors, located in four different plases inside the tanks array.
- ARGO YBJ (Astrophysical Radiation with Ground-based Observatory at YangBaJing) [21]. It is located in Tibet at an altitude of 4300 m, and is characterized by an energy threshold $\sim$100 GeV. It is formed by a single layer of Resistive Plate Chambers 110$\times$100 m^2, and characterized by an energy threshold between 500 GeV and 1 TeV.
- HAWC (High Altitude Water Cherenkov) [22]. It is located on the slopes of the Sierra Negra volcano, Mexico at an altitude of 4100 m. It is formed by 300 water tanks, each 4 m high and 7.3 m in diameter. It operates at energies between 100 GeV and 100 TeV, and at high energies it has a better sensitivity than the air Cherenkov telescopes.

1.4.2 IACT Tecnique

As seen in Section 1.4.1, the ground-based Cherenkov telescopes do not detect directly γ-rays, but the products of their interaction with the atmosphere, in particular the Cherenlov light emitted due to the shower particle induced by the γ-ray, moving through the atmosphere. By detecting such weak short ligh, it is possible to reconstruct the properties of the incoming γ-ray. This tecnique, called Imaging Atmospheric Cherenkov Tecnique (IACT), is based on the analysis of the shape of the image that such light produces onto the telescope cameras.

One of the main problem is to discriminate between images generated by the electromagnetic shower and the hadronic ones. Moreover, this is complicated by the fact that the ratio betwwen the electromagnetic and hadronic shower is $1{:}10^4$, since the γ-rays represent a very small percentage of the cosmic-rays. The best way to discriminate among them, is to analyze the shape of the images they form onto the detectors plane. As seen in Section 1.1.2, and how can be seen in Figure 1.12, hadronic showers are much larger and spread than the electromagnetic ones, so their images will be characterized by a different time and shape stamp. Moreover, the images generate by hadronic showers, reresenting part of the background, are isotropically distributed on the camera, while those generated by the γ-ray coming from the same source converge to the same point of the camera.

The longitudinal developement of an air-shower can be divided in three regions: (i) the head, corresponding to the beginning of the shower and collecting the fist products of the γ-ray interaction; (ii) the core, indicating the shower maximum; and (iii) the tail, corresponding to the final part of the shower. As explained in Section 1.1.3, photons originating in the head of the shower reach the ground with an smaller incidense angle that those originating in the core and the tail. At each incidence direction, β, corresponds a position onto the camera given by the relation $r \sim \sin(\beta) f$, where r is the distance of the focalizaion point from the center of the camera, and f the telescope focal lenght. Let's consider an air-shower whose direction is parallel to the telescope axis, the image on on the camera plane is an ellipse with the major axix pointing towards the camera center. The ellipse region further from the centers is originating by the Cherenkov photons emmitted in the head, the central region by those emmitted in the core, and the closest ones those by emmitted in the tail. In Figure 1.13 the image formation process is represented.

The temporal and spatial distribution of the ellipse - determined through the shape, the orientation and the luminous intensity of the image - gives important information about the longitudinal developement of the shower, on the incident direction, energy and nature of the primary particle. Each ellipse is characterized through the so-called Hillas parameters [24] related to the physical quantity describing the air-shower. The main Hillas parameters, shown in Figure 1.13, are the following:

- *size*. It corresponds to the total number of photoelectrons associated to the image. This quantity is directly related to energy of the primary γ-ray;

- *width*. It is the semi-minor axis lenght of the ellipse. It is related to the trasversal developement of the shower and is a very important discriminator between the hadronic showers (much larger) and the electomagnetic ones;

- *lenght*. It is the semi-major axis lenght of the ellipse. It is related to the longitudinal develop of the showers that, in turn, depend on the energy of the primary γ-ray;

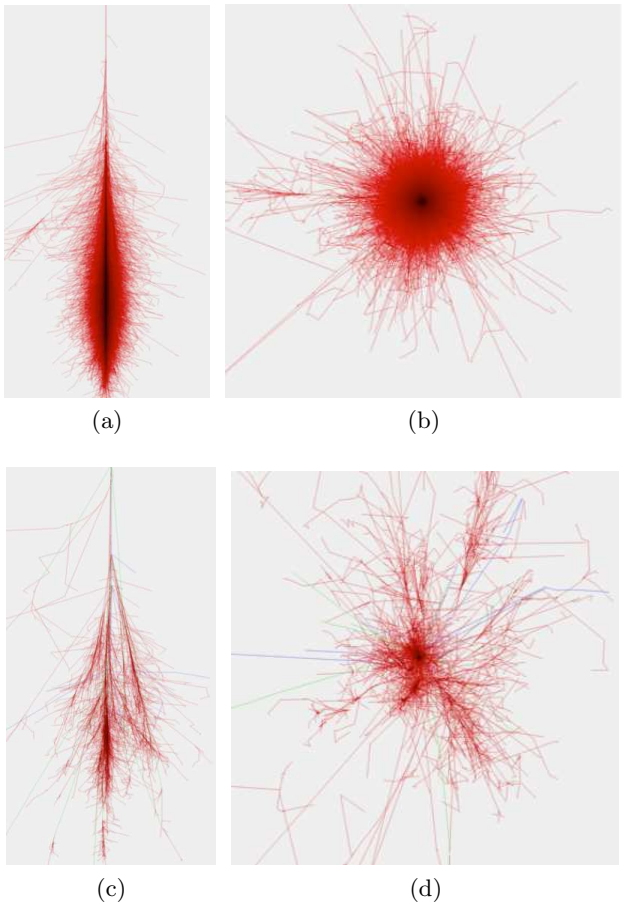

(a) (b)

(c) (d)

Figure 1.12: On top: simultated showers generated by a 1 TeV electron: lateral view (a) and face on view (b). On bottom: simultated showers generated by a 100 GeV protn: lateral view (a) and face on view (b). From [23].

- *alpha*. It is the angle between the semi-major axis and the segment that connencts the ellipse centroid and the point of the camera where the source is supposed to be. It is a foundamental parameter for the discrimination between the two kind of showers. In fact, the electromagnetic showers are characterized by low *alpha*-values, since they points towards the source direction in the camera; instead of the hadronic shower that are characterized by a rather flat *alpha*-distribution, because they are events randomly distributed in the sky;

- *dist*. It is the distance between the ellipse centroid and the center of the camera. It is related to (i) the altitude of maximum developement of the shower, and (ii) the distance from the telescope and the intersection point between the ground and the shower axis;

- *numIsland*. It is the number of compact illuminated pixels of the camera, and represents the image frammentation. In fact, such islands of pixels are present in the hadromic images, and are due to particolarly strong sub-electromagnetic showers;

- *Leakage*. It is the signal fraction contained in the edge pixels of the camera, when an

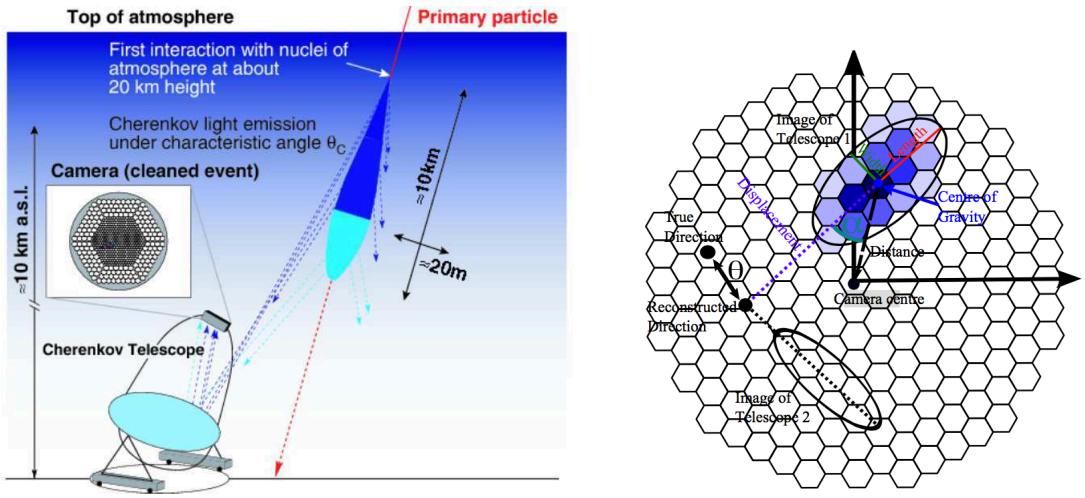

(a) (b)

Figure 1.13: (a): Image formation process due to an air-shower characterized by an incident direction parallel to the axix of the telescope [5]. (b): Image on the camera firmed by an electromagnetic air-shower; some of the Hillas parameters are superimposed on the ellipse *Credits*: Marcel Strzys.

image is not fully contained in the camera itself. This parameter estimates the signal loss percentage due to a too large impact parameter. In such a way all the images that cannot be parametrized properly are rejected;

- *Concn.* It is the fraction of photoelectrons contained in the most illuminated pixel. This provide information on the properties of the shower core;
- *M3long.* It is the third longitudinal moment of along the major axis. It distinguishes between the head and the tail of the shower. If is is positive it means that the ellipse region nearer to the center of the camera is generated by the head shower, otherwise by the tail.

1.4.3 Space Detectors

The γ-ray space telescopes detect lower energy photons than the Cherenkov telescopes ones. In fact, as seen in the previous sections, MeV photons are not energetic enough to be detected from ground. They are characterized by a small effective area (around ~ 1 m^2) that traduces in a low sensitivity that limits the observations of point-like γ-ray sources to photons below 10 GeV. Moreover, they are characterized by a wide field of view that allows the whole sky to be observed in relative short time.

The γ-ray cannot be reflected by any material, because their wavelenght is comparable to the atomic and sub-atomic dimensions, and hence they are very easily absorbed by the matter. For this reason, the detection tecnique of the the γ-ray telescopes is very similar to that implied for particle accelerators. In Figure 1.14[3] the main components of their equipement are shown. They consist in:

[3]https://www-glast.stanford.edu/instrument.html

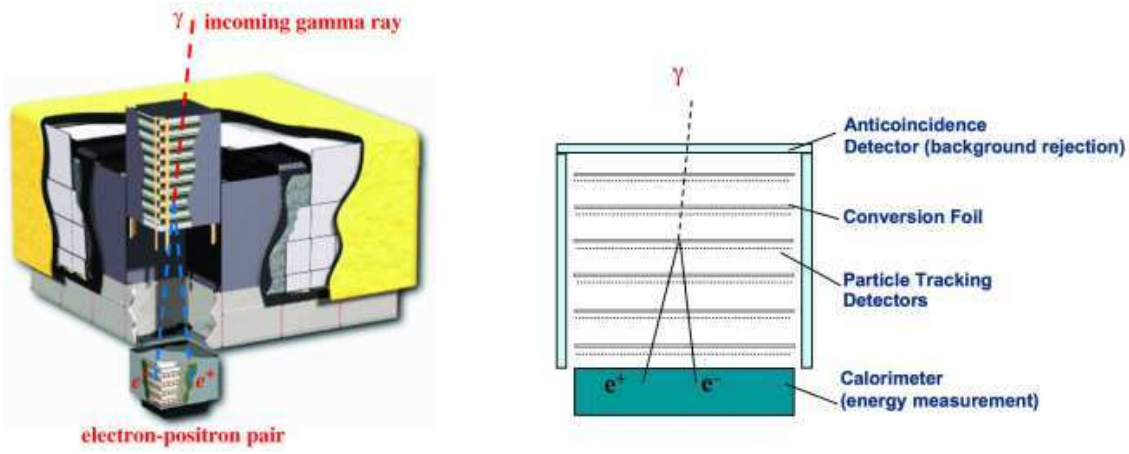

(a) (b)

Figure 1.14: Detection tecnique used by the γ-ray space telescopes. This Figure the Fermi-LAT design (left) and a schematic viwe of the detection process (right).

- an anticoincidence electronic. The detector is shielded by an anticoincidence layer that blocks the undesirable events due to the background. This layer is usually formed by plastic scintillators, material that manifest luminescence when is excited by ionizing radiation. This scintillators shield the tracker from charged particle, while other special materials recognize the γ-rays of non-cosmic origin;
- a tracker. It is formed by alternated tungsten foils and silicon strip detectors. A γ-ray that has overcame the ainticoincidence shield, enters the tracker and interact with the atoms of the tungsten foils, producing an electron-positron pair. These particles, traveling through the tracker, leave traces on the silicon strips that allow the particle paths to be reconstructed.
- a calorimeter. At the base of the tracker there is a calorimeter that measures the particles energies. The electrons e^+ and the positrons e^-, entering the calorimeter, create a shower particles. The energy os these particles is measured by a scintillator material, whose ionized atoms re-emit the particle energy in the optical waveband. Such light is converted into an electrical signal proportional to the particle energies.

By combining all the infomation coming from the anticoincidence detector, the tracker, and the calorimeter it is possible to reconstruct the energy and the direction of the incident γ-ray.

- EGRET (Energetic Gamma Ray Experiment Telescope) [25] is mounted on the Compton Gamma Ray Observatory (CGRO). It is characterized by an effective area of 0.15 m^2, and a large field of view of $\sim 80°$. It detects γ-rays at energies between 20 MeV and 30 GeV through pair conversion e^+e^- due to the interactions of the γ-rays with the detector.
- AGILE (Astrorivelatore Gamma ad Immagini LEggero) space telescope [26]. It works in the energy range 30 MeV - 50 GeV, and it is characterized by a large field of view of ~ 3 sr. The detection technique is inherited from its predecessor EGRET.
- FERMI Gamma-ray Space Telescope [27]. This satellite is composed by two instruments: LAT (Large Area Telescope) to detect γ-rays between 20 MeV and 300 GeV, and GBM (Gamma-ray Burst Monitor) working in the range 10 KeV-25 MeV. Thanks

to an effective area of $\sim$1 m^2 Fermi LAT improved over the EGRET performances by two orders of magnitude.

1.5 γ-ray sources

γ-ray sources can be divided into Galactic and extragalactic. In turn Galactic sources can be divided into point-like and extended sources. Due to their proximity, their γ-emission is not affected by absorption from the cosmic background radiation. In the extended sources particle acceleration - and the ensuing γ-emission - is supposed to originate from the interaction between the source and the surrounding environment, whereas in point-like sources it originates inside the jets or in connection with relativistic fluxes. There are also a diffuse emission that includes very extended sources such as diffuse emission from the Galactic disk, Fermi Bubble, Cygnus cocoon, and AGN halos.

The main galactic γ-ray sources are:

- **Supernova remnants** (SNRs). They are the results of supernova explosions. A giant star, approaching the end of its life, starts to collapse very quickly. Part of the energy of the collapse is transformed in shock waves - that bounce on the heavy nucleus - and is transferred to the external layers. Such layers are wildly ejected far away from the central nucleus - causing the disintegration of the star. Such ejected envelope forms the supernova remnant. Supernovae are considered excellent particle accelerators (through the Fermi I mechanism, see Section 1.2.4), and their spectral distribution are given by a superposition of synchrotron spectra due to different electron populations interacting with the strong magnetic field sorrounding the star. The synchrotron contribution peaks at keV energies, but it can extend from the radio to the γ-band. There is also an inverse Compton component - from soft to VHE γ-rays - generated by the interactions between relativistic electrons and the photon field - that includes synchrotron, cosmic microwave background, and thermal photons from the progenitor star. In such sources also hadronic mechanisms (see Section 1.2.6) play an important role, especially through the neutral pion decay. At present, the leptonic and hadronic contributions are difficult to disentangle.

- **Pulsar Wind Nebulae** (PWN). They are fast rotating neutron stars characterized by very strong magnetic fields, misaligned with respect to the rotation axis. The simultaneous presence of rotation and magnetic field produces a strong radiation at the poles, that a hypotetical observer see as pulsed emission. The rotating magnetic field generates a high electric field that is supposed to extract charged particles from the star surface, filling the magnetosphere. There is a zone, called *light cylinder*, out of which the open magnetic field lines allow particles to be ejected and accelerated. The electromagnetic pulsar emission is explained mainly by two models that differ on the location of the emission region: (i) the Polar Cap (PC), able to accelerate particles up to $\sim$ 10 GeV, and (ii) the Outer Gap (OG), able to accelerate particles up to $\sim$ 100 GeV. The γ-emission is dominated by the pulsed emission coming from the star at energy below GeV, and by the stable emission of the nebula above GeV energies. Also in this case, the spectral energy distribution is due to the synchrotron emission and inverse Compton scattering due to the electrons accelerated through the Fermi I mechanism (see Section 1.2.4) in the nebula region. All PWN spectra show a cutoff at high energies.

The reasons of such a cutoff depend on the model and the magnetic field intensity. The PC models for strong magnetic fields ($B \sim 10^{11} - 10^{13}$ G) predict a super-exponential cutoff in the region 10 MeV - 10 GeV, while the OG models predict an exponential cutoff.

- **Binary systems**. In these systems a star - orbiting around a compact object such as a neutron star or a black hole - loses matter due to gravitational interaction. Such matter forms a compact disk, heated by the strong viscosity forces, that emits X-rays. Usually, also two collimated jets shot off the central region and perpendicular to the disk plane, are associated with these sources. The plasma ejected by the jet, by encountering the sorrounding disk matter, generates shock waves that can accelerate particles. Both leptonic and hadronic mechanisms are supposed to be at the base of the γ-emission, since electrons, protons, and heavier particles are all part of the emitting plasma.

- **Galactic center**. There are three main candidates for origin the γ-ray emission coming from the Galactic center: (i) the shell-type SNR SgrA East, (ii) the PWN G359.94-004, and (iii) the central black hole SgrA. Several mechanisms are supposed to be responsible for the observed γ-ray emission: the inverse Compton scattering due to high energy electrons, the neutral pion decay produced in the interactions between the interstellar medium and high energy hadrons, bremsstrahlung radiation from UHE particles located near SgrA, and dark matter annihilation. However, the lack of variability - over an year timescale - in the γ-band makes both SNRs and PWN the favoured sources for particle acceleration.

- **Diffuse Emission**. Two specific (very) extended sources, detected by Fermi-LAT, are (i) the diffuse emission from the Milky Way disk and (2) the so-called Fermi Bubbles, i.e., large (10 kpc high) areas of increased γ-ray surface brightness centrally perpendicular, on both sides, to the Galaxy disk [28]. At TeV energies, the former was detected by HESS early on, during the Galactic Plan Survey [29], whereas the latter are very hard to detect with current IACTs due to their presumably low level of TeV emission and their large angular extension (if compared with the small field of view of the current instruments). In astrophysical perspective, the diffuse HE emission from the Milky Way's disk and (Fermi) bubbles is the local (Galactic) counterpart of the HE emission from the nearby starburst galaxy M82. In this latter galaxy, data can be modeled as SN-powered diffuse emission from the galaxy's nuclear starburst and disk, plus a superwind [30]. Similarly, in the Milky Way the diffuse disk emission is spectrally consistent with hadronic illumination (i.e., with the current SN rate), whereas the Fermi bubbles have been interpreted as a Galactic superwind triggered, a few million Myr ago, by a starburst in the very central region of our Galaxy and its possible interaction with the supermassive black hole sitting there (e.g., [31]).

The γ-ray extragalactic sources are:

- **Gamma Ray Bursts** (GRBs). They are the most powerful transient events in the Universe. It is not possible to define a characteristic time scale for their emission: they are merely divided in (i) long GRBs, that last up to few hundred seconds (the typical duration is ~ 20 s), and (ii) short GRBs with a mean duration of 0.2 s. Also in the light curves it is not possible to recognize any typical feature, common to all GRBs. The

long GRBs are supposed to originate from stellar objects such as the collapse of a giant star into a neutron star or into a black hole, whereas the short ones may come from the collapse of a binary system. In both cases the γ-emission results from the conversion of gravitational into radiant energy. Such transformation can occur through internal or external shocks. The former are due to collisions between shells of plasma characterized by different Lorentz factors, while the latter are due to the slowdown of these shells in the interstellar medium. The so-called fireball model tries to explain both the *prompt emission* and the following *afterglow*, i.e., the temporally longer emission detectable in several energy ranges, from optical to X-rays band, and sometimes also in the radio band.

- **Active Galactic Nuclei** (AGNs). An AGN is a galactic nucleus whose luminosity far exceeds the luminosity of the host galaxy. According to the unified model (Sect. 1.6.2), the engine of these sources is thought to be a supermassive black hole that accretes matter from its surroundings, in particular theough an accretion disc. The matter falling into the black hole loses angular momentum through viscous processes and emits radiation, from UV to hard X-rays. Farther out in radius, there is a spherical region, the so-called broad-line region, where gas clouds in fast orbital motion emits Doppler-broadened optical lines. This central region is surrounded by a dense dusty torus spinning coplanar to the disk. Beyond such torus and much farther out from the central region, colder and smaller clouds, moving at lower speeds, emit narrow optical lines (this is called narrow-line region). Occasionally, two highly collimated relativistic jets shoot out perpendicular to the disk plane in opposite directions. Jets are very interesting because they are supposed to be the place where the very high energy radiation is generated. Their spectral energy distribution is characterized by two bumps: one at lower energies (from optical to X-rays) due to the electron synchrotron radiation rays, the other at higher energies (from X-rays to γ) due to inverse Compton scattering of the synchrotron photons by their same parent electrons. A deeper discussion on AGNs is presented in Section 1.6.

- **Star-forming Galaxies**. The starburst and the ULtraluminous InfraRed Galaxies (ULIRG) with high rates of supernova explosions and high gas densities can reach flux levels detectable with the current instruments.

- **Potential γ-ray Sources**. There are some potential γ-ray sources, that have not yet been detected. They include the **Satellite Galaxies of the Milky Way** and the **Galaxy Clusters**. The former are characterized by a high M/L ratio, as well as the dwarf galaxies, and are the best candidate for detecting γ-rays generated by dark matter annihilation. The latter are big systems that can contain a significative population of non thermal particles, produced by the acceleration processes due to the accretion cluster processes and to supernova activity in member galaxies.

1.6 Active Galactic Nuclei

Since the work in this thesis concerns the spectral energy distribution modeling of Mkn 501, an AGNs belonging the the blazar class, a brief summary on the AGN properties is presented in the following. For a complete discussion see [32] and [33].

1.6.1 Classification

AGNs are galaxies whose nuclei show a very strong variable non-thermal emission, associated with strong emission lines. They represent $\sim 3\%$ of the total galaxy population, and differ from their luminosity and peculiarities in the emission profile. In fact, AGNs spectrum is charachterized by emission lines, with strong emission in the UV, IR, X-, and γ-band.

The classification of AGNs tends to be rather confusing since it is based more on the way to observe them, than to the intrinsic differences amog the various types. There are generally three observative parameters that lead to AGNs' classification: (i) the radio emission, (ii) the optical emission related to the presence of emission lines, (iii) the luminosity, and (iv) the morphological profile. In the following list the main types of AGNs and their characteristics are summarized.

- **Seyfert galaxies**. They are lower-luminosity AGNs whose host galaxy is visible. They are generally spiral galaxies with a very bright nucleus. They are characterized by an optical emission, while the radio emission is absent. They can be distinguished into: (i) **Seyfert I**, charcterized by optical emission lines, both large permitted lines (such as HI, HeI, HeII, FeII) and narrow forbidden lines (OIII). The lines widening is of kinematic origin and indicates that they are originated by sources with velocity up to $v \sim 10000$ km/s for the large lines, and $v \sim 1000$ km/s for the forbidden lines. They have a brighter continuum and emit more in the X-band than the Seyfert II; (ii) **Seyfert II**, characterized only by narrow lines, generated by sources with $v \sim 500$ km/s. Sometimes they do not show the X-emission.

- **Quasars**. They are point-like sources, generally located at high redshift, whose luminosity exceed by a factor of 10^5 the luminosity of standard galaxies. They are characterized by a very strong variable γ-ray emission. 90% of quasar are radio quiet. Their are very bright in the UV-band, anf for this reason they appear as blue sources. They are characterized also by the presence of large emission lines emitted by sources with $v \sim 10000$ km/s.

- **Blazars**. They are point-like sources, generally belonging to elliptical galaxies, and are the most luminous γ-ray AGNs. They show a consistent radio emission. Their optical emission, as well as their emission lines are absent or rather weak. They are very fast variable sources, over the day - or even shorter - timescale. Their luminosity can vary by up to 20% in a day timescale and even by up to a factor 100 over longer timescales. A subclass of blazars are the so-called **Flat Spectrum Radio Quasar** (FSRQ), characterized by a rather flat spectrum with a spectral index $\alpha \sim -0.5$.

- **Radio galaxies**. They are characterized by a very strong radio emission. Their morphology shows two radio lobes (quite extended) that emerge from the galaxy center. The radio emission is not of thermal origin, but due to the synchrotron radiation generated by relativistic charged particles. The radio emission can be originated in the lobes, but also in compact cores within the nucleus. Often, relativistic jets are associated to the radio lobes.

1.6.2 Unified Model

All the sources described in the previous Section show so many different features that they appear to belong to different source classes. However, all belong to the same class - the AGN class - and present the same morphology. Their different observational features can be explained by their different orientations with respect to our line of sight.

The strong emission of these sources is due to the presence of a supermassive central black hole, and to the ensuing conversion of gravitational energy into luminous energy. This conversion is expressed by the relation:

$$L_{acc} = \epsilon \frac{dm}{dt} c^2 \tag{1.30}$$

where L_{acc} is the luminosity due to the mass accretion on the black hole, ϵ the process convertion efficiency, and dm/dt the mass accretion rate onto the black hole.
The structure of AGNs can be summarized as follows:

- *Supermassive central black hole.* It is supposed to be the central engine of AGNs.
- *Accretion disk.* To conserve angular momentum, the infalling matter spirals around the black hole and forms an accretion disk around it. Such a disk is heated by viscous processes and emits UV through to soft-X–ray radiation. The typical dimension of an accretion disk is 10^{-3} to 10^{-2} pc.
- *Broad line region* (BLR). It is a region located beyond the accretion disk, sorrounding the whole central part. It has a spherical shape, with typical dimensions ranging from 10^{-3} to 10^{-2} pc. It is formed by an ensemble of small gas clouds ($\sim 10^7 - 10^8$), charachterized by a high density ($n_e \sim 10^9 - 10^{11}$ cm^{-3}) and a low temperature ($T_e \sim 2\,10^4$ K). The large emission lines are generated in this region. The continuum emitted by the accretion disk ionizes the gas in the BLR, that in turn, re-emits radiation. The line broadening has kinematic origin, due to the high velocity ($v \sim 2000$ km/s).
- *Dust torus.* It is located farther on the BLR. Its thickness (~ 1 pc) is larger than its diameter. It is formed by dust and it is responsable of the dimming of the central region if the AGN is observed with an angle $\theta \sim 90^\circ$ with respect to our line of sight.
- *Narrow line region* (NLR). It is located above and below the dust torus. It is formed by gas cloud (fewer and smaller than those in the BLR) in relativistic motion around the black hole. The narrow lines are generated in this region. They are narrower than those generated in the BLR because the velocities involved are $v \sim 1000$ km/s.
- *Relativistic jets.* They are formed by higly collimated relativisc plasma shot out from the central region, perpendicularly to the disk plane. Although the mechanisms responsible for jet formation are still not understood, jets are supposed to be generated by strong magnetic fields dragged by the rotation of the black hole. Such tangled magnetic fields would be able to remove plasma from the central region through the Blandford-Znajek process.

Summarizing, the asymmetric model of AGNs makes allow them to look different depending on their orientation with regard to the observer's line of sight. AGNs whose jets are perpendicular to the line of sight belong to Seyfert II or Radio Galaxies. In this case the central region is obscured by the torus and only narrow lines can be found in their spectra. AGNs whose jets form an angle ranging from 30 to 60 degrees belong to Seyfert I galaxies or Quasars. Due to their orientation, the torus does not obscure completely the central region, so spectra present both broad and narrow lines, coming respectively from the broad and the

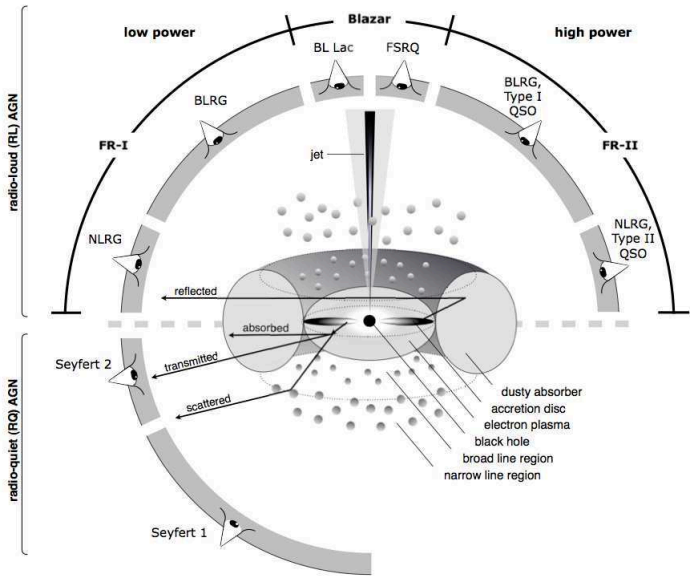

Figure 1.15: Morphology of AGNs. Their classification and spectral properties - depending on their orientation with respect to the line of sight - are also shown.

narrow line region. Finally, blazars are AGNs whose jets point directly to the observer. Figure 1.15 shows the morphology of AGNs, and the observed features depending on the line of sight.

1.6.3 Blazar Spectral Energy Distribution

Blazars (and AGNs in general) are characterized by a strongly variable non-thermal emission, whose SED - shown in Figure 1.16 - is characterized by two peaks: the first located at low energies (in the infrared - X-rays range), which is thought to arise from synchrotron emission (see Section 1.2.1), and the second one located at high energies (in the MeV-TeV range), that is usually interpreted as Comptonized emission from some local photon field off relativistic electrons (see Section 1.2.3)[4]. Both peaks are required to sample the SED, because the synchrotron emissivity is degenerate in magnetic field and electron density. So, the knowledge of the Compton peak provides the second equation needed to remove the degeneracy, since its emissivity is proportional to the synchrotron emissivity and to the electron density. The nature of the synchrotron peak is well known, whereas that of the Compton peak is still under discussion. The several different emission models supposed to generate the Compton peak are described in the next section.

Blazars γ-ray emission is supposed to origin iside the relativistic jets, formed by ionized material in relativistic motion, ejected along the rotation axis of the galaxy. Such jets are highly collimated and permeated by strong magnetic fields. The idea that γ-emission arises from the jet and not from the central region is formulated to solve an intrinsic contradiction. In fact, in the central region the density is so high that γ-photons cannot excape. In particular,

[4]SEDs are usually represented in logarithmic scale, in ν and $\nu\, I_\nu$ units. This permits to have an immediate idea of the contribution on the flux given by the single frequency intervals, since it is proportional to the area subtended by the SED function.

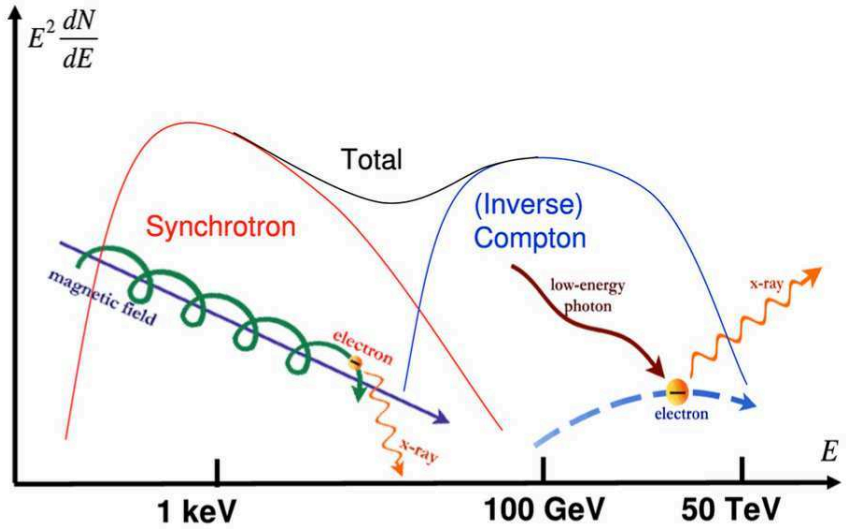

Figure 1.16: Typical blazar spectral energy distribution. It is characterized by two peaks: the first due to synchrotron radiation at lower anergy, and the second one due to inverse Compton scattering at higher energies. From [34].

because of high density and photon-photon optical depth ($\tau_{\gamma\gamma} \gg 1$), γ-rays are reabsorbed and generate an e^+e^- pair that, in turn, re-generate γ-photons through inverse Compton. This process keeps going on until the energy of the γ-photons decreases below the energy threshold for the pairs production. At that point, the process becomes transparent and the photons can freely escape from the dense central zone to reach the regions permeated by the relativistic electrons.

One of the most important consequences of jet concerns the so-called *beaming effect*. This causes a distortion of the observed parameters for an observer whose line of sight is almost aligned with the jet axis - e.g., in the case of blazars. Suppose we have a source emitting isotropically in its reference system. In the observer's reference system, where the source is seen as moving close to the light speed ($\beta = v/c \sim 1$), three effects manifest:

1. *superluminal motions*. The time intervals for the photon emission are different from their arriving time intervals. This leads, through merely geometric considerations, to observe particles that move apparently with velocity higher than the light speed. Such apparently velocity v_{ap} is given by:

$$v_{ap} = \frac{v \sin(\theta)}{1 - \beta \cos(\theta)} \tag{1.31}$$

   where θ is the angle between the line of sight and the jet axis. For small $\theta \sim 0$ and $\beta \sim 1$, the observed velocity exceeds the speed of light in the vacuum.
2. *Doppler boosting*. Due to relativistic effects, in the observer's reference system, the photons are emitted inside an angle expressed by the relation $\sin(\theta) = 1/\gamma$, where $\gamma = 1/\sqrt{1-\beta^2}$ is the Lorenz factor of the emitting region. This means that the photons emitted in the whole solid angle are seen as emitted inside a small angle in the observer's reference system. This leads to an amplification of the observed flux, $F_{obs}(E)$, given by $F_{obs}(E) = \delta^p F_{emit}(E)$ (where the $\delta = 1/[\gamma(1 - \beta\cos(\theta))]$ is the Doppler factor, and p an

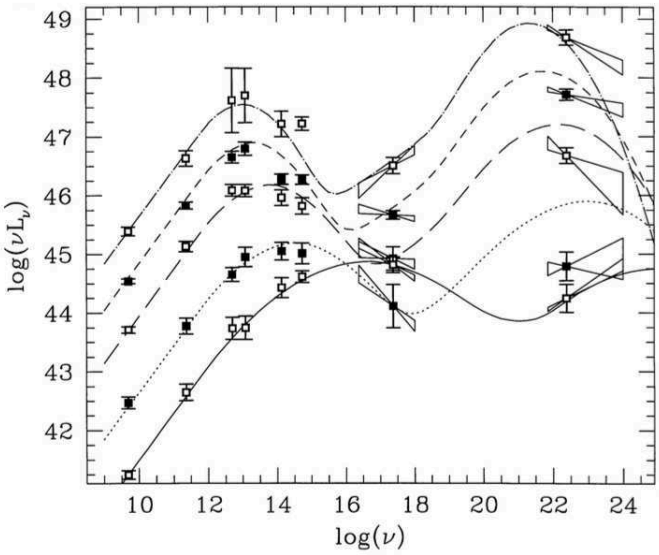

Figure 1.17: Blazar sequence. The change in the blazar spectral energy distribution are shown as a function of their radio luminosity. From [35].

index depending on the geometry of the system). Also the observed luminosity exceeds the emitted one by a factor δ^p.

3. *Blueshift in frequencies.* The observed frequencies, ν_{obs}, are higher than the emitted ones, ν_{emit}, with the ensuing blue-shift of the observed spectrum. The relation between the frequencies is $\nu_{obs} = \delta\nu_{emit}$.

Interesting features of the blazar SEDs, are highlighted by the so called *blazar sequence* [35]. Starting from a selection of blazars, the mean SED was computed, according to their radio luminosity. The Figure 1.17 puts in evidence four main aspects:

- the synchrotron peak is anticorrelated with the source luminosity, ranging from $10^{16} - 10^{17}$ Hz for less luminous sources, and from 10^{13} to 10^{14} Hz for the most luminous ones. This means that blazars characterized by higher bolometric luminosity have the synchrotron peak at lower frequencies and present a more red SED;
- for increasing luminosity, the X-ray spectrum becomes harder while the γ-ray one becomes softer. This indicates that the Compton peak moves to lower frequencies from 10^{24} to 10^{25} Hz for less luminous sources, and from 10^{21} to 10^{22} Hz for the most luminous ones;
- the frequencies of the synchrotron and the Compton peak are correlated: their ratio is almost constant;
- for very high (bolometric) luminosity the Compton component becomes stronger than the synchrotron one. This means that for high luminosity, the γ component dominates.

Such differences cannot be explained by focusing only on the source orientation with respect to the line of sight, but are due to the different cooling processes of the electrons responsible of the emitted radiation. The most important conseguence is that the blazar luminosity seems to be related to their physical properties and the radiative emission mechanisms inside the jets. HBLs, such as Mkn501, are characterized by the lowest luminosities and the highest peak frequencies.

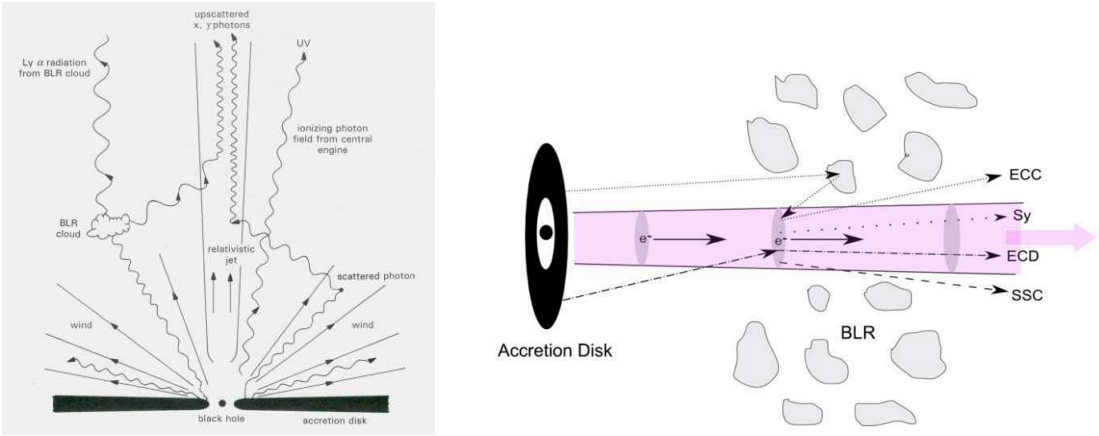

Figure 1.18: Differences between the leptonic emission mechanisms, generating blazars' SEDs. The figure on the left is from [2].

1.6.4 Emission Models

As described in the privious section, the γ-rays in AGN are suppsed to be originated inside the jets. There are two kind of processes to explain the γ-emission: the leptonic and the hadronic ones. Both require the presence of ultra-relativistic particles - accelerated through the Fermi I mechanism - whose energy distribution is described by a power-law function. In the leptonic models the relativistic particles involved are electrons, while in the hadrons ones are mainly protons. However, the validity of a model versus others is still under debate, and in most of cases it depends on the specific source. Nevertheless, leptonic models are favoured because of the low mass: in fact, they can quickly accelerated and cool down, providing a valid explanation for the AGNs fast variability. However, thier fast cooling does not explain how the particles can reach very high energies.

Leptonic Models

When leptonic processes are involved, the mechanism leading to γ-rays production is the inverse Compton scattering (see Section 1.2.3). Because different Inverse-Compton processes possibly contribute to the high-energy peak, each model depends principally on the source of seed photons scattering off the relativistic electrons in the jet. For these reason, the leptonic models can be divided into two main categories: the Synchrotron-Self-Compton (Synchrotron-Self-Compton, henceforth SSC) models if the Compton photons are the synchrotron photons upscattered by the same parent electrons, and the External Compton (EC) models if the scattered photons come from regions outside the jet, such as the disk or the BLR. Differences among leptonic emission models are visualized in Figure 1.18.

Among the leptonic models, the most popular used to describe blazars emission is the one-zone SSC (henceforth SSC1). It assumes that the SED is produced within a single, homogeneous, spherical blob of magnetized non-thermal plasma, in relativistic motion along the jet. The blob is filled with a homogeneous tangled magnetic field and by a population of relativistic electrons, whose spectrum can be described by different power-law functions of energy. The particle and photon distributions are isotropic in the source frame. The Self Synchrotron model is not suitable for all the sources, especially if the contribution due to the

external photon fields is not negligible. For this reason this model is suitable for sources - such as BL Lac objects - where the lack of emission lines in their spectra indicates a weak thermal component. The model is also applied to sources whose variability is dominated by one characteristic timescale, because this indicates only one characteristic size of the emitting region. Finally, it is also suitable for sources that show a strict correlation between the X-ray and VHE γ-ray variability; in fact this suggests that the emission in the two band (corresponding to the two bumps in the SED) is generated by the same electron population. Some well-known blazars with *bona-fide* SSC emission are Mk421, Mk501, and BL Lac.
The one-zone SSC model is often described by nine free parameters: six describing the electrons distribution (normalization, two slopes, two limiting energies, one break energy) and three describing the emitting region (magnetic field strength, and blob radius and Doppler factor). Usually $\gamma_{min} = 1$ (this is also suggested by the low-energy shape of the synchrotron emission), so the one-zone SSC model is typically described by eight free parameters.

A slightly different version of the SSC1 is the two-zone SSC (SSC2) model. The main idea, supported by the observation of two different timescales in the source variability, is that the emission is generated by two different electron populations. The emission mechanism is exactly the same, but in this case two blobs of plasma are involved. This implies a doubling of the free parameters.

In the EC models, the inverse Compton scattering occurs through photons generated in regions outside the jets. These photons are generally UV or soft X-photons irradiated directly from the accretion disk, deviated through scattering from the broad line region clouds, or reprocessed from the dust of the narrow line region. These photons reaching the jet, interact with the relativistic electrons and increse their energy up to the γ-range by inverse Compton scattering. Both the SSC and the EC models are consistent with the spectral shape of the AGNs and with the γ-ray emission of blazar.

Hadronic Models

According to these models, the jet is mainly formed by relativistic protons and carries out a large part of the energy emitted by the central region. Such protonic component in the jet would be subjected to less synchrotron losses as compared with the electrons and could be accelerated more efficiently, up to 10^{20} eV. These protons - interacting with matter, ambient photons and magnetic field - induce electromagnetic cascades that contribute to form the Compton peak, especially through neutral pion decays (see Section 1.2.6).

Chapter 2

The MAGIC Telescopes

In this Chapter the MAGIC telescopes and the data analysis techniques will be described. After a brief overview in Section 2.1, the stereo configuration before and after the major upgrade in 2011-2012 will be reported in Sections 2.2 and 2.3 respectively. Attention will be paid on the main subsystems and on the performances. Finally, in Section 2.5, the standard analysis chain for the MAGIC data reduction will be described.

2.1 Overview

The *Florian Göebel* Major Atmospheric Gamma-ray Imaging Cherenkov (MAGIC) telescopes is a system of two imaging Cherenkov telescopes for ground-based gamma-ray observations, located at 2200 m a.s.l. at Roque de los Muchachos Observatory in La Palma ($28°N$, $18°W$, Canary Islands, Spain). The Astrophysics Observatory at Roque de los Muchachos, operated by the *Instituto de Astrofisica de Canarias*, hosts several different telescopes, due to the optimal atmospheric conditions that makes Roque de los Muchachos one of the best observative sites of the Northern emisphere. However, for the MAGIC purposes a good knowledge of the atmospheric transmission night by night is foundamental for data analyses.

The MAGIC collaboration involves 24 institution from 10 different countries (Spain, Germany, Italy, Swiss, Japan, Croatia, Finland, India, Poland and Bulgary), and with its two telescopes of 17 meter of diameter and an area of about 246 m^2 is a very sensitive instrument for studying the high energy processes of the Universe from the ground. It operates in a wide range of the gamma-ray spectrum, from 50 GeV to 30 TeV.

The first telescope, MAGIC I, was built in 2004, while the second one, MAGIC II, was completed in autumn 2009, so enabling observations in stereo mode. Since the beginning, MAGIC went through several phases, of which the most significant are:

- Autumn 2004: MAGIC started operation with MAGIC I telescope in mono mode;
- February 2007: the Siegen (300 MHz) readout of MAGIC I was replaced by the MUX FADCs (2 GHz) system;
- Autumn 2009: started operation with both MAGIC I and MAGIC II in stereo mode. MAGIC II had a different, improved camera and a different readout system based on DRS2 chips (2 GHz);

Figure 2.1: On the left: site of the MAGIC telescopes, Roque de los Muchachos Observatory, La Palma (Canary Island, Spain). On the right: MAGIC telescopes, *Credits*: Robert Wagner.

- Summer 2011: readout of both cameras was replaced with a system based on DRS4 chips (2 GHz);
- Summer 2012: MAGIC I camera was replaced by a new one, identical to MAGIC II.

The main goal of the MAGIC experiment consists in lowering the energy threshold of ground-based IACT observations to contribute solving the still-open questions in high energy astrophysics. In fact, by lowering the energy threshold MAGIC not only can access an unexplored energy range, but can also extend the *gamma*-ray horizon, discovering more and more sources. Moreover, its high sensitivity allows us to resolve short time source variations and to better characterize their spectra. MAGIC observations involve several targets. Since not all of them have been yet detected by MAGIC, a distinction between the detected and undetected sources must be done. Among the detected sources there are:

- *pulsars*. Pulsars are fast-rotating, highly-magnetized neutron stars emitting strong radiation. Such radiation is emitted in a narrow cone and, due to the fast rotation, it is visible as a pulsed signal when the emission cone crosses our line of sight. There are two main pulsar emission models that predicts different cut-offs in the energy spectrum: ~ 50 GeV for the *polar cap* and ~ 100 GeV for the *outer cap*. The lower energy threshold and the high sensitivity of MAGIC allow detections to be made that are able to discriminate between these models.

- *Supernova remnants* (SNR). The end of a massive star is characterized by a great explosion that spreads a huge amount of matter and radiation all around it. The ejected matter forms a *nebula*, called SNR, that surrounds a leftover pulsar or black hole. These objects are supposed to be the place where cosmic rays are accelerated up to TeV energies. However, the respective roles of protons and electrons still remain an open question. MAGIC, entering the domain above 10 GeV, can find distinctive signatures in SNR spectra due to different emission mechanisms involving protons and electrons.

- *Active Galactic Nuclei* (AGN). Active Galactic Nuclei were described deeply in Chapter 1.6. The very high energy emission is supposed to be originated inside their jets. Several models have been proposed to describe it. MAGIC observations are foudamental to sample the inverse Compton peak (see Section 1.2.3), and thus to discriminate amog different models. Moreover, as AGNs are spread in a wide redshift range, they are the optimal candidates to determine, or to put strong constraints to, the *Extragalactic Light Background* (EBL). The γ-rays emitted by AGN, travelling across the Universe, interact with the EBL photons, producing e^+ e^- pairs. Assuming that the intrinsic AGN emission is known, such as the $\gamma\gamma \rightarrow e^+$ e^- cross section, it is possible to extrapolate and characterize the EBL spectrum.

- *Binary systems*. Studies on these systems, especially on the accreating ones (such as X-ray binaries and microquasars) are very useful because they reproduce what happens in AGN in shorter time scale.

The sources observed by MAGIC, but still undetected are:

- *Gamma Ray Burst* (GRB). They are the most energetic events occuring in the Universe. They are characterized by the so called *prompt emission*, where the most of γ-ray emission occurs in few seconds, and by the *afterglow*, where the emission extends to other wavelenghts and may last several days. There are several models trying to explain the GRB emission. The most common is the *Fireball model*, but the nature of the GRB henomenon remains unknown. The light stucture of MAGIC allows for a fast repositioning in case of a GRB alert in order to capture the *prompt* emission. The detection of these transient objects at MAGIC energies is foundamental to understand the nature of the source and its environment.

- *Dwarf galaxies*. They have large dark matter component, i.e. that their mass-to-light ratio is very high. For these reason, thorough the observations of nearby dwarf galaxies, MAGIC can carry out studies on dark matter [36], [37]. According to the Super Symmetry Model (SUSY), a candidate dark matter particle, called *neutralino*, can annihilate producing two γ-photons or a γ photon plus a Z boson [38]. Since dwarf galaxies are not expected to emit high energy γ-rays (since they are very old systems) if the latter will be detected, they would be probably related to a dark matter discovery. As none γ-emission have been detected so far, observations of dwarf galaxies set strong constraints on dark matter self annihilation cross section.

Besides source characterizations and emission modeling, MAGIC can also contribute to the characterization of the *Diffuse Galactic Emission* (even if it is difficult to be detected through the IACT technique, see Section 1.4.2), and quantum gravity. In particular, concerning whether the latter, studies on of the delay of two γ photons with different energies can establish the photon progagation velocity depends on photon energy. Moreover, also studies on the axion-like-particles can be carried out [39].

As seen in Section (IACT), the ground-based gamma-ray telescopes can achieve information about a γ-ray entering the atmosphere through the detection of the Cherenkov light produced by the ensuing atmospheric particle shower. Beeing the Cherenkov flash light very short and dim, the telescopes need a big area to collect such light. Before describing MAGIC subsystems in deeper detail, it is worth following the main path of the signal through the

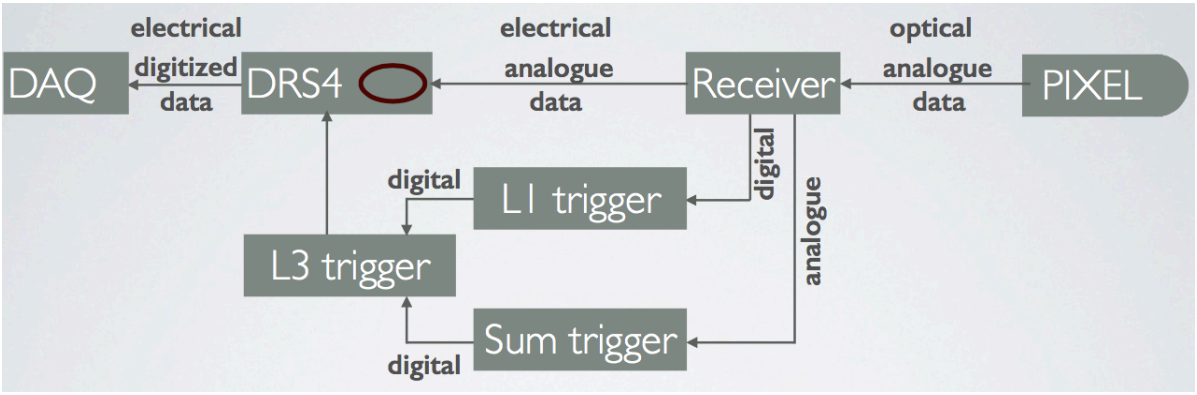

Figure 2.2: Signal path in the MAGIC hardware chain, from camera pixels to data acquisition system. *Credits*: Daniel Mazin.

hardware chain (Figure 2.2). When the Cherenkov radiation - mostly produced in the ultra violet and in the optical band - hits the mirror dishes of the telescopes, it is reflected into the camera and detected by several photomultiplier tubes (PMTs). After that, the electrical signal coming out from the PMTs is converted to an optical one and carried to the readout electronics through long ($\sim$ 160 m) optical fibers. There, the optical signal enters the receiver boards where it is converted back to an electrical one. Different levels of a trigger system, combined with a signal sampling, are then responsible for the discrimination of the gamma Cherenkov events from the background noise. In the receiver boards the signal is split into an analog branch directed to a ring buffer, where it is stored for a limited time interval, waiting for a trigger signal. Other two branches are sent to the trigger systems: a digital signal reaches the standard trigger, and an analog one reaches the *Sum Trigger II*. If a trigger signal occurs, the data stored in the DSR4 chips are read and digitized by the acquisition system, and stored on disks later on.

2.2 Pre-upgrade Stereo Configuration

At the end of its construction in 2009, MAGIC II was a clone of MAGIC I, except for some hardware improvements [40]. At the beginning of the stereo mode observations the main differences between the two telescopes (summarized in Table 2.1) were the following:

- the two cameras differed on numbers and diameters of PMTs. MAGIC I camera was composed by 577 PMTs (one PMT corresponds to one pixel), divided in 397 smaller pixels (1 inch diameter each, corresponding to 0.1°) in the central region of the camera, and 180 larger ones (2 inch diameter each, corresponding to 0.2°) in the outer region. Instead, MAGIC II camera is homogeneous and consists on 1039 hexagonal pixels, all of the same size of 1 inch diameter. Both camera had a field of view of 3.5°;

- the active trigger region area of MAGIC I (0.9° in radius) was 1.7 times smaller than the area of MAGIC II (1.2° in radius);

- the calibration boxes of MAGIC I is equipped with different coloured LEDs, while the calibration box of MGIC II is based on a frequency tripled passively Q-Switched Neodym

YAG microchip laser (pulse width of 700 ps at 355 nm), plus two rotating attenuation filters wheels to provide a large dynamical range;

- the readout system was based on different tecnologies. MAGIC I readout consisted on an optiacal multiplexer and off-the-shelf Flash Analog to Digital Converters (FADCs) (MUX-FADC referenza); and the readout of MAGIC II was based on DRS2 chip, that was more compact and cheaper, but whose performances were worse than FADCs;
- the receivers boards of MAGIC I suffered from aging problems that made the failure probability quite high.

Table 2.1: Main differences between the camera, readout and calibration system of the MAGIC telescopes before the major upgrade in 2012, from [40].

Parameter	MAGIC I	MAGIC II
N pixels	577 (1 inch) + 188 (2 inch)	1039 (1 inch)
N trigger pixels	325	347
Trigger area [deg^2]	2.55	4.30
Field of View [deg]	3.5	3.5
Camera shape	hexagonal	round
Readout system	MUX-FADCs	DRS2
Sampling freq. [GS/s]	2.00	2.05
Dead time [μ/s]	25	500
Calibration box	coloured LEDs	Neodym YAG microchip laser

As in this thesis the pre-upgrade data will be analyzed and used for further analysis, it is worth dwelling on the different components and performance that distinguish the pre and post-upgrade configuration. Parts that remained the same as in the current operative configuration, will be described in Section 2.3.

2.2.1 MAGIC I Camera

In this Section the camera of MAGIC I will be described. As the MAGIC II camera mantained its original design since its installation, it will be presented in Section 2.3 describing the current configuration.

The camera originally installed on MAGIC I [41], [42], showed in Figure 2.3, had a dimension of 1.5 m in diameter and a total weight of 450 kg. It was composed by 397 PMTs - 1 inch diameter, corresponding to 0.1° field of view - in the inner part, surrounded by 180 PMTs, 2 inch diameter, corresponding to 0.2° field of view. Both PMTs types (Electron Tubes 9116A and 9116B) were characterized by a time response FWHM lower then 1 ns. All 577 hemispherical PMTs are arranged in hexagonal board and connected to an ultrafast low-noise trans-impedance preamplifier. They are characterized by six dynodes and by a low gain (2×10^4) in order to work efficiently also with a high rate of the night sky background. Their quantum efficiency is enhanced up to 30% thanks to a special coating able also to extend it

Figure 2.3: First MAGIC I camera. On the left: inside view of the hexagonal camera with the smaller pixels in the inner region surrounded by the bigger ones [42]. On the right: the camera installed on the telescope [41].

to the UV band [43]. Moreover, in front of each PMT is placed a light collector that acts as a guide to avoid the loss of photons with large incidence angles ($\sim 40°$) and dead area between the pixels. These alluminum collectors, called Winston cones, have an hexagonal shape and are 5 cm long.

In order to calibrate the signal, i.e. to homogenize the responce of each pixel, the camera was equipped with a calibration box based consisting of a light pulser (in three different wavelenghts: 370 nm, 470 nm, and 520 nm) and a continuous light source to simulate the night sky background [44].

Once amplified, the outcoming electrical signal is converted into an optical one by Vertical Cavity Surface Emitting Laser drivers (VCSELs) and coupled to multimode optical fibers ($\sim$ 150 m long) to be transported to the readout system placed in the counting house.

2.2.2 MAGIC I and MAGIC II Readout Systems

Once the optical signal reaches the receiver boards, it is converted back to electrical, amplified and splitted into a digital and analog signal respectively. The digital signal - once the time delay was adjusted - is transmitted to the trigger branch (see Section 2.3.4), while the analog one is sent to the readout branch. When MAGIC started observing in stereo mode in 2009, the telescopes mantained a different readout system until its replacement by a new one in autumn 2011.

The readout system of MAGIC I [41], [42] was based on the Flash Analog to Digital Converter (FADC). The analog signal coming from the receiver boards is further split and stretched to 7.8 ns into a high and low gain line to increase the dynamic range. In the high gain line the signal is amplified by a factor 10 and in the low gain line is delayed by 55 ns. In the case signal exeeds a predefined, adjustable threshold both lines are combined through a GaAs analog switch, otherwise only the signal coming out from the high gain line is digitized by the 8 bit 300 MHz FADCs and stored continuously into a 32 kByte long ring. When a trigger signal is sent, if the signal is still inside the buffer time window ($\sim 100\mu$s), it is written to a 512 kByte FiFo buffer (maximum rate of 80 MByte/s). The buffer readout time was very short: 20 μs for 1kHz trigger rate that amounts to $\sim$ 2% of observational time. Finally, the

data that succesfully fill the above criteria was recorded in dedicated RAID disks system.

The readout system of MAGIC II [45] was based on a different technology with respect to MAGIC I. It is based on a Domino Ring Sampler (DAQ), a low power analog sampler. The analog signal is stored in a multi capacitor bank (1024 cell in a DRS, version 2), where all capacitors are organized in a ring buffer. Since the speed of the domino wave depends on several factors (such as temperature, supply voltage), each capacitor is sequentially enabled by a shift register driven by an internally generated 2 GHz clock locked by a phase-locked loop (PLL) to a common synchronization signal. The time response of the chip is not homogeneous because of its channels are subjected to a delay, depending on the position of the readout window inside the domino ring. However, this effect can be removed thanks a calibration procedure. When a signal was received from the trigger unit, the domino wave was is stopped, freezing the contents of the capacitors. Then, the buffer content is read out by a register at 40 MHz frequency and digitized externally by a 12 bits resolution Analog to Digital Converter (ADC).

The different readout system implied a different conversion from integrated counts to photoelectron: for MAGIC I the value is around 0.01 phe/counts (for the smaller pixels) and around 0.002 phe/counts for MAGIC II. Moreover, even if the readout of MAGIC II was newer, more compact and cheaper than MAGIC I, it presented a big disadvantage: it increased the dead time of $\sim 10\%$, leading to a loss of $\sim 12\%$ of observational time.

2.2.3 Performance

Since MAGIC telescopes have starded to work in stero mode, the performance improved significantly with respect to the mono observations. The stereo MAGIC performance was estimated analyzing 9 hours of good quality Crab data at low zenith angle ($\leq 30°$), observed in wobble mode (i.e., an observation mode where the source position is placed $0.4°$ off the camera center, see Section 2.4) between November 2009 and January 2011 [40]. In what follows the energy resolution, the angular resolution, both the integral and differential senitivity will be described.

The energy reconstruction performance is computed by using Monte Carlo simulations. In a simulated γ-ray the true energy is known, and it can be easily compared with the reconstructed one. The resolution is then obtained by fitting the histogram containing the $(E_{rec} - E_{true})/E_{true}$ with a Gaussian distribution. The energy resolution corresponds to the standard deviation of such a distribution, and it is worth remembering that it depends on the θ^2 cut (see Section 2.5.6): the stronger are the cuts, the better is the energy resolution. The performance in the energy reconstruction, showed in Figure 2.4 (a), depends also on the energy range, and shows it is better in the medium range, being 16% at few hundred GeV. At low (≤ 100 GeV) energy it is poorer due to a lower photon number and hence to a higher noise, while at high (≥ 300 GeV) energies it is worse because of the truncation of large images and a lower statistic in the training sample. There are also a bias effect introduced by the method and estimated as the mean of the Gaussian distribution, but it is corrected during the analysis in the unfolding procedure (see Section 2.5.8).

The angular resolution is defined as the radius θ_{Gauss} that contains 39% of the γ-ray coming from a point like source, and it can be obtained by fitting the reconstructed event direction with Gaussian distribution. The achieved angular resolution, using the stereo DISP RF method (see Section 2.5.5), is $\sim 0.07°$ at 300 GeV, but even better at higher energies, as shown in Figure 2.4 (b). An alternative method consists in computing the angular resolution

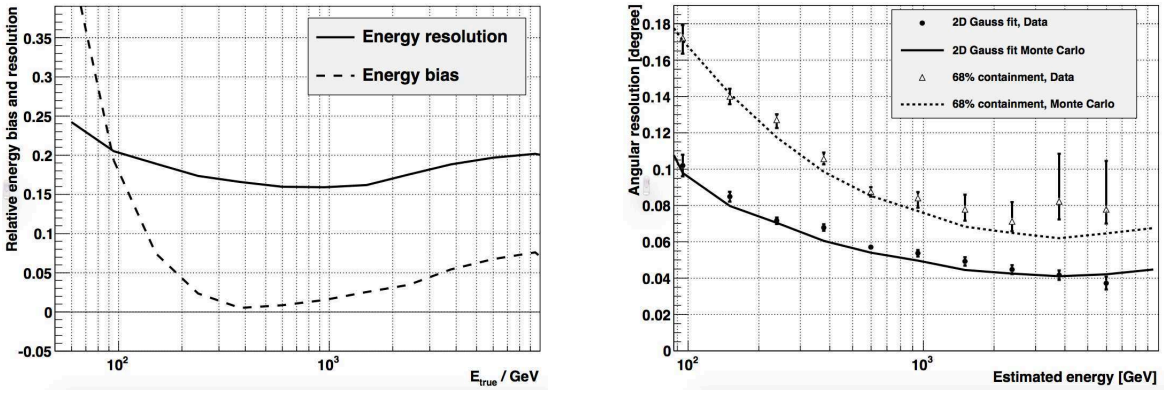

(a) (b)

Figure 2.4: (a) Energy resolution (solid line) and bias (dashed line) as functions of the true energy. (b) Angular resolution as function of the estimated energy obtained both with Gaussian fit (filled circles for Crab Nebula data and solid line for Monte Carlo simulations) and the 68% containment radius (triangles for Crab Nebula data and dashed line for Monte Carlo simulations). From [40].

within the distance $\theta_{0.68}$ that encloses the 68% of the events. Tipically $\theta_{0.68} \sim 1.5\,\theta_{Gauss}$.

The sensitivity is defined as the flux of a given source able to produce a significance $N_{excess}/\sqrt{N_{bkg}} = 5$ in 50 effective hours of observational time, where N_{excess} and N_{bkg} are respectively the number of the excess events and the estimated number of events related to the background. Since the previous definition, the significance is a simplified formula that can be applied in case of weak sources togheter with a perfectly known background, in most astrophysics applications it is commonly obtained using the Equation 17 in [46]. When the telescopes started to operate in stero mode, the integral sensitivity increased significantly: by a factor 2 in the medium range, reaching $0.76 \pm 0.03\%$ C.U. (Crab Unit) and up to a factor 3 at lower energies. Also the differential sensitivity, i.e. the sensitivity in a narrow energy band, improved: at medium energy it reached $\sim 1.5 - 2.5\%$ C.U. and $\sim 10\%$ C.U. below 100 GeV. Both integral and differential sensitivity are shown in Figure 2.5.

2.3 The Major Upgrade

As seen in the previous Section, the main differences between the two telescopes concerned the cameras, the readout and the trigger systems. In order to homogeneize the system, and therefore to improve the stereoscopic performance and sensitivity, an upgrade that made the two telescopes essentially identical, followed between summer 2011 and 2012. This upgrade touched mostly MAGIC I and all details can be founded in [47]. Briefly the main operation regarded the replacement of:

- the MAGIC I camera by a new camera, identical with the MAGIC II camera;
- the readout of both telescopes with a system based on DRS4 chips;
- the MAGIC I trigger system;

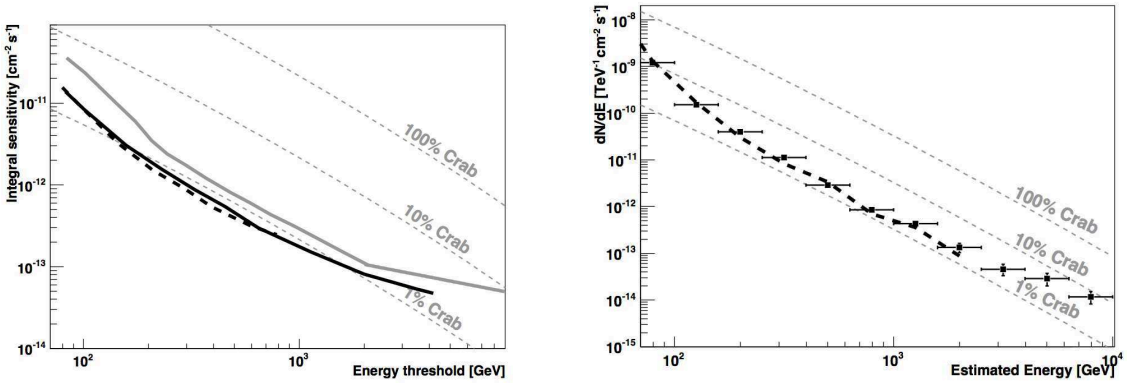

(a) (b)

Figure 2.5: (a) Integral sensitivity as a function of energy obtained with Crab Nebula data (black solid line) and Monte Carlo simulations (black dashed line). A gray solid line only refers to MAGIC I. (b) Differential sensitivity as a function of the estimated energy (horizontal bars mark each energy bin) obtained with Crab Nebula data (black squares) and Monte Carlo simulations (black dashed line). In both panels, gray dashed lines refer to different fractions of the Crab integral flux for comparison. From [40].

- both calibration boxes with a slight improvements with respect to the previous MAGIC II calibration box.

This upgrade improved considerably the performances of the system. In particular, the MAGIC I camera replacement allowed the trigger area to be enlarged in order to increase the flux sensitivity to extended sources and to better estimate the background noise in wobble-mode observations. Furthermore, the smaller pixels in the central region of the camera allows a better reconstruction of the image parameters and, accordingly, of the properties of the incoming γ-ray. Also the exchange of both readout systems, currently based on DRS4 chips, had a crucial role in the performances. For the construction of MAGIC II, DRS2 chip was choosen despite of the MUX-FADC, because of their more compact size and cheapness. Notwithstanding these advantages, DRS2 chips were affected by worse performances, in particular in what concern the electronic noise and in dead time that increase untill 500 μs instead of the previous 25 μs.

After the upgrade, moving to the new generation of DRS4 chips allowed a good compromise to be achieved among chip size, cheapness and performance. The lower noise of the DRS4 chips allowed to decreased the analysis energy threshold. Moreover, by reducing the dead time to 27 μs, a gain of 12% in the observational time was achieved with respect to the previous configuration.

After the major upgrade MAGIC entered in its best era, as for stability and performances. The homogeneity reduced a lot the probability of incurring in thechnical problems and, consequently the expert manpower intervents. The description of the current operating system can be found in the following Sections.

2.3.1 Stucture and Drive

The structure supporting the mirrors is a net of carbon fiber tubes ($\sim$ 8 tons). The structure supporting the camera side (including counter weights) is made of aluminum, for a total weight of $\sim$ 3.4 tons. Adding the weight contribution due to mirrors ($\sim$ 9 tons), camera ($\sim$ 0.89 tons), camera towers ($\sim$ 20.2 tons) and the base structure (including the motor drives), MAGIC reaches a total weight of about 67 tons. This allows the telescope to fast reposition in case of incominig alerts of Gamma Ray Burst (GRB): the telescopes can slew 180° in the azimuth direction in less than 30 seconds.

The structure is controlled by a drive system, based on an Alt-Azimuth mount. There are two allowed movements: elevation that controls the zenith position and horizontal movements that controls the azimuth position. The telescopes can move in the azimuth angular range between $-90°$ and $-400°$, and in a zenith range between 100° and $-73°$, where the zero-point corresponds to the local zenith and the angle are clockwise counted in the direction of the camera in park position. The 100° configuration was designed to allow MAGIC to point towards the ocean for neutrino searches, while the so-called reverse mode (positions $\leq 0°$) is used only for mantainance. There are three drive motors Bosh Rexroth MHD112C-058 (two for the horizontal movements and one for the elevation) that exert the power on drive chains with a minimum slip. The backlash in the elevation are avoided thanks to a proper balancing. The movements are controlled by two shaft encoders (Heidenhain ROQ 425), one located on the west tower, and the other on top of the central axis. The telescopes' structures suffer of both imperfections and deformations due mainly to gravitational stresses. To reduce their impact on the pointing position, bending models are applied both to the software controlling the drive system and on the analysis chain.

2.3.2 Mirrors and Active Mirror Control

The first approach of the Cherenkov light with the telescopes, occurs on the mirror dishes. Both reflectors are placed 85 m away from each other. They are 17 m in diameter, with a focal to diameter ratio $f/D \sim 1$, and a parabolic shape to mantain as much as possible the temporal structure of the events generated by air-showers.

During the MAGIC lifetime, the mirror configuration did not remain the same and it underwent to several exchanges and replacements. MAGIC I dish was originally composed by 964 mirrors whose main structure consists, from bottom to top, is composed of: an alluminum base, a micro-holed hexcell-honeycomb that confers rigidity to the whole structure, high temperature conductivity and low weight, a heating wire to avoid the dew or ice formation inside the mirrors, a flat square AlMgSi-alloy of 495 mm side, contaminated with silicon, covered by a thin ($\sim$ 100 nm) protective quartz (with some admixture of carbon) layer. Each mirror is then mounted on a back panel that host 3-4 mirrors, for a total weight of $\sim$ 25 kg. There are two mirror models installed on the dishes that differs for minority features (Figure 2.6): one designed by the *Max Planck Institute for Physics* (MPI) in Munich, and the other by the *Istituto Nazionale di Fisica Nulceare* (INFN) in Italy. Mirrors designed by MPI (244 installed) are characterized by a 0.6 mm-thick plate as base, a micro-holed hexcell-honeycomb 20.7 mm-thick, and a AlMg plate 0.6 mm-thick with 12 Ω heating wire. On the other hand, mirrors designed by INFN (740 installed) are characterized by 1mm-thick aluminum box that wraps the whole mirror, the same micro-holed hexcell-honeycomb, a 1 mm-thick Vetronite^{TM} foil, with a 46 Ω impedance printed circuit wire. Moreover the two designs differ also for the

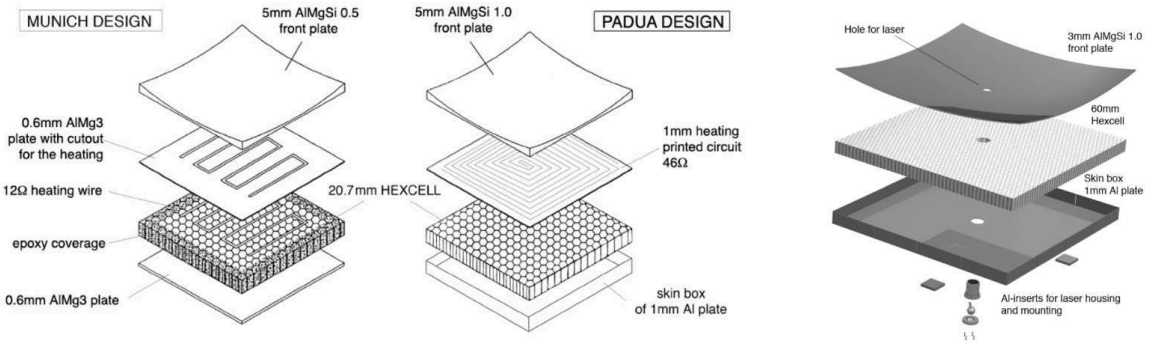

(a) (b)

Figure 2.6: (a): MPI Munich and INFN Padua mirrors design for MAGIC I reflector; (b): upgraded design of INFN mirrors for MAGIC II reflector. From [48].

silicon contamination in the surface layer. The average reflectivity of MAGIC I mirrors is around 85%.

After a couple of years, some MAGIC mirrors showed deformations due to water infiltration, and mainly for this reason 100 damnaged mirrors were replaced by new sligthly different ones developed by INFN. In the new design the plastic heater board was removed (and replaced with an external element on the back) to favour the coupling of the alluminum layers. Moreover the mirror box was built a little smaller then the other panels to avoid water and humidity infiltration.

The mirrors of MAGIC II were scaled up to 1 m^2, allowing for faster installation and lower weight ($\sim$ 18 kg), and avoiding the intra-panel allignement and a backplane support. Also in MAGIC II were installed two different mirror types: 143 units with the INFN upgraded design in the central part, surrounded by 104 new glass mirrors designed by *Istituto Nazionale di AstroFisica* (INAF) in Italy. Respect to MAGIC I, the INFN mirrors have a thicker honeycomb layer that increase the structure rigidity, and a better focussing power. The INAF mirrors are built by the so called *cold slumping technique*: a thin 1-2 mm-thick glass foil is slowly and elastically deformed - through vacuum aspiration - until it reaches the convex form given by an apposite mold. The honeycomb structure is placed in between the surface glass and another glass sheet, and glued by epoxy adhesive. Finally, the surface glass is alluminized and covered by a quartz protective coat.

Padua INFN developed another mirror model, trying to solve the humidity infiltration, still affecting the mirrors even if strongly reduced. Mirrors are composed by two glass layers, separated by steel cylinders to avoid ice problem. Moreover the reflective glass layer is precoated to avoid expensive and delicate coating procedure. In order to test these new model, few mirrors have been installed on MAGIC I.

To summarize, currently MAGIC I dish has a total reflective area of 236.2 m^2 and it is composed by:

- some MPI 50×50 cm mirrors aluminum-honeycomb sandwich;

- several INFN-PD 50×50 cm aluminum-honeycomb sandwich;

- some INFN 1×1 m aluminum-honeycomb sandwich;

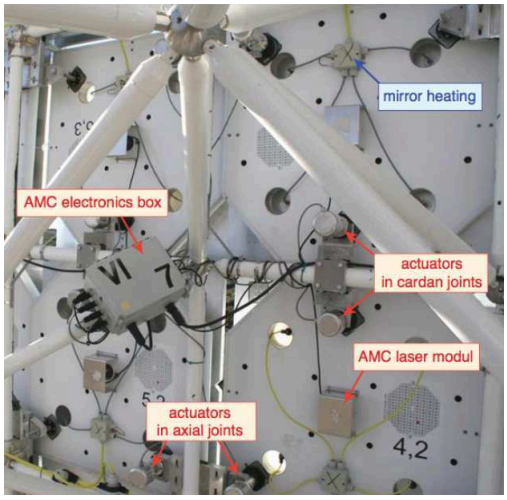

Figure 2.7: Back side of four mirror units and in the center the AMC electronic box. For each mirrors there is the mirror heating box, the laser module and two actuators in the cardian and axial joints, respectively. *Credits*: Markus Garczarczyk.

- some INAF 1×1 m cold-slumped mirrors;

while MAGIC II dish has a total reflective area of 236.8 m^2 and it is composed by:

- 143 INFN-PD 1×1 m aluminum-honeycomb sandwich;

- 104 INAF 1×1 m cold-slumped mirrors.

During repositioning and source tracking, the dishes of the telescopes are subjected to different stresses due to different gravitational loads and weather effects. This leads to small deformations from the optimal configuration that need to be corrected to ensure the best performance in detecting the Cherekov light coming from the air showers. The main conseguence of the dish deformations is the degradation of the Point Spead Function (PSF). In order to avoid such an effect, the mirrors have to be continuolsly realigned through the *Active Mirror Control* (AMC) system [49]. Each panels is connected to the main structure in three points, two of these equipped with two actuators, mounted in the cardian and axial joints respectively, as shown in Figure 2.7. The actuator mounted in the cardian joints has only one-direction free movement, while that mounted in the axial joint can move in two directions. The actuators moves differently each mirrors according to values stored in the *Look Up Talbles* (LUTs), obtained through a dedicated calibration procedure. Basically the LUTs contains the position of each actuator for every 5° zenith interval (the dependence in the azimuth direction is negligible). The actuators can move the mirrors with a precision lower than 20 μm that correspond to a distance lower than 1 mm in the camera plane.

The mirrors have to be continuosly realligned to garantee a focused system. Each mirror is equipped with a laser module in the centre, pointing directly into the camera. However, this focussing method is not used anymore because of too long focussing time (about 3 minutes) and pointing accuracy problem due to different matherial thermal extension coefficients. The AMC system is equipped with a SBIG camera in order to focus all mirrors, by using star images to fill the LUTs. The goal of this procedure is to minimize the point spread function (PSF). The tipical MAGIC PSF is currently lower then 12 mm. The main components of the

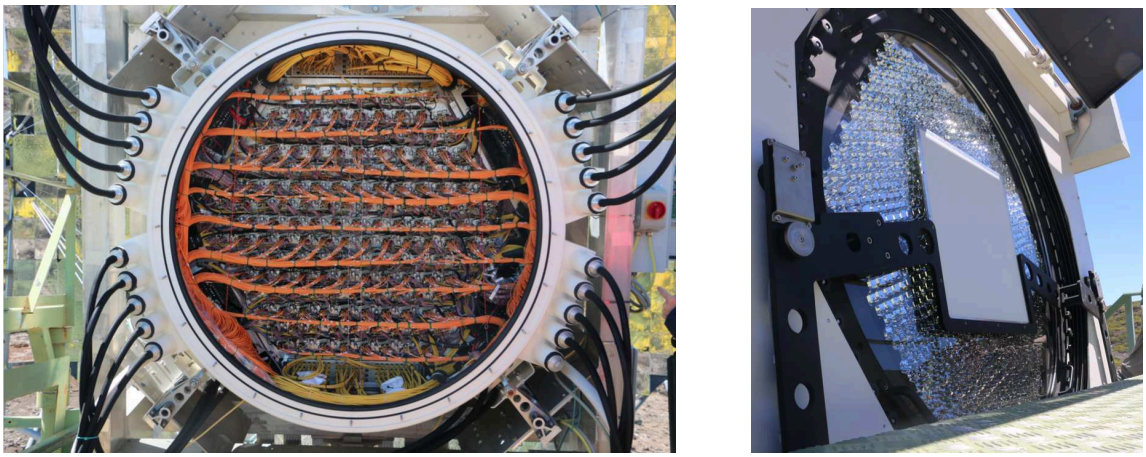

(a) (b)

Figure 2.8: MAGIC I new camera from the back (a) and front (b) side.

SBIG camera is are: a Nikon MF 180/2.8 ED objective, a CCD camera SBIG STL 1001E and different filters. Besides focussing, the SBIG camera is also responsible for the measurement of the individual mirror PSF (that spans between 3 and 6 mm), the reflectivity measurement of the reflector at different wavelenghts, and finally long time monitoring of both PSF and reflectivity.

2.3.3 Camera and Calibration System

The Cherenkov light reflected by the mirrors are focused into the camera, placed on the focal plane of the telescopes. The camera, shown from both sides in Figure 2.8, has a circular shape 1.2 m diameter for a total weight of $\sim$ 850 kg. The 3.5° Field of View (FoV) is mapped by 1039 photomultiplier tubes (0.1°) from Hamamatsu (type R10408), 25.4 mm diameter with an hemisferical photocathode and 6 dynodes. PMTs convert the UV-photons of the Cherenkov shower into an electric signal and, since the high quantum efficiency and a very fast responce are the key elements to detect short Cherenkov flashes, they are characterized by a high quantum efficiency of about 33% at 350 nm, a gain of $3-4\,10^4$, and a signal response of about 1 μs.
Thus the camera has 1039 module pixels, each constituted by: a PMT, its own high voltages generator (tipical HV $\sim$ 1250 V), a preamplifier with a dyod to prevent damages due to strong current spikes, and, finally, a VCSELs to convert the electrical signal into an optical one. In turn, 7 PMT modules are grouped in a cluster.
On the top of each PMTs a hexagonal structure, called *Winston cone*, is mounted to collect the light up to an 45° of incidence. Behind the Winston cones there is a UV-transparent plexiglass and, finally, all the camera is protected from daylight by two lids. Since the VCSELs need to work to a constant temperature, the camera has an its own cooling system to mantain the temperature around 14°. Details of MAGIC I and MAGIC II cameras can be found in [50] and [51].

The gain of each PMT is not exactly the same, thus, to avoid responce inhomogeneities a flatfilding procedure has to be performed. This procedure allows to find PMT high voltage values to be applied on each pixel in order to ensure the same pixel responce when the camera

is equally illuminated. For this purpose, in the center of each telescope dish, a calibration box is istalled to provide a uniform camera illumination through well known light pulses of different intensity. A 355 nm Nd-YAG laser produce 0.4 n pulses whose intensity is adjusted by filters (that can regolate the beam intensity from 1 to 1000 photoelectrons) and diffused by an Ulbricht sphere that streatchs the FWHM up to 1 ns [52].

2.3.4 Receivers and Trigger System

When the Cherenkov light is reflected into the camera PMTs and an electric signal is produced, it is converted into an optical one by the VCELs and transported to the *Counting house* through ~ 162 m long optical fibers, where all the readout electronic is placed. Firstly, PMTs signals go into the receiver boards that convert them back into analog electrical signals. Further on the same signal is split in three branches: the readout branch carring an analog signal to the DRS4 ring buffer, and the trigger branches trasporting both analog and digital signals to different trigger systems.

All signals captured from the telescopes do not belong always to γ-ray events, but most of them contributes to the night sky background. In fact, only about 1 event every 10^4 is produced by a γ-ray entering the atmosphere. Sources, classified as background, are:

- *Hadronic Showers.* The cosmic rays are constituted not only by γ-rays, but also by hadrons such as protons, electrons, neutrons and heavier nuclei, and all of them produce a shower entering the atmosphere. Fortunately, hadron-induced shower are characterized by different features (see Section 1.4.2) with respect to those induced by γ-rays and can be quite easily discriminated. In a hadronic shower a lot of decays take place, and they significantly contribute to spread the shower extension and to make it quite irregular. The principal decay in these kind of showers is $\pi \rightarrow \gamma\gamma$.

- *Secondary Showers induced by Electrons.* When an air shower develops, many electron-positron pairs are formed. In turn, electrons produce a minor air shower with lower intensity, but very similar characteristics to shower induced by a γ-ray

- *Muon events.* Several muons are producted inside a hadronic shower. Due to their long lifetime, they can easily reach the ground and produce Cherenkov light very close to the telescope. This means that most of muon events are not seen by the other telescope. Moreover they form a circular shape on the detector, very easy to be distinguished.

In addition, also electronic noise has to be taken into account. It is purely due to the electonic components (PMTs, VCSELs, recivers, DRS4 chips) and not to a real incoming signal. It can be both continuous and pulsed, and can be treated with special data called *pedestal* and *subpedestal*. Finally, also all the other environmental light sources contribute to the night sky background, increasing the average illumination of the camera. They are basically the zodiacal light, lights coming from the town and reflected by the clouds, accidental car flashes and even bright stars in the field of view.

These events can be distinguished from each other because the images produced on the camera have differen shapes and develop in different time intervals.
Based on these considerations, MAGIC is equipped with a digital trigger system able to identify Cherenkov events, but not able to discriminate between γ and hadron shower. It is based on an algorithm that searches for neighbouring pixels that exceed an adjustable

discriminator threshold (DT) (that could be different for each pixel) whitin a fixed time window ($\sim$ ns, characterisic time for γ-ray shower). It is a decisional system, built on three levels: the first and second levels (the so called *Local Trigger*) work independently for each telescope, while the third (*Stereo Trigger*) combines the signals coming from each one. The task of each level is briefly described in what follows:

- *Level 0* (L0). When the analog signal coming from each pixel exceeds the DT value, the pulse width is defined, the signal is digitized and sent to the next trigger level (see Figure 2.9). The digital trigger is produced directly in the receivers board.

- *Level 1* (L1). The L1 trigger receives the information about the status of each pixel: on or off, depending if the incoming signal exeeds the DT or not. L1 trigger is responsible for finding spatial and temporal coincidences coming from L0 trigger in order to discriminate between NSB or Cherenkov events. In fact, while the firsts are quite randomly distributed, the latter have a very compact shape and generate signals in only few nanoseconds. Based on these considerations, L1 trigger first check if x pixel - belonging to a compact group - show any signal. This is the so called x *Next Neighbor* (xNN) logic, where x can be fixed to 2,3,4 or 5 (in the current stereo trigger, x is set to 3). Such a signal in searched in 19 overlapping indipendent hexagonal zones, called *Macrocells*, grouping 37 pixels each. Finally L1 trigger checks if the signal in the x group of pixels is generated within a narrow time window ($\sim$ 9 ns). The signals coming out from each macrocells is processed by indipendent LT1 boards and sent to the *Trigger Processing Unit* (TPU) that computes the final trigger, combine the signals of all macrocells in an OR gate to be sent to the last trigger level.

- *Level 3* (L3). L3 trigger receives the information from L1 levels of both telescopes. If two L1 signals occur within a limited time window of 200 ns, they are coupled because they are generated by the same event. The consequent stereo trigger signal is sent to the prescaler board (that accept different kind of trigger signals such as L1T, calibration, pedestal, pulse injection, and eventually applies scaling factors). At this level, because of different light paths (depending on zenith-azimuth position) between the two telescopes, in order to synchronize L1 signals, digital delays are applied. Then, the final trigger signal is prepared and sent to the acquisition system.

The current stereo trigger allows events to be capture events with an energy threshold down to 50-60 GeV. In order to lower this threshold, other trigger systems has been developed: the *Sum Trigger II* (STII) [53] (currently operative on MAGIC) and the *Super TOPOlogical Trigger* [54] (still under commissioning).

γ-ray events are supposed to generate well-shaped and compact images on the camera plane. However, sometimes (mostly so in the case of low energy events) they can produce images that show subfeatures such as small branches. So, searching for too structured images, can lead to miss some events. In order to avoid this it is necessary to relax a bit the topological contraints, developing an alternative trigger system. The concept behind this kind of trigger consists in summing the charge contained in a compact group of pixels and to put a threshold on it – instead of on each individual pixel. In this way it will be possible to capture energy events that would be missed with the standard trigger.

Differently from the standard trigger, the ST trigger area is smaller. It is divided in 55 hexagonal macrocells (with a wider overlapping), containing 19 pixels each. The output

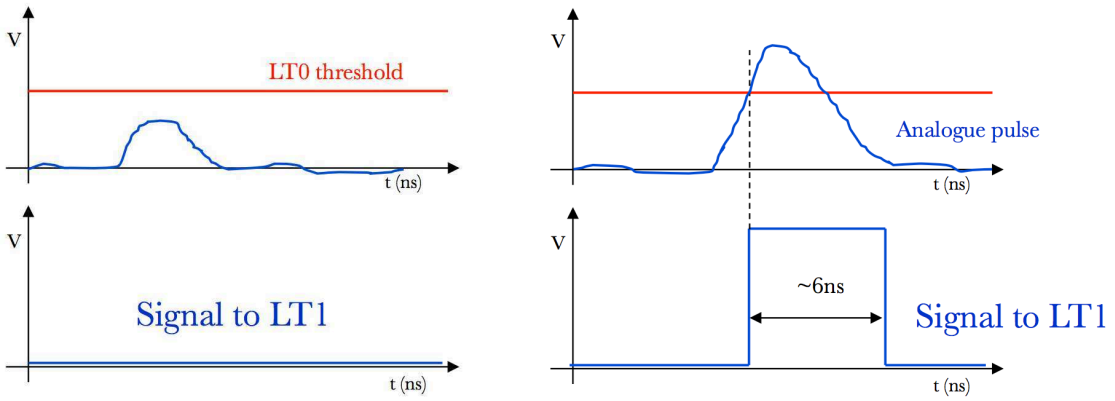

Figure 2.9: Level Trigger 0 (LT0). Digitalization of the analogue pulses above a fixed threshold in case of no signal (a) and signal (b). In the upper panels it is shown the analog pulses coming from the camera in function of time, while in the lower panels the related digital signal transmitted to the next trigger level (LT1). *Credits*: Francesco Dazzi.

analog signal has to be: (i) delayed ($\sim$ 6.5 ns), to correct delays introducted by PMTs and fibers; (ii) equalized, to obtaine the same responce for each channels; and (iii) clipped, to avoid fake triggers generated by after-pulses due to the release of a proton in the first dynode. ST II shows better performance at 50-60 GeV, but can reach down to 25 GeV, so lowering the energy threshold of MAGIC by a factor 2.

2.3.5 Readout and Data Acquisition System

When the L3 trigger recognizes that two L1 triggers (coming from MAGIC I and MAGIC II respectively) belong to the same event, all camera pixel signals have to be read and stored into a disk. The readout system togheter with the software *Domino Data Aquisition System* (*Domino*DAQ) [55] are responsible for this process.

The readout system before the major upgrade in 2012 is described in Section 2.2.2. After the major upgrade, both redout systems are based on DRS4 chips that allowed to heavily reduce the dead time of the previous configuration, from 500 to 27 μs. These chips are characterized by a lower noise ($\sim$ 0.5 phe per cell that corresponds to 6-10 counts) and a larger bandwidth (700 MHz) with respect to DRS2 chips, but keep showing a temperature dependence [56]. Each DRS4 chip has a ring of 1024 capacitors that contain, for a limited time, the analog signal coming from the receivers. The analog signal flow through the capacitors and it is overwritten every 512 μs, that corresponds to the maximum memory buffer due to a sampling frequency of 2 GHz/s. When the L3 trigger sends a signal, the flow inside the capacitors is freezen, and the the ring buffer is read (33 MHz frequency) and digitized by the *Analog to Digital Converter* (ADC). The time needed from the trigger to the storage moment is around 300 μs, this means that only triggers coming in with a time delay lower than 200 μs can be recordered. Due to different paths, the signals coming from the telescopes operating in stereo mode have to be delayed, according to their zenith and azimuth position. However it remains a zone, the so called *Dead Zone* that corresponds to a particular azimuth and zenith intervals, where the the delay between the signals is higher than 200 μs and the stereo events

are lost. This problem was solved lowering the sampling speed in order to expand the time window.

DRS4 chips are installed on PULSer And Recorder (PULSAR) boards. There are 12 PULSAR boards for each telescopes, plus some extra board such as digital board that add information (time, number) for each event, BUSY board that produces busy signals, stopping the trigger during the readout. Each PULSARS contains 4 mezzanines, each of them hosts 3 DRS4 chips. Each chip has 8 channels (each corresponding to one pixel), so every PULSAR board can digitize the signal coming from 96 pixels.

2.3.6 Other Subsystems

There are other important subsystems and programs that monitor and control atmospheric and technical conditions during data taking.

- **LIDAR**. It is a single-wavelength elastic Rayleigh LIDAR (LIght Detection And Ranging) [57] operating at 532 nm wavelength. It works togheter with the MAGIC telescopes, computing - every 10 minutes - the transparency of the atmosphere in order to apply atmospheric corrections in data analysis. It is composed by a frequency-doubled, passively Q-switched, pulsed Nd:YAG laser (532 nm), a small telescope (1.5 m of focal length and an aluminum mirror 60 cm diameter) computer-controlled by an equatorial mount, Hybrid Photo Detector (HPD), and a FADC card for digitizing data to be recordered. The principle to determine the air transparency is simple: (i) the laser fires along the telescope axis direction, pointing to a region close to the MAGIC observation field of view, (ii) part of this light is reflected back by the molecules and particles present in the atmosphere, (iii) by using the arrival time and the intensity of the returning signal, both atmosphere transparency and cloudy layers height can be computed. Currently, LIDAR allows moderately cloudy data to be efficiently corrected, recovering $\sim 15\%$ of lost observation time.

- **Pyrometer**. It is a radiation pyrometer Heitronics KT 19.82, installed on the edge of the MAGIC I reflector. It can provide the sky cloudiness by measuring the sky temperature - with 0.01° of resulution - through the IR radiation between 8 and 14 μm reflected by clouds. The cloudiness is computed through the empiric relation $C = 1.54(T_{sky} - 0.31\,T_{air} - 0.1\,u - f(z))$, where T_{sky} is the temperature provided by the pyrometer, T_{air} is the air temperature, u is the air relative humidity and z is the zenith angle. The relation between the cloudiness values provided by, respectively, the LIDAR and the pyrometer are under investigation.

- **Weather Station**. It is a Reinhardt MWS 5MV station, placed on the roof of the counting house. It provides measurements of temperature, relative humidity, wind speed and direction every 2 seconds. These information are always available on the weather website.

- **TNG Dust Particle Counter**. Observations may occasionally be strongly affected by *calima*,wind-born sand from Shara. The main effect is a decrease of the transparency. To monitor the dust density, every two hours a TNG dust particle counter - installed at Italy's TNG (Telescopio Nazionale Galileo) site - returns the dust concentration, ρ_d, through a laser scattering. The air is considered clean when $\rho_d < 5$ μg/m^3; during *calima* $\rho_d \leq 100\mu$g/m^3.

- **All Sky Camera**. This instrument, complementary to the LIDAR and the pyrometer, instantly shows the sky conditions. The main difference lies in the fact that All Sky Camera can monitor the whole sky and not only a narrow zone close to the pointing position. It is composed by a kodak KAI 340 CCD (Charge-Coupled Device) of 640×480 pixels, equipped with a fisheye lens 1.4 mm focal lenght. It provides an updated sky image every 2 minutes. An additional script can superimpose the position of the sources to be observed during the night, bright stars and Solar System objects. Moreover, it shows 30° and 60° zenith circles, and the *dead zone*.

- **ATCA Guard**. It is a C++ program that collects all the computed quantities from the LIDAR, pyrometer, and weather station. It provides warnings and alerts when the conditions are approaching to the saefety limits. ATCA feedback, togheter with all plots related to the weather conditions, are available on line in real time during observations.

- **GRB alert**. The program managing alerts and GRB obervations is called *GSPOT* (Gamma Sources POinting Trigger). It runs continuously in background mode and it is connected with the GRB Coordinate Network (GCN). When a GRB is triggered by a satellite (Swift-BAT, Swift-XRT, Fermi-GBM, Fermi-LAT or AGILE), *GSPOT* receives a GRB alert from the GCN server, and checks whether: (i) the Sun is below the astronomical horizon; (ii) the alert is received within 4 hours of the GRB trigger; (iii) the error on the GRB position is $< 1.5°$; (iv) the GRBs zenith angle (for MAGIC) is $< 60°$; (v) the GRBs-Moon distance is $> 30°$. If all these criteria are fulfilled, a fully automatic procedure for GRB observation is enabled.

- **MOLA**. Magic OnLine Analysis is a C++ program [55] that provides a quick analysis of the observed sources in almost real time. All events recordered by the DAQs are processed within few seconds of their trigger time to provide preliminary information about source detectability. θ^2 plot, flux and the light curve are computed (see Section 2.5.6 and 2.8). MOLA is very useful for the observing crew to help them decide whether to on with further observation, or not, based on signal (or lack thereof) it returns.

2.3.7 Performance

The performance of the MAGIC system after the major upgrade and the comparison with the previous configuration is described deeply in [47]. Performance is estimated using Crab Nebula data taken under different conditions between October 2013 and January 2014. Moreover, all the following quantities are defined and estimated using the same approaches briefly described in Section 2.2.3.

The energy resolution for medium range, obtained through Monte Carlo simulations, is about 15%, while it worsens at high energies as well as at low energies. Figure 2.10 show energy resolution as a function of true energy.

The angular resolution improved by 5-10% after the upgrade. The resolution obtained from a bidimensional Gaussian fit (for $\theta^2 < 0.025°$) is 0.07° at medium energies (around 250 GeV) and ever better at higher energies, reaching 0.04° above few TeV. Figure 2.11 shows the angular resolution obtained with the two methods (described in Section 2.2.3).

The integral sensitivity, obtained for Crab Nebula-like spectrum, is about 0.55% C.U. in the medium range at few hundred GeV. At lower energies, between 60 and 100 GeV, the sensitivity improves significantly, decreasing from 10.5% to 6.7% and allowing to reduce the

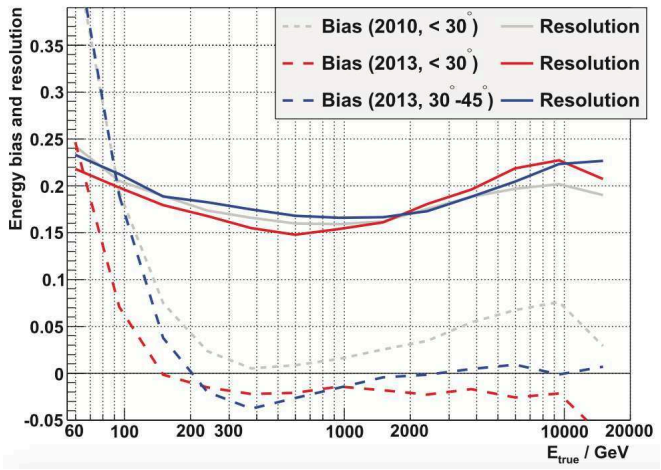

Figure 2.10: Energy resolution (solid lines) and bias (dashed) lines as function of true energy, obtained with Monte Carlo simulations. Gray curves are referred to pre-upgrade data at low zenith angles ($< 30°$), red curves to post-upgrade data at low zenith angles ($< 30°$), and blue curves to post-upgrade data at medium zenith angles ($between 30° and 45°$). From [47].

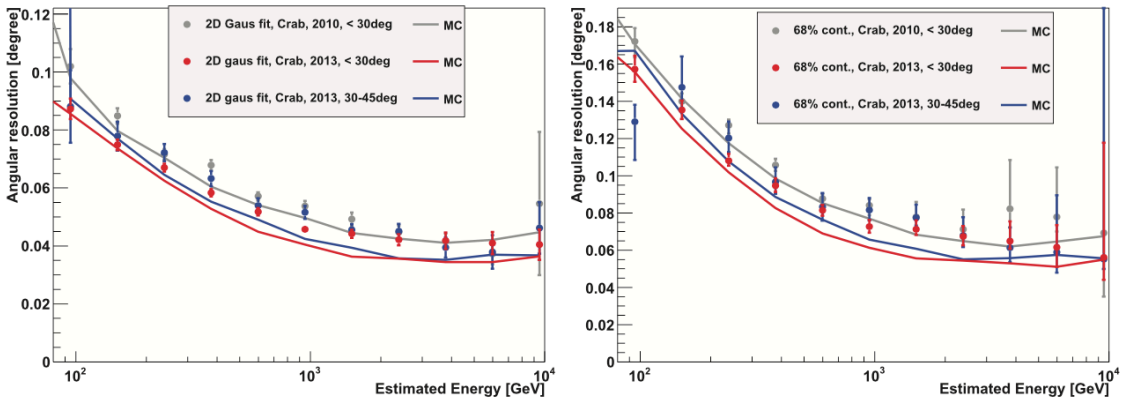

Figure 2.11: Angular resolution obtained with the bidimensional Gaussian fit (left panel) and 68%containment radius (right panel). Filled circles are refferred to Crab Nebula data and solid lines to Monte Carlo simulations. Colors are referred to different period and zenith angles: gray to pre-uprade data at low zenith angles ($< 30°$), red to post-upgrade at low zenith angle and blue to post-upgrade at medium zenith angles ($between 30° and 45°$). From [47].

observational time by a factor 2.5 at medium zenith angle. Figure 2.12 shows the evolution of the integral sensitivity during MAGIC periods and the differential sensitivity computed in narrow energy bins (5 for decade).

Finally the systematic uncertaintes is estimated $< 15\%$ for the energy scale, from 11 to 18% for the flux normalization and ± 0.15 for the energy spectrum power law slope.

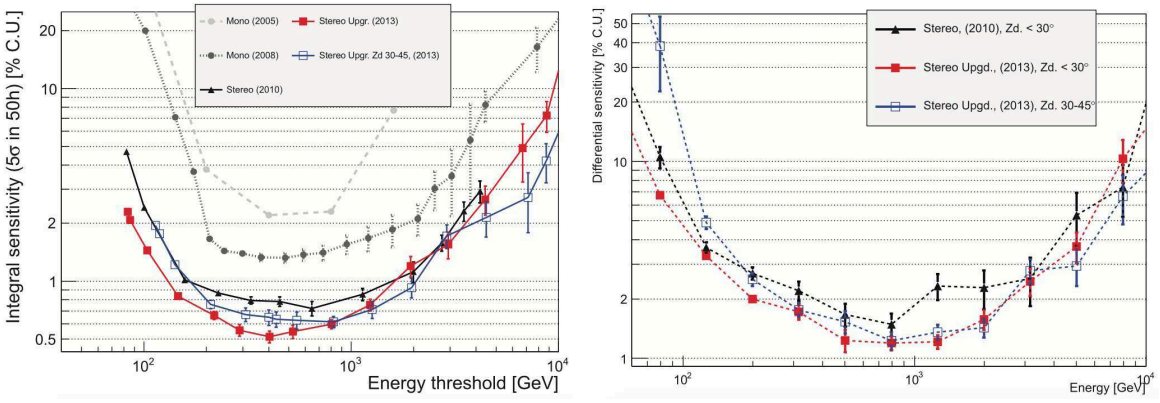

(a) (b)

Figure 2.12: (a) Evolution of integral sensitivity of MAGIC systems as function of energy. Simbols are referred to Crab Nebula data and curves to Monte Carlo simulations. Red and blue are referred to the stereo post-upgrade configuration for low ($< 30°$) and medium zenith respectively (between 30° and 45°), black to the stereo pre-upgrade configuration, dark and light grey only to MAGIC I for Siegen and MUX readout respectively. (b) Differential sensitivity as function of energy (5 bins for decade). Simbols are referred to Crab Nebula data and curves to Monte Carlo simulations. Red is referred to the post-upgrade configuration and low zenith angles ($< 30°$), blue to the post-upgrade configuration and medium zenith angles ($between 30° and 45°$), and black to the pre-upgrade configuration and low zenith angles ($< 30°$). From [47].

2.4 Data Taking

MAGIC can operate in different pointing modes:

- *ON/OFF* mode. Two different kind of data have to be taken for data analysis. During *ON* observation, the source position coincides with the center of the camera, while *OFF* data are taken as close as possible to the source, but in a region where the γ-ray emission is not expected. *OFF* observations are needed for background estimation. The main disadvantage of this pointing mode is that the source data and those used for the background estimation are not strictly simultaneous. Moreover the time spent for *OFF* observations is taken out from the *ON* ones.

- *Wobble* mode. It is used for most of MAGIC observations. In this pointing mode the source position does not coincide with the camera center, but it is placed 0.4° far from it. The background estimation is performed by using a region of the camera opposite to the source position, as shown in Figure 2.13. Several equally-spaced regions can be used for background estimation. The *wobble* mode avoids waste of time, and allows background estimation to be calculated simultaneously with the source data as well.

- *Drift Scan* mode. In this mode the telescopes point to a fixed direction. This occurs in special observations, called *drift scan*, where a source simply passes through the field of view, or when the telescopes point to the sea for neutrino studies.

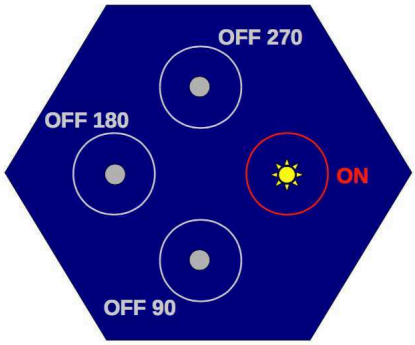

Figure 2.13: Source (in red) and OFF (in gray) *wobble* positions. Each position lies at a 0.4° from the camera center. At every changhe of *wobble*, the source moves to another position. *Credits*: Julian Krause.

Data can be taken under different light conditions: in the so called *dark* and *moon* time, depending on the presence of the Moon in the sky. The MAGIC telescopes were built to work principally in *dark* time, so they reach their best performance in such a condition. However, thanks to the low gain of the PMTs it is possible to observe also in *moon* conditions, except for 3 or 4 days around the full Moon phase. Before starting observations, the discriminator thresholds (DTs) for the L0 trigger (see Section 2.3.4) are set for each pixel. In addition, an Individual Pixel Rate Control (IPRC) system adjusts the individual DTs according to the current observation rate. In order to limit the effects due a higher night-sky background during the *moon* time, the DTs have to be increased. The typical mean L0 rate is 800 kHz and 500 kHz for *dark* and *moon* time, respectively. The IPRC lower the individual DTs if L0 rate gets down 250 kHz in *dark* and 150 kHz in *moon* time, and increase them if L0 rate exceeds 1200 kHz and 700 kHz respectively. Recently, moon filters have been built to allow observations even to be carried out during the full Moon phase. They are occasionally mounted on both cameras, but data taking and the following analysis is still under test.

Finally, data can not be taken in any weather conditions, but some safety limits have to be respected. Data taking is automatically stopped when the average wind speed exeeds 50 km/h, or wind gusts are above 40 km/h. When humidity increases above 90%, the high voltages have to be switched off to avoid damages. Light conditions also have to be continuously monitored because they influence the PMTs currents: observations have to be stopped if PMT currents exceed 47μ A, or their mean value exceed 30 μA. If a bright star is inside the field of view, and the current of some PMTs exceeds the safety limits, an automatic security procedure automatically reduces the high voltages of these pixels.

2.5 The Standard Analysis Chain

From now on the recorded data, i.e. those events that have overcame the trigger and the DAQ systems, are ready to be analyzed. The MAGIC data analysis is performed by the *Magic Analysis Reconstruction Software* (MARS), a package written in C++, that collects several macros and algorithms. MARS can be divided into three processing levels:

- *Low level.* These steps are normally done by the *On-Line Analysis* (OSA) at La Palma, and later reprocessed at *Port d'Informació Científica* (PIC) at *Universitat Autónoma de Barcelona* (UAB), where all MAGIC data are currently stored. Three algorithms are used to prepare data for the further level: (i) *Merpp* converts data from *raw* to *root* format and merges subsystem reports with data; (ii) *Sorcerer* calibrates each pixel in charge and time; (iii) *Star* cleans and parametrizes event images.

- *Intermediate level.* These steps are done by analyzers using the following macros: (i) *SuperStar* recognizes and compute the stereo parameters of the images coming from the two telescopes, but generated by the same event; (ii) *Coach* trains the gamma/hadron separation, the position reconstruction, and the energy estimation through the Random Forest algorithm; (iii) *Melibea* applies the results of the training process to both observed and Monte Carlo data.

- *High level.* In these steps the main quantities for each source are computed: (i) *Flute* computes the source flux and light curve; (ii) *Odie* computes the significance of a given observation; (iii) *Caspar* produces the skymap (particularly important for extended sources); (iv) *CoumbUnfold* unfolds the spectra and the spectral energy distributions provided by *Flute*.

In addition to these algorithms, there are several macros, such as *Quate* for automatic data selection once some criteria are assigned, *Pasta* for fast data information extraction, *Ape* for extracting error codes or messages in each step of file-processing, and so on. In the following Sections, the standard analysis chain for a point like source is described step by step.

2.5.1 Calibration

The routine responsible for the calibration of MAGIC data is called *Sorcerer* (Simple, Outright Raw Calibration; Easy, Reliable Extraction Routines). It is used to calibrate both DRS2 and DRS4 data. A calibration process consists in measuring the response of a detector exposed to a known light flux. In case of MAGIC, the final goal of the calibration process is to obtain the number of photoelectrons (i.e., the charge) and their arrival time for each pixel of the camera. Figure 2.14 shows the typical signal of a single pixel belonging to a given event. The counts (i.e., the number of photoelectrons) are shown as a function of time. The signal is contained in the highest peak, while the lower peaks correspond to the so called after-pulses and can be easily removed from the analysis.

The first step is to estimate the value of the baseline to be subtracted from the pulses. The baseline corresponds to the average of counts that randomly occurs in absence of pulses. Two methods may be used to estimate such a baseline. The first consists in taking random trigger events (pulses excluded), called *pedestal*, then building a counts histogram, and taking the mean of its Gaussian fit as baseline. This method is currently used for the DRS4 chips because the baseline is considered stable enough. However, a further correction is applied during the data acquisition because each capacitor presents different *pedestals*, and, moreover, such *pedestal* also depends on the position of the readout window in the ring buffer. The second method takes the average value of counts as baseline, calculated in a fixed time slot before each pulse. In such a way, a different baseline is assiciated to each event. This method was used mainly for the DRS2 chips because the baseline was not stable among the events.

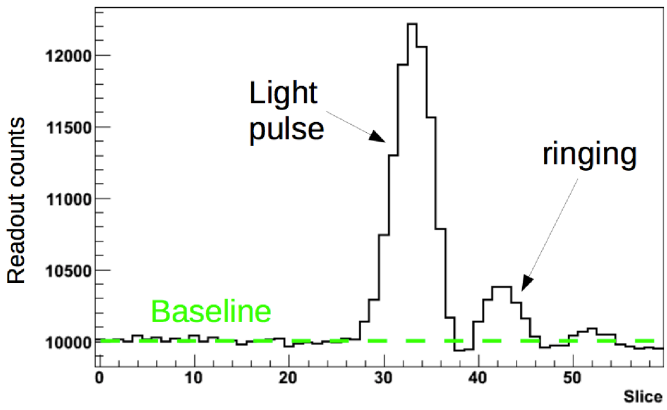

Figure 2.14: The typical waveform of a single pixel belonging to a given event. The counts are shown as a function of time (a slice corresponds to $\sim$ 0.5 ns). *Credits*: Julian Sitarek.

The second step is the signal extraction, obtained by integrating - above the baseline - the counts supposed to belong to the pulse. Also in this case, two different methods can be used: the *fixed* or *sliding window* method. The former performs a counts histogram over a fixed time window where the signal is supposed to be. Clearly, the time window must be large enough to contain the whole signal, but this might increase the signal to noise ratio. In the latter method, the time window still has a fixed width (3 ns, comparable with the air shower duration), and it moves along the time axis, scanning an interval 30 ns long. The integration time slot containing the maximum signal is associated to the pulse generated by the shower. In the past other methods were implemented for signal extraction, such as analytic fits with a specific shape pattern or spline interpolations. Currently, the *sliding window* method performs the signal extraction.

At this point, the integrated counts for each pixel have to be converted into numbers of photoelectrons through the so called F-factor method, described in [58]. This method provides both the number of photoelectrons and the conversion factor for each pixel by using dedicated calibration data. Assuming that 1 count corresponds on average to a certain number C of photoelectrons, a pulse containing N_{PHE} photoelectrons produces a signal characterized by a mean intensity $MEAN = N_{PHE}/(C\,N_{counts})$ and a root mean square $RMS = \sqrt{N_{PHE}}/(C\,N_{counts})$, where N_{counts} is the number of counts and assuming a Poissonian statistic. Once the $MEAN$ and the RMS have been measured using the calibration run, from the previous formula both the number of photoelectrons N_{PHE} and the conversion factor C can be achieved. Actually, a correction due to a non-Poissonian responce of the PMTs and to *pedestal* fluctuations has to be taken into account. So, the number of photoelectrons is given by:

$$N_{PHE} = F^2 \frac{MEAN^2}{RMS^2_{signal} - RMS^2_{pedestal}} \tag{2.1}$$

where F is an intrinsec parameter of each PMT, and the conversion factor is given by:

$$C = \frac{N_{PHE}}{MEAN} \tag{2.2}$$

However, the conversion factor can change during the night due mainly to temperature vari-

ations. For this reason dedicated *calibration run* are taken and stored with a 25 Hz frequency during data taking. Summarizing, the calibration procedure follows these steps (with a final *caveat*):

- the MAGIC calibration boxes (see Section 2.3.5) send short and constant light impulses into the cameras;
- the events generated by such pulses are stored and labeled as *calibration run*;
- from the *calibration run*, for each pixel the mean intensity and its root mean square are computed;
- the intensity root mean square of the *pedestal run* is computed ($\sim$ 1 photoelectron in perfect dark conditions);
- by using Equations 2.1 and 2.2, the mean number of photoelectrons and the conversion factor are calculated for each pixel;
- the high voltage of each pixel is adjusted in order to obtain the same response when the camera is homogeneously illuminated;
- finally (this is the *caveat* mentioned above), since the PMTs differ from one another, and this affects the pulse width by up to 10%, in order to have the same response in all camera pixels, the calibration is done in equivalent photoelectrons (not real photoelectrons) according to:

$$C_{pixel} = \frac{N_{camera\,average}}{MEAN_{pixel}} \tag{2.3}$$

Finally, the arrival time has to be computed. It corresponds to the average time of the integration window (formed by several time slices), where each slice is weighted according to the count number it contains. For the DRS4 chips, a further time calibration is needed, because a synchronous signal in the camera does not reach all the readout channels at the same time. This is mainly due to small differences in the optical fiber lenghts and in differences in the electronic paths.

2.5.2 Image Cleaning and Parametrization

When a trigger occurs, the information contained in all the camera pixels has to be read and stored. However, the image generated by an air shower is contained only a small region of the camera whereas the remaining signal is due to fluctuations of the night-sky background. To ensure a good Hillas parameters reconstruction (see Section 1.4.2), efficient image cleaning and background rejection procedures are needed. The relevant routine is called *Star*.

After the calibration process described in the previous Section, for each camera pixel the stored information are the charge (expressed in terms of equivalent photoelectrons) and their arrival time. In this muddle of information, an image cleaning algorithm is able - by analyzing the output provided by *Sorcerer* - to identify only those pixels that contain the signal generated by an air shower. Morphology and time consistency are discriminating parameters, especially to identify low-energy events ($\leq$ 100 GeV). Different image-cleaning algorithms exit:

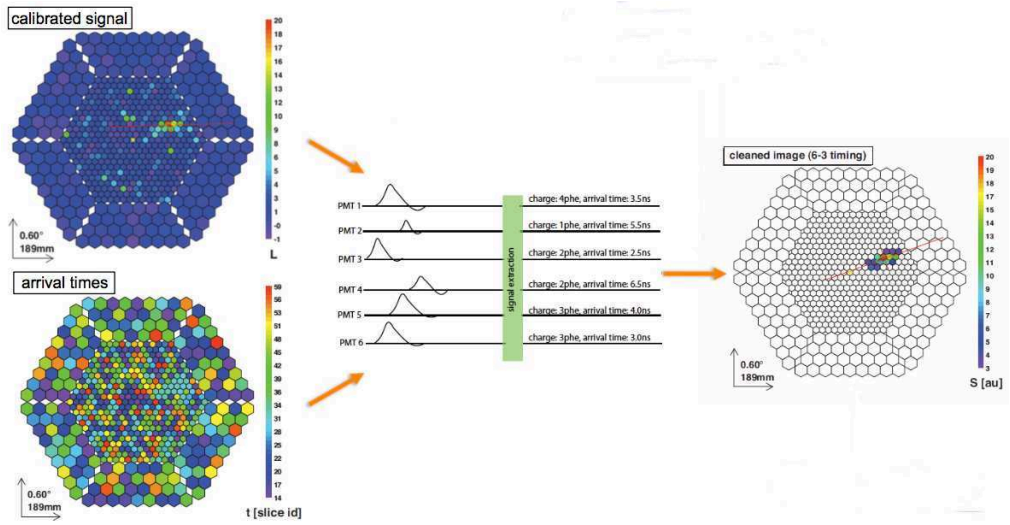

Figure 2.15: Example of *ABSOLUTE Time-Contrained Cleaning* process. On the left and in the middle: results of the calibration process performed by *Sorcerer* algorithm. For each pixel the charge and the arrival time are known. On the right: the remaing signal after the cleaning process. *Credits*: Saverio Lombardi.

- *ABSOLUTE Time-Constrained Cleaning.* Two charge thresholds, Q_{core} and $Q_{boundary}$, are defined to identify the so-called *core pixels* and *boundary pixels*. In addition, two time windows, ΔT_{core} and $\Delta T_{boundary}$, are set for the arrival time. All pixels whose charge exceeds Q_{core}, and which have a neighboring pixel with $Q > Q_{core}$ at least, are selected. Then, the mean arrival time of the *core pixels* candidates is computed. If the arrival time of each candidate stays within a ΔT_{core} interval - with respect to the mean arrrival time - it is labeled as a *core pixel*, otherwise it is rejected. Once the *core pixels* have been identified, their neighboring pixels are taking into account. Those pixels whose charge exeeds the $Q_{boundary}$ threshold became immediatly *boundary pixels* candidates. Among them, only pixel whose arrival time stays within a time interval $\Delta T_{boundary}$ of their mean arrival time are labeled as *boundary pixels*. Both charge and time threshold are optimized for each telescope through Monte Carlo simulations. This algorithm is the most stable and robust, and it used for standard analyses. Moreover, the adjustable thresholds makes it suitable for image cleaning of data taken in different light conditions, such as *moon* or *twilight* (moderate Moon). An *ABSOLUTE Time-Contrained Cleaning* example is shown in Figure 2.15.

- *SUM Cleaning.* It is based on the same principle of the *ABSOLUTE Time-Contrained Cleaning*, except for the fact that the *core pixels* are identified considering an additional quantity, involving the sum of a compact group of $X - NN$ (Next Neighbour) pixels (where X can be 2, 3, or 4). Pixels belonging to a group of $X-NN$ pixels, whose clipped sum signal exeeds the quantity $Q_{X-NN} > Q_{core}\, Q_{core_{X-NN}}\, X$ (where $Q_{core_{X-NN}}$ is the $X-NN$ rescaled signal threshold for the *core pixels*) and whose arrival time stays within a ΔT_{core} interval with respect to their mean arrival time, are marked as *core pixels*. The strategy to single out the *boundary pixels* is the same as in the previous method. The *SUM Cleaning* algorithm, can recover more pixels, and by lowering the energy threshold

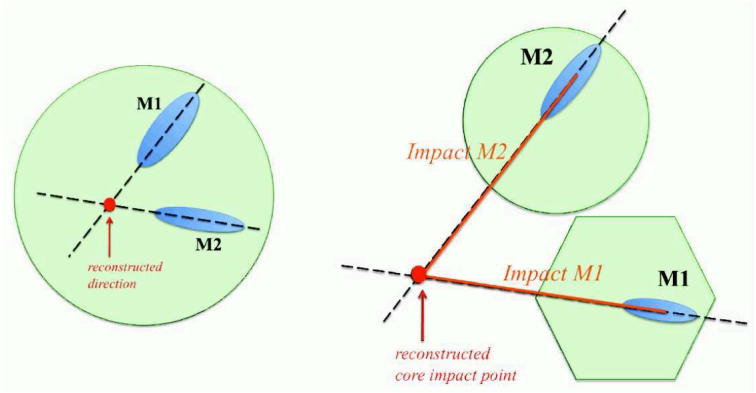

Figure 2.16: On the left: reconstructed shower direction obtained by overlapping the two camera images and by crossing their major axes. On the right: the impact point of shower axis on the ground, and the impact parameter of each telescope. *Credits*: Pierre Colin.

it allows lower-energy events (< 100 GeV) to be detected more efficiently.

- *DYNAMIC Cleaning.* Differently from the previous algorithm, the *Dynamic Cleaning* takes into account the size of each event in order to further lower the analysis energy threshold. The parameters involved in this cleaning are the same of the *Sum Cleaning*, plus a dynamic scale factor F_{dyn}. Once a first *SUM Cleaning* has been applied, for each event a further *Sum Cleaning* is performed according to a new threshold for both *core pixels* ($Q_{core\,dyn} = size\, F_{dyn}\, Q_{core}$) and *boundary pixels* ($Q_{boundary\,dyn} = size\, F_{dyn}\, Q_{boundary}$). If $Q_{core\,dyn} < Q_{core}$ no scaling is applied. By using this cleaning a better and clearer image confinement can be achieved.

Once the Cherenkov images have been properly cleaned, their Hillas parameters are computed. Such a parametrization is still performed by *Star* routine. Parameters (for a more detailed description, see Section 1.4.2) are distinguished as: (i) source-indipendent parameters, such as *size*, *CoG*, *widht*, *length*, *Conc*, *number of islands* and *leakage*; (ii) source-dependent parameters such as *Dist*, *Alpha* and *M3Long*; and (iii) time-dependent parameters, such as *time gradient* and *time-RMS*.

2.5.3 Stereo Parameters Reconstruction

So far, the routines *Merpp*, *Sorcerer* and *Star* worked separately on data coming from the two telescopes. From now on, all images generated by the same air shower are combined to obtained a tridimensional view of the event. For each event, the routine *SuperStar* provides, through geometrical considerations, the following preliminary stereo parameters:

- *Shower direction.* The shower axis should point towards the source from which it was generated. It is geometrically defined as the angle formed between the shower and the telescope axis. So, in absence of fluctuations in shower development, the major axix of the image in the camera plane identifies also the direction of the source in the sky. Due to the different perspective of telescopes, the two shower images are different, but their main axis must individuate the same direction in the sky. So, the reconstructed shower direction can be obtained by overlapping the two camera images and by crossing their

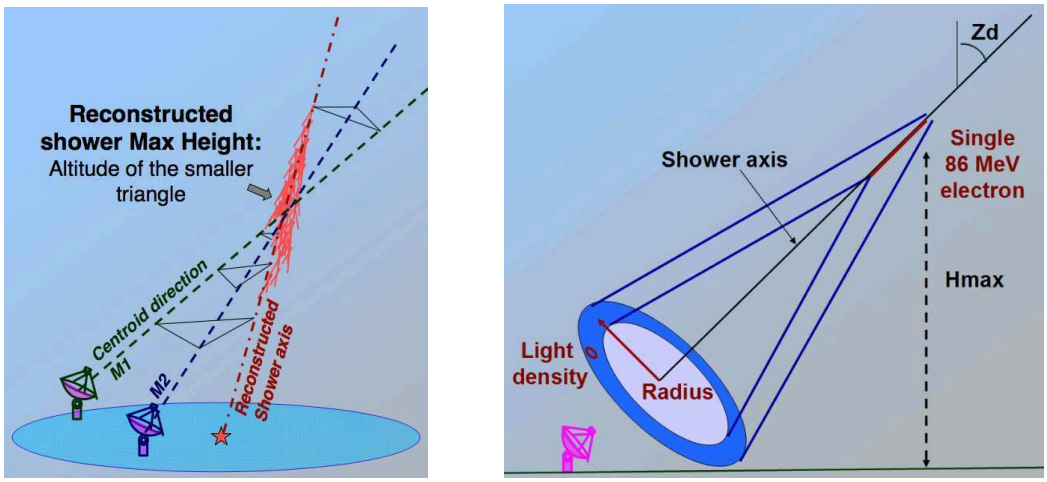

(a) (b)

Figure 2.17: (a): Maximum shower height obtained by minimizing the distance of the reconstucted shower axis and two *CoGs* directions. (b): Cherenkov pool radius and density generated by an 86 MeV electron at the maximum shower height. *Credits*: Pierre Colin.

major axes extensions, as shown in Figure 2.16. Each position in the camera corresponds to a position in the sky, according to $\sin\theta = d/f$, where F is the focal lenght of the telescope and d the distance from the camera center. This technique works quite well when the angle between the two axis is $> 30°$.

- *Impact point*. It is the point where the shower axis intersect the ground (Figure 2.16), and it is obtained by crossing the major axis of the shower images, starting from the telescope positions. This works only if the telescopes pointed the zenith position, so a correction has to be applied taking into account the distance between the camera planes.

- *Impact parameter*. Once the impact point has been determined, it is easy to obtain the impact parameters, defined as the distance between the impact point and the distance of the telescope position projected in a plane perpendicular to the shower direction.

- *Maximum shower height*. It is the height from the ground at which the shower maximum developes. Its height depends on the energy of the incoming γ-ray: the higher the energy, the lower the height shower maximum is. By using the shower reconstructed direction and the *CoG* directions (corresponding to the shower core) of the images seen by two telescopes, it possible determine the altitude of such maximum. In principle such directions should intersecate each another around the core shower, but this rarely happens. So, the maximum altitude is defined as the altitude that minimize the distance among these lines, as shown in Figure 2.17 (a).

Once the parameters described above have been computed, also parameters characterizing the Cherenkov light can be estimated: (i) the *Cherenkov radius*, i.e., the radius of the Cherenkov light pool at the ground, assuming that all the Cherenkov light is emitted by a single 86 MeV electron at the maximum shower height; (ii) the *Cherenkov density*, i.e., the

photon density of such Cherenkov light pool. Both radius and density are calculated in a plane perpendicular to the shower axis, and are represented in Figure 2.17 (b).

2.5.4 Building Random Forests

At this point of the analyses, both hadron and electromagnetic images have been parametrized, but a discrimination among them is needed. The Random Forest (RF) method is used to perform such discrimination. It is based on a large collection of decisional trees, through which each event is passed and classified. The routine that builds such decisional trees is called *Coach*, Compressed Osteria Alias Computation of the Hadronness, where *Osteria* was the routine used for mono analyses. *Coach* does not process any data, but it builds:

- the RF matrices for the γ-rays/hadrons separation;
- the RF matrices for the source position reconstruction used later on by the DISP STEREO method (see Section 2.5.5);
- the energy Look Up Tables (LUTs) or the RF matrices for the event energy estimation.

In the following, the building of the RF for the γ-rays/hadrons separation is described. For this purpose, the RF method matrices are based on the typical parameter distributions of the images induced by electromagnetic showers. The final goal is to find out the parameter combinations with the highest discriminating power, through a training with known data. Each RF contains about 100 decisional trees that, in turn, contain about 20000 nodes. Each node represents a cut of a given parameter. The steps needed to build a RF tree, shown in Figure 2.18, are the following:

- choose a Monte Carlo sample of simulated γ-ray events, whose characteristics are known *a priori*. In order to have a better discrimination, Monte Carlo data are selected, according to the observing conditions (zenith angle, light conditions and so on), to be as similar as possible to the observed data;
- choose the so called *Off* sample that contains hadron events. These events are not simulated, but taken from observations where no gamma sources are supposed to be in the field of view. The main reason is that they are much harder and more diffucult to simulate than γ-rays;
- merge the Monte Carlo and *Off* samples;
- choose a random parameter, among those describing the shower images, as the starting point;
- establish the best cut value of the choosen parameter that best separates γ-ray and hadron events. This cut defines two new directions in the space parameter, called *branches*, by which the sample is splitted into two subsamples. These new subsamples can contain both γ-ray and hadron events, depending on the aforementioned cut. This cut is established by minimizing the so called Gini index, that corresponds to minimizing the variance of the two new subsamples. The Gini index is a number between 0 and 1: the closer to 0 is it, the more homogeneous are the populations;

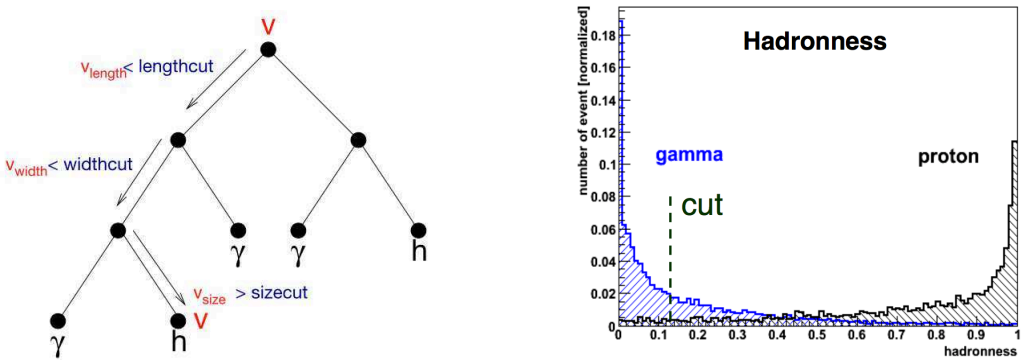

(a) (b)

Figure 2.18: (a) Part of a RF tree. Each node (black dot) splits the sample in two subsamples through a parameter cut. From [59]. (b) *Hadroness* histogram obtained once each real event have been processed and labeled by the RF trees. A cut in the *hadroness* (dotted line) can be applied to select only events with a high probability to be γ-like events. *Credits*: Pierre Colin.

- repeate the procedure described in the previous points for each new branch until a stopping criteria is fullfilled: for example when the number of events per node reaches down to a certain threshold, or when each node contains only one event. The last nodes of a tree are called *leaves*.

- labeling each *leaf* with a number called *hadronness* (1 stands for hadron-like event, 0 stands for γ-like event). In case the leaf contains more than one event, the associated *hadronness* is computed as the average among all the events contained in it.

During the RFs building, some shrewdnesses have to be taken into account. First of all, the number of trees must be large enough to ensure the convergence of the error on the estimated *hadronness* (usually such an error stabilizes at $\sim$ 30 trees). Then, the number of trials to optimize the cuts should be $\sqrt{N}$ for each node, where N is the number of parameters involved in the tree. Finally, also the final number n of events for each leaf should be $1 < n < 10$.

The building of the RFs for position reconstruction and energy estimation is based on the same principles. For a deeper discussion on the RFs applications in MAGIC analysis chain, see [59].

2.5.5 Hadronness, Position Reconstruction and Energy Estimation

Melibea is the routine that performs the γ/hadron separation, the source position reconstruction, and the energy estimation using the RFs provided by *Coach* (see Section 2.5.4).

Concerning the γ/hadron separation, each event passes through each tree of the RF, and *hadronnes* is associated to it. Once *hadronnes* has been assigned to each event (computed as the mean *hadronnes* assigned by each tree), it is possible to build a histogram like the one shown in Figure 2.18b. At this point, a *hadronnes* cut is applied to select only events with a high probability to be γ-like events. The more restrictive is the cut, the stronger is the background rejection. However, strict cuts implies also a higher probability to lose γ-ray events, so a compromise must be achieved. Finally, it is also possible to estimate a

characteristic efficiency of the separation process, defined as the surviving fraction of γ-ray event. Another method to discriminate γ-ray and hadron events is called *Supercuts*. Cuts on parameters (estimated through Monte Carlo simulations) are directly applied to each event, because parameters such as *width* and *lenght* proved to be good discriminators for events with energy > 100 GeV. However, in the current analysis, the RFs method is used.

The source position reconstruction is performed again with *Melibea*. A preliminary source position is calculated by *Superstar* (see Section 2.5.3) in a purely geometric way; on the contrary *Melibea* uses the so-called Stereo DISP (Distance between the Image centroid and the Source Position) method. This method is applied to each single telescope, and it presents an ambiguity between two reconstructed positions (see Figure 2.19(a). A $DISP$ parameter, defined as the distance between the CoG of the image and the source position, can be estimated through a correlation involving other parameters:

$$DISP = A(size) + B(size)\frac{width}{lenght} + \eta(size)\, leakage \tag{2.4}$$

where coefficients A, B, and η are optimized by Monte Carlo simulations. Alternatively, the $DISP$ parameter can be obtained by using the RFs. Starting from a γ-ray sample (with known source position), several decisional trees are built, and each event is passed through such trees, to estimate the related $DISP$. Obviously, both methods are Monte Carlo dependent. The parameter $DISP$ identifies two different positions from the CoG along the major axis. For the single telescope, the *Ghost busting* method has been developed to discriminate between these positions. It analyzes the image's time gradient and photon concentration to estabilish the most realiable source position. This method identifies the head and the tail of the shower, because photons arrive first from the head, where they are also more concentrated. In the stereo analysis, an additional help of parameters directly correlated to $DISP$, such as the *impact parameter* and the *maximum shower height*, is used. The source position is determined through the *TurboBoosting* method, shown in Figure 2.19(b). It identifies the closest two positions among fours candidates (a pair for each telescope), and it performs a weighted average according to:

$$\begin{cases} DISP_x = x_{disp1}\, w_1 + x_{disp2}\, w_2 \\ DISP_y = y_{disp1}\, w_1 + y_{disp2}\, w_2 \end{cases} \tag{2.5}$$

where (x_{disp1}, y_{disp11}) and (x_{disp1}, y_{disp11}) are the coordinates of the the two closest positions, and w_1, w_2 the relative weights, according mainly to the image quality, sizes, and angles between major axes. Finally, *Melibea* re-calculates the stereo parameters provided by *SuperStar*, assuming new image axes according to the new source position. The current method used in the standard analysis is the Stereo DISP method togheter with the *TurboBoosting*. It does not require any assumption on the source position, and, contrary to the geometric method of *SuperStar*, it works well even for small angles between the major axes. The achieved angular resolution is discussed in Sections 2.2.3 and 2.3.7 for both pre and post upgrade configuration.

The energy reconstruction can be attempted either with a parametrization involving image parameters connected to the energy, or with the RFs method described above. However in the current standard MAGIC analysis, the energy reconstruction is performed with the Energy Look-Up Tables (LUTs). They are multidimensional tables based on a model describing the photon distribution at the ground level, using the Cherenkov radius r_c, the Cherenkov density ρ_c, and other parameters related to the energy such as *size* and *impact parameter*. The LUTs

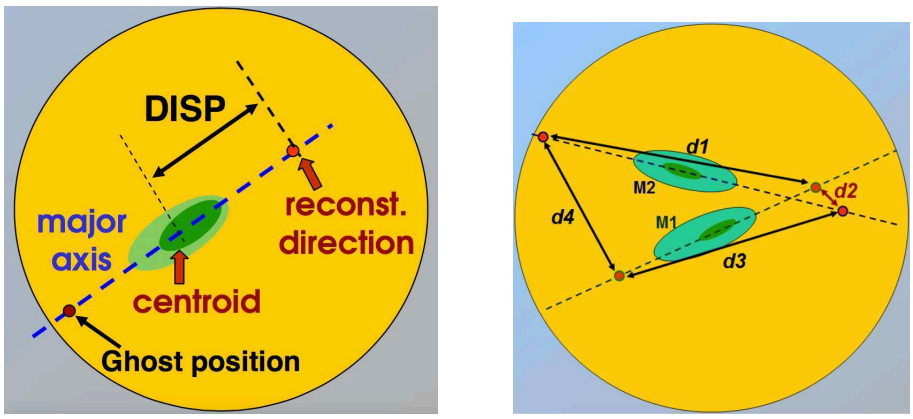

(a) (b)

Figure 2.19: (a): DISP method applied with the *Ghost busting* to a single telescope. 2 candidate source positions are identified through the parameter *DISP*, that corresponds to the distance between the image *CoG* and the reconstructed source position. (b): DISP method applied with the *TurboBoosting*. Once 4 candidate source positions have been identified (2 for each telescope), it computes the most reliable one. *Credits*: Pierre Colin.

(shown in Figure 2.20) are built independently for each telescope, starting from a Monte Carlo sample, where the energy E_{true} is known for each event. Several multidimensional bins are created and filled with the Monte Carlo events, according to the parameters range that characterizes each bin. The energy associated to each bin corresponds to the mean energy of all the events contained in it, while the error on energy to the root mean square of their energy distribution. Once the LUTs have been built, each observed event is assigned to a specific bin, according to its parameters. The energy representing that bin is, in turn, associated to all events belonging to it. This assignement procedure is done separately for each telescope, and the final event energy is given by their weighted average, where the weight is given by the uncertaintes of each bin. Finally, some correctios has to be applied: (i) a zenith correction, because the *Cherenkov density* hides a $\cos^2(z)$ dependence; (ii) a *leakage* correction, because only a fraction of the truncated images at camera edge is used; (iii) a geomagnetic field correction, because this field slightly deflects electrons and positrons, spreading the air shower and diluiting the Cherenkov photons. The energy resolution is limited by the amplitude of the bins and by computational power. In fact, each multidimensional bin of LUTs has to be filled with a minimum number of events and the distribution among bins should be as homogeneous as possible. The energy resolution is discussed in Sections 2.2.3 and 2.3.7 for pre and post upgrade configuration, respectively.

2.5.6 Signal Search

The next step in the analysis chain consists in determining the statistical significance of an excess from a given direction in the sky, in order to estabilish if the observed source is detected or not. This is done by a program routine called *Odie* that builds and applies several different cuts to the so called θ^2-plot. As shown in Figure 2.21 (a), θ is defined as the angular distance between the assumed source position and that reconstructed by the Stereo DISP method (see Section 2.5.5). For a given observation, once the source position has been reconstructed for

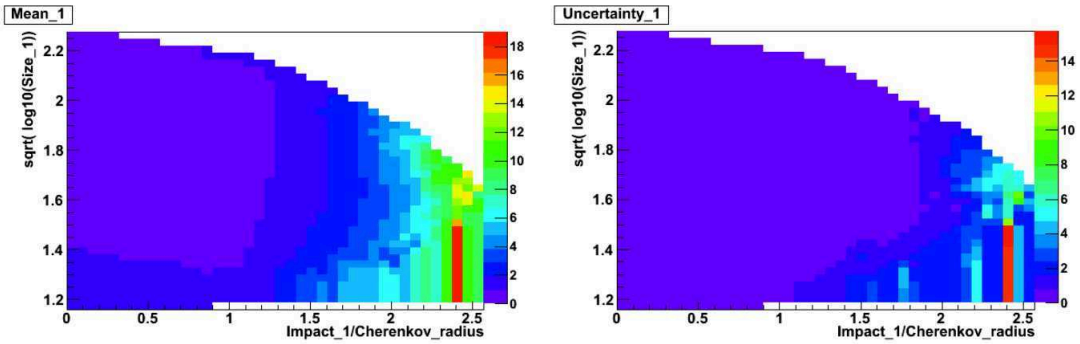

Figure 2.20: Look-Up Table for the energy reconstruction (left) and its related uncertainty (right). Bins are defined by the $\sqrt{size}$ on ordinates, and by the ratio *impact parameter/Cherenkov radius* on the abscissa. The *impact parameter* has to be taken into account because the *Cherenkov density* depends on it. Since the energy is proportional to the number of electrons at the shower maximum (given by the ratio *size/Cherenkov density*), LUTs can be also filled expressing the ordinates by E_{true} *size/Cherenkov density*, instead of $\sqrt{size}$. *Credits*: Pierre Colin.

each event, a θ^2 histogram is filled with the number of events following within every θ^2-bins. The θ^2 is used instead of θ because what matters is the relative angular distance from the assumed source position (γ-ray events are expected within a certain radius from the source), and because the background is expected to present an almost flat distribution as a function of θ^2. In Figure 2.21 (b), an example of θ^2-plot is represented, and it shows both an ON and OFF distribution. ON-distribution contains both background and potential signal events and it should peak around 0, i.e., where source is supposed to be. OFF-distribution should contain only background events, since it is obtained for a source-free region, and it is expected to have a roughly flat trend. Once an excess with respect to the OFF-distribution has been identified, it is necessary to compute its significance in order to evaluate the probability that it is not caused by background fluctuations.
The significance is computed using the Li&Ma formula [46], based on the maximum likelihood approach [60]:

$$\begin{aligned} S &= \sqrt{-2\ln\lambda} \\ &= \sqrt{2}\left(N_{ON}\ln\left[\frac{1+\alpha}{\alpha}\left(\frac{N_{ON}}{N_{ON}+N_{OFF}}\right)\right] + N_{OFF}\ln\left[(1+\alpha)\left(\frac{N_{ON}}{N_{ON}+N_{OFF}}\right)\right]\right)^{1/2} \end{aligned} \tag{2.6}$$

where N_{ON} and N_{OFF} are the numbers of ON and OFF events within a given θ^2 respectively, α is the ratio between the observation time spent for ON and OFF, and λ is the is the maximum likelihood ratio given by:

$$\lambda = \left[\frac{1+\alpha}{\alpha}\left(\frac{N_{ON}+N_{OFF}}{N_{ON}}\right)\right]^{N_{ON}}\left[\frac{1+\alpha}{\alpha}\left(\frac{N_{ON}+N_{OFF}}{N_{OFF}}\right)\right]^{N_{OFF}} \tag{2.7}$$

If the above formula gives as a result a significance $\sigma > 5$ for two independent analyses, a source detection is claimed. To compute the significance, a further events selection has to be applied. It is based on several adjustable cuts, among which the most common are:

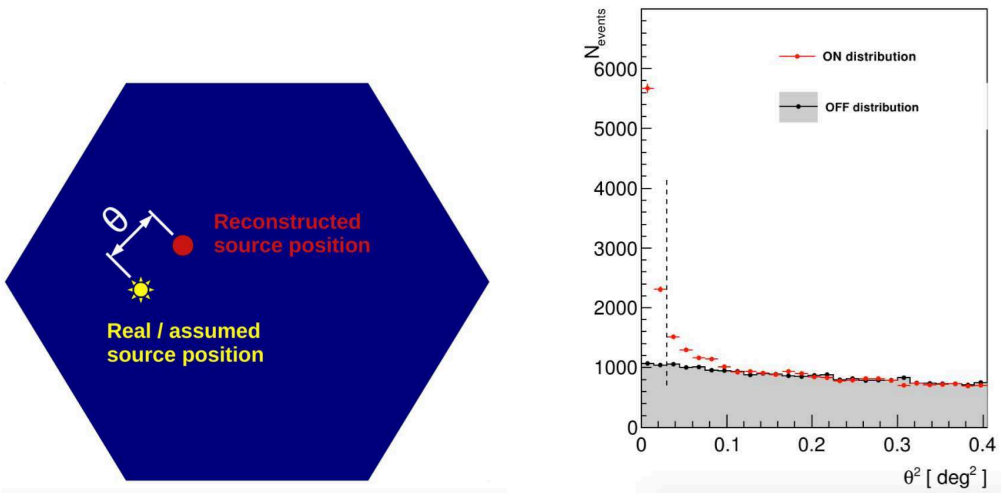

(a) (b)

Figure 2.21: (a): θ definition. It is defined as the distance between the assumed and reconstructed source position. (b): θ^2-plot. Number of events as a function of θ^2. Both ON-distribution (red) and OFF-distribution (black) are shown. *Credits*: Julian Krause.

- *hadronnes* cut. It is applied to remove hadronic events. The more restrictive is the cut, the higher is the probability to lose some γ-ray events or, in other words, to miss part of the signal;
- *size* cut. It is used to remove ugly events. They are usually low-energy events, characterized by poorer quality images. *Size cut* is zenith-dependent;
- *energy* cut. Analysis can be performed on three different energy ranges: (i) low energy, (ii) medium to high energy, (iii) high energy;
- θ^2-cut. It is used to select the region of the sky searched for the signal. It depends on the source extension, on the energy range, and on the Point Spread Function (PSF, defined as the width of a two dimensional Gauss fit to a point-like γ-ray source, containing 39% of the of overall excesses).

In addition to the cuts just described above, analyzers can apply further cuts on other parameters. A good choice of cut values reflects also on the sensitivity (see Sections 2.2.3 and 2.3.7). The cuts used in the standard analysis chain, are listed in Table 2.2.

Table 2.2: Standard cut values for different energy ranges in the standard analysis chain.

Energy range	*hadronnes*	θ^2	*size*
Low energy	< 0.28	< 0.02	> 60
Medium-high energy	< 0.16	< 0.009	> 300
High energy	< 0.1	< 0.007	> 400

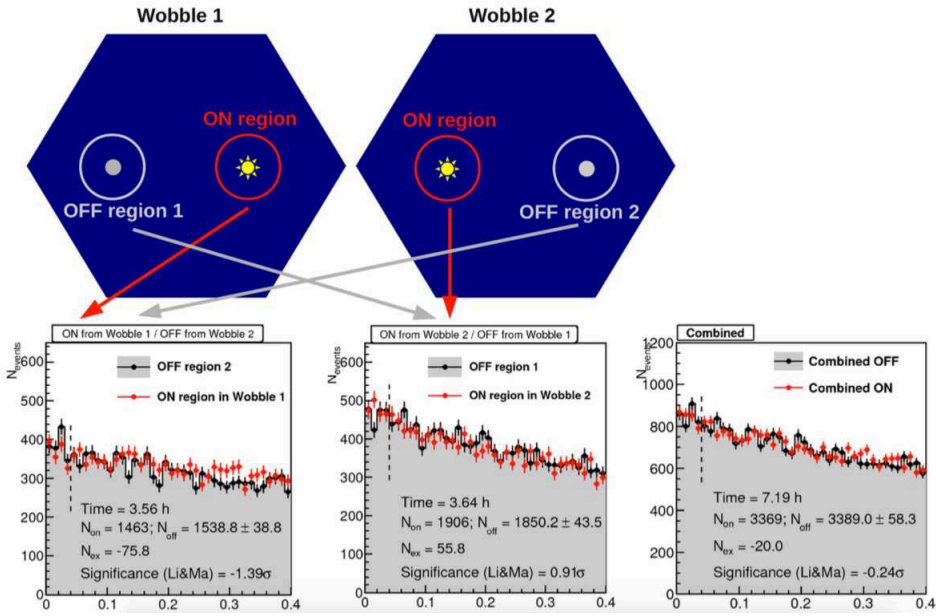

Figure 2.22: *OFF from wobble partner* (OfWP) background estimation. On top: source region (red circle) and OFF region (gray circle) in two different *wobble* positions W1 and W2. On bottom: θ^2 plots for the two source position. Plot on the left: the ON distribution is computed from W1 and the OFF distribution from W2. Plot in the middle: the ON distribution is computed from W2 and the OFF distribution from W1. Plot on the right: combined ON and OFF distribution from the two wobble positions. *Credits*: Julian Krause.

Finally, a very crucial point in computing the significance, is a good estimation of the background level. For *wobble* mode observations, the standard way to estimate the background is the *Standard 1 OFF* method, but it requires that the source lies at the center of observation and that each *wobble* position has been observed for the same amount of time. To obviate this problem, the *OFF from wobble partner* (OfWP) method - currently in use - has been implemented. It is a generalization of the previous method for arbitrary source positions and for different observational times among *wobbles*. For any *wobble* position, the related OFF is determined in the same camera region, as shown in Figure 2.22, and the differences in the observational time are taken into account by scaling the OFF accordingly. An arbitrary number of *wobble* positions can be used for the background estimation, allowing a better background statistics whit an ensuing higher significance. For observations with N *wobble* positions, OfWP usually offers $N-1$ OFF positions. This method suffers of rapidly variable weather conditions: in this case the advantage of taking the OFF in the same source region is canceled by different conditions. Moreover, additional sources in the field of view can contaminates the OFF estimation in different positions, and can enter at high θ^2, generating bumps in the OFF distribution. A reasonable proof that a good background estimation is performed is that the ON and OFF distributions match at high θ^2, i.e., in regions supposed to be signal-free.

2.5.7 Spectrum

At this point of the analysis, all events have been completely processed, the γ-rays/hadrons separation has been performed and the main stereo parameters of the source have been computed. From now on, it is is possible to obtain the flux of the observed source and all its related quantities. All these tasks are performed by a routine called *Flute* (FLUx versus Time and Energy). The γ-ray flux Φ is defined as the number of γ-rays N_γ, collected per unit of time and area. It is given by the Equation:

$$\Phi = \frac{d^2 N_\gamma}{dS\, dt} \tag{2.8}$$

and it is expressed in unit of $\mathrm{cm}^{-2}\ \mathrm{s}^{-1}$. As it can be seen from the above formula, to obtain the flux it is necessary to compute three quantities: (i) the number of detected γ-rays, (ii) the effective observational time, and (iii) the effective collection area.

The number of γ-rays is obtained from the excess of events with respect to the estimated background in a selected region around the source. First of all, the energy range is divided in an arbitrary number of bins. For each bin, the excesses number N_{excess} is computed through the same process performed by *Odie* (see Section 2.5.6), and it is given by the difference between the number of ON and OFF events within a certain θ^2 value. *Flute* uses another Monte Carlo sample to establish - for each energy bin - the best *hadronnes* and θ^2-cut values to perform the γ-rays/hadrons separation, once a separation efficiency has been choosen. Usually these cuts are more relaxed than those used to compute the significance because they assure a better estimate of the collection area. The uncertainty on the number of excesses is obtained assuming a Poissonian statistics, and it is given by $\Delta N_{excess} = \sqrt{\Delta N_{ON}^2 + \Delta N_{OFF}^2}$.

The effective observation time does not coincide with the difference between the beginning and the end of the observation. This happens because after an event has been recordered, there is a little amount of time, called *dead time*, during which the detector is unavailable and unable to accept other events. For this reason, the real event rate λ is different from the triggered one $\lambda^{'}$, that results a bit lower. Assuming that the real event rate can be described by a Poisson distribution, the interval time Δt between two consecutive events follow an exponential distribution. In other words, the probability of observing n events at time t is given by:

$$P(n,t) = \frac{(\lambda\, t)^n\, e^{-\lambda t}}{n!}$$

It follows that the probability of observing the next-event (from a given one) after a time t is:

$$P(t_{next} > t) = P(0,t) = e^{-\lambda t}$$

that can also be written as:

$$P(t_{next} > t) = \int_t^\infty \frac{dP(t_{next} = t)}{dt} dt\ .$$

That leads to:

$$\frac{dP(t_{next} = t)}{dt} = \lambda\, e^{-\lambda t}\ .$$

The last equation represents the time evolution of the probability of observing the next-event from a given one. The evolution with time of the number N of recordered events follows the same relation:

$$\frac{dN}{dt}dt = N_0 \lambda \, e^{-\lambda t}$$

where N_0 is the number of real events. In case of fixed dead time d per event, the previous Equation becomes:

$$\frac{dN}{dt}dt = N_0 \lambda \, e^{-\lambda (t-d)}$$

where $N_{d,0}$ is the number of triggered events. From this expression the effective time t_{eff} can be calculated as:

$$t_{eff} = \frac{N_{d,0}}{\lambda}$$

where the event rate λ is obtained by fitting to an exponential function an histogram containing all the time differences between each event and the previous triggered one. Finally, on the base of the previous considerations the effective time is also given by:

$$t_{eff} = \frac{t_{obs}}{(1 + \lambda d)}$$

where t_{obs} is the time spent on the source, including the *dead times*.

The effective collection area A_{eff} is defined as the area of an ideal detector with efficiency $\epsilon = 1$ which would collect all the events and see the same γ-ray rate as the real detector. It is given by the integral of the detector efficiency $\epsilon(x, y)$ on a plane orthogonal to the direction of the incoming γ-rays:

$$A_{eff} = \int_{-\infty}^{\infty} \int_{-\infty}^{\infty} \epsilon(x, y) \, dx \, dy \tag{2.9}$$

The effective collection area corresponds roughly to the Cherenkov pool area, so it is a function of parameters such as energy and zenith angle. A_{eff} increases with energy because the collection efficiency is larger due to higher amount of Cherenkov light. Also the distance of the telescopes from the shower axis, for a given energy, affects the effective area. As the distance increases with zenith angle, the shower crosses a thicker atmosphere layer. This makes the Cherenkov pool larger, but also dimmer, and thus the collection area increases with zenith. In Figure 2.23 both the energy and the zenith angle dependences are shown. Other, lighter dependencies are on: the azimuth angle, the geomagnetic field, and the source position in the field of view. Also the cuts applied in the analysis chain play an important role in the effective collection area, because the efficiency in identifing the γ-rays does depend on them. The effective collection area is calculated through Monte Carlo simulations: due to the two strong dependencies mentioned above, it is computed in bin of energy and zenith angle. The efficiency mentioned in the Equation 2.9 is given by:

$$\epsilon(x, y) = \frac{N_{\gamma, fin}(x, y)}{N_{\gamma, sim}(x, y)} \tag{2.10}$$

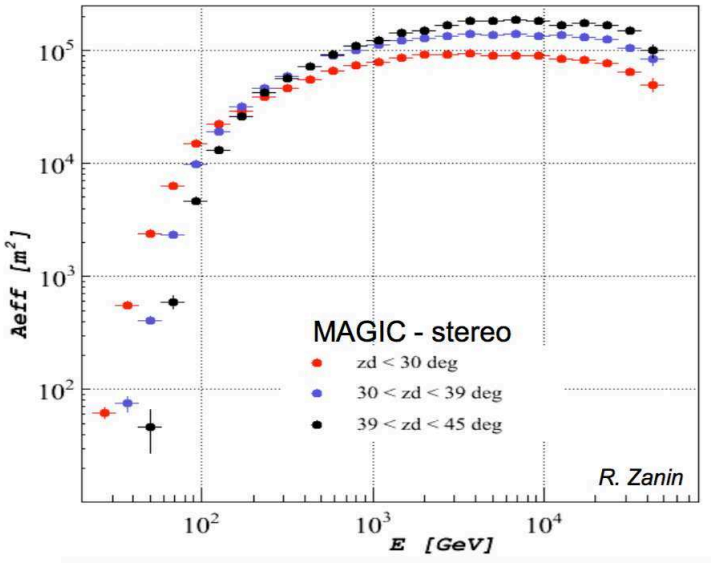

Figure 2.23: Energy and zenith dependence for the effective collection area. *Credits*: Roberta Zanin.

where $N_{\gamma,fin}$ is the number of γ-ray events revealed at the end of the analysis chain, and $N_{\gamma,sim}$ is the number of the simulated γ-ray events. The former can, in turn, be written as:

$$N_{\gamma,fin} = \int_{-\infty}^{\infty}\int_{-\infty}^{\infty} N_{\gamma,fin}(x,y)\,dx\,dy \tag{2.11}$$

and the latter by:

$$N_{\gamma,sim}(x,y) = \frac{N_{\gamma,sim}}{A_{MC,tot}} \tag{2.12}$$

where $A_{MC,tot}$ is the area within $N_{\gamma,sim}$ Monte Carlo γ-rays are simulated. By inserting Equations 2.10, 2.11 and 2.12 in Equation 2.9, it is easy to note that the effective collection area is given by the global efficiency times the area on which the Monte Carlo γ-rays are generated:

$$A_{eff} = \frac{N_{\gamma,fin}}{N_{\gamma,sim}} A_{MC,tot}\ .$$

The uncertainty on the effective collection area depends on the uncertainty on the ratio $N_{\gamma,fin}/N_{\gamma,sim}$ and it is computed from the standard binomial statistic as:

$$\epsilon = \frac{N_{\gamma,fin}}{N_{\gamma,sim}} \pm \sqrt{\frac{w(1-w)}{N_{\gamma,sim}}}$$

where $w = N_{\gamma,fin}/N_{\gamma,sim}$. If the effective collection area has to be computed for a wide energy bin, it becomes:

$$\langle A_{eff}\rangle_{E_1<E<E_2} = \frac{N_{\gamma,fin}(E_1,E_2)}{N_{\gamma,sim}(E_1,E_2)} A_{MC,tot}\ .$$

However, such value depends on the energy spectrum used in Monte Carlo simulations, because the trigger efficiency depends on energy as well. The ideal procedure would consist in generating the Monte Carlo data with the expected spectral index of the observed source. In this case the effective area would be:

$$\langle A_{eff} \rangle_{E_1<E<E_2} = \frac{\int_{E_1}^{E_2} \frac{d\Phi}{dE} A_{eff}(E) dE}{\int_{E_1}^{E_2} \frac{d\Phi}{dE} dE}$$

where the numerator represents the γ-rays rate in the energy range $[E_1, E_2]$. It can be estimated from the excesses - within the effective time t_{eff} - in that energy bin as:

$$\int_{E_1 d}^{E_2} \frac{d\Phi}{dE} dE = \frac{\frac{dN_\gamma}{dt}}{\langle A_{eff} \rangle_{E_1<E<E_2}} \approx \frac{N_{excess, E_1<E<E_2}}{t_{eff} \langle A_{eff} \rangle_{E_1<E<E_2}} \, . \tag{2.13}$$

The differential energy spectrum is the flux per γ-ray energy interval, expressed in unit of $\mathrm{cm}^{-2}\ \mathrm{s}^{-1}\ \mathrm{TeV}^{-1}$. It can be obtained deriving the Equation 2.8 with respect to the energy, and can be written as:

$$\frac{d\Phi}{dE} = \frac{d^3 N_\gamma}{dS\, dt\, dE} \, . \tag{2.14}$$

Finally, according to the Equation 2.13 and to the treatment explained in [61], the differential energy spectrum for each energy bin $[E_1, E_2]$ is:

$$\frac{d\Phi}{dE}(E) \approx \frac{N_{excess, E_1<E<E_2}}{t_{eff} \langle A_{eff} \rangle_{E_1<E<E_2} (E_2 - E_1)} \, . \tag{2.15}$$

Once the flux has been calculated, the light curve can be computed. It is the time evolution of the integral flux (obtained by integrating the Equation 2.14 in a given energy range) with time:

$$\Phi_{E>E_0} = \int_{E_0}^{\infty} \frac{d\Phi}{dE} dE \approx \frac{N_{excess, E_{est}>E_0}}{t_{eff} \langle A_{eff} \rangle_{E>E_0}} \, . \tag{2.16}$$

As mentioned above, the energy spectrum and related quantities have to be computed by dividing the energy range in bins. For the bins in which the signal is not significant, Upper Limits (ULs) can be calculated, following the method described in [62]. A confidence level ($\sim 95\%$), a systematic error ($\sim 30\%$) and a a power-law with spectral index Γ are assumed. Then, the number of the maximum expected counts N_{ul}, according to the assumptions and measurements, is computed. If the assumed spectral shape is

$$\Phi(E) = K\, S(E) = \left(\frac{E}{E_0} \right)^{-\Gamma} \tag{2.17}$$

the integral flux is obtained by integrating Equation 2.17 above a certain energy E_{min}:

$$K_{ul} = \int_{E_{min}}^{\infty} \Phi(E) dE = K \int_{E_c}^{\infty} S(E) dE = \frac{N_{ul}}{\int_{E_{min}}^{\infty} \int_0^{t_{obs}} A(E) dE dt}$$

where t_{obs} is the observation time. The integral flux UL becomes:

$$K_{ul} < \frac{N_{ul}}{T \int_{E_{min}}^{\infty} S(E)A(E)dE} \tag{2.18}$$

and the relative spectral point is placed in the position according to the treatment in [61].

2.5.8 Unfolding

The final goal of the MAGIC analysis consists in finding the energy distribution of the γ-rays emitted by a source. However, since the IACT is an indirect detection technique, the energy distribution can not be measured directly. In particular, as seen in Section 2.5.5, the parameters correlated with the energy, and the ensuing estimated energy E_{est}, have a finite resolution. Moreover, the MAGIC telescopes has a limited acceptance, in other words, they are not able to collect all the incoming γ-rays due to the limited collection area, trigger event selection, and further analysis cuts. So, in order to obtain the real energy distribution E_{true}, an unfolding procedure has to be applied. This means that the observed parameters have to be transformed into the desired ones through a deconvolution. The routine responsible of such a transformation is called *CombUnfold*. The measured distribution of a given parameter $g(y)$ can be written using the Fredholm integral:

$$g(y) = \int M(y,x)\, f(x)\, dx + b(y) \tag{2.19}$$

where $f(x)$ represents the true energy spectrum, $b(y)$ is the observable background distribution, and $M(x,y)$ is the so called Migration or Response function. The latter involves not only the detector response, but also terms due to geometry, atmosphere, coordinates, Earth magnetic field, and it is computed through Monte Carlo simulations. Equation 2.19 can be written in matricial form:

$$\mathbf{g} = M\,\mathbf{f} + \mathbf{b}\ . \tag{2.20}$$

Since the measured distributions are binned, a discretization of the problem is needed. Thus, Equation 2.20 becomes:

$$g_i = \sum_j M_{ij} \cdot f_j + b_i$$

where $g_i = \int_{y_{i-1}}^{y_i} g(y)dy$ and $b_i = \int_{y_{i-1}}^{y_i} b(y)dy$. Here the tensor M_{ij} represents the probability that an event with energy E_{true} associated to bin j, falls in bin i of estimated energy E_{est}. There are two possible approaches to find the function $\mathbf{f}$: the matrix inversion and the minimization.

For what concerns the matrix inversion approach, it can be seen from Equation 2.20 that the function $\mathbf{f}$ can be easily obtained by inverting the response matrix:

$$\mathbf{f} = M^{-1}(\mathbf{g} - \mathbf{b})$$

and the covariance matrix of the desired quantities can be obtained from the covariance matrix of the measured ones:

$$V(\mathbf{f}) = M^{-1}\, V(\mathbf{g})\, (M^{-1})^T\ .$$

However, sometimes the matrix is not invertible, or the solution oscillates.

Due to problems affecting the inversion matrix method, a minimization approach is preferred. It consists in minimizing the following expression:

$$\chi_0^2 = (\mathbf{g} - M\mathbf{f})^T V(\mathbf{g})^{-1}(\mathbf{g} - M\mathbf{f}) \; ; \tag{2.21}$$

however the minimization can be performed only if the observed quantities follow a Gaussian distribution, and it is not suitable for bins characterized by low statistics. In the latter case, a Poisson statistic has to be taken into account and a likelihood approach is preferred. However, also the minimization approach could lead to solutions characterized by strong fluctuations and to wide deviations from the true physical distributions. Such fluctuations can be generated by small and amplified contributions in the response matrix, but they can be suppressed recurring to a regularization that smooths the function $\mathbf{f}$. This regularization adds a term $Reg(\mathbf{f})$ to the Equation 2.21, that becomes:

$$\chi^2 = \frac{\omega}{2}\chi_0^2 + Reg(\mathbf{f})$$

where ω is an adjustable parameter representing the inverse of the regularization strength. The regularization strength has to be balanced because a too strong regularization leads to a very smooth $\mathbf{f}$ and to a loss of information. On the other hand, too a weak regularization does not remove spurious fluctuations and unphysical features might not be removed. There are several unfolding methods (Tikhonov [63], Schmelling [64], Bertero [65]) that differ from one another by the regularization term. However, a first try is performed through the so called *Forward unfolding*. It assumes a spectrum shape, described by the function $f(x, \mathbf{q})$, where the vector $\mathbf{q}$ contains the spectrum parameters. By minimizing the Equation 2.21, the spectral parameters $\mathbf{q}$ are obtained. Although this method provides smooth solutions without recurring to regularization, it is model-dependent and it is not sensitive to particular spectral features. For this reason it represents a good starting point to set the unfolding constraints, but other unfolding methods have to be applied as cross-checks. For more details on the unfolding methods applied to the MAGIC analysis chain, see [66].

2.5.9 Systematic Uncertaintes

Since during my PhD for the MAGIC collaboration I have been the cross-checker of the analysis of 2011 Mkn501 data (see Chapter 4.2), the SED modeling will be attempted by using the data I analyzed. Since they belong to the pre-upgrade era, only the systematic uncertaintes related to that period will be discussed.

The IACT technique (Section 1.13), based on an indirect reconstruction of the incoming γ-ray, is subject to several different factors that contribute to the systematic errors. In the following list the main factors that lead to an increase of the systematic uncertaintes in the energy scale, flux normalization and spectral slope, are reported. Their amount are computed as described in [40], and summarized in Table 2.3.

- *Atmosphere*. The atmosphere is used as a huge calorimeter where the particle shower develops after the impact with a γ-ray. For this reason, the atmospheric condition, such as the density profile and the transparency, should be known precisely in every moment. Obviously this is impossible in practice because the atmosphere continuolsly changes due to weather conditions and this reflects on the energy scale as a systematic uncertainty of $\leq 10\%$.

- *Mirrors.* The light amount focused on the camera by the mirrors, is known but for some uncontrollable parameters such as the variable dust deposit on the mirrors, loss of performance due to aging, deformances due to water infiltration, and finally malfunctioning of AMC that can slightly change the available mirror area from night to night. So, uncertainties on mirror reflectivity and AMC contribute a systematic error $\sim 8\%$ on the energy scale.

- *Night Sky Background.* The Nigh Sky Background (NSB) depends mainly on two factors: the source position in the sky (inside or outside of the galactic plane) and the night light conditions (dark, twilight, moon). A high level of NSB inreases the signal fluctuation, affecting the Hillas parameter estimation. In the end, the NSB produce a systematic error $\sim 4\%$ on the flux level.

- *Camera.* Several components in the camera contribute to the uncertainty on the energy scale, related to the conversion coefficient of the photons into photoelectrons. In particular $\sim 4\%$ is due to the Winston Cone, $\sim 5\%$ to the elcectron collection efficiency of the first dynode, $\sim 4\%$ to the quantum efficiency of the PMTs, $\sim 10\%$ to their F-Factor, and finally $\sim 2\%$ to the temperature dependence. However the sum of these effects are strongly reduced thanks to a muon calibration [67] togheter with an inter-telescope cross-calibration. To homogeneize the response of the camera, a procedure of flat fielding is adopted. However it introduces an uncertaintes $\sim 6-8\%$ in the energy scale (≤ 2 at higher energies). A further 3% on the uncertaintes of the flux normalization is due to broken channels or pixels.

- *Readout and Trigger.* The readout of MAGIC II is based on the DRS2 chips that are characterized by a non-linearity that lead to a systematic uncertaintes on the spectral slope of ~ 0.04. The deadtime introduced by the readout of MAGIC II is corrected in the analysis data chain and implies a negligible error $\leq 1\%$. Finally, also the inefficiency of the trigger system of both telescopes are negligible (less than 1%).

- *Signal Extraction.* The signal extraction contributes $\sim 3\%$ on the uncertaintes on the energy scale. This is basically due to the size of the extraction window.

- *Mispointing.* The mispointing of one telescope or of the relative pointing between the two telescopes influences the reconstruction of the stereo parameters during the analysis chain. The single mispointing of both MAGIC I and MAGIC II is less then 0.02° and the total effect on the flux normalization uncertaintes is $\leq 4\%$.

- *Background subtraction.* The evaluation of the NSB is one of the most critical point to obtain a good estimation of the spectra. The inhomogeneities intrinsic to the camera, can lead up to an uncertaintes $\sim 10\%$, but thanks to the observation in wobble mode, this effect are strongly reduced and the error on the NSB becomes less than 2%.

- *Analysis Chain.* Finally, some systematic errors are introduced during the data analysis. They are due mainly to the difference between the Montecarlo simulations and the real data. The choice of the cuts applied during the data analysis can lead up to 10% (at medium energies) or 15% (low energies) in the extraction of the γ-signal. Moreover also the unfolding procedure (see Section 2.5.8) is responsible for an error of 0.1 on the spectral slope.

Table 2.3: Contributions to systematic uncertaintes to the energy scale (ES), flux normalization (FN) and spectral slope (SL) from [40].

Effect	Systematic contribution
F-factor	10% ES
Atmospheric transmission	$\leq$ 10% ES
Mirror reflectivity	8% ES
Night Sky Background	1-4% FN
PMT quantum efficiency	4% ES
PMT electron collection efficiency	5% ES
Winston cones	5% ES
Signal extraction	3% ES
Background subtraction	1-8% FN
Charge flat-fielding	2-8% ES, FN
Analysis and MC discrepancies	$\leq$ 10-15% FN
Gain temperature dependence	2% ES
Broken channel/pixels	3% FN
Mispointing	1-4% FN
Trigger	1% FN
Unfolding	0.1 SL
Non-linearity readout	0.04 SL

Summarizing, the systematic uncertainties depend not only on all the factors mentioned above, but also on the energy range. The latter dependencies are due to the telescope capability to detect the Cherenkov light produced in a shower after a γ-ray enters the atmosphere. The lower is the energy of the incoming γ-ray, the weaker is the image formed in the camera, and the harder is the parameter reconstruction. On the other hand, the reconstruction is hard even if the energy of the incoming $\gamma - ray$ is too high: in this case the probability that the event is not entirely contained in the camera is high. The uncertaintes described above, are independent of one another, so to obtain the total systematic uncertainty they can be added in quadrature. For the low-energy range the energy scale is known with a precision of about 17% and the flux normalization of about 19%. While for the medium energy range the error on the energy scale is 15%, and 11% (without the uncertaintes on the energy scale) for the flux normalization. Finally the systematic uncertainty on the spectral slope, due to the non-linearity of the readout and the unfolding procedure, amounts to 0.15. Concerning a strong source, systematic errors dominate over statistical errors. As a last consideration, it is important to underline that systematic errors can affect data in different ways if observations are spread over a long period. Studies conducted on the Crab Nebula [40] showed that the relative systematic error for observations within few days and similar conditions is $< 9\%$, and for longer periods (months) it is $\sim 12\%$.

Chapter 3

Spectral Energy Distribution Modeling

The Spectral Energy Distribution modeling represents a new challenge in the multi-frequency observation era, and from now on it can be performed in a rigorous statistical way. In this Chapter the statistical approach used to fit the observational data of the spectral energy distribution (SED) of blazars is described. It consists in a χ^2-minimization, presented in Section 3.2, and performed through the Levenberg-Marquardt method, described in Section 3.4. In Section 3.4 the steps of the algorithm and the SED model implemented in the C++ code I develope, are described. Finally, a discussion on the uncertaintes related to the model parameters is dealt with in Section 3.4.3.

3.1 State of Art

So far, the blazar SED modeling has been attempted only in a heuristic way, mainly due to the lack of simultaneous multi-frequency data, and to the difficulties in combining data coming from different instruments. In other words, until recent times - and often to this very day - blazar SEDs were modeled not through a rigorous χ^2-minimization but only by eye-ball fitting (e.g., see [68]). This means that - starting from a combination of several parameters - many SEDs are built. Among such SEDs, the one that appears to best match the data, is chosen as a solution. For this reason, results coming from different analyses are not comparable to one another. Further, this eye-ball approach does not provide a measure of the goodness of the solution nor an estimate of the parameter uncertainties.

The feasibility study in attempting the SED modeling through a rigorous statistical approach was carried out in [69], and [70]. Even if such studies were performed on old datasets, the minimization procedure did provide plausible results. However, their limitation was that all insights on the solutions' reliability and convergence were missing.

The work presented in this thesis is a developement of the approach presented in [69], and [70]. In particular, the original aspect consists in verifying if the current conditions (i.e., the SED models and the quality of datasets) allow SED modeling to be attempted with a rigorous statistical approach. In particular, the indipendence of the minimization algorithm from the initial starting points, and the possible correlations among the SED model parameters are investigated. Moreover, after a statistical analyses on the results coming from a large number of minimizations, a method to estimate the uncertainties related to the parameters

is proposed.

In what follows, I review some of the most common and robust algorithms and point out their strengths and weaknesses in order to argue the choice of the Levenberg-Marquardt methods for the minimization process.

3.2 Non-linear Least Square Minimization

In physics problems the main application of the least square minimization is represented by data fitting. Given a set of N observational data (x_i, y_i) with $i = 1, ..., N$ and a model function $f(x_i, \mathbf{p})$ depending on j parameters $\mathbf{p} = (p_1, p_2, ..., p_j)$, the aim of a minimization process is to determine the value of the p_j parameters that better reproduce the observed dataset. The process consists in minimizing an objective function, often rapresented by the sum of the squares of the residuals $r_i(\mathbf{p}) = y_i - f(x_i, \mathbf{p})$, with $i = 1, ..., N$:

$$F(\mathbf{p}) = \sum_{i=1}^{N} r_i^2(\mathbf{p}). \tag{3.1}$$

In the most of cases, it is possible to minimize the weighted of the residuals, according to the observations, where the weights are the reciprocal of the variances associated to each observed point. Moreover, if such residuals are supposed to belong to a normal distribution, the object function becomes a χ^2-distribution, defined as:

$$\chi^2(\mathbf{p}) = \frac{1}{2} \sum_{i=1}^{N} \left[\frac{y_i - f(x_i; \mathbf{p})}{\sigma_i} \right]^2 \tag{3.2}$$

The model function $f(x_i; \mathbf{p})$ is usually a linear function in the parameters $\mathbf{p}$ and can be expressed as:

$$\mathbf{f}(x, \mathbf{p}) = \sum_{k=0}^{j} p_k \, X_k(x)$$

where the quantities X_k are fixed function of x called basis functions. These functions can be non-linear functions of the variable x, because in this context the concept of linearity is referred only to the dependence on the parameters p_j. When the function describing the model can not be expressed by a linear combination of the basis functions and the parameters p_j, the model function is called non-linear. All methods for non-linear minimization are numerical and iterative. Starting from an initial points in the space parameters $\mathbf{p}_0$, they try to find a perturbation that little by little will approach to a local minimizer.

Most of the physical problems, in particular these concerning data fitting, are solved by a non-linear least square χ^2-minimization. There are several processes to treat such cases, and in the following Section the most robust and commonly used method will be described.

3.3 Levenberg-Marquardt Algorithm

The Levenberg-Marquardt [71] is the most common method used to solve non-linear least square problems as, for example, fitting a parametrized function to a set of observational data points. As seen in the previous Section, when the model function is not linear in the

parameters, the process is called non-linear least square minimization. It is an iterative process, performed numerically, that at each step tries to find a perturbation of the model parameters that results in a lower χ^2-value. This algorithm combines two different methods: the steepest descent [72] and the Gauss-Newton one [73], and in the following Sections it will be described how each method works to reach the minimum of the χ^2-manifold.

However, before going further, it is worth remembering the χ^2 definition and all the quantities involved in its expression, related to the SED modeling of Mkn501, that is the topic of this thesis. The quantities involved in the Equation 3.2 are

- (x_i, y_i): set of observational data points of Mkn501; They represent the frequencies and the fluxes, respectively;
- σ_i: uncertaintes associated to flux points;
- $f(\mathbf{p})$: SED model describing the emission of Mkn501 (see Section 3.4.1);
- $\mathbf{p}$: parameters involved in the SED model (see Section 3.4.1);

where the function $f(\mathbf{p})$ is a non-linear function of the parameters $\mathbf{p}$.

3.3.1 Steepest Descent Method

Let consider a set of N observational data points (x_i, y_i) with their related uncertaintes σ_i. The main idea of the steepest descent method (also called the gradient method) is that a local minimum can be reached by descending in the opposite direction of the gradient of the χ^2 with respect to the parameters $\mathbf{p}$. The χ^2-gradient can be easily obtained from the Formula 3.2:

$$\nabla\chi^2(\mathbf{p}) = -\sum_{i=1}^{N}\left[\frac{y_i - f(x_i, -\mathbf{p})}{\sigma_i}\,\frac{\partial f(x_i, \mathbf{p})}{\partial \mathbf{p}_j}\right] \tag{3.3}$$

that, using a more compact matrix notation, becomes:

$$[\nabla\chi^2(\mathbf{p})]^T = -[\mathbf{y} - f(x_i, \mathbf{p})]^T\ \mathbf{\Sigma}\ \mathbf{J} \tag{3.4}$$

where $\mathbf{y}$ is the N-dimensional vector containing the dependent variable, $\mathbf{\Sigma} = diag(1/\sigma_i^2)$ is the diagonal matrix containing the squares of the uncertainties associated to $\mathbf{y}$, $[\mathbf{y} - f(x_i, \mathbf{p})]$ represents the difference between the vector containing the dependent-variable observed data and the vector containing the dependent-variable values estimated according to the model described by the function $f(x, \mathbf{p})$, and, finally, $\mathbf{J} = (\partial_p \mathbf{f}(\mathbf{p}))$ is the Jacobean matrix of the model function $f(x, \mathbf{p})$.

Once the χ^2-gradient has been determined, the steepest descent method moves into the opposite direction in the parameters space by performing a perturbation of the parameters $\mathbf{p}$. This is procedure is repeated several times, until the convergence criteria are satisfied and the minimum is reached. At the $k+1$ iteration the parameter update is given by:

$$\mathbf{p}_{k+1} = \mathbf{p}_k - \mu\ \nabla_p\ \chi^2(\mathbf{p}_k) \tag{3.5}$$

that corresponds to

$$\delta\mathbf{p} = \mathbf{p}_{k+1} - \mathbf{p}_k = -\mu\ (-\mathbf{J}^T\ \boldsymbol{\Sigma}\ (\mathbf{y} - \mathbf{f}))$$

that leads to the final expression for the parameters update:

$$\delta\mathbf{p} = \mu\ \mathbf{J}^T\ \boldsymbol{\Sigma}\ (\mathbf{y} - \mathbf{f}) \tag{3.6}$$

where μ is a positive real number representing the length of the step in the space parameter along the minimum direction. The value of μ can be determined by several tecnique such as the line search or the soft line search (see Frandsen 2004).

If the model function depends on a large number of parameters, the minimization can be attempted only through the steepest descent method. It is very efficient in case of simple model functions, but for complex ones it does not take into account the curvature of the χ^2-manifold. For this reason it can happen that the algorithm moves in the parameter space by too large steps in the steep regions, or too short in the flatter ones. On the other hand, analyzing the curvature of the manifold through the hessian matrix is computational expansive. Moreover, if the manifold presents a lot of substructures or a strong roughness, the process could not reach the convergence.
Although the steepest descent method gets slower approaching to the minimum, it works very well far from it, showing the best performace in the initial stages of the iterative process. The convergence of this method is expected to be linear.

3.3.2 Gauss-Newton Method

The foundamental assumption of the Gauss-Newton method is based on a linear approximation to the components of the model function. This means that, at each step, it works by recurring to the linearized model function in the neiborghood of the current point of the space parameter. The model function can be written by using the Taylor expansion as:

$$\mathbf{f} = \mathbf{f}_0 + \mathbf{J}\ \mathbf{p}\ . \tag{3.7}$$

The linear approximation of the model function, described by the above formula, can be inserted in the χ^2 vectorial form of the Equation 3.2:

$$\chi^2(\mathbf{p}) = \frac{1}{2}\left[\frac{\mathbf{y} - \mathbf{f}_0 - \mathbf{J}\mathbf{p}}{\sigma_i}\right]^2\ .$$

The χ^2 becomes:

$$\begin{aligned}\chi^2 &= \frac{1}{2}(\mathbf{y} - \mathbf{f}_0)^T\ \boldsymbol{\Sigma}(\mathbf{y} - \mathbf{f}_0) + \frac{1}{2}\mathbf{p}^T\ \mathbf{J}^T\ \boldsymbol{\Sigma}\ \mathbf{p} - \frac{1}{2}2(\mathbf{y} - \mathbf{f}_0)\boldsymbol{\Sigma}\ \mathbf{J}\ \mathbf{p} \\ &= \frac{1}{2}(\mathbf{y} - \mathbf{f}_0)^T\ \boldsymbol{\Sigma}(\mathbf{y} - \mathbf{f}_0) + -(\mathbf{y} - \mathbf{f}_0)\boldsymbol{\Sigma}\ \mathbf{J}\ \mathbf{p} + \frac{1}{2}\mathbf{p}^T\ \mathbf{J}^T\ \boldsymbol{\Sigma}\mathbf{p}\end{aligned}$$

and its gradient:

$$\begin{aligned}\nabla\chi^2(\mathbf{p}) &= \nabla\left(\frac{1}{2}(\mathbf{y} - \mathbf{f}_0)^T\ \boldsymbol{\Sigma}(\mathbf{y} - \mathbf{f}_0) + -(\mathbf{y} - \mathbf{f}_0)\boldsymbol{\Sigma}\ \mathbf{J}\ \mathbf{p} + \frac{1}{2}\mathbf{p}^T\ \mathbf{J}^T\ \boldsymbol{\Sigma}\mathbf{p}\right) \\ &= -(\mathbf{y} - \mathbf{f}_0)^T\ \boldsymbol{\Sigma}\ \mathbf{J} + \mathbf{p}^T\mathbf{H}\end{aligned}$$

where $\mathbf{H} = \mathbf{J}^T\ \mathbf{J}$ represents the Hessian of the quadratic approximation to the χ^2 obtained by linearizing the model function and not to the real one. It is important to bear in mind that the Hessian of the real model function is never computed during the minimization process. The minimum of the quadratic approximation to the χ^2 can be found by setting its gradient to zero:

$$-(\mathbf{y} - \mathbf{f}_0)^T\ \mathbf{\Sigma}\ \mathbf{J} + \mathbf{p}^T\mathbf{H} = 0$$

At each step, such a minimun does not correspond to the real one, but represents a good starting point for the next iteration:

$$\mathbf{p}_{min}^T = \mathbf{H}^{-1}\ (\mathbf{y} - \mathbf{f}_0)^T\ \mathbf{\Sigma}\ \mathbf{J}$$

that leds to:

$$\begin{aligned}
\mathbf{p}_{min} &= \mathbf{H}^{-1}\ \mathbf{J}^T\ \mathbf{\Sigma}\ (\mathbf{y} - \mathbf{f}_0) \\
&= \mathbf{H}^{-1}\ \mathbf{J}^T\ \mathbf{\Sigma}\ (\mathbf{y} - \mathbf{f} - \mathbf{J}\mathbf{p}) \\
&= \mathbf{H}^{-1}\ \mathbf{J}^T\ \mathbf{\Sigma}\ (\mathbf{y} - \mathbf{f}) + \mathbf{H}^{-1}\mathbf{J}^T\mathbf{\Sigma}\mathbf{J}\ \mathbf{p} \\
&= \mathbf{H}^{-1}\ \mathbf{J}^T\ \mathbf{\Sigma}\ (\mathbf{y} - \mathbf{f}) + \mathbf{p}
\end{aligned}$$

In such a way, at the $k+1$ iteration the new minimum of the quadratic aproximation is:

$$\mathbf{p}_{min(k+1)} = \mathbf{H}^{-1}\ \mathbf{J}^T\ \mathbf{\Sigma}\ (\mathbf{y} - \mathbf{f}) + \mathbf{p}_{min(k)}$$

so, the final parameters update $\delta\mathbf{p} = \mathbf{p}_{min(k+1)} - \mathbf{p}_{min(k)}$ is given by:

$$\delta\mathbf{p} = \mathbf{H}^{-1}\ \mathbf{J}^T\ \mathbf{\Sigma}\ (\mathbf{y} - \mathbf{f}) \tag{3.8}$$

The assumption of a linear approximation of the model function is justified by the fact that around the minimum it tends to behave as a quadratic form. For this reason the Gauss-Newton method is very efficient around the minimum where the shape of the χ^2-manifold can be better approximated by a paraboloid. At each iteration the model function is linearized in the neiborghood of the minimum point founded at the previous iteration. In this way it is possible to take into account the local curvature of the χ^2-manifold, without calculating the second derivative because the Hessian matrix can be obtain directly from the Jacobian one. This allows to save a lot of computational time, and approaching faster the minimum by using the curvature information. Although the Gauss-Newton method is a generalization of the Newoton method for the non-linear case, the convergence is different. While for the Newtons'method the convergence is quadratic, for the Gauss-Newton a linear convergence is expected. However, if the function has small curvatures, it is characterized by a superlinear convergence.

3.3.3 Levenberg Marquardt Method

The method proposed first by Levenberg [74] and afterwards improved by Marquardt [75] is an hybrid method that combines both the steepest descent [72] and the Gauss-Newton method [73], joining their best performances in complementary situations. In fact, as seen in the previous Sections, the steepest descent method works better far from the minimum, while the Gauss-Newton works better close to it. For this reason, the Levengerg-Marquardt

algorithm acts as the first method when the parameters are far from their best value, and as the latter when they are close to the minimum ones. When the model function is non-linear in the parameters, the minimization process must be performed numerically, through an iterative procedure. At each minimization step, the algorithm tries to minimize the sum of the squares of the differences between a set of observational points and a model function, valuated according to the observed data. This is done through an update of the parametres that, hopefully, results in a lower χ^2-value. The parameter update is given combining the Equations 3.6 and 3.8, that are the updates related to the steepest descent and Gauss-Newton method respectively. The parameter update results:

$$\delta\mathbf{p} = (\mathbf{H} + \lambda\mathbf{I})^{-1}\ \mathbf{J}\ \mathbf{\Sigma}\ (\mathbf{y} - \mathbf{f}) \tag{3.9}$$

where λ is a positive real number that determines the relative weight of each method. If after an iteration step the solution improves, λ will be increased and the contribution of Gauss-Newton method dominates. Otherwise λ will be decreased, the contribution of the Gauss-Newton becames negligible and the algorithm behaves accordingly to the steepest descent method.

The major problem of the hybrid methods is related to the mechanism responsible of the switching between the methods. Parameter λ is arbitrarily choosen at the begining of the minimization process and subsequently adjusted by a fixed factor during the iterations. In this way, an optimal criteria to determine the relative weight of the two methods could be missed. Moreover, for large value of λ, the information contained in the Hessian matrix is not used at all. In fact, the gradient, once calculated, returns information about the local slope of the χ^2-manifold, but does not reveal how extended the slope is. Having a look into the Equation 3.5, Marquardt realized that the components of the Hessian matrix could give some information about the scale of that problem [75]. In fact, the χ^2 is a non-dimensional quantity and the component of its gradient $\nabla_p\chi^2(\mathbf{p})$ has the dimension of $1/p_j$ which is well-dimensioned. Through the dimensional analysis of the Equation 3.5, it is quite easy to see that the constant of proportionality between the steps in the parameter space and the χ^2-gradient has to be of the order of p_j^2. By scanning the Hessian matrix the only quantities whose dimensions correspond to those of p_j^2 are the reciprocal of its diagonal elements. So the constant of proportionality can be written becomes:

$$\delta p_k = \frac{1}{\lambda H_{jj}}\nabla\chi^2 \tag{3.10}$$

and μ assumes the form:

$$\mu = \frac{1}{\lambda H_{jj}} \tag{3.11}$$

where λ regulates the step lenght, because the scale determined only through the Hessian diagonal elements could be too large.

In order to make the effect of λ in the previous formulation less problem-specific, Marquardt [75] suggested a slighlty modified expression for the Equation 3.9, by replacing the identity matrix with the diagonal of the Hessian one:

$$\delta\mathbf{p} = (\mathbf{H} + \lambda diag(\mathbf{H}))^{-1}\ \mathbf{J}\ \mathbf{\Sigma}\ (\mathbf{y} - \mathbf{f}) \tag{3.12}$$

The Levenberg-Marquardt method combines the steepest descent and the Gauss-Newton one in order to merge the advantages of both methods. The main advantage consists in taking into account the curvature of the χ^2-manifold, avoiding the calculation of the second derivatives and saving a lot of computational time, thanks to the linear approximation of the model function. Although it is considered as the most roboust algorithm to solve non-linear least square curve fitting problem, unfortunately it does not ensure to find the global minimum. Sometimes it can drop in local minimums, depending on the starting point in the space parameter. For well-behaved functions and reasonable starting parameters, the Levenberg-Marquardt algorithm tends to be a bit slower than the Gauss-Newton one. However, the advantage of the Marquardt's modification avoids slow convergence in the direction of small gradient and the convergence near the minimun gets faster. In the following Section it will described the implementation of the Levenberg-Marquardt method step by step.

3.4 The SED Modeling Code

I implemented in a C++ code - for the first time - the whole minimization process, focused in finding the most likely parameters of blazar SEDs. In the following, the main ingrdients needed to model the blazars SED are reported. In Section 3.4.1 the model used to describe Mkn501 SED is introduced. In Section 3.4.2, the implementation of the Levenberg-Marquardt method - based on that one described in [71] - is presented, and, finally in Section 3.4.3, a discussion about the method used to estimate the uncertainties related to the parameters is carried out.

3.4.1 The model

The SED model implemented in the code is a self-synchrotron one-zone model (see Section 1.6.4), in particular, the one described in [76]. It is the simplest model to describe balzars emission because it considers that the emission comes from a single zone and that it is produced by a single electron population. Such a model is considered suitable to describe the Mkn501 emission because studies conducted on its variability shown that the synchrotron and the inverse Compton peack change in a correlated way [77], [78]. This suggests that the emission is generated by the same electron population. Moreover the absence of emission lines in Mkn501 spectra indicates a weak thermal component; this is in favour of a lack of external photons, leaving the synchrotron photons the only ones avaiable to be scattered by inverse Compton. Finally the variability of Mkn501 is characterized by one timescale, that suggests that the emission is produced in a single region.

This model assumes that all the emission is generated inside a single homogeneous region inside the jets, and that such a region can be approximated as a spherical blob. This blob moves relativistically along the jet towards the observer (characterized by a bulk Lorentz factor Γ) and with a small angle θ with respect to the line of sight. This blob is permeated by an homogeneous tangled magnetic field of inensity B, and by relativistic electrons whose distribution N_e is described by a broken power low characterized by two spectral slopes (n_1 and n_2) smoothly connected:

$$N_e(\gamma) = \frac{K\,\gamma^{-n_1}}{1 + \left(\frac{\gamma}{\gamma_b}\right)^{n_2 - n_1}} \tag{3.13}$$

where γ_{min} and γ_{max} represent the minimum and the maximum Lorentz factor of the electrons respectively,[1] γ_b the Lorentz factor corresponding to the energy at which the spectral index change from n_1 to n_2, and K is the normalization factor of the electron spectral distribution. Generally, it is possible to chose among different electron spectral distributions: e.g., exponentially cut-off power law, broken double law, smoothed double power law, log-parabola power law, and others. The choice of a particular electron distribution is typically suggested by the detailed shape of the observed X-ray spectrum, which usually samples the synchrotron component at, or near, its peak.

The electron density is given by integrating the electron distribution over the whole energy range:

$$n_e = \int_{\gamma_{min}}^{\gamma_{max}} N_e(\gamma) d\gamma \ . \tag{3.14}$$

This kind of distribution is justified by the observed spectral shape because it requires that the electrum spectrum becomes steeper with increasing energy. The same electrons are moving relativistically along the jet, and the ensuing effects are described by the relativistic Doppler factor:

$$\delta = \frac{1}{\Gamma(1 - \beta \cos\theta)]} \tag{3.15}$$

Summarizing, the self synchrotron model is described by nine parameters. Six parameters charachterize the electron spectral distribution:

- γ_{min}, the minimum Lorentz factor of the electrons distribution (related to their minimum energy);
- γ_b, the Lorentz factor corresponding to the change of the electrons spectral slope;
- γ_{max}, the maximum Lorentz factor of the electrons distribution (related to their maximum energy);
- n_1, electrons spectral index below γ_b;
- n_1, electrons spectral index above γ_b;
- K, the normalization factor of the electron spectral distribution;

and the remaining three parameters describing the property of the emitting region:

- B, intensity of the magnetic field;
- R, radius of the spherical blob;
- δ, Doppler factor of the blob.

The parameters described above are linked to the observational quantities. In particular the spectral index n_1 and n_2 are related to the left and right slopes respectively of the synchrotron bump. B, K, γ_b, and δ are related to both the synchrotron and inverse Compton frequencies peaks, and luminosities. Finally R is related to the timescale varaibility, t_{var}, of the source through the expression $R \leq c\, t_{var}\, \delta/(1+z)$ (where z is the redshift of the source).

Starting from a set of the model parameters described above, the SED model is built by calculating the synchrotron and inverse Compton emissivity in a given frequency range.

The emissivity of a single electron by synchrotron radiation, j_{sync}, in the ultra-relativistic limit is derived in [2]. It can be written as:

[1] These quantities are related to the minimum and maximun energy of the electron distribution.

$$j_{sync}(\nu) = \frac{\sqrt{3}e^3 B \sin(\alpha)}{mc^2} F(x) \tag{3.16}$$

where α is the pitch angle, and $F(x)$ is defined as:

$$F(x) = x \int_x^\infty K_{5/3}(y)\, dy$$

with $K_{5/3}$ modified Bessel function of fractional ordes 5/3. The total synchrotron emissivity, J_{sync}, is obtained by integrating the Equation 3.16 over the whole electron energy distribution 3.13:

$$J_{sync} = \int_{\gamma_{min}}^{\gamma_{max}} N_e(\gamma)\, j_{sync}(\nu)\, d\gamma \tag{3.17}$$

At this point, it is necessary to consider that the synchrotron photons are propagating through the plasma, and hence there is a probability that they will scatter off the synchrotron electrons. This process is known as synchrotron self-absorption. The change of the synchrotron emissivity is given by the equation of the radiative transfer:

$$\frac{dI(\nu)}{dx} = J_{sy}(\nu) - k_\nu\, I(\nu) \tag{3.18}$$

where k_ν is the self-absorption coefficient. The solution of the above Equation is:

$$I(\nu) = \frac{J_{sy}(\nu)}{k_\nu} \left(1 - e^{-k_\nu l}\right) \tag{3.19}$$

where l is the thickness of the traveled region. The emitting electrons exchange synchrotron photons in a quasi-thermal-equilibrium; this mean that the total flux reaching the observer is much fainter than if all the photons escaped the source. The electron spectrum is described by a relativistic power-law distribution of particle energies, and each particle emits and receives radiation only at its characteristic energy. Hence the self-absorption cross-section depends on the electron distribution, aside from the magnetic field. For such a distribution, and for a homegeneous magnetic field, the self-absorption coefficient [2] is given by:

$$k_\nu = \frac{\pi e^3 kc B^{(n+2)/2}}{64\pi^2 \epsilon_0 m} \left(\frac{3e}{2\pi m^3 c^4}\right)^{n/2} \frac{\Gamma\left(\frac{3n+22}{12}\right) \Gamma\left(\frac{3n+2}{12}\right) \Gamma\left(\frac{n+6}{4}\right)}{\Gamma\left(\frac{n+8}{4}\right)} \nu^{-(n+4)/2} \tag{3.20}$$

The self-absorption increases at higher wavelenght, and for these sources it manifests strongly at radio frequencies. For this reason, the emission at lower frequencies can escape only from a very thin shell of the source surface. On the contrary, higher is the frequency of the photons, deeper are the region they escape, and higher its flux density is. At a certain frequency, where the self-absorption becomes negligible, the electron power-law distribution is completely recovered.
The synchrotron emissivity is calculated in the range (ν_{min}, ν_{max}). nu_{min} is the limit fixed by the self-absorption and given by the approximation obtained in [79]:

$$\nu_{min} = 2.8 \times 10^4\, B \left[6.5 \times 10^{-10}\, K\, \frac{R}{B} \left(\frac{3}{2}\right)^{-1}\right]^{\frac{2}{n_1+4}}$$

and ν_{max} is calculated as the frequency peak of electrons characterized by the maximum energy γ_{max}. It is given by: $\nu_{max} = 2.8 \times 10^6\, B\, \gamma_{max}$.

Once the synchrotron emissivity and its self-absorption have been computed, it is possible to calculate the emissivity of the inverse Compton process. The spectrum of the photons scattered by a high energy electron from a segment of an isotropic photon gas of differential density $n(\epsilon)d\epsilon$ is derived in [7], by using the full Klein-Nishina cross section reported in [80]. The number of the photon of energy $\epsilon = h\nu$ - in unit of time and frequency - scattered off an ultra-relativistic electron of energy γmc^2 is given by:

$$\frac{dN_{\gamma,\epsilon}}{dt\, dE_1} = \frac{2\pi r_0^2 mc^3}{\gamma} \frac{n(\epsilon)d\epsilon}{\epsilon} \left[2q\ln(q) + (1+2q)(1-q) + \frac{1-q}{2}\frac{(\Gamma_e q^2 q)^2}{1+q\Gamma_e} \right] \tag{3.21}$$

where $\Gamma_e = 4e\gamma/mc^2$ is a parameter that determines the domain of the scattering, and $q = E_1/\Gamma(1-E_1)$ with E_1 that represents the initial electron energy (the energy of the of the scattered photons, ϵ_1, is expressend in units of the initial electron energy by the relation $\epsilon_1 = \gamma mc^2 E_1$). By replacing the $n(\epsilon)d\epsilon$ with the relation:

$$n(\epsilon)d\epsilon = \frac{n_p(\nu)d\nu}{h^2\nu} \tag{3.22}$$

the Equation 3.21 becomes:

$$\frac{j_{IC}(\gamma,\nu_1,\nu)}{d\gamma d\nu_1} = \frac{2\pi r_0^2 c}{\gamma^2 h^2 \nu^2} n_p(\nu) \left[2q\ln(q) + (1+2q)(1-q) + \frac{1-q}{2}\frac{(\Gamma_e q^2 q)^2}{1+q\Gamma_e} \right] \tag{3.23}$$

where $j_{IC}(\gamma,\nu_1,\nu)$ is the single emissivity as a function of the electron energy and of the photon frequency, and n_p the numerical density of the target photon (i.e. the synchrotron ones). The latter quantity is given by:

$$n_p(\nu) = \frac{U(\nu)}{h\nu}$$

where $U(\nu)$ is the energy density of the synchrotron target photon, computed as:

$$U(\nu) = \frac{4\pi R}{3c} j_s(\nu)$$

where $j_S(\nu)$ is the synchrotron emissivity given by the Equation 3.16.

Finally, the total emissivity J_{IC} is obtained by integrating the single-electron Compton emissivity over the photon spectrum and over the electron energy distribution 3.13:

$$J_{IC}(\nu) = \int_{\gamma_{min}}^{\gamma_{max}} N_e(\gamma) \int_{\nu_1} n_p(\nu_1)\, j_{IC}(\gamma,\nu_1,\nu)\, d\nu_1\, d\gamma\ . \tag{3.24}$$

As last step, to obtain the observed fluxes for both the synchrotron and inverse Compton contribute, their total emissivity has to be corrected (following the relations expressed for example in [81]) for the luminosity distance D_L and for the bulk motion following the relation:

$$J_{IC,observed}(\nu) = \frac{J_{IC}(\nu)\,\delta^3}{4\pi\, D_L} \tag{3.25}$$

The contributions of both the synchrotron and the Inverse Compton peaks are calculated for several narrow frequency bins, and then are added to one another. So, the SED model function is not known analytically, but only through a numerical sample of points. To obtain the value of the SED at any frequency, an interpolation process (e.g. a cubic spline interpolation) has to be performed.

The model described above is that one implemented and used for the SED modeling of Makn501, whose results are presented in Chapter 5. However, in the code other electron distributions -reported in the following list - have been implemented.
Single power-law:

$$N(\gamma) \propto \gamma^{-\alpha} \, . \tag{3.26}$$

Smoothed double power-law, with $(\beta - \alpha = 1)$:

$$N(\gamma) \propto \gamma^{-\alpha} \left(1 + \frac{\gamma}{\gamma_b}\right)^{(\alpha-\beta)} \, . \tag{3.27}$$

Exponential cutoff power-law:

$$N(\gamma) \propto \gamma^{-\alpha} e^{-(\gamma/\gamma_b)} \, . \tag{3.28}$$

Exponential cutoff smoothed double power-law:

$$N(\gamma) \propto \gamma^{-\alpha} \left(1 + \frac{\gamma}{\gamma_b}\right)^{(\alpha-\beta)} e^{-(\gamma/\gamma_b)} \, . \tag{3.29}$$

Curved distribution (e.e., log-parabola):

$$N(\gamma) \propto \gamma^{-[\alpha - \beta \log(\gamma/\gamma_b)]} \tag{3.30}$$

3.4.2 Implementation

As seen in Section 3.2, if the model function is non-linear in the parameters, the minimization process must be iterative. This means that the minimum of the χ^2-manifold is approached in several steps, where at each step a better approximation of such a minimum is searched for. The characteristic Equations 3.6 and 3.8 of the steepest descent and the Gauss-Newton method, describing the parameters update at each minimization steps, can be written in more compact form:

$$\mathbf{p} = -\mu \nabla \chi^2(p) \tag{3.31}$$

$$\mathbf{p} = \mathbf{H}^{-1}[-\nabla \chi^2(p)] \tag{3.32}$$

to put in evidence the presence of the χ^2 gradient, $\nabla\chi^2$, and the Hessian matrix, $\mathbf{H}$ (here $\mathbf{H}$ is the Hessian of the χ^2 obtained by linearizing the model function). To use these equations, both the first and second derivatives of the χ^2 have to be computed. Recalling the Equation 3.3, the first derivative is given by:

$$\frac{\partial \chi^2}{\partial p_k} = -\sum_{i=1}^{N} \left[\frac{y_i - f(x_i, -\mathbf{p})}{\sigma_i} \, \frac{\partial f(x_i, \mathbf{p})}{\partial \mathbf{p}_j} \right] \tag{3.33}$$

while the second derivative is given by:

$$\frac{\partial^2\chi^2}{\partial p_k \partial p_l} = 2\sum_{i=1}^{N}\frac{1}{\sigma_i^2}\left[\frac{\partial y(x_i,\mathbf{p})}{\partial p_k}\frac{\partial y(x_i,\mathbf{p})}{\partial p_l} - [y_i - y(x_i;\mathbf{p})]\frac{\partial^2 y(x_i;\mathbf{p})}{\partial p_k \partial p_L}\right]$$

where the second term can be neglected if it is small enough with respect to the first derivative terms. Moreover, for a succesful model the terms $[y_i - y(x_i;\mathbf{p})]$ - corresponding to the difference between the observed data and the model - once summed over i, tends to be very small, since the positive and negative differences cancel to one another. So the previous equation becomes:

$$\frac{\partial^2\chi^2}{\partial p_k \partial p_l} = 2\sum_{i=1}^{N}\frac{1}{\sigma_i^2}\left[\frac{\partial y(x_i,\mathbf{p})}{\partial p_k}\frac{\partial y(x_i,\mathbf{p})}{\partial p_l}\right] \tag{3.34}$$

By defining:

$$\alpha_{kl} \equiv \frac{1}{2}\frac{\partial^2\chi^2}{\partial a_k \partial a_l} \tag{3.35}$$

$$\beta_k \equiv -\frac{1}{2}\frac{\partial\chi^2}{\partial a_k} \tag{3.36}$$

the Equations 3.31 and 3.32 can be rewritten as:

$$\delta a_l = \mu \times \beta_l \tag{3.37}$$

$$\sum_{l=1}^{j}\alpha_{kl}\delta a_l = \beta_k \tag{3.38}$$

where j is the total number of parameters. The matrix α is equal to one-half time the Hessian matrix, and it is called *curvature matrix*.

The algorithm of Levenberg Marquardt combines the steepest descent and the Gauss-Newton method, making one of them more or less dominant at each minimization step. As seen in the previous section, the lenght of the step in the steepest descent method is defined by the parameter μ through the reciprocal of the diagonal elements of the Hessian matrix. By inserting the definition of α in the Equation 3.11, the new definition of the step lenght becomes $\mu = 1/\alpha_{ll}$. Since the steps can be still too large, μ is further scaled by a fudge factor $\lambda > 1$, giving $\mu = 1/\lambda\alpha_{ll}$. In this way the Equation 3.37 can be replaced by:

$$\delta a_l = \frac{1}{\lambda\alpha_{ll}}\beta_l \tag{3.39}$$

At this point, the Equations 3.39 and 3.38 related to the steepest descent and the Gauss-Newton method can be combined by introducing a new matrix α', whose diagonal elements are increased by a factor λ, i.e.

$$\alpha'_{jj} \equiv \alpha_{jj}(1+\lambda)$$
$$\alpha'_{jk} \equiv \alpha_{jk}\ .$$

This leads to the final formulation of the Levemberg-Marquardt method through:

$$\sum_{l=1}^{M} \alpha'_{kl} \delta a_l = \beta_k \ . \tag{3.40}$$

This Equation is the same as the Equation 3.12. If λ assumes large values, the previous equation behaves as the steepest descent method (Equation 3.39), since the matrix α' is diagonally dominant. On the other hand, if λ assumes small values, the Equation 3.40 turns into the Equation Gauss-Newton Equation3.38.

Once the model function $f((p))$ (see Sect. 3.4.1), and the routine performing a complete step of the Levemberg-Marquart method have been implemented, the minimization process proceeds as follows:

1. a starting $\mathbf{p}$ vector - containing the initial values of the model parameters - is set. Each parameter is choosen in a large, but reasonable, physical range;
2. the initial value of $\chi^2(\mathbf{p})$ is computed, and the minimization loop is started;
3. the initial value of λ is fixed to a small quantity (i.e., 0.001);
4. the linear Equation 3.40 is solved for the update of the parameters $\delta\mathbf{p}$, whose determines the next starting point in parameter space;
5. the new $\chi^2(\mathbf{p} + \delta\mathbf{p})$ is computed;
6. the difference between the current and the previous χ^2 is evaluated;
7. if $\chi^2(\mathbf{p} + \delta\mathbf{p}) - \chi^2(\mathbf{p} \geq 0$ it means that the new starting point is probably moving in the minimum direction. So, the value of λ is increased by a factor 10 in order to reduce the step lenght in the space parameter, and to increase the contribution of the Gaussian-Newton method);
8. if $\chi^2(\mathbf{p}+\delta\mathbf{p})-\chi^2(\mathbf{p} < 0$ it means that the new starting point is probably moving far from the minimum. So, the value of λ is decreased by a factor 10 in order to increase the step lenght in the space parameter, and to increase the contribution of the steepest-descent method);
9. the algorithm goes back to point 4, and repeat points 4-8, until one of the exit criteria are satisfied;
10. once the convergence is reached, the covariance matrix calculates the uncertaintes related to the model parameters $\mathbf{p}$.

As described in the above list, the algorithm does not exit the minimization loop until some convergence criteria are achieved. When such conditions are satisfied, the current values of the parameters are considered a good enough approximation of the absolute minimum. There are two stopping criteria:

- if the χ^2 decreases by a negligible amount for one or two consecutive iterations. A change in the χ^2 lower than 10^{-2} or some fraction of 10^{-3} is considered statistically meaningless. To be conservative, this amount is fixed to 10^{-3}, while the number of consecutive iterations to 4;

- if $\lambda > 10^{20}$. When such a value is so high it means that the steps in the parameter space are very short. From experience - in this context - when λ exceeds the value of $10^5 - 10^6$, rarely the χ^2 decreased again. To be conservative also in this case, the λ-threshold is set to 10^{20}.

The flow chart of the code is shown in Figure 3.1.

All the model parameters are defined positive. However in the minimization algorithm they undergo a trasformation in such a way to allow all the space parameter to be explored. The parametrization consists in applying a logaritmic function to the physic parateter $\mathbf{p_k}$, so the parameter P_k used by the algorithm is

$$P_k = \log p_k \ .$$

In such a way the algorithm is free to move also in directions where the physical parameters are negative (because the logarithm is always a quantity defined positive). Once the algorithm have exited the minimization loop, the parameters have to be transformed back by the inverse transformation:

$$p_k = e^{P_k} \ .$$

Since the SED modeling of blazar is not an easy standard application of the non-linear least square minimization, some remarks have to be pointed out. During each step of the minimization loop, the calculation of χ^2 requires the evaluation of the SED for all the observed frequencies. Usually, the model function is known analytically, so these evaluations are a straightforward algebraic process. In our case, instead, we know the model function only through a numerical sample and it is unlikely that an observed point will be one of the sampled points coming from the implementation of the [76] model. Nevertheless, it will in general fall between two sampled points, which allows us to use interpolation to approximate the value of the SED. The Levenberg-Marquardt method requires the calculation of the partial derivatives of χ^2 with respect to the eight fitted SSC parameters. Contrary to the usual case, in which all derivatives can be obtained analytically from knowledge of the model function, in our case they have also been obtained numerically by evaluating the incremental ratio of χ^2 with respect to a sufficiently small, dynamically adjusted increment of each parameter. Finally, the minimization process should be repeated several times, starting from different values of parameters to avoid the possibility to find a local minimum, due to the complicated shape of the χ^2-manifold.

3.4.3 Parameter Uncertaintes

Covariance Matrix

Once the most likely parameters of the SED model have been identified, it is necessary to estimate their uncertaintes. Usually, in a non-linear least square fitting they are computed through the covariance matrix, C, that is defined as the reciprocal of the curvature matrix 3.35:

$$[C] \equiv [\alpha]^{-1} \ . \tag{3.41}$$

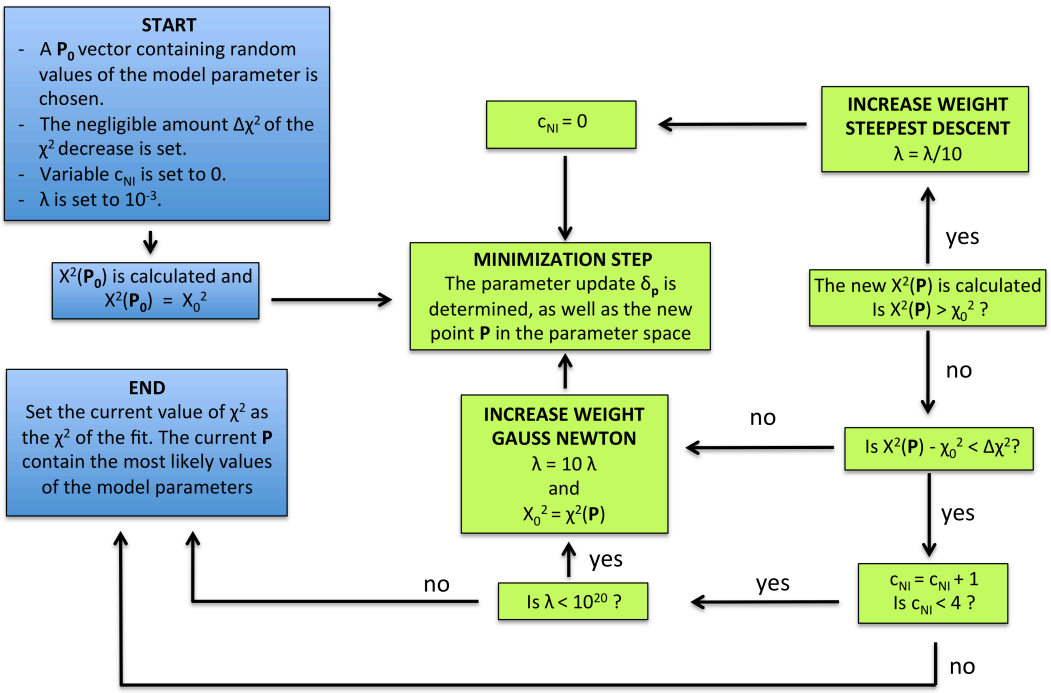

Figure 3.1: Flow chart of the minimization procedure (minimization loop in green).

In particular, the diagonal elements C_{kk} of the covariance matrix represents the squared uncertaintes associated to the fitted parameters $\mathbf{p}$, while the other elements C_{kl} represents the covariances between the parameters $\mathbf{p}_k$ and $\mathbf{p}_l$.

However, the uncertaintes given by the covariance matrix can be related to the parameters uncertaintes only if the errors measurements associated to the data points are normally distributed [71].

Due to the parametrization explained in the previous section, also the parameter uncertaintes have to be transformed. The physical parameter, p, is related to the parameter used by the algorithm, P, through a function $p = f(P)$. The error on the parameter P, ΔP, is evaluated through the covariance matrix, so its uncertainty range is symmetric with respect to the parameter P. Since the relation that links the physical parameter p to P is an exponential function, the uncertainty range of the parameter p is determined by the quantities $\delta^- = e^{P-\Delta P}$ and $\delta^+ = e^{P+\Delta P}$. Contrary to the uncertainty range on P, that related to the physical parameter p is not symmetric.

Confidence Limits

When the covariance matrix is not suitable to estimate the uncertainties related to the fitted parameters, a valid alternative consists in recurring to the confidence limits. Here, the probability distributions of the errors is defined through a confidence region, that is a sub-region of the space parameter containing a certain percentage of the total probability. Such a region is naturally centered on the fitted values parameters $\mathbf{p_{min}}$. When the fitting procedure is carried out with a non-linear χ^2 minimization, the choice of the shape of the confidence limits is standard [71]. If the parameter vector $\mathbf{p_{min}}$ represents the best approximation of

the minimum of the χ^2-manifold, the confidence limits methos is based on a perturbation of such a minimum. By moving far from the minimum, the chi^2 is supposed to increase; the regoin inside which the χ^2 does not exceed a certain amount $\Delta\chi^2$, defines a confidence region around $\mathbf{p}$. The typical confidence limits are defined in such a way to have the 68%, 90% (and so on) of the probability to find the parameters p in such a region.

Usually, the confidence limits is not related to the full dimensional space of the parameters, rather than to the confidence region of each parameter taken separately. That region, in the one-dimensional parameter subspace corresponds to the projections of the M-dimensional regions - defined by $\Delta\chi^2$ - on to the one-dimensional space of interest.

In the one-dimensional case, let's consider the minimum χ^2_{min}, identified by the parameter vector $\mathbf{p} = [p_1^{min}, p_2^{min}, ..., p_M^{min}]$. Once a confidence level α has been chosen, the equations:

$$\chi^2(p_1^{min}, p_2^{min}, ..., p_M^{min}) = \chi^2_{min} + \alpha \tag{3.42}$$

$$\chi^2(p_1^{min}, p_2^{min}, ..., p_M^{min}) = \chi^2_{min} - \alpha \tag{3.43}$$

has to be solved twice for each parameter in order to find the related uncertainty range. The parameter α fixes the confidence level: usually $\alpha = 1.2$ corresponds to a 68% confidence level, $\alpha = 2.71$ to 90% and $\alpha = 16.61$ to 99%. Once the value of $M - 1$ have been fixed to value corresponding to χ^2_{min}, the above-mentioned equations are solved (one for the lower and one for the upper uncertaintes) for the remaining parameter. The lower uncertaintes σ_i^l is given by $p_i^{min} - p_i^l$, where p_i^{left} is calculated by solving the Equation 3.43, while the upper uncertaintes σ_i^u is given by $p_i^{min} - p_i^u$, where p_i^u is calculated by solving the Equation 3.42. The resulting uncertainty range is asymmetric with respect to the parameter value and is given by $[p_i^{min} - \sigma_i^l; p_i^{min} - \sigma_i^u]$.

Chapter 4

Markarian 501: Multi-frequency Data

In this Chapter, after briefly presentating the Markarian 501 (henceforth: Mkn501; Sect. 4.1), I present the MAGIC analysis results of 2011 data (Sect. 4.2). Based on the latter I also perform a FERMI-LAT analysis to obtain simultaneous HE data (Sect. 4.3). Also, simultaneous X-ray and UV data are obtained from Swift's UVOT and XRT space telescopes (Sect. 4.4). Finally, the resulting seven SED datasets are reported in Section 4.5.

4.1 Markarian 501

Markarian 501 (shown in Figure 4.1 as seen by the GALEX telescope) is an AGN located at RA(J2000)=16 h 53 m 52.2 s and Dec(J2000)= $+39^\circ\,45'\,37''$. It is located at redshift $z = 0.034$ which corresponds to a distance of 148 Mpc, determined from the Virgo-infall corrected radial velocity [82]. Mkn501 was firstly discovered thanks to an ultraviolet survey [83], and further on also in the very high energy band ($E > 100$ GeV) [84]. With its jet pointing to the Earth, it belongs to the class of the high-frequency peaked BLLac object (HBL) according to the classification in [85]. Its spectral energy distribution is characterized by two peaks, the former due to the synchrotron emission due to the interaction of electrons inside the jet with a tangled magnetic field [86], and the latter due to the inverse Compton process occurring between the same electron population and the synchrotron photn field [87] or an external one [88] (for more details, see Section 1.6). Mkn501 is an extremely variable source, it has shown an exceptionally flaring activity in 1997 reaching a flux (for energies $>$ 350 GeV) of the order of 10 Crab units, and showing a synchrotron frequency peak shifted by two order of magnitude with respect to the quiet state [77]. In 2005 Mkn501 went through another importan flaring state, showing an extraordinary intrinsic time scale variability [66].

Two main reasons make Mkn501 one of the best candidate to study the properties of blazars and the high energy processes: (i) its spectral energy distribution can be measured quite accurately in almost the whole domain thanks to its brightness; and (iii) its location at low redshift that results in a negligible EBL absorption of the flux above 1 TeV.

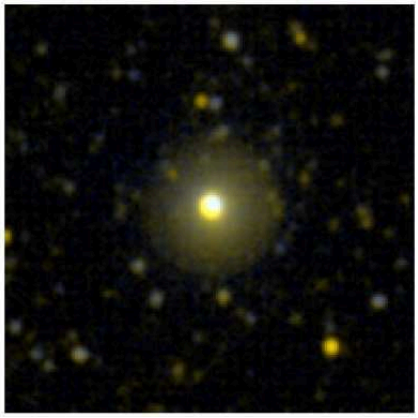

Figure 4.1: Markarian 501 observed by the Galaxy Evolution Explorer (GALEX) telescope in the far- and near-UV bands (1516 and 2267 Åeffective wavelenghts) [82].

4.2 MAGIC Analysis

In this section I present the MAGIC data (2011) analysis results on Mkn501. The software version used for the analysis are: ROOT 5.34.21[1] and MARS v2-14-3[2], internal MAGIC Collaboration software. In order to perform the analysis, four different dataset are required:

- **Mkn501 data**: all the available stereo data taken from March to June 2011. Data are taken in *wobble* pointing mode (Sect. 2.4), at low zenith angles ($10° < ZA < 35°$), and in different light conditions: *dark*, *twilight* and *moon*. All these data are summarized in Table 4.1.

- ***Off* data**: data where γ-ray emission from point-like or extended sources is not expected. These data are needed to provide the hadron events with which to build the Random Forests, in order to perform γ-ray/hadron separation (Sect.s 2.5.4). These data are associated to sky regions supposely free of sources. The *Off* data must be preferably taken in the same observation period of Mkn501, and in absolutely the same zenith range and light conditions. The conditions must be as similar as possible to avoid introducing biases or further systematic errors. The *Off* sample is summarized in Table 4.2.

- **Monte Carlo data**: they contain only simulated γ-ray events. The Monte Carlo data are divided into two subsamples: (i) 2/3 (the so-called *train sample*) needed to build the Random Forests in order to perform the γ-ray/hadron separation (Sect. 2.5.4) and the source-position reconstruction (Sect. 2.5.5), and (ii) 1/3 (the so-called *test sample*) to establish the analysis cuts in *Flute* (Sect. 2.8). The used Monte Carlo data are the Pre-Upgrade MC (ST.01.02), suitable for the stereo analysis of data taken between November 2009 and June 2011, with MUX readout in MAGIC I telescope and DRS2 readout in MAGIC II. They are simulated in the low zenith range $5° < ZA < 35°$ and for the *wobble* pointing mode. They are available from the *Superstar* analysis level

[1] https://root.cern.ch
[2] *Magic Analysis Reconstruction Software*

(Sect. 2.5.3), after an image-cleaning is 6-3 for MAGIC I and 6-4.5 for MAGIC II has been applied (Sect. 2.5.2).

- **Crab Nebula data**: they are analized, as a test, to validate the reliability of the Random Forests and the Look Up Tables, built starting from Monte Carlo and *Off* data. If the resulting Crab spectrum is well reproduced, then the Random Forest is trustable and can be used for Mkn501 analysis. Also the Crab Nebula sample should resemble as much as possible the conditions under wich Mkn501 data were taken. Unfortunately, for such observation period there are no sufficient Crab Nebula data to cover the whole zenith range, so such a test is performed only for $24^\circ < ZA < 35^\circ$. Crab Nebula data used for the test are summarized in Table 4.3.

Table 4.1: MAGIC observations of Markarian 501 in 2011.

Date	MJD	Obs.time [h]	Zenith [◦]	Light conditions
2011-03-03	55622	0.53	$16.1 < z < 26.2$	*dark* (0.4 h), *twilight* (0.13 h)
2011-03-25	55644	0.38	$17.4 < z < 21.6$	*moon*
2011-03-30	55649	1.07	$11.0 < z < 16.4$	*moon* (1.03 h) *twilight* (0.04 h)
2011-04-11	55661	0.33	$11.0 < z < 12.1$	*dark*
2011-04-26	55676	1.50	$12.6 < z < 27.0$	*dark* (0.67 h), *moon* (0.83 h)
2011-05-08	55688	1.30	$14.8 < z < 30.3$	*dark*
2011-05-14	55694	1.45	$17.5 < z < 33.0$	*dark* (1.03), *twilight* (0.42)
2011-05-23	55703	1.40	$14.9 < z < 29.6$	*dark* (0.72 h), *moon* (0.68)
2011-05-29	55706	1.00	$16.9 < z < 27.5$	*dark*
2011-06-04	55715	1.32	$16.7 < z < 31.7$	*dark*
2011-06-10	55721	1.45	$11.0 < z < 15.2$	*moon*

4.2.1 Data Quality Check and First Analysis Steps

The standard analysis starts from the *Star* data available at PIC servers. At *Star* stage, the calibration process, the image-cleaning and the parametrization (described in Sections 2.5.1 and 2.5.2) have been already performed by the OSA. Before the analysis all data have to be checked. This phase is called quality-check, and can be performed following different criteria, depending mainly on the final purpose (or at the analyzer's discretion). In this analysis attention is paid to:

- *Technical Problems.* Every night a *runbook* is filled in by the shifters with relevant information concerning the data taking: weather conditions and evolution, event rates, and technical problems related to the hardware or the software of all the subsystems. In case of technical problems, the analyzer can decide to remove part of the affected data.

- *Rate.* The L3 event rate in optimal conditions should be between 250 and 350 Hz during *dark* time, and ... during *moon* time. Suddend weather changes can make

Table 4.2: *Off* data used for building the Random Forest for the γ-rays/hadrons separation.

Source	Date	MJD	Zenith [$\circ$]	Light conditions
Segue J	2011-03-03	55623	$12.9 < z < 30.3$	*dark*
	2011-03-25	55645	$12.9 < z < 28.2$	*dark*
	2011-03-30	55650	$13.0 < z < 30.0$	*dark*
	2011-04-07	55658	$13.5 < z < 30.0$	*dark*
	2011-04-25	55676	$13.0 < z < 30.0$	*dark*
4C+4922	2011-05-22	55703	$21.0 < z < 35.0$	*dark*
	2011-05-24	55705	$22.6 < z < 34.2$	*dark*
PKS1717+177	2011-05-09	55690	$11.0 < z < 31.0$	*dark*
	2011-05-10	55691	$11.0 < z < 25.0$	*dark*
	2011-05-11	55692	$11.0 < z < 26.0$	*dark*
MS1050.7+4946	2011-05-03	55684	$25.5 < z < 32.0$	*dark*
	2011-05-26	55707	$28.9 < z < 35.0$	*dark*

Table 4.3: Crab Nebula data used for testing the reliability of the Random Forests and the Look Up Tables.

Date	MJD	Zenith [$\circ$]	Light conditions
20110302	55621	$24.4 < z < 35.0$	*dark*
20110324	55643	$25.0 < z < 35.0$	*dark*

it quite unstable. Sometimes, even car lights - by hitting the telescope dishes - can generate conspicuous spikes in the rate. Data with strong fluctuations or spikes have to be removed.

- *Cloudiness.* The cloudiness is strongly correlated with the L3 rate. An increasing of the cloudiness corresponds to a drop in the rate. Usually data taken with cloudiness $> 40\%$ are rejected, unless LIDAR corrections are applicable.

- *Dark Currents.* DCs vary depending on the light conditions: during *moon* time they are higher then in *dark* time. The transition between the *dark* and *moon* time is smooth, but an objective criteria is needed to discriminate between these conditions. Usually, during observations, when MAGIC II DCs exceed 1 mA, the DTs and IPRC setting is changed. In the analysis process, the discrimination between the *dark* and *moon* data can be based mainly on the DCs. For the mono configuration, data with DC < 2.5 mA can be considered as *dark*, and Monte Carlo data can be used without any corrections. For both pre- and post-upgrade stereo configurations, the threshold is more conservative: DCs should be < 1.5 mA. For the analysis of Mkn501 in 2011, since no Monte Carlo data are available for *moon* condition, all data with MAGIC II DCs > 1.5 mA are rejected.

based on quality-check, 2 days were excluded due to technical problems; and one further day had to be excluded due to problems in data files causing *Melibea* to crash:

- 2011-03-03: only one *wobble* position available, and problems with *Melibea* files;
- 2011-03-25: *moon* data with too high DCs;
- 2011-04-26: too low trigger rate, L3 $\sim$ 60 Hz.

Once the data quality check and selection have been performed on Mkn501, Crab, and *Off* data, then *SuperStar* is applied to each sample to compute the preliminary stereo parameters (Sect. 2.5.3). After that, the RFs and the LUTs are built by *Coach* using *Off* and Monte Carlo training samples, following the procedure described in Section 2.5.4. In order to compute the hadronness for each event, the position reconstruction, and the energy estimate, *Melibea* applies the RFs and the LUTs on Mkn501, Crab, and Monte Carlo test samples (see Sect. 2.5.5).

4.2.2 Signal Search

After *Melibea* processing, data can be investigated to see if a detection can be claimed. The signal search on Mkn501 is done day by day through the *Odie* routine (Sect. 2.5.6). To estimate the background, the *OFF from wobble partner* method with OfWP=1 is adopted, since only 2 wobble positions are available for each day. The signal search is performed in the full-energy range, applying the standard cuts. For period from March to June 2011, the characteristic dead time is $0.5\,10^{-3}$ s, the PSF radius is 0.063∘, and the θ^2-cut is adjusted case by case, as suggested by *Odie*. In Table 4.4 the significance σ calculated according to Eq.(17) in [46] is reported for each day. The source is considered detected if $\sigma \geq 5$. Figure 4.2 shows the daily θ^2-plots and their significance.

Table 4.4: Markarian 501 results for the signal search.

Date	MJD	Eff. time [h]	θ^2	$N_{excesses}$	Significance σ
2011-03-30	55649	0.77	0.0180	91	9.70
2011-04-11	55661	0.29	0.0221	17	4.30
2011-05-08	55688	1.11	0.0174	272	20.13
2011-05-14	55694	1.08	0.0160	478	24.04
2011-05-23	55703	0.66	0.0194	36	5.37
2011-05-29	55706	0.88	0.0169	132	12.24
2011-06-04	55715	0.96	0.0197	49	6.73
2011-06-10	55721	0.59	0.0280	42	6.38

NOTES – Col.(1): Observation date. Col.(2): Modified Julian Date (MJD). Col.(3): the effective observation time once the dead times have been removed. Col.(4): θ^2-cut suggested by *Odie*. Col.(5): the number of excesses. Col.(6): significance σ calculated according to Equation 17 in [46].

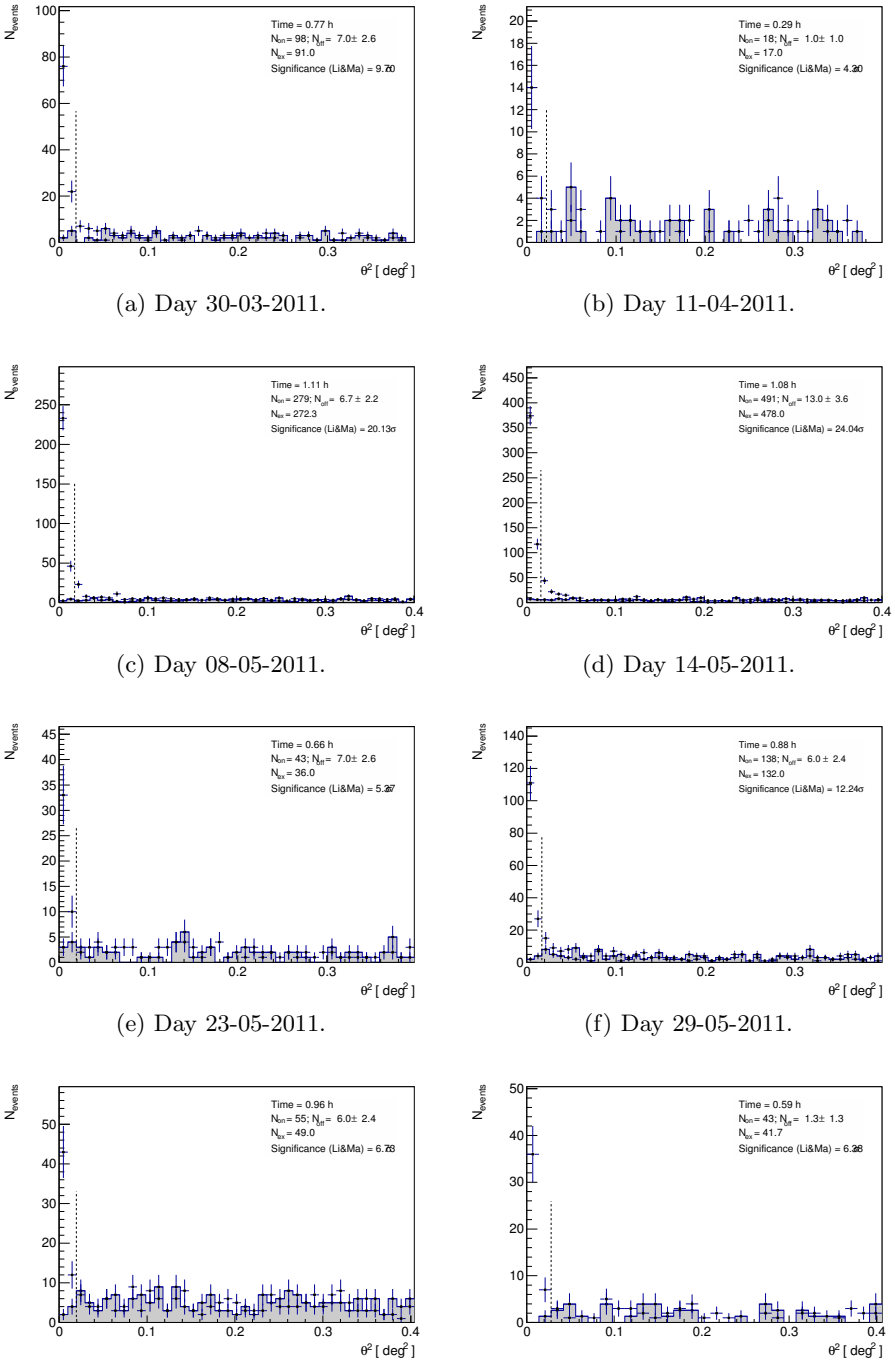

(a) Day 30-03-2011. (b) Day 11-04-2011.

(c) Day 08-05-2011. (d) Day 14-05-2011.

(e) Day 23-05-2011. (f) Day 29-05-2011.

(g) Day 04-06-2011. (h) Day 10-06-2011.

Figure 4.2: Markarian 501 θ^2-plot for each observation day resulting from *Odie*. The number of both ON and OFF events are plotted as a function of θ^2. The number of excesses N_{ex} and the significance σ are computed in the zone below the θ^2-cut marked by the dotted vertical line. Also the effective observation time is reported.

4.2.3 Day by Day Spectra

Mkn501's spectra, and light-curve are computed using the *Flute* routine, as described in Section 2.8. *Flute* needs Mkn501 data and Monte Carlo test data, processed by *Melibea* as input. These are used to estabilish the best *hadronness* and θ^2-cut values to perform the γ-ray/hadron separation, once a separation efficiency has been choosen. In order to compute spectra, the photon energy range is divided into 20 or 15 bins, and the cuts mentioned above are determined for each bin using Monte Carlo data. The θ^2-efficiency is set to 0.75, the *hadronness* efficiency is set to 0.9, and the minimum size for each event corresponds to 55 photoelectrons. In Figure 4.3 the SED obtained for each day is shown[3].

As last check, before computing Mkn501's flux, I performed a test on the Crab Nebula data. If the Crab Nebula spectrum is well reproduced, it means that the Random Forests and the Look Up Tables are trustable. The data used for such a test are summurized in Table 4.3. Unfortunately, there are not enough data to cover the whole zenith range, so the test is performed only for zenith $24° < ZA < 35°$. In Figure 4.4 the Crab Nebula θ^2-plot and Crab SED are reported. The sensitivity is computed for the full-energy range, by using 1.26 hours of effective time, and by estimating the background with the *OFF from wobble partner* method, setting OfWP=1. The resulting sensitivity is $0.87 \pm 0.13\%$, compatible with the nominal one $\sim 0.8\%$ before the upgrade. A good agreement is reached for the Crab Nebula SED, even though it gets worse at very high energies, ≥ 3 TeV.

4.2.4 Light Curve

Once the spectrum of Mkn501 is computed for each day, *Flute* can produce also the light curve, shown in Figure 4.5, for the whole observation period of Mkn501 (Sect. **??**). Moreover, the intra-night variability is investigated during both the higher-flux days (08-05-2011 and 14-05-2011). Hence, a light curve with both 10 and 20 minutes binning is performed. The results shown in Figure 4.7 confirm that no intra-night variability is revealed during the higher-flux day 14-05-2011. In Figure 4.6 0508 invece?...
Once the SED modeling has been performed by a rigorous statistical method, it will be possible to study the model parameter variations of the source in these different activity states.

As last consideration,

4.2.5 Spectral Energy Distributions

The SEDs obtained in the previous section are expressed as a function of the estimated energy. In order to obtain those SEDs as a function of the true energy, an unfolding procedure has to be applied, as explained in Section 2.5.8. The unfolding process is performed paying attention to:

- range of estimated energy. This range is divided into several bins, and only bins containing a significant signal (1.5-2 counts) are taken into account.

- range of true energy. This range is chosen in such a way to allow the migration matrix to be computed properly. The true energy range should be more or less the same as the estimated one: if it is chosen correctly, the migration matrix is diagonal;

[3]Day 2011-04-11 is excluded from further analysis because its significance does not reach 5σ (Table 4.4).

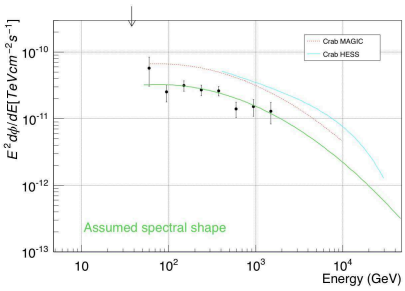

(a) Day 30-03-2011, 20 energy bins.

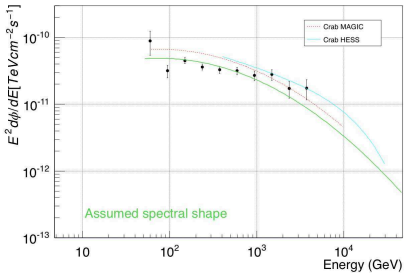

(b) Day 08-05-2011 20 energy bins.

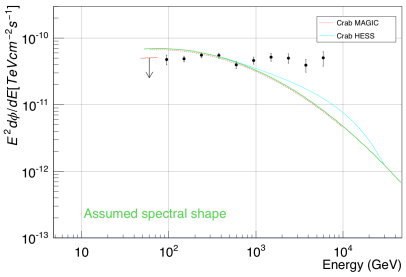

(c) Day 14-05-2011 20 energy bins.

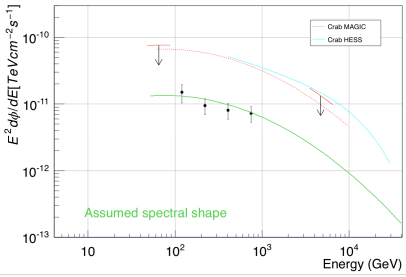

(d) Day 23-05-2011 15 energy bins.

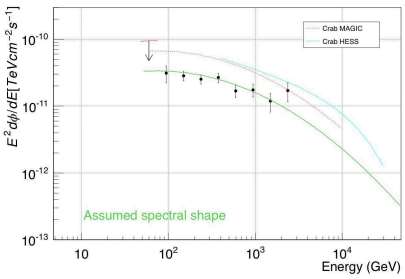

(e) Day 29-05-2011 20 energy bins.

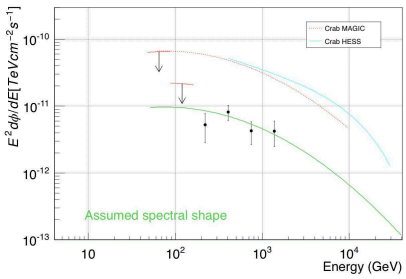

(f) Day 04-06-2011 15 energy bins.

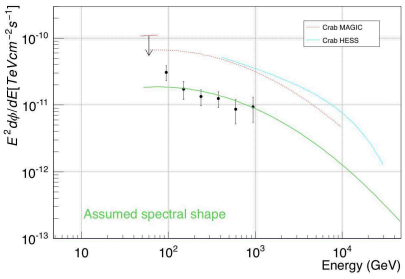

(g) Day 10-06-2011 20 energy bins.

Figure 4.3: Markarian 501 SEDs for each observation day resulting from *Flute*. The quantity $E^2\, d\Phi/dE$ is reported as a function of the estimated energy. The ULs (arrows) are computed as described in Section 2.8, and the spectral points are placed according to [61]. Crab Nebula SED computed by both MAGIG [89] and HESS [90] is reported as comparison. The assumed source spectral shape is shown by the green line.

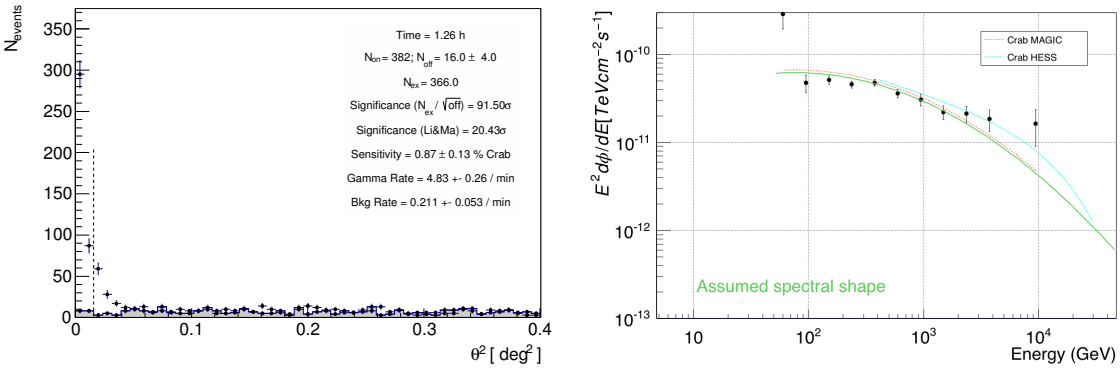

Figure 4.4: Left: Crab Nebula θ^2-plot and related quantities computed by *Odie*. Right: Crab Nebula SED obtained with *Flute*; references MAGIC [89] and HESS [90] SEDs are shown as comparison in red and blue dotted lines respectively. Data used for this test are summarized in Table 4.3.

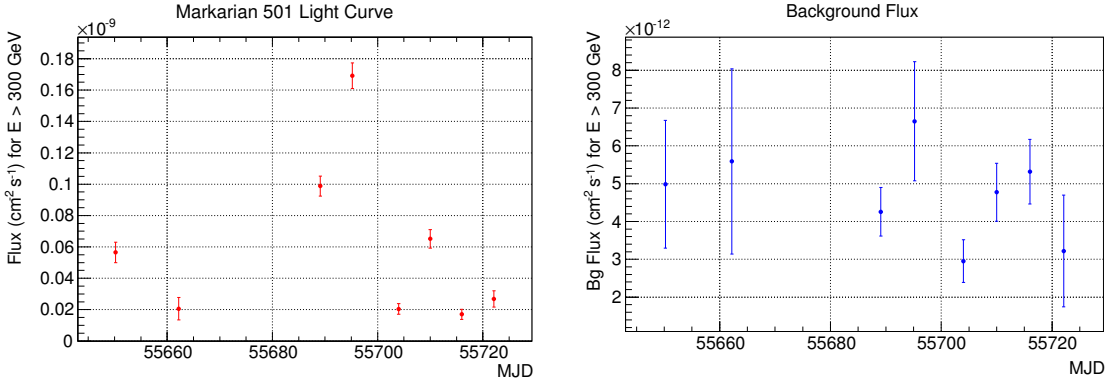

Figure 4.5: Markarian 501 light curve (left) and the respective background estimate (right) for energy ¿ 300 GeV. Day 11-04-2011 is still included, even if its significance is 4.30 σ

- collection area. The calculated collection area for each energy bin should be above 2000 m^2;

- regularization weight. It needs to be changed if the spectral point are too much alligned or spread.

Six different unfolding methods are used: (i) Schmelling with minimization performed by the Gauss-Newton method, (ii) Tikhonov with minimization performed by MINUIT[4], (iii) Bertero for the under-constrained cases, (vi) Forward unfolding, (v) Schmelling with minimization performed by MINUIT, and (vi) Bertero for the over-constrained cases. The daily spectra and SEDs are shown in Figures 4.8-4.11, along with the comparison among all results from different unfoldings to verify that they are compatible with one other.

After the unfolding, it is necessary to compute the analysis energy threshold for each day, because all spectral points much below that threshold are meaningless and they have to be removed. The energy threshold is computed from the Monte Carlo data (test sample)

[4]http://seal.web.cern.ch/seal/snapshot/work-packages/mathlibs/minuit/

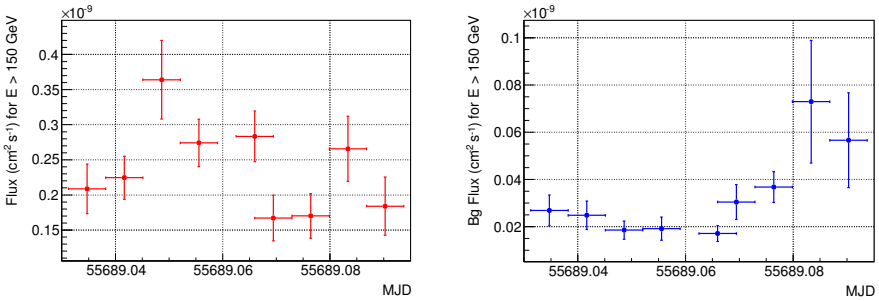

(a) Light curve 10 minutes-binning.

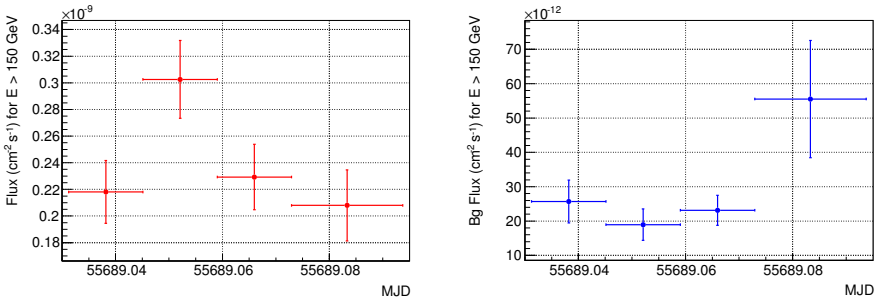

(b) Light curve 20 minutes-binning.

Figure 4.6: Day 08-05-2011 (*pre-flaring state*). Light curves with different binning (left panels) and relative background flux (right panels).

processed by *Melibea*. They are generated for different zenith angles, and with a spectral power index of -1.6. Since Monte Carlo data should resemble the real data sample as much as possible, first of all they have to be rescaled according to the expected source spectral index and to its zenith observation range. In fact, if the observed source is characterized by a harder spectral index then Monte Carlo data, it means that it emits fewer γ-photons at high energies, and more at low energies. Assuming that Monte Carlo data are characterized by an event distribution $\propto E^{-\alpha_1}$ and the source by another one $\propto E^{-\alpha_2}$, each Monte Carlo event has to be weighed according to:

$$w = \frac{E^{-\alpha_1}}{E^{-\alpha_2}}$$

The energy threshold can be estimated at different stages of the analysis. By using the Monte Carlo test data processed until the *Melibea* stage, all effects contributing to the increase of the trigger threshold (such as image cleaning, quality data selection, and signal extraction cuts) are taken into account. The energy threshold is then estimated by fitting a Gaussian distribution around the energy peak of the rescaled Monte Carlo test data: it is taken to correspond to the peak's energy of the fitting gaussian. The energy threshold is computed daily. Spectral parameters obtained after the unfolding process and the computed energy thresholds are summarized in Table 4.5[5].

[5]Results shown in the table report only the ststistic uncertaintes for both the flux normalization and the spectral slope. The systematic uncertainty on flux normalization are discussed in Section 4.2.7, whereas the systematic uncertainty on the spectral slope is estimated to be 0.15 [40].

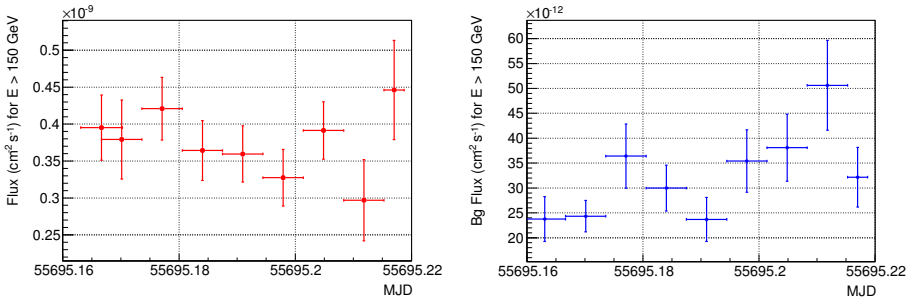

(a) Light curve 10 minutes-binning.

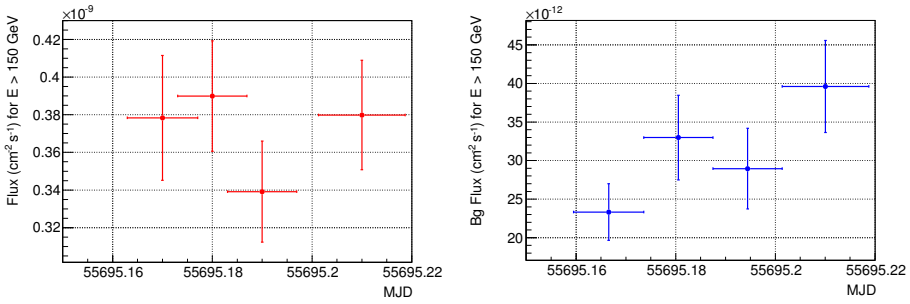

(b) Light curve 20 minutes-binning.

Figure 4.7: Day 08-14-2011 (*flaring state*). Light curves with different binning (left panels) and relative background flux (right panels).

Table 4.5: Markarian 501 fitted spectral parameters obtained after the unfolding procedure.

Date	Unfolding	$f_0 \pm Err_{f_0}$ $[10^{-11}$ cm^{-2} s^{-1} TeV$^{-1}]$	$\alpha \pm Err_\alpha$	ZA [deg]	E_{th} [GeV]
2011-03-30	Tikhonov	1.58 ± 0.28	2.33 ± 0.10	$10 < z < 17$	~ 88
2011-05-08	Tikhonov	2.81 ± 0.22	2.17 ± 0.05	$14 < z < 31$	~ 98
2011-05-14	Tikhonov	4.70 ± 0.20	2.06 ± 0.04	$17 < z < 32$	~ 103
2011-05-23	Bertero	0.46 ± 0.13	2.53 ± 0.20	$21 < z < 30$	~ 96
2011-05-29	Tikhonov	1.65 ± 0.22	2.32 ± 0.09	$17 < z < 28$	~ 94
2011-06-04	Tikhonov	0.45 ± 0.18	2.19 ± 0.28	$16 < z < 32$	~ 100
2011-06-10	Tikhonov	0.69 ± 0.31	2.57 ± 0.22	$11 < z < 15.5$	~ 79

NOTES – Col.(1): observation date. Col.(2): adopted unfolding method. Col.(3) and Col(4): best-fit spectral parameters and related errors. The spectrum is described by an energy power law: $dF/dE = f_0\, E^{-\alpha}$. Col.(5): ZA range (used to rescale Monte Carlo data). Col.(6): analysis energy threshold.

4.2.6 Extragalactic Background Light Correction

As seen in Section 1.3, γ-rays coming from far sources have to travel long distances before reaching the Earth. Along their path, they interact with the EBL photons generating e^+ e^-

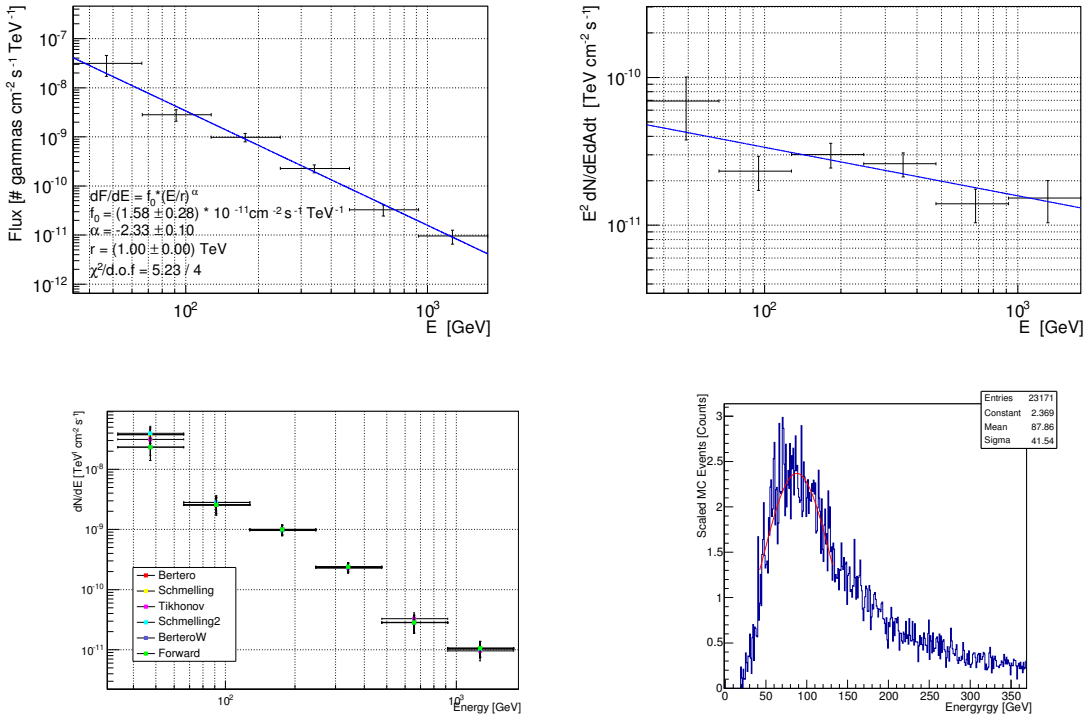

Figure 4.8: Tikhonov unfolding results for day 03-30-2011. On top: enegy spectrum (left), and SED (right) obtained after *CombUnfold*. On bottom: comparison between the results obtained with different unfolding methods (left), and analysis energy threshold (right) estimated as the mean of the Gaussian fit around the energy peak of the rescaled Monte Carlo test data.

pairs. This interaction results in a decrease - proportional to the source distance - of the observed flux, especially at the VHE. Even if Mkn501 is a relative near source, located at $z = 0.034$, its SEDs have to be deabsorbed for EBL. In order to apply auch a correction, I use the model described in [13], where by exploring the cosmological surveys from sub-millimeter to far UV, and by fitting all the data with a multi-frequency backward evolutionary model, the background photon density and its evolution with redshift has been reconstructed. Then, the photon-photon opacity, and the ensuing deabsorption is computed for each redshift. For the flux correction, I use the multiplicative absorption factor $e^{-\tau(z,E_\gamma)}$ tabulated in [13], calculated for $z = 0.03$. The EBL correction is applied directly at the unfolding stage (Sect. 2.5.8).

4.2.7 Systematic Errors

To compare the MAGIC results with other data coming from different instruments, the systematic uncertaintes on the flux normalization (those on the energy scale are not taken into account) have to be added to each spectral point. As discussed in Section 2.5.9 and in [40], the systematic uncertainties strongly depend on the energy range. Since the daily energy threshold are largely above 80 GeV[6] (Table 4.5), and no spectral points below 90 GeV are

[6]Except for day 10-06-2011 that corresponds to 79 GeV.

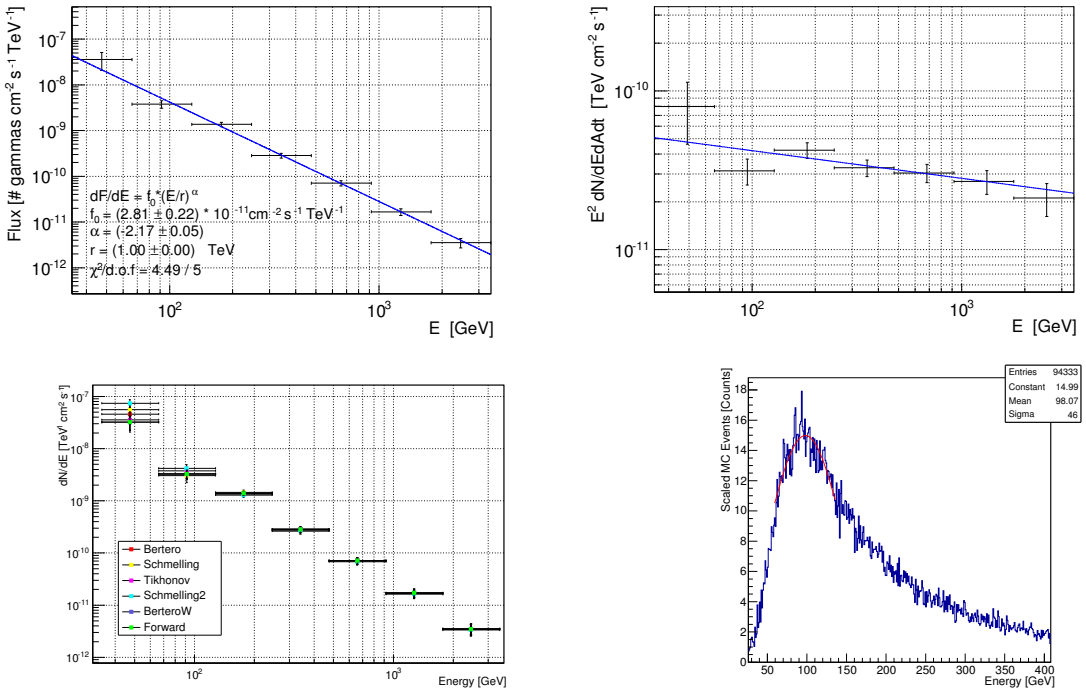

(a) 08-05-2011: Tikhonov unfolding results.

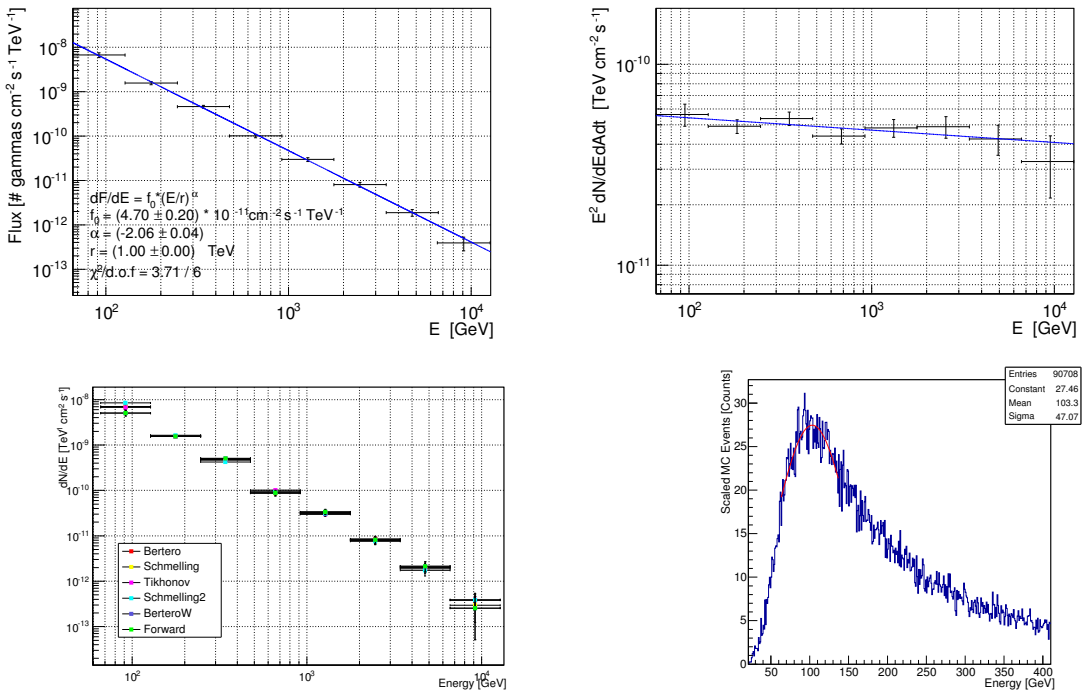

(b) 14-05-2011: Tikhonov unfolding results.

Figure 4.9: Same caption as Figure 4.8 for both (a), and (b).

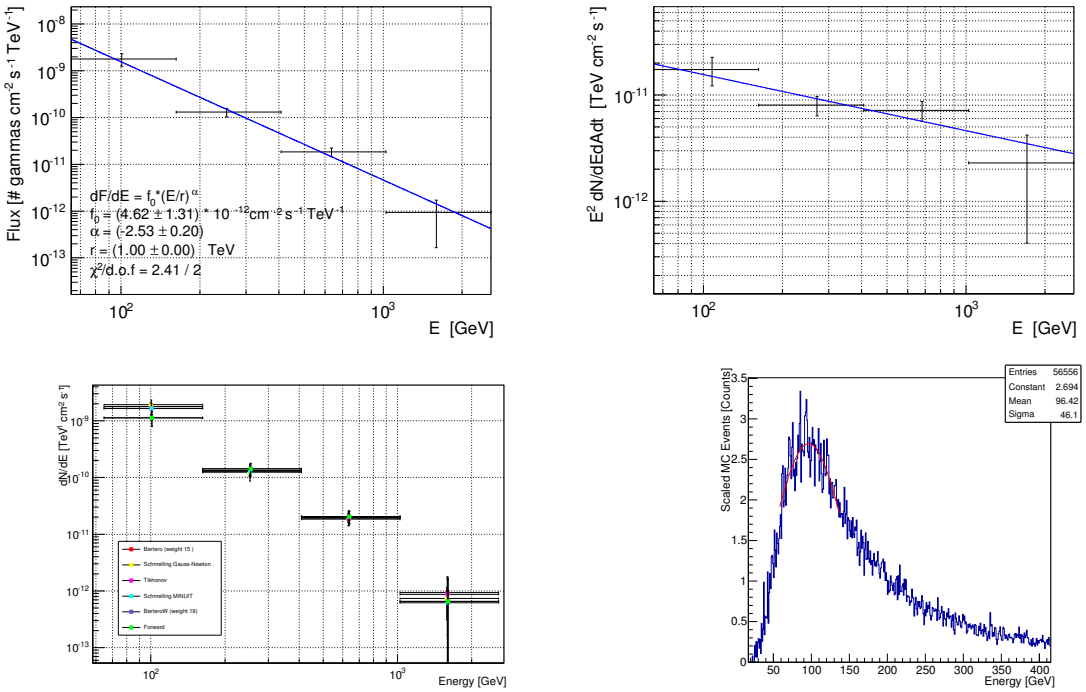

(a) 23-05-2011: Bertero unfolding results.

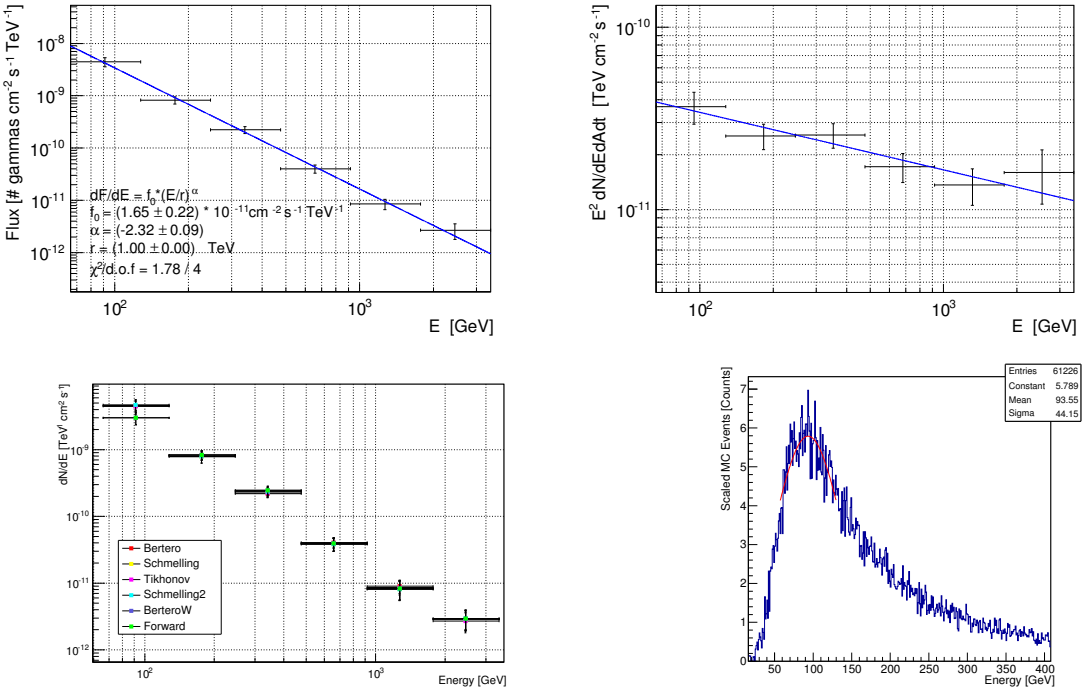

(b) 29-05-2011: Tikhonov unfolding results.

Figure 4.10: Same caption as Figure 4.8 for both (a), and (b).

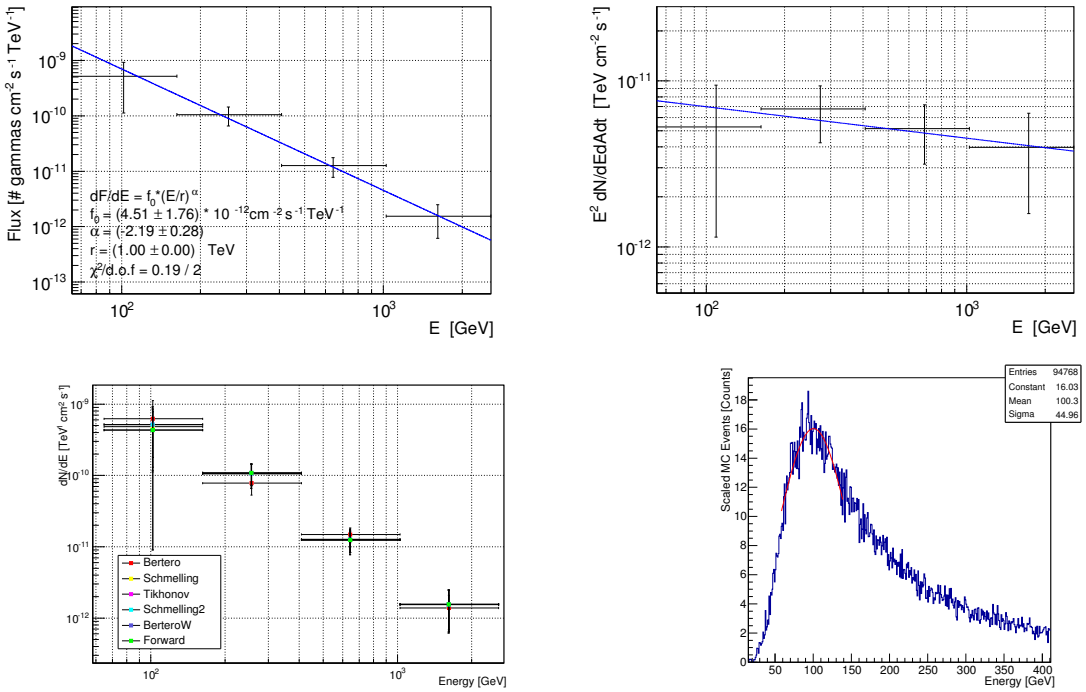

(a) 04-06-2011: Tikhonov unfolding results.

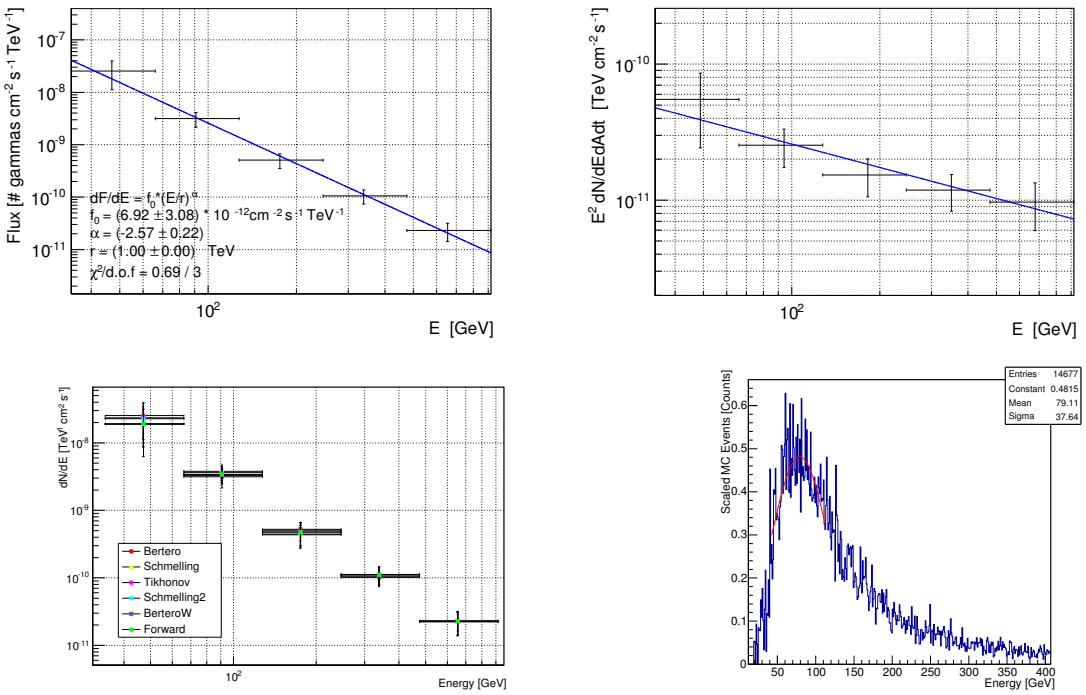

(b) 10-06-2011: Tikhonov unfolding results.

Figure 4.11: Same caption as Figure 4.8 for both (a), and (b).

Table 4.6: Markarian 501 fitted spectral parameters after the EBL-absorbtion correction.

Date	Unfolding	$f_0 \pm Err_{f_0}$ $[10^{-11}$ cm^{-2} s^{-2} TeV$^{-1}]$	$\alpha \pm Err_\alpha$
2011-03-30	Tikhonov	2.01 ± 0.37	2.22 ± 0.10
2011-05-08	Tikhonov	3.69 ± 0.30	2.04 ± 0.05
2011-05-14	Tikhonov	6.35 ± 0.28	1.90 ± 0.04
2011-05-23	Bertero	0.59 ± 0.17	2.39 ± 0.21
2011-05-29	Tikhonov	2.16 ± 0.29	2.18 ± 0.09
2011-06-04	Tikhonov	0.59 ± 0.42	2.05 ± 0.52
2011-06-10	Tikhonov	0.81 ± 0.36	2.50 ± 0.22

NOTES – Col.(1): observation date. Col.(2): adopted unfolding method. Col.(3) and Col(4): best-fit spectral parameters and related errors. The spectrum is described by an energy power law: $dF/dE = f_0\, E^{-\alpha}$.

reconstructed, I apply the systematic uncertainty estimated for the medium energy range (> 100 GeV), that amounts to $\sim 11\%$ of the total flux. This estimate is computed for the same offset that, however, can slightly change in time. For this reason another (smaller) uncertainty should be added due to run-to-run changes. To quantify this further systematic effect, a study on the Crab Nebula was performed [40]. The samples collect 40 minutes-bin data taken in November 2009 and January 2010. The systematic error - in reproducing the Crab Nebula's flux - was estimated $\sim 9\%$ within a few days, and $\sim 12\%$ within months. However, at the time of such a study, the intrinsic variability of the Crab Nebula had not yet been ascertained. For this reason, the run-to-run systematic uncertainty should be considered with caution and treated as an upper limit.

In the end, the total systematic uncertainty on MAGIC data is due to both the contributions mentioned above. These terms are independent from each other, hence they are added in quadrature, to a total systematic uncertainty $Err^2_{syst} = Flux^2(0.11^2 + 0.09^2) = Flux^2 \cdot 0.0202$.

Finally the total error, Err_{tot}, on the flux is given by the contribution of the systematic uncertaintes, Err_{syst}, and the statistical ones, Err_{stat}:

$$Err_{tot} = \sqrt{Err^2_{stat} + Err^2_{syst}}\ . \tag{4.1}$$

Considering that: (i) the Mkn501 analyses are performed daily, (ii) the run-to-run uncertaintes are just given as upper limits, and (iii) the study on this kind of systematic has been carried out on a source that shows an intrinsec variability, I consider adding a run-to-run systematics $\sim 9\%$ conservative enough. In addition, the statistical errors on MAGIC analyses are quite large, and even adding a run-to-run systematic $\sim 12\%$ do not weigh too much on the final error.

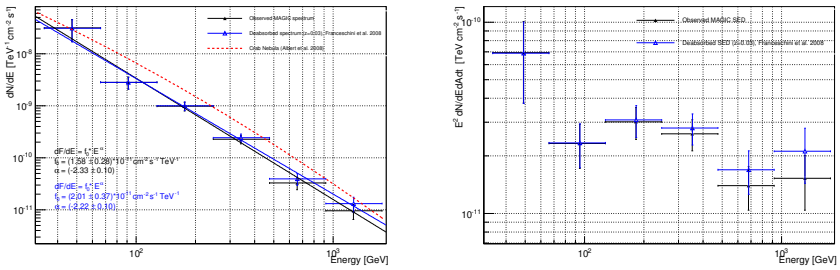

(a) Day 30-03-2011.

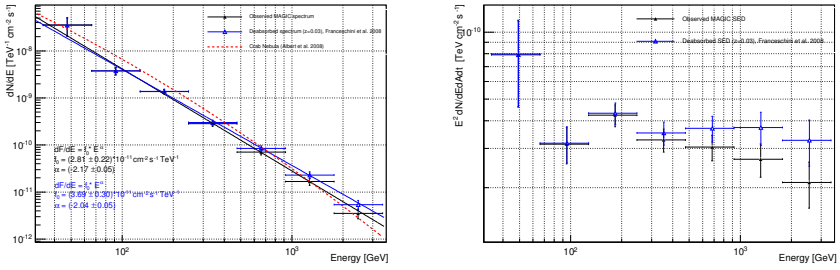

(b) Day 08-05-2011.

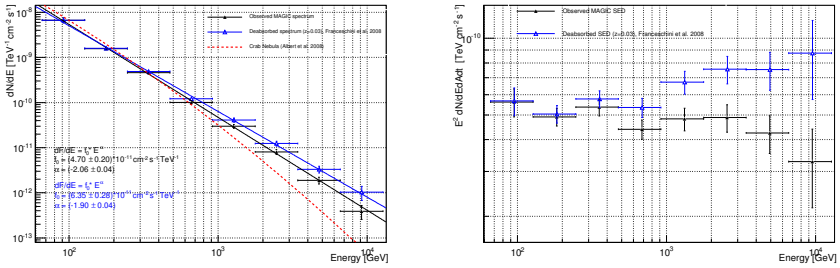

(c) Day 14-05-2011.

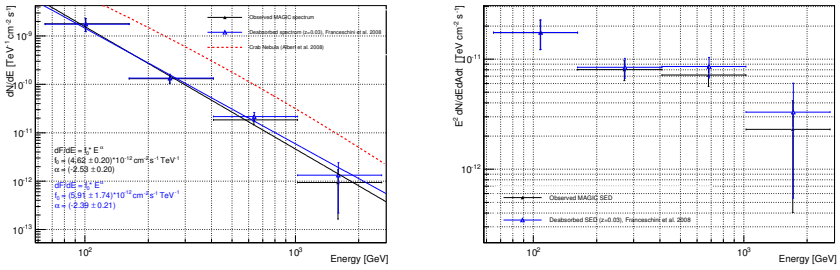

(d) Day 23-05-2011.

Figure 4.12: EBL corrections of MAGIC SEDs. Left panels: Markarian 501 observed (black) and EBL-corrected spectrum (blue). Crab spectrum (red dotted line) is reported as comparison. Right panels: Markarian 501 observed (black) and EBL-corrected (blue) SED. EBL-corrections are applied following the model described in [13], for $z = 0.03$.

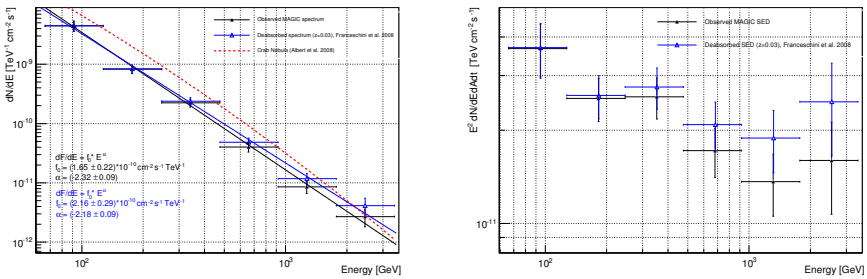

(a) Day 29-05-2011.

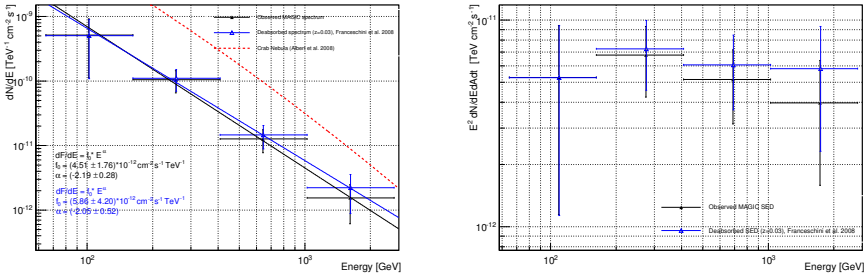

(b) Day -30-2011.

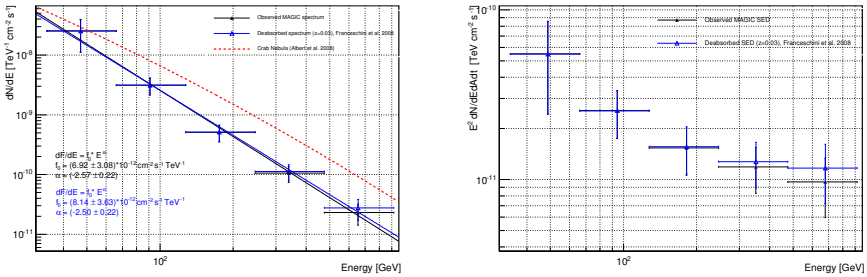

(c) Day 03-30-2011.

Figure 4.13: Same as Figure 4.12.

4.3 Fermi LAT Analysis

The *Fermi* Gamma-ray Space Telescope was designed to explore the sky in the energy range between $\sim$ 20 MeV and 300 GeV [91]. It has a wide field of view of 2.4 sr, and scans all the sky in less than 3 hours. It is equipped with two instruments: the Large Area Telescope (LAT) and the Gamma-ray Burst Monitor (GBM).

Fermi LAT is a pair conversion telescope, composed by a 4×4 array of identical towers, 40×40 cm^2 each. In turn, each tower is composed by a tracker, a calorimeter, and a data acquisition system. The traker is formed by alternating layers of tungsten conversion foils that converts the entering γ-rays into e^+ e^- pairs, and silicon strips able to track their paths. The γ-ray direction is reconstructed through the e^+ e^- paths that are, however, subjected to multiple scattering and limited by the tracker resolution. Finally, the pair members enter the calorimeter where they generate an electromagnetic shower that allows the energy of the γ-ray

to be reconstructed. The *Fermi* LAT is surrounded by an anti-coincidence layer to reject the most of the background events, i.e. all the other cosmic rays that exeed the γ-ray rate by a factor $10^2 - 10^5$. The typical trigger rate ranges from 10 kHz to $\sim$ 400 Hz per second, but only $\sim 2 - 5$ Hz γ-photons are of primary interest.

The *Fermi* GBM was designed to provide low-energy spectra and temporal measurements of GRBs, occuring inside the *Fermi* LAT field of view, and in the energy range from 10 keV to 25 MeV. It detects and localizes the burst allowing the *Fermi* LAT to be repointed better, and providing a fast notification to the ground in order to coordinate multi-frequency observations.

In what follows, the steps of the standard *Fermi* LAT likelihood analysis are described. For further details, see [92].

4.3.1 Maximum Likelihood Analysis

The likelihood analysis represents a common approach to estimate the parameters involved in many astrophysical phenomena [93]. This approach has been adopted also for the *Fermi* data analysis, as it had been done for its predecessor, the Energetic Gamma Ray Experiment Telescope (EGRET) [94]. The likelihood L is defined as the probability that the observed data can be obtained from a given model. So an input model is needed to describe the spatial distribution of the γ photons in the sky, the source spectrum, and the source position. Once a model has been chosen, its spectral parameters are changed in order to maximize the likelihood and find the best values of the model parameters. Maximizing the likelihood is equivalent to minimize the χ^2, since the latter corresponds to $-2\log(L)$.

All photons (i.e., counts) detected by the *Fermi* LAT are characterized by several variables, and for this reason divided and associated to different bins. The observed number of counts n - for each bin in a given interval time t - follows a Poisson distribution:

$$P(n) = e^{-\lambda}\frac{\lambda^n}{n!}$$

where λ is the average number of counts for an interval time t. Assuming that m_i is the expected number of counts in the i-bin, the probability p_i to detect n_i counts in that bin is given by:

$$P_i = m_i^{n_i}\,\frac{e^{-m_i}}{n_i!}\ .$$

Then, the likelihood is given by the product of the probability P_i computed for each bin:

$$L = \prod_i \frac{m_i^{n_i}}{n_i!}\,e^{-m_i}$$

where the first term depends from both model and data, and the last one only from the model. The sum of the expected counts over all bins corresponds to the total counts predicted from the model. Two different analyses can be performed: (i) the binned likelihood, with a finite size bin, and with a number of counts $n_i > 1$ for each bin; and (ii) the unbinned likelihood, with an infinitesimal size bin, with a number of counts $n_i = 0$ or $n_i = 1$ for each bin. The unbinned likelihood is more accurate than the binned one, but due to the computational effort, can be applied only for a reasonable number of counts. In this work, all *Fermi* analyses are performed by using an unbinned likelihood. Since $\prod_i e^{-m_i}$ corresponds to $e^{-\sum_i m_i} = e^{-N_{exp}}$

(where N_{exp} is the number of counts that the model predicts should have been detected), the likelihood can be written as:

$$L = e^{-N_{exp}} \prod_i m_i \tag{4.2}$$

where the index i is now referred to each count, and no more to each bin.

The standard *Fermi* LAT analysis is performed using the ScienceTools software package (version v10r0p5) available at the *Fermi* Science Support Center. The version of the data used in the following analyses is the PASS 8 [95]. Each PASS in the *Fermi* lifetime (from 6 to 8) refers to a whole package that includes the instrument simulations, the Instrument Response Functions (IRFs), the event reconstruction algorithm and others models and templates. The analysis step can be summurized as follows:

1. **download data**. Two files are needed to start the *Fermi* analyses: the event data file and the spacecraft file. They can be easily downloaded from the LAT Data Server, filling a simple query form.[7] The form has to be filled with the following information at least: (i) the source name; (ii) the coordinate system (J2000); (iii) the search radius (30°); (iv) the observation interval time; (v) the time system (Gregorian); (vi) and the LAT data type (photons);

2. **select the data**. As a first step, all the events in the event file are selected according to the source position, the interval time, the energy range, and the photon type. A further step takes into account the good interval time during which *Fermi* LAT was effectively taking data;

3. **make a live-time cube and an exposure map**. These quantities are necessary to performed the fit because they take into account the event reconstruction efficiency, which depends on the IRFs, position, and time that *Fermi* LAT spent observing the source. So, once a set of photons have been selected, both live-time cube and the exposure map are invariable. Since the likelihood analysis is an iterative procedure, it is worth precomputing them, to speed up the fitting process;

4. **create a source model**. All the sources within the selected area must be taken into account. In fact, due to the large PSF of *Fermi* LAT, their emission region can overlap with that of the interested source. In other words, the detected γ-rays are given by the sum of the central source emission and that coming from the nearby ones. Finally, also the diffuse γ-ray background has to be added to the model.

5. **compute the diffuse responses**. Determining the diffuse contribution - especially the Galactic and the extragalactic background - is computationally expansive because it requires an integration over the whole sky. For this reason it is computed before performing the fit.

6. **perform the likelohood fit**. The model is fitted to the data recurring to a maximun likelihood analysis. Among the resulting best-fit parameters there are: the fluxes, the flux errors, and the spectral indices of all the sources involved in the model.

[7] http://fermi.gsfc.nasa.gov/cgi-bin/ssc/LAT/LATDataQuery.cgi

Data Selection

The *Fermi* LAT space telescope continuously monitors the whole sky, unless special observations - called Target of Opportunities (ToOs) - are required. For this reason, to analyze a given source, a region of the sky around that source must be selected. The size of the selected region depends mainly on the PSF ($\sim 3.5^\circ$ at 100 MeV) and on the probability that nearby sources can contaminate the emission region of the analyzed one. Due to this contamination, also the nearby sources has to be modeled and taken into account. So, two different zones can be distinguished: a smaller one, the so-called *Region of Interest* (ROI), centered in the analyzed source's coordinates, and a larger one, the so-called *Source Region*, that takes into account also the emission of the nearby sources. According to the experience, for point-like source as Mkn501, the assumed values for the ROI is 20° and for the *Source Region* is ROI $+10^\circ$.

The analysis is performed on FITS files (Flexible Image Transport System), the standard digital format used for astronomical data. They contain multi-dimensional arrays and tables storing different information (such as spectra, images, data cubes) and a header with keywords providing immediate information about the data. The tool that deals with the data selection is *gtselect*.[8] It needs the event data file as input, containing information about each detected event such as time, energy, position, and quality of reconstruction. As first step of the analysis, this tool applies some cut to the events: (i) the event class, to select the most appropriate set of photons according to the source type and the event quality reconstruction (`evtclass=128` for point-like sources and `evttype=3` for photons converted both in the front and in the back section of the tracker; (ii) the time range, to select the analysis interval time; (iii) the energy range; and (iv) the maximum zenith angle (set to 100°), to avoid contamination by the atmospheric γ-rays coming from the Earth limb.

Another crucial information for data selection concerns the *Fermi* LAT's pointing and observing efficiency at the time of a detection. This information is contained in the spacecraft file, and is used by the tool *gtmktime*.[9] It makes a further time cut, starting from a list of Good Time Intervals (GTIs) where the *Fermi* data can be considered valid. The GTIs takes into account when *Fermi* LAT does not collect data, i.e. when it flies over the Southern Atlantic Anomaly, when it undergoes software updates, or when it is involved in special maneuvers. Moreover, *gtmktime* can exclude periods - through other filters - when the data quality is affected. The recommended filters are: (i) DATA_QUAL, an integer value set by the LAT instrument team, indicating the quality of data; and (ii) LAT_CONFIG, an integer value indicating the LAT configuration. The recommended filter for the standard analysis are DATA_QUAL>0 that includes both good and GPS 13 μs timing anomaly, and LAT_CONFIG$=1$ that refers to science configuration.

The Exposure Map

The exposure map is used to evaluate the expected number of photons - within the ROI - of the diffuse components in the source model. Due to the quite large PSF ($\sim 3.5^\circ$, 68% containment at 100 MeV), even sources lying out of the ROI can contribute with their counts in the same emission region of the interesting source, and must be taken into account. Such a map is computed by integrating the total instrument response functions (IRFs), that involve

[8] http://fermi.gsfc.nasa.gov/ssc/data/analysis/scitools/help/gtselect.txt
[9] http://fermi.gsfc.nasa.gov/ssc/data/analysis/scitools/help/gtmktime.txt

the effective area, the energy resolution, and the PSF, over the whole ROI.

The first step to generate the exposure map is to compute a live-time cube through the tool *gtltcube* [10] that takes into account the effective amount of time that *Fermi* spent in observing the source. Since the instrument response functions depends on the angle between the source direction and the *Fermi* LAT normal (the so-called inclination or off-axis angle), the number of detected counts depends on the time spent at different inclinations during the observation. These information are contained in the live-time cube, defined on a HEALPix (Hierarchical Equal Area isoLatitude Pixelization) grid[11] of a sphere, and it is a 3-D function of the sky position, the inclination angle, and the live-time (i.e., the time in which *Fermi* is actually taking data). The live-time cube is computed for the whole sky, and it not a continuous function of the abovementioned quantities, but it is provided by dividing the sky coordinates and the inclination angle in bins. The tool *gtltcube* uses the information contained in the spacecraft file and in the filtered event data file processed by the *gtmktime*. Other parameters that have to be specified are: (i) the bin size of the spatial grid, set to 1°; (ii) the inclination angle binning, defined in $\cos(\theta)$ steps, set to 0.025; and (iii) the maximum zenith angle over the livetimes are intgrated, set to 90°.

Once the live-time cube has been computed, the tool *gtexpmap*[12] generates the exposure map. The LAT exposure map is expressed by:

$$\epsilon(E,\hat{p}) = \int_{ROI} R(E',\hat{p}';E,\hat{p},t)dE'\,d\hat{p}'\,dt$$

where E' and $\hat{p}'$ are the measured event energy and direction respectively, and $R(E',\hat{p}';E,\hat{p},t)$ the total instrument response function that makes the exposure map photon-energy dependent. In other words the exposure map is the total exposure area multiplied by the effective observation time computed for a given region of the sky, whose photons contribute to produce counts inside the ROI. From the exposure map it is then possible to compute the number of predicted photons, N_{pred}, coming from the source:

$$N_{pred} = \int \epsilon(E,\hat{p})\,S_i(E,\hat{p})\,dE\,d\hat{p}$$

where $S_i(E,\hat{p})$ corresponds to the intensity of the source's photons. So, the counts detected by the *Fermi* LAT is given by the integral of the emitted flux and the exposure map.

The tool *gtexpmap* needs the filtered event data file, the spacecraft file, and the live-time cube as inputs. Further quantities have to be specified: (i) the IRFs package, `P8R2_SOURCE_V6`; (ii) the *Source Region* radius, set to 30°; (iii) the number of longitude points, set to the default value of 120 corresponding to half-degree pixels; (iv) the number of latitude points, set to the default value of 120 as for the longitude; and (v) the number of energy bands to be considered, set to the default value of 20.

The Source Model

As pointed out at the beginning of this section, the likelihood is defined as the probability that the observed data can be obtained from a given model. So, an XML-model has to be created to perform the analysis. Such a model contains both the best positions and the spectral

[10] http://fermi.gsfc.nasa.gov/ssc/data/analysis/scitools/help/gtltcube.txt
[11] http://healpix.jpl.nasa.gov/
[12] http://fermi.gsfc.nasa.gov/ssc/data/analysis/scitools/help/gtexpmap.txt

information of all the sources within the *Source Region*, and can be created by using the tool `make3FGLxml.py`[13]. It extracts from the third *Fermi* Gamma-ray LAT (3FGL) catalog [96] all the sources within the ROI+10°, and sets - for each of them - the proper spectral form and the best-fit parameters. There are two types of sources that can be included in the model: the point-like sources and the diffuse ones. Both are characterized by spectral and spatial components described by several parameters. Each parameter can be fixed or let vary in a specific range during the fitting process, depending on the source position and its significance within the *Source Region*. In generating the model, the following quantities are specified: (i) `radLim`= 5°, the radius (from the center of ROI) beyond which the source parameters are fixed to the catalog value; (ii) `maxRad`= 10° combined with `varFree`, radius out to wich the normalization is set free only for variable sources; (iii) `ExtraRad`= 10°, the radius beyond the ROI out to which the sources are included with fixed parameters; (iv) `sigFree`= 5, the significance below which source parameters are fixed; and (v) `family psForce`=False, used to force the extended source to behave as point-like ones.

Several spectral models are available to describe the emission of the point-like sources.[14] Mrk501 is modeled by using a simple power low function (`PowerLow2`), defined between two energies as:

$$\frac{dN}{dE} = \frac{N(\alpha+1)\,E^{\alpha}}{E_{max}^{\alpha+1} - E_{min}^{\alpha+1}}$$

where N is the integrated flux (free parameter), α is the spectral index (free parameters), and E_{min}, E_{max} are the minimum and maximum energy respectively (fixed parameters). Moreover, a spatial model, called `SkyDirFunction` is added. It describes the source direction in the sky and it is used only for the point-like sources.

As last step, the background emission has to be added. There are two types of background: the galactic and the extragalactic one; both are treated as diffuse sources. To calculate the galactic diffuse emission, firstly, the HI and the CO spectral lines are used to map the interstellar gas distribution; then the diffuse γ-ray emission of these regions is computed by fitting the γ-ray emissivity in different energy bands. It is described by a power law spectrum:

$$\frac{dN}{dE} = N_0 \frac{E}{E_0}^{\alpha}$$

where N_0 is the prefactor, α is the spectral index and E_0 is the energy scale. The spatial model is described by a function of the sky coordinates and of the energy, called `MapCubeFunction` that allows a spectral variation as a function of sky coordinates.

Finally the extragalactic background emission has to be added. This consists in an isotropic emission that takes into account the extragalactic γ-ray emission beyond a galactic longitude of 30°, and all the residual cosmic-ray emission. The spectrum model is given by an isotropic spectral template containing -for each energy band - the central energy value, the differential flux in that band, and its related uncertainty. The spatial model, called `ConstantValue`, returns a fixed value for each sky position[15].

[13] http://fermi.gsfc.nasa.gov/ssc/data/analysis/user/readme_make3FGLxml.txt

[14] http://fermi.gsfc.nasa.gov/ssc/data/analysis/scitools/source_models.html

[15] For the PASS8 data, the spatial model `gll_iem_v06.fits` for the galactic diffuse emission, and the isotropic template `iso_P8R2_SOURCE_V6_v06.txt` for the extragalactic emission are used. Both are availabe from the web page http://fermi.gsfc.nasa.gov/ssc/data/access/lat/BackgroundModels.html

The Diffuse Source Responce

The distribution of the expected photons - used to perform the likelihood analysis - is given by the convolution of the spectral model with the IRFs. This convolution is computed by integrating the source model with the instrument response evaluated at the observed photon direction, energy and arrival time. Since such an integral for both galactic and extragalactic diffuse component is computationally expensive - because it is done over the whole sky - it is performed before starting the likelihood analysis. This is precomputed by the tool *gtdiffrsp*,[16] that adds to the filtered event data file the contribution due to all the diffuse sources incorporated in the XML-model file. As inputs it needs: (i) the filtered event data file; (ii) the spacecraft file; (iii) the source model previously generated as an XML file; and (iv) the IRFs (`P8R2_SOURCE_V6`).

The Unbinned Likelihood Analysis

The unbinned likelihhod analysis is computed by the tool *gtlike*[17] that returns the best-fit parameters of the input source model. For the model fitting, to maximize the logarithm of the likelihood function (Eq. 4.2), the `NEWMINUIT` optimization algorithm is adopted. It uses only the `MIGRAD` and `HESSE` algorithms from `MINUIT`. To perform the fit, *gtlike* requires (i) the filtered event data file, (ii) the spacecraft file, (iii) the exposure map, (iv) the live-time cube, (v) the source XML-model, and (vi) the response function `P8R2_SOURCE_V6`, then it returns the best-fit parameters and the related Test Statistic (TS) value for each source included in the model. The TS is estimated through the likelihood ratio test [94], and its natural logarithm is defined as $-2(\ln(L_0) - \ln(L_1))$, where L_0 and L_1 are the null hypotesis (i.e., no point source is present) and the alternative hypothesis (i.e., the point source is present), respectively. The TS is directly linked to the significance of a detection, that can be estimated as approximately $\sqrt{TS}$.

4.3.2 Results

In this section I present the results of the standard *Fermi* LAT analysis of Mkn501. Starting from the MAGIC data, I obtained seven corresponding *Fermi* SEDs. Since Mkn501 is fainter in the *Fermi* energy range than in the MAGIC one, the signal must be integrated over many days to obtain significative spectral points. On the other hand, since blazars are variable sources, the requirement of having simultaneous multi-frequency data must be also satisfied. So, a compromise must be achieved. Considering that the closest MAGIC observations are 6 days apart from each other, and in order to guarantee the indipendence of each dataset, I integrate in this time interval.[18] With such an integration time, one or two spectral points can be obtained with a significance > 25. To evaluate the trend of Mkn501 activity state in the *Fermi* energy band - during the MAGIC observation period - I produce a 6 days-bin light curve (Fig. 4.14). It is obtained by performing - for each time bin - a likelihood analysis (Sect. 4.3.1). It shows no evidence of extra activity in the *Fermi* band. The trend is quite flat and almost all points are compatible to one another within the error bars: the flux ranges between ~ 0.3 and $\sim 1.4 \times 10^{-7}$ photons cm^{-2} s^{-1} that, for a variable source as Mkn501, can be considered a normal fluctuation of the quiet state. In literature, longer integration

[16] http://fermi.gsfc.nasa.gov/ssc/data/analysis/scitools/help/gtdiffrsp.txt
[17] http://fermi.gsfc.nasa.gov/ssc/data/analysis/scitools/help/gtlike.txt
[18] Except for 30-03-2011 that allows a longer integration period.

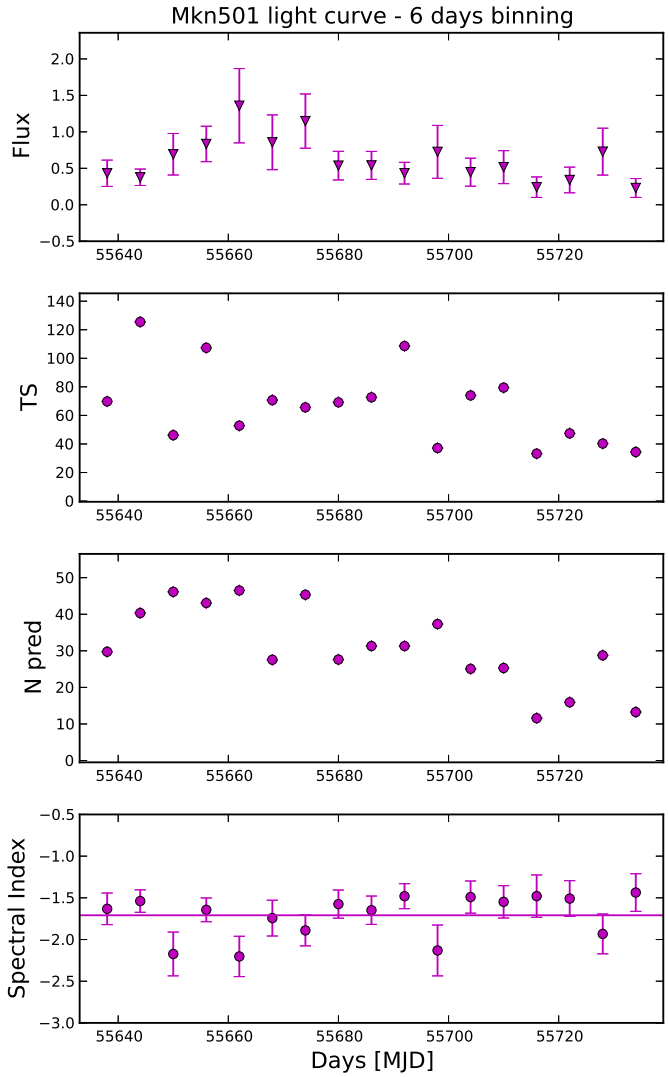

Figure 4.14: Mkn501 *Fermi* 6 days-bin light curve, from 15-03-2011, 00:00 to 25-06-2011, 00:00. In panels from top to bottom are shown (i) the flux expressed in number of photons cm^{-2} s^{-1}; (ii) the Test Statistic of the likelihood analyses; (iii) the total number of counts predicted by the model; and (iv) the spectral index. Bin number 2, 3, 4 and 6 are affected by low statistic due to the ToO observations.

periods (from 7 days up to 30) have been adopted for Mkn501 SED modeling [97] [98]; so an integration time of 6 days can be considered conservative enough.

During the MAGIC observation period of Mkn501, *Fermi* LAT dealt with two ToOs:[19]

1. CYG X-3 (RA= 308.1100°, Dec= +30.9800°), starting from 2011-03-24 around 15:32:58, for ∼5.8 days (500 ks);

2. Crab Nebula (RA= 86.6330°, Dec= +12.0140°), starting from 2011-04-12 around 15:49:43, for ∼3.5 days (300 ks).

[19]http://fermi.gsfc.nasa.gov/ssc/observations/timeline/too/

Considering that the coordinates of Mkn501 are RA= 253.468° and Dec= +39.7602°, during the Crab Nebula ToO it is placed at the very edge of the field of view. The *Fermi* field of view has an useful response out to $\sim 60°$ from the instrument axis, however it gets worse for higher inclination angles. On the contrary, during the CYG X-3 ToO, Mkn501 is out of the *Fermi* field of view. These ToO observations must be taken into account when inspecting the light curves, because they are responsible for the lack of statistics in some bins, that leads to a decrease of the significance and to an increase of the uncertainties on the flux and the spectral index.

The treatment for day 30-03-2001 is slightly different. Since the gap between it and the successive MAGIC observation (08-05-2011) is quite wide, the constraint on the integration time can be relaxed. However, to justify this way to proceed, the source must show the same activity in the whole integration period. To verify the latter condition, I produced and checked a 5 days-bin light curve, reported in Figure 4.15. Also in this case, almost all points are compatible to one another within the error bars, and the source can be consider to be in an approximately constant state.

Spectral Energy Distribution

In order to obtain the spectral points the energy range have to be divided into bins, and for each of them an unbinned likelihood analysis (Sect. 4.3.1) is performed. Once the data have been selected and filtered, the tool `likeSED.py`[20] can be used to generate the spectral points. It needs the products of the likelihood analysis (i.e., an object containing the filtered event file, the spacecraft file, the live-time cube, the exposure map, and the IRFs `P8R2_SOURCE_V6`), the source name, and the number of energy bins as inputs. Also the source XML-model needed to perform the fit, and the optimizer (`NEWMINUIT`) have to be specified. In the following analyses the energy range is selected according to the minimum and maximum photon energies, found by inspecting the event data files, once they have been filtered by the tools *gtselect* and *gtmktime*. The central energy point of each bin is estabilished by weighing the number of counts according to their energy. At last, an upper limit is calculated for that bins whose TS < 9 (that corresponds to a significance detection of 3σ).

Once the likelihood analyses have been performed for each bin, the spectral points are finally placed over a butterfly plot (calculated by the tool `likeSED.py` as well) that identifies the 1σ contour lines of the nominal fit. To generate the butterfly plot, the following quatities are required: the differential flux, the pivot energy E_0 (i.e., the energy at which the error in the differential photon flux is minimal), the spectral index γ, and the related errors. The differential flux is given by:

$$F(E) = N_0 \left(\frac{E}{E_0}\right)^{-\gamma} .$$

The pivot energy, also called decorrelation energy, is calculated through the following formula:

$$\log E_0 = \frac{\log E_1 - \epsilon \log E_2}{1-\epsilon} - \frac{1}{1+\gamma} - \frac{cov_{I,\gamma}}{I\, cov_{\gamma\gamma}}$$

where E_1 and E_2 are the lower and the upper limit respectively of Mkn501 spectral model, ϵ is equal to $(E_2/E_1)^{(\gamma+1)}$, I is the integral flux, and the suffix *cov* refers to the elements of the covariance matrix. The prefactor N_0 of the differential flux is given by:

[20] Available at http://fermi.gsfc.nasa.gov/ssc/data/analysis/user/

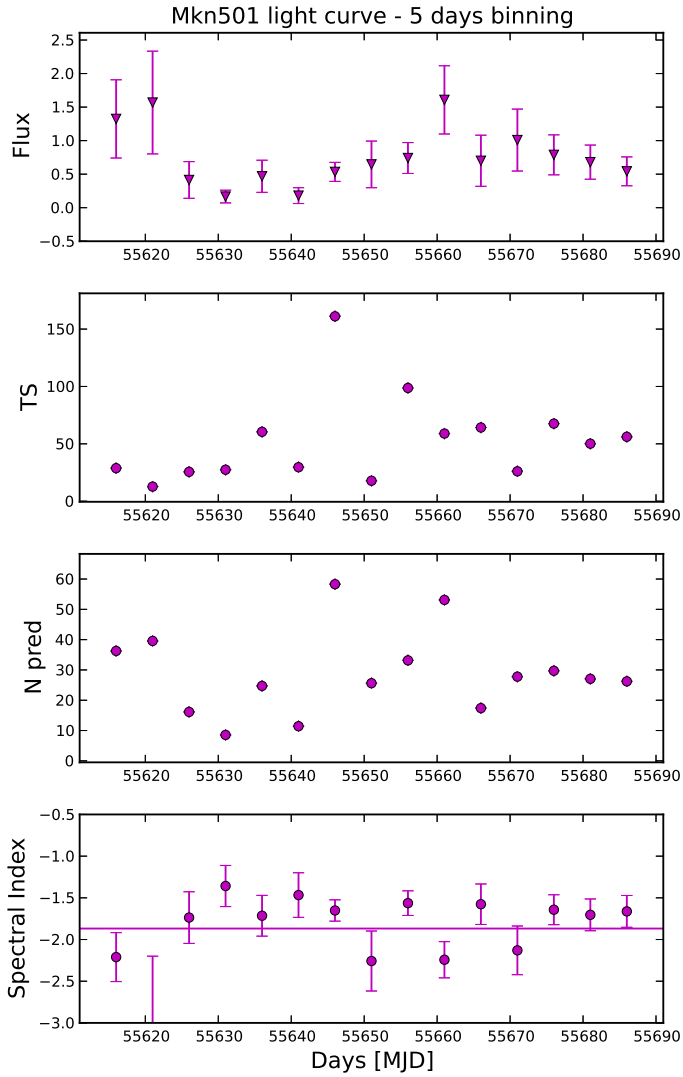

Figure 4.15: Mkn501 *Fermi* 6 days-bin light curve, centered on 30-03-2011. It is obtained for a period 70 days long, from 21-02-2011, 12:00 to 07-05-2011, 12:00. Panels are the same as Figure 4.14. Bin number 7, 8, 10 and 11 are affected by low statistic due to the ToO observations.

$$N_0 = \frac{I(\gamma - 1)}{E_0 \left[\left(\frac{E_1}{E_0} \right)^{1-\gamma} - \left(\frac{E_2}{E_0} \right)^{1-\gamma} \right]} .$$

The related error on the differential flux is given by:

$$\Delta F(E) = F(E) \sqrt{\frac{N_{0\,Err}^2}{N_0^2} + \log^2 \left(\frac{E}{E_0} \right) \sigma_\gamma^2}$$

where $\sigma_\gamma = cov_{\gamma\gamma}$ is the error on the spectral index obtained from the covariance matrix, and

the error on N_0 is expressed by:

$$N_{0\,Err} = \frac{N_0}{I}\sqrt{cov_{II}}\sqrt{1 - \frac{cov_{I\gamma}^2}{cov_{II}cov_{\gamma\gamma}}}\ .$$

Finally, the quatities that identify the butterfly contours lines $F(E) \pm \Delta F(E)$ - multiplied by E^2 - are computed. In Figures 4.16 and 4.17 are shown the results of the seven *Fermi* analyses, performed with the aim to add simultaneous spectral points to the MAGIC SEDs (Sect. 4.2). Up to this step of the analysis chain, only the statistic errors have been taken into account.

Systematic uncertaintes

The best-fit parameters resulting from the likelihood analysis do not include the systematic errors. In order to compare these results with those obtained from different instruments, and to use them for the SED modelling, they have to be added. In fact, the obtained source flux is subject to variations up to 10% (especially at the beginning of the mission) due to the dependence of the detection efficiency on the amount of the particle background.[21] Ultimately, the systematic uncertaintes on the flux is estimated $\sim 5\%$ at 560 MeV, and $< 10\%$ above 10 GeV. To be conservative, a systematic error of $\sim 10\%$ is added at energy > 10 GeV. The systematic errors and the statistical ones are added in quadrature.

4.4 Swift UVOT and XRT data

The *Swift* Gamma Ray Burst Explorer [99] is a multi-frequency space observatory mainly dedicated to the study of the GRBs. It is equipped with three instruments: (i) the Burst Alert Telescope (BAT), to provide GRB triggerS; (ii) the X-ray Telescope (XRT), to determine fluxes, spectra and light curves of GRBs and their afterglows; and (iii) the UV/Optical Telescope (UVOT), to provide low resolution spectra and UV/visible photometry of several sources. Even if *Swift* has been designed mainly for GRBs science, it includes additional goals such as to provide the most sensitive hard X-ray survey (that contributed to discover more than 400 AGNs, and several Seyfert 2 galaxies), to widen the studies on Supernovae, and to give a crucial contribute to the AGNs multi-frequency campaigns.

Swift XRT is a focusing X-ray telescope, that covers the energy range between 0.2 and 10 KeV. It has an effective area of 110 cm^2, a field of view of $23^{'}$ and a PSF of $18^{''}$ half-energy width. It can operate in three different readout modes: (i) the *imaging* mode, to obtain integrated images only and to achieve spatial information of bright sources, characterized by a flux $\geq 7 \times 10^{-7}$ erg cm^{-2} s^{-1}; (ii) the *windowed timing* mode, dedicated to high time resolution and bright spectroscopy of sources characterized by a flux $\leq 10^{-7}$ erg cm^{-2} s^{-1} - ; and (iii) the *photon counting* mode, to obtain spectra and spatial information for sources characterized by lower fluxes, ranging from 2×10^{-14} to 2×10^{-11} erg cm^{-2} s^{-1}.

Swift UVOT is a modified Ritchey-Chrétien 30 cm diameter telescope - co-aligned with XRT - designed to provides low-resolution spectra of GRBs and UV/visible photometry. It has a field of view of $17^{''} \times 17^{''}$, and a PSF of $0.9^{''}$ FWHM at 350 nm. It carries two detectors, each equipped with two grism - $\sim$ 1 nm pixel^{-1} resolution - optimized for UV and visible

[21] http://fermi.gsfc.nasa.gov/ssc/data/analysis/LAT_caveats.html

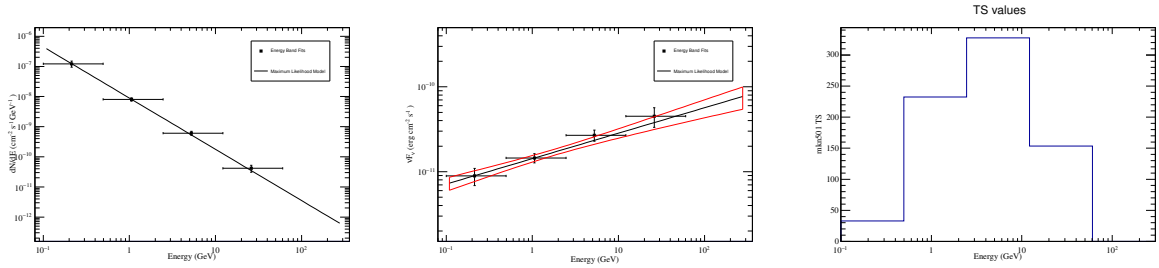

(a) 30-03-2011. Integration time: 72 days. 4 energy bins.

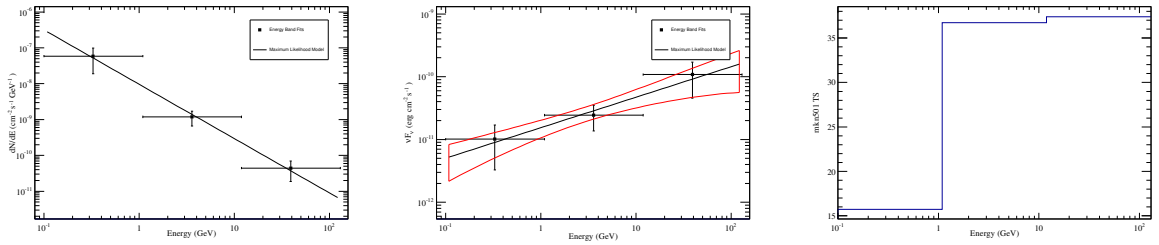

(b) 08-05-2011. Integration time: 6 days. 3 energy bins.

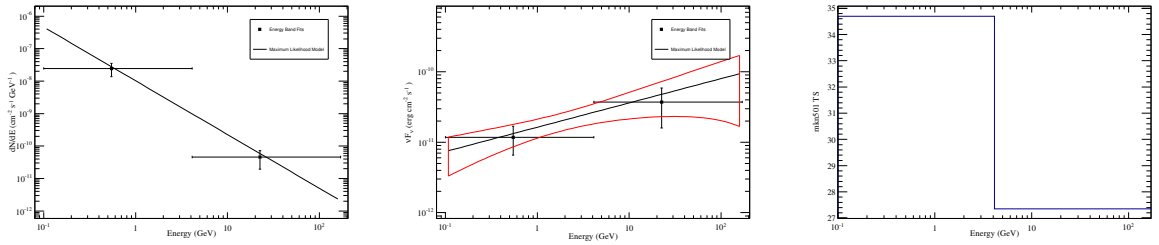

(c) 14-05-2011. Integration time: 6 days. 2 energy bins.

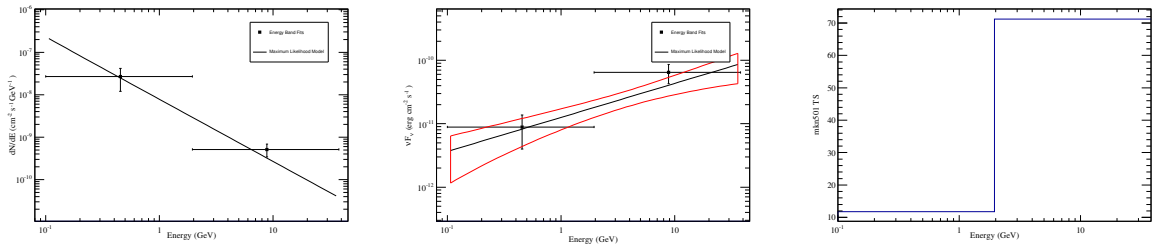

(d) 23-05-2011. Integration time: 6 days. 3 energy bins.

Figure 4.16: Fermi analysis results. Left panels: fitted energy spectrum. Central panels: spectral energy distribution; the red lines (butterfly plot) identify the 1σ contours of the nominal fit (black line). Right panels: Test Statistic value of the likelihood analysis of each energy bin.

band respectively. It has three optical filters, U (3501 Å), B (4329 Å), and V (5402 Å), plus three broadband UV filters, UVW2, UVM2, and UVW1 centered respectively on 2030, 2231, and 2634 Å.

The *Swift* satellite observed Mkn501 57 times between 2011 March 3 and 2011 December

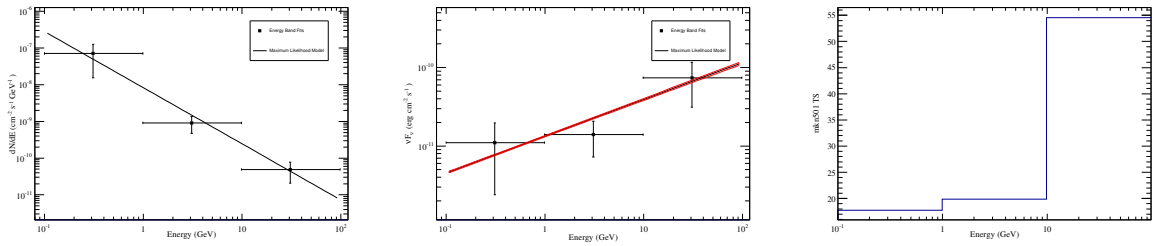

(a) 29-05-2011. Integration time: 6 days. 3 energy bins.

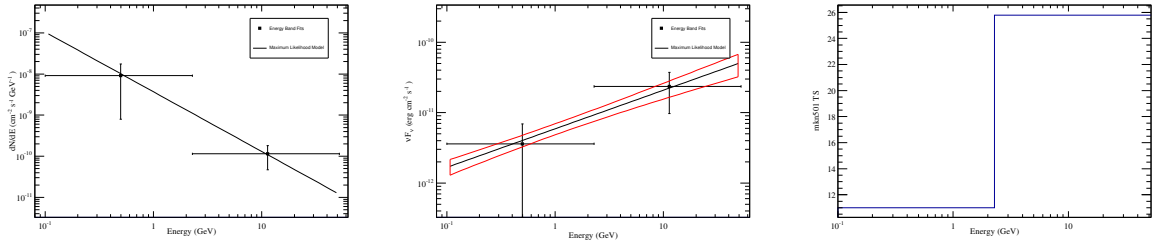

(b) 04-06-2011. Integration time: 6 days. 2 energy bins.

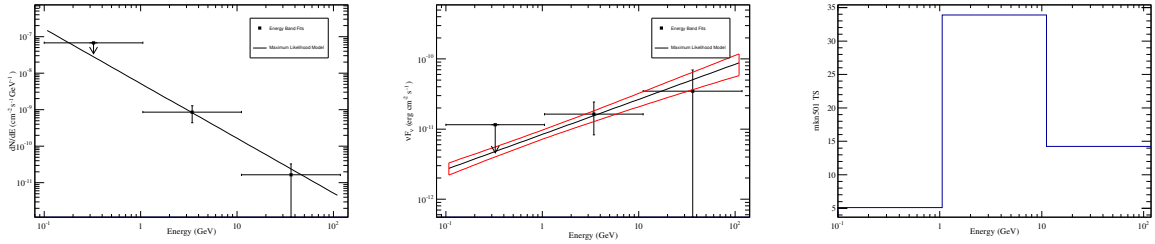

(c) 10-06-2011. Integration time: 6 days. 3 energy bins.

Figure 4.17: Same as Figure 4.16.

27 in *windowed timing* mode, providing both X-ray and UV data. The *Swift* XRT analysis was carried out by Matteo Perri from the ASI Science Data Center (ASDC) in Rome.[22] The datasets are processed with the XRTDAS software package (version 3.1.1) developed at ASDC and distributed by HEASARC within the HEASoft package (version 6.17). Event files are calibrated and cleaned with standard filtering criteria with the *xrtpipeline* task using the calibration files available in the *Swift* XRT CALDB (version 20150721). Events for the spectral analysis are selected within a circle of 20 pixels-radius (corresponding to ~ 47 arcsec, i.e., $\sim 95\%$ of the PSF) centered on the source position. The background is estimated from a nearby circular region of 40 pixel-radius. The source spectrum is binned to ensure at least 20 counts per bin, in order to use the χ^2-minimization fitting technique. The ancillary response files (ARFs) are generated by the *xrtmkarf* task, using the cumulative exposure map to apply corrections due to PSF losses, and CCD defects. The *Swift* XRT average spectrum in the 0.3-10 keV energy range is fitted using the XSPEC package. The adopted model is a log-parabolic one [100], and spectra are corrected by assuming an absorption hydrogen-equivalent column density of 1.56×10^{20} cm^{-2} [101] fixed to the Galactic 21 cm value in the direction of

[22] http://www.asdc.asi.it

Mkn501. Finally, the systematic uncertainty on flux is estimated $\sim 3\%$ in the $0.3 - 10$ keV energy range.[23]

The *Swift* UVOT analysis was carried out by Francesco Verrecchia - with the collaboration of Cristina Leto - also from ASDC in Rome. Data are processed by using the standard UVOT software distributed within the HEAsoft package (version 6.16) and the calibration pipeline described in [102] (calibration files are available in the *Swift* XRT CALDB, version 20111031). For each filter observation, an aperture photometry was performed with a standard aperture $5''$ radius, centered on the source position. The background estimate is performed within an anular region with a $26''$ of minimum radius, and a size of $8''$. The flux values are corrected for Galactic extintion, by dereddening the magnitudes using the mean interstellar extinction $E(B-V) = 0.0165$ [103]. Finally, fluxes are converted in mJy according to the CALDB conversion factors for each effective filter wavelength. The systematic uncertaintes evaluation is already included in the calibration process [104].

La valutazione dei sistematici Ã¨ inclusa nelle calibrazioni (Breeveld et al 2011) e opzionalmente sommabile in quadratura dal sw ufficiale, cosa che noi in genere attiviamo sempre

Starting from the obtained MAGIC SEDs (Tab. 4.6), I select the most simultaneous as possible available *Swift* data (see Table 4.18; UVOT and XRT data were taken at the same time). Figure 4.18 shows the Mkn501 UVOT light curve for the whole observation period.

Table 4.7: *Swift* UVOT and XRT data, selected basing on the available MAGIC data.

MAGIC		*Swift*		*Swift* exposure time
date	MJD	date	MJD	[s]
30-03-2011	55650	02-04-2011	55653.51	508.9
08-05-2011	55689	08-05-2011	55689.03	1114.1
14-05-2011	55695	15-05-2011	55696.53	918.0
23-05-2011	55704	22-05-2011	55703.96	1304.7
29-05-2011	55710	28-05-2011	55709.98	796.3
04-06-2011	55716	03-06-2011	55715.94	936.2
10-06-2011	55722	10-06-2011	55722.02	1150.1

4.5 Multi-frequency Datasets

Starting from the available MAGIC data, I collected seven datasets. I built each dataset as follows:

- by collecting data coming from four different instruments: *Swift* UVOT data in the optical band, *Swift* XRT data in the X-ray band, *Fermi* LAT data in the HE band, and MAGIC data in the VHE band;

- by choosing data as close to simultaneous as possible. Since Mkn501 is a variable source data must be taken when the source persists in the same activity state. Both

[23] http://heasarc.gsfc.nasa.gov/docs/heasarc/caldb/swift/docs/xrt/SWIFT-XRT-CALDB-09_v8.pdf.

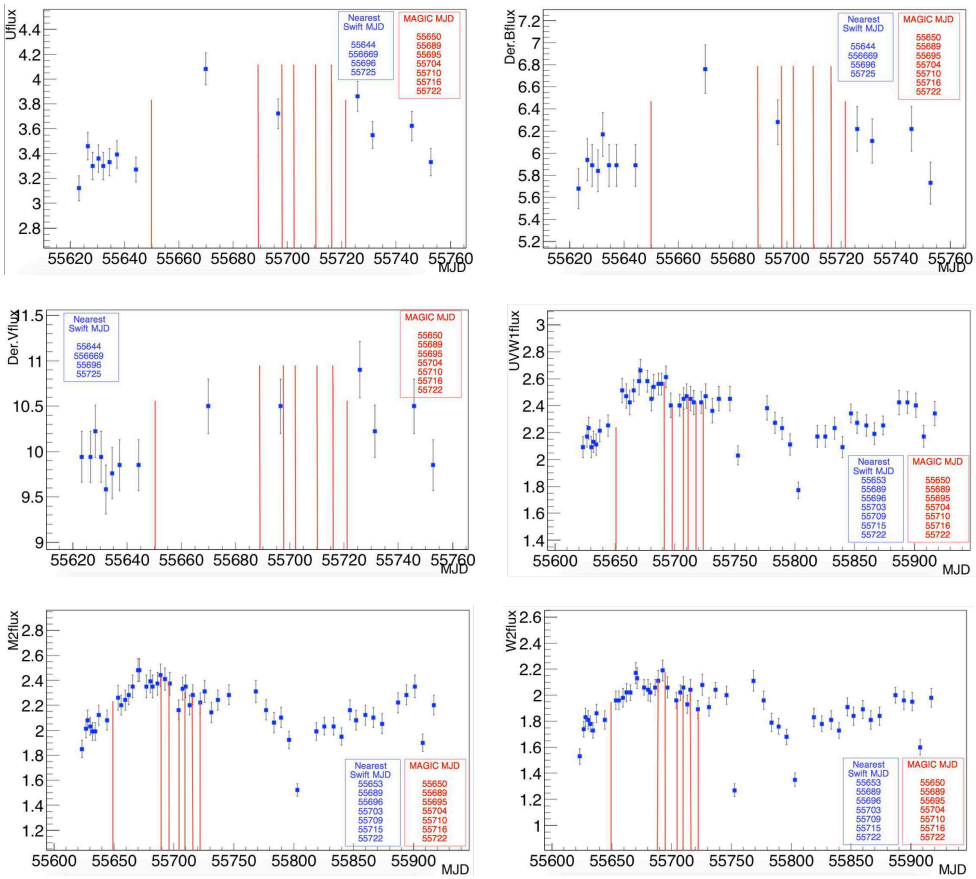

Figure 4.18: *Swift* UVOT light curve for each observation filter, obtained for the whole Mkn501 observation period (*Credits*: Francesco Verrecchia). Fluxes are expressed in mJy. In the red table, days in which the MAGIC SEDs are available are listed. The corresponding red lines are placed in the plot. The blue table resumes the selected *Swift* observations that contribute to the simultaneous dataset.

Swift UVOT and XRT data are taken with a maximum delay of three days from the MAGIC observation date, while Fermi data must be integrated over a longer period - centered on the MAGIC observation date - to obtained significantive spectral points;

- by performing the analyses of MAGIC and *Fermi* LAT data. *Swift* UVOT analyses were carried out by Matteo Perri from ASDC, and *Swift* XRT analyses by Francesco Verrecchia and Cristina Leto, also from ADSC;

- by applying the EBL correction to the MAGIC data, following the model proposed in [13];

- by adding the systematic errors to compare data coming from different instruments and for the SED modeling. The analysis chain of *Swift* UVOT data returns a flux uncertainty already including the systematic one. For *Swift* XRT a systematic of 3% is added to the spectral points. For *Fermi* LAT the systematic uncertainty amounts to 5% and 10% for energies below and above 10 GeV, respectively.

In the following the seven datasets are presented (Figures 4.19-4.21). Each dataset is labeled with the corresponding MAGIC observation date. All information is reported in Tables 4.8.

Table 4.8: 30-03-2011 Mkn 501 multi-frequency dataset.

Instrument	MJD	Obs. time	Log (ν) [Hz]	Log [νF_ν] [$erg\,cm^{-2}\,s^{-1}$]	Err_{flux} [$erg\,cm^{-2}\,s^{-1}$]	Syst. Error [% Flux]
30-03-2011						
Swift UVOT	55653.515	508.9 s	15.05622	-10.55997	1.435619	$< 3\%$
			15.16932	-10.53842	1.550969	$< 3\%$
Swift XRT	55653.515	508.9 s	17.07061	-10.27735	3.309581	3%
			17.20845	-10.28635	3.218255	3%
			17.34630	-10.24792	2.725364	3%
			17.48414	-10.29711	2.673840	3%
			17.62199	-10.26654	2.982234	3%
			17.75983	-10.25644	3.733632	3%
			17.89767	-10.17238	4.090391	3%
			18.03552	-10.26765	5.278190	3%
Fermi LAT	55650.0	72 days	22.71286	-11.04998	0.1015842	5%
			23.40828	-10.83835	0.05861443	5%
			24.10370	-10.57038	0.06878239	5%
			24.79912	-10.34638	0.1206372	10%
MAGIC	55650.215	4098 s	25.35934	-10.42932	0.1280867	$\sim 20\%$
			25.64505	-10.31676	0.1028164	$\sim 20\%$
			25.93077	-10.37938	0.1011469	$\sim 20\%$
			26.21648	-10.65013	0.1268431	$\sim 20\%$
			26.50219	-10.61195	0.1505809	$\sim 20\%$
08-05-2011						
Swift UVOT	55689.031	1114.1 s	15.05622	-10.53554	0.01357115	$< 3\%$
			15.12833	-10.48428	0.01601815	$< 3\%$
			15.16932	-10.50640	0.01646516	$< 3\%$
Swift XRT	55689.032	1114.1 s	17.07061	-10.27226	0.02230233	3%
			17.20845	-10.21916	0.02125442	3%
			17.34630	-10.20336	0.01869123	3%
			17.48414	-10.18745	0.01780188	3%
			17.62199	-10.16623	0.01960801	3%
			17.75983	-10.15266	0.02318843	3%
			17.89767	-10.12991	0.02476161	3%
			18.03552	-10.16270	0.02829916	3%
			1.817336	-10.14751	0.04049370	3%
Fermi LAT	55689.0	6 days	22.89971	-10.99395	0.2889697	5%
			23.93767	-10.61231	0.1902776	5%
			24.97564	-99.65525	0.2515133	10%
MAGIC	55689.063	5322 s	25.36159	-10.29430	0.1008982	$\sim 20\%$
			25.64731	-10.15934	0.07836393	$\sim 20\%$
			25.93302	-10.24796	0.08030527	$\sim 20\%$
			26.21873	-10.22778	0.08407425	$\sim 20\%$
			26.50445	-10.22363	0.09613797	$\sim 20\%$
			2.679016	-1.028165	0.1185553	$\sim 20\%$
14-05-2011						
Swift UVOT	55696.533	918.0 s	15.05622	-1.056357	0.01628509	$< 3\%$
			15.12833	-1.049692	0.01649120	$< 3\%$
			15.16932	-1.051681	0.01686475	$< 3\%$
Swift XRT	55696.530	918.0 s	1.707061	-10.27607	0.02342740	3%
			1.720845	-10.22982	0.02295199	3%

Table 4.8: 30-03-2011 Mkn 501 multi-frequency dataset.

			1.734630	-10.22967	0.02006797	3%
			1.748414	-10.18352	0.01876579	3%
			1.762199	-10.15625	0.02063451	3%
			1.775983	-10.14350	0.02471626	3%
			1.789767	-1.0.10860	0.02628300	3%
			1.803552	-10.06677	0.02805118	3%
			1.817336	-10.12173	0.04289589	3%
Fermi LAT	55695.0	6 days	23.12116	-1.092987	0.1907070	5%
			24.7363	-1.042869	0.2495010	10%
MAGIC	55695.188	5294 s	25.36271	-10.04135	0.0820045	$\sim$ 20%
			25.64843	-10.09275	0.07062068	$\sim$ 20%
			25.93414	-10.03324	0.07001625	$\sim$ 20%
			26.21985	-10.06720	0.07229257	$\sim$ 20%
			26.50557	-9.967380	0.07594452	$\sim$ 20%
			26.79128	-9.916887	0.08170383	$\sim$ 20%
			27.07700	-9.918296	0.09603239	$\sim$ 20%
			27.36271	-9.853484	0.1603510	$\sim$ 20%
23-05-2011						
Swift UVOT	55703.960	1304.7 s	15.05622	-10.56357	0.01447581	$<$ 3%
			15.12833	-10.53721	0.01608406	$<$ 3%
			15.16932	-10.53842	0.01329421	$<$ 3%
Swift XRT	55703.960	1304.7 s	1.707061	-10.35182	0.02388077	3%
			1.720845	-10.32985	0.02345762	3%
			1.734630	-10.32403	0.02028162	3%
			1.748414	-10.28757	0.01899046	3%
			1.762199	-10.26528	0.02115149	3%
			1.775983	-10.31546	0.02642840	3%
			1.789767	-10.27966	0.02836386	3%
			1.803552	-10.28374	0.03326340	3%
			1.817336	-10.30616	0.04922887	3%
Fermi LAT	55704.0	6 days	23.04009	-11.05239	0.02373597	5%
			24.32999	-10.19160	0.01458392	10%
MAGIC	55704.021	5590 s	25.41854	-10.55303	1.437509	$\sim$ 20%
			25.81854	-10.86935	1.083914	$\sim$ 20%
			26.21854	-10.86252	1.102607	$\sim$ 20%
			26.61853	-11.27661	3.582317	$\sim$ 20%
29-05-2011						
Swift UVOT	55709.981	796.3 s	15.05622	-10.55108	0.01582362	$<$ 3%
			15.12833	-10.50060	0.01663154	$<$ 3%
			15.16932	-10.51681	0.01686475	$<$ 3%
Swift XRT	55709.981	796.3 s	17.07061	-10.29152	0.02619152	3%
			17.20845	-10.26628	0.02399117	3%
			17.34630	-10.23925	0.02080091	3%
			17.48414	-10.21698	0.02029576	3%
			17.62199	-10.19705	0.02259837	3%
			17.75983	-10.16153	0.02709369	3%
			17.89767	-10.12512	0.02784097	3%
			18.03552	-10.16939	0.03280920	3%
			18.17336	-10.14401	0.04831628	3%
Fermi LAT	55710.0	6 days	22.87640	-10.95609	0.3328752	5%
			23.87347	-10.85412	0.2086724	5%
			24.87054	-10.13009	0.2512279	10%
MAGIC	55710.003	3875 s	2536047	-10.22729	0.1050947	$\sim$ 20%
			25.64618	-1.038202	0.09257837	$\sim$ 20%

Table 4.8: 30-03-2011 Mkn 501 multi-frequency dataset.

			25.93189	-1.035487	0.09024705	$\sim 20\%$
			26.21761	-1.047648	0.09983351	$\sim 20\%$
			26.50332	-1.051961	0.1161382	$\sim 20\%$
			26.78904	-1.040253	0.1557094	$\sim 20\%$
04-06-2011						
Swift UVOT	55715.937	936.2 s	15.05622	-10.55997	0.01615052	$< 3\%$
			15.12833	-10.51373	0.01523762	$< 3\%$
			15.16932	-10.52105	0.01703007	$< 3\%$
Swift XRT	55715.937	936.2 s	17.07061	-10.32316	0.02528678	3%
			17.20845	-10.28464	0.02377939	3%
			17.34630	-10.26076	0.02064857	3%
			17.48414	-10.24070	0.01995475	3%
			17.62199	-10.22577	0.02237462	3%
			17.75983	-10.18805	0.02573608	3%
			17.89767	-10.22671	0.02863878	3%
			18.03552	-10.26770	0.03424613	3%
			18.17336	-10.28677	0.05264452	3%
Fermi LAT	55715.0	6 days	23.07984	-11.44266	0.3854160	5%
			24.43784	-10.62744	0.2552940	10%
MAGIC	55715.981	5010 s	25.42321	-11.07374	3.382495	$\sim 20\%$
			25.82321	-10.93421	1.712245	$\sim 20\%$
			26.22321	-11.01184	1.805916	$\sim 20\%$
			26.62321	-11.03018	2.644467	$\sim 20\%$
10-06-2011						
Swift UVOT	55722.022	1150.1 s	15.05622	-10.55997	0.01435619	$< 3\%$
			15.12833	-10.52531	0.01564940	$< 3\%$
			15.16932	-10.55422	0.01608406	$< 3\%$
Swift XRT	55722.022	1150.1 s	17.07061	-10.29654	0.02272011	3%
			17.20845	-10.24608	0.02156857	3%
			17.34630	-10.23934	0.01906882	3%
			17.48414	-10.21738	0.01808580	3%
			17.62199	-10.17036	0.01994146	3%
			17.75983	-10.12482	0.02288545	3%
			17.89767	-10.11871	0.02495379	3%
			18.03552	-10.11618	0.02891060	3%
Fermi LAT	55722.0	6 days	23.91964	-1.078820	0.2.121546	5%
			24.94361	-1.045861	0.4.260696	10%
MAGIC	55722.040	5492 s	25.35792	-10.38908	0.1485260	$\sim 20\%$
			25.64364	-10.60154	0.1472709	$\sim 20\%$
			25.92935	-10.69040	0.1439799	$\sim 20\%$
			26.21507	-10.72808	0.1760210	$\sim 20\%$

NOTES – Col.(1): instruments from which data are taken. Col.(2): mean Modified Julian Date (MJD) of the observation. Col.(3): total effective observation time. Col.(4): logarithm of the frequency expressed in Hz. Col.(5): logarithm of the flux multiplied by the frequency in uniti of $erg\,cm^{-2}\,s^{-1}$. Col.(6): error on the quantity of col. 5. Col.(7): systematic error expressed in flux percentage already includend in flux of col.(5).

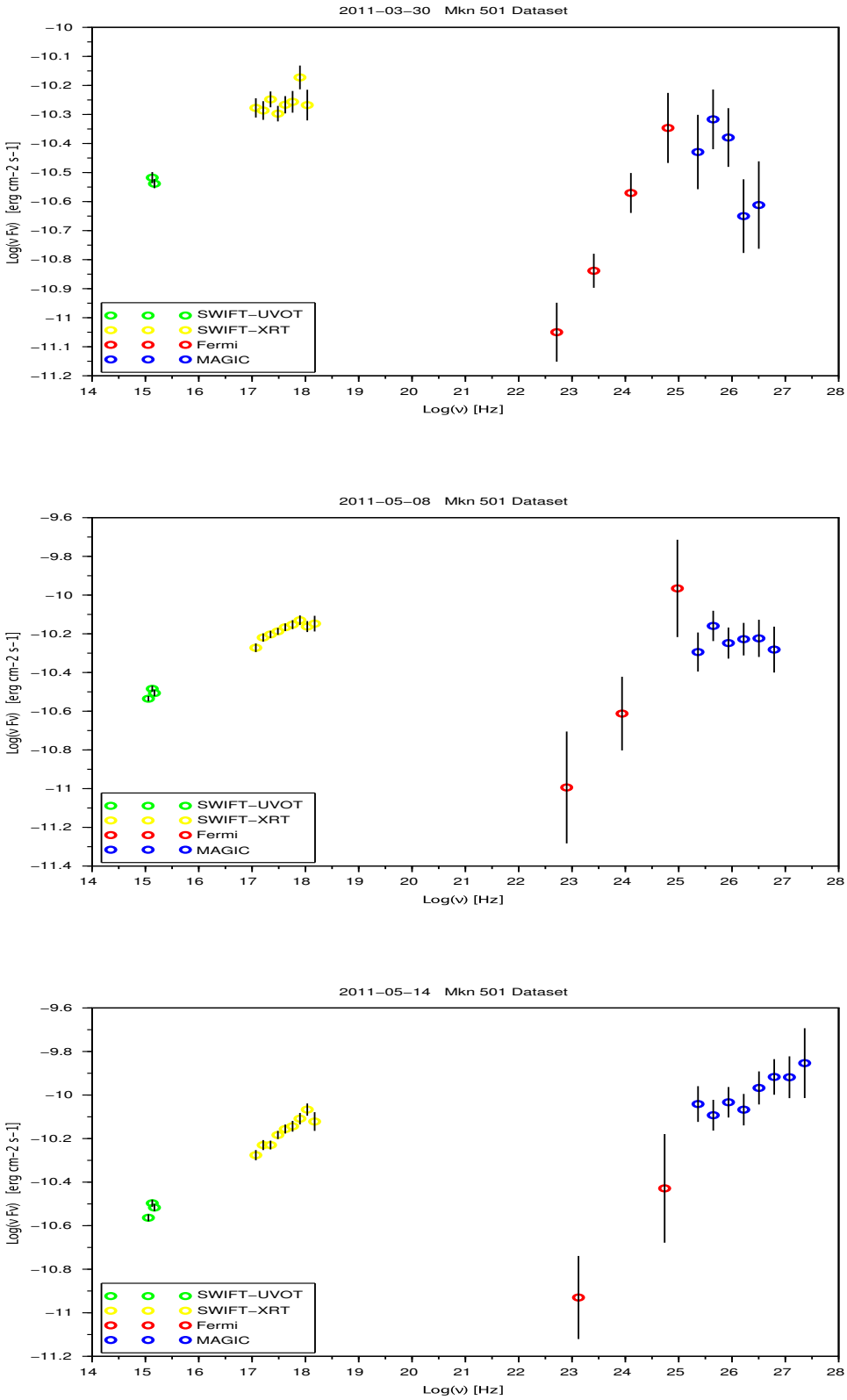

Figure 4.19: Mkn501 multi-frequency datasets (30-03-2011, 08-05-2011, 08-14-2011).

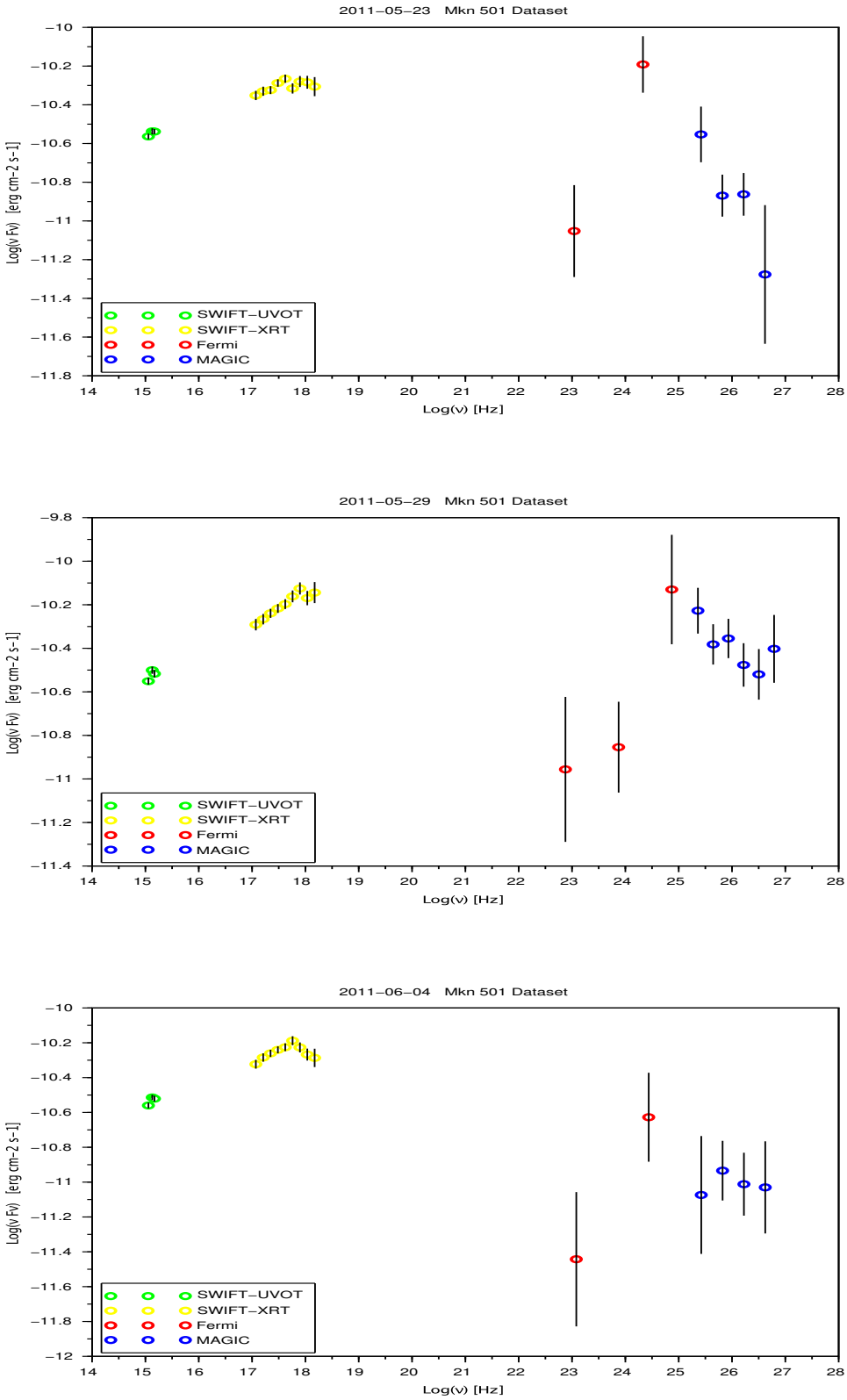

Figure 4.20: Mkn501 multi-frequency datasets (23-05-2011, 29-05-2011, 04-06-2011).

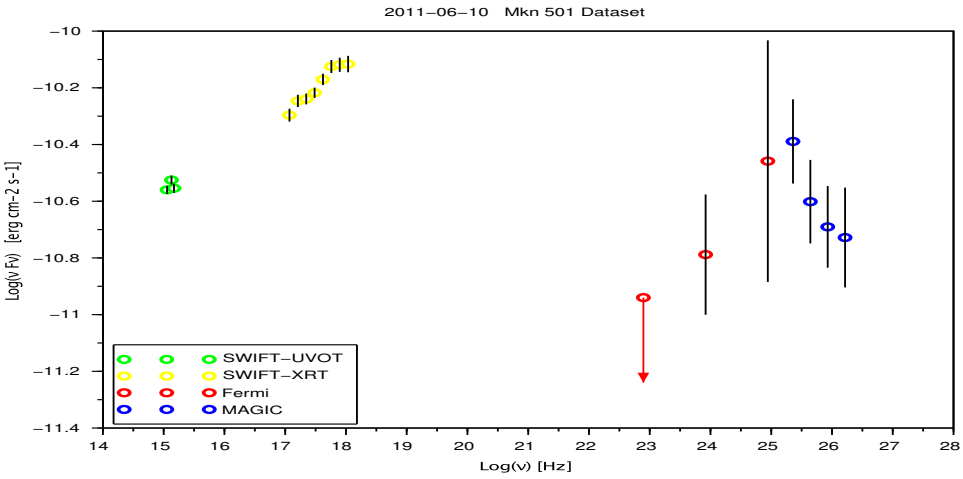

Figure 4.21: Mkn501 multi-frequency datasets (10-06-2011).

Chapter 5

Mkn501 SED Modeling

In this Chapter, after a brief discussion on some aspects related to the minimization process (Sect. 5.1), and after describing the minimization procedure (Sect. 5.2), I present the results of the SED modeling for the seven Mkn501 datasets (Sect. 5.3), shown in the previous Chapter.

5.1 Remarks on the Minimization Process

Once the multi-frequency datasets have been obtained, the SED modeling can be attempted through a non-linear χ^2-minimization that involves the Levenberg-Marquardt method, as described in Chapter 3. Such a minimization process aims at finding the χ^2-manifold global minimum, that corresponds to the most-likely values of the SED model parameters. Since several parameters - both physical and phenomenological - are involved in the model, the χ^2-manifold may present peculiar features that, in some cases, makes it difficult to approach to the global minimum. Moreover, the χ^2-minimum itself may show an intrinsic roughness that aggravates the problem, and its shape can not be exactly known because of the finite resolution in the space parameters exploration.

For this reasons, it is not granted at all that minimizations starting from different initial points converge to the same minimum. By repeating several times the minimization process - starting from different points in the space parameters - different scenarios can manifest:

(i) the algorithm always converge to the same minimum;
(ii) the algorithm rarely converge to local minima;
(iii) the algorithm often converge to minima sufficiently close to the global one;
(iv) the algorithm always converge to different minima, completely uncorrelated each other;

Among these cases, (i) and (iv) are the extreme ones. The former represents the most appetible situation one wants to achive, while the latter the most undesiderable. However, this does not depend on the minimization algorithm, but strongly depends on the nature and the physics of the problem. In other words, case (i) should happen for relatively simple, analytic and well known problems, while case (iv) is clearly a symptom that something is going wrong with the data and/or the model. An intermediate situation is represented by cases (ii) and (iii). These cases happen - often concurrently - for problems in which the χ^2-manifold has a complicated shape, such as in the SED modeling of Mkn501. Here, the same solution is not always achieved, but an area in the space parameter around the presumed global minimum

can be identified. Figuratively, the global minimum can be thought of as being inherently rough, where different solutions correspond to the little valleys that characterize its profile. If this were the case, I would expect that the values of each parameter - coming from all the minimizations - rank in a peaked distribution. Otherwise, their distributions would be rather flat, reflecting the presence of totally uncorrelated minima.

The portrait resulting from Mkn501 SED modeling includes cases (ii) and (iv). The main difficulties found in the fitting procedure can be related to two different factors:

- the poorness of the dataset. In the concept of poorness I enclose different aspects: (i) the energy of the data ranges over several orders of magnitude, and data are not homogeneously distributed; (ii) data are taken from different instruments, and are characterized by very different flux errors. In particular the higher errors in the HE and VHE fluxes weakly constrain the inverse Compton peak; (iii) the lack of data in the MeV-energy region do not put any contraint on the valley between the synchrotron and the inverse Compton peak; (iv) the not well known amount of the systematic uncertaintes - especially over the HE - can lead to an overestimation of the errors, with the ensuing relaxation of the constraints;
- the SED model. Blazars' emission is something very complicated to model because what happens in the emission region inside the jets is not still well understood. Moreover several different processes are supposed to be concurrent and it becames complicated to take them into account all together. The simplest model describing balzar SEDs is the one-zone SSC, and there are good reasons to suppose that it can describe the emission of Mkn501 (see Sect. 4.1). However this model involves phenomenological parameters that may contribute to introduce spurious correlations between the parameters. In such a case, it becomes considerably complicated to identify the global minimum.

To verify that the differences in the solutions are due to the roughness that characterizes the global minimum, a very simple test can be performed. Such a test reflects the stability of the fit process by examining the trend of the error - associated to the mean value of each parameter - as a function of the minimization number. If the abovementioned hypothesis was correct, I would expect a decreasing trend, that stabilizes with the increasing of the minimization number.

Finally, to better understand if the model can influence the χ^2-manifold, a study on the correlations between the parameters is carried out by calculating their Spearman's correlation index [105]. The Spearman correlation index measures the statistical dependence between two variables. In this case, it quantifies how a monotonic function can describe the distribution of two model parameters. This index is particularly suitable even if the parameters' relationship is not linear; moreover it is less sensitive to strong outliers than other linear coefficients. It is defined as:

$$\rho_s = 1 - 6\frac{\sum_i D_i^2}{N\left(N^2-1\right)} \tag{5.1}$$

where N is the number of the solutions, and $D_i = r_i - s_i$ is the difference between the rank of the first variable r_i and the second one s_i.

5.2 SED Modeling Procedure

The whole minimization process consists in the following steps:

1. to generate a starting vector, containing the initial values of the SED parameters. The value of each parameter is randomly chosen in a reasonable physical range. Such ranges are: $10^6 < g_{max} < 10^8$; $10^4 < g_b < 10^6$; $1 < n_1 < 2$; $2 < n_1 < 3$; $10^{-1} < B < 1$ G; $10^3 < K < 10^4$ cm^{-3}; $10^{15} < R < 10^{16}$ cm; and $10 < \delta < 100$ (for parameter definitions see Sect. 3.4.1);

2. to choose an electron distribution for the model. The SED is described by the one-zone SSC model (Sect. 3.4.1), and the selected electron distribution is a broken power law. This is the most common distribution used, and I adopt this one in order to easily compare the results with those presented in literature. However many other distribution can be chosen;

3. to perform the non-linear χ^2-minimization through the Levenberg-Marquardt algorithm implemented in the C++ code, described in Section **??**. The minimization process returns the best-fit values of the SED parameters, the related χ^2, and the covariance matrix.

For each dataset, 250 minimizations are performed by repeating the points listed above for each minimization. Finally, once all minimizations have been completed, it is possible to carry out a statistical analysis on the results. Such results are treaten as follows:

1. the solutions coming from unsuccessful minimizations are rejected. These results clearly belong to local minima, and are characterized by a high χ^2-value. For numerical reasons, the minimization algorithm sometimes was not able to escape from such a minimum in a reasonable number of iterations. These solutions are rejected by inspecting the χ^2-histogram, resulting from all the minimizations. The χ^2-threshold - above which the solutions are excluded - is evaluated case by case, depending on the histogram's features;

2. the solutions characterized by a parameter which value exceeds 3 times its standard deviation are rejected. Basically these solutions presents unlikely physical values of the parameters, and are excluded. Sometimes, for some parameters, more severe criteria must be applied (see Section 5.3.1);

3. once the solutions have been selected, the histogram, the mean and the standard deviation are calculated for each parameter ;

4. the trend of the error associated to the mean value of each parameter is plotted as a function of the minimization number. Such error is given by the parameter's standard deviaton, σ_{par}, divided by the square root of the minimization number N;

5. the correlations among the model parameters are calculated. For solutions that approximately correspond to the same χ^2, all the possible couples of parameter are plotted each other. All the solutions are divided in four narrow χ^2 ranges, and the Spearman correlation index (Eq. 5.1) is calculated for all the 28 parameter combinations;

6. finally, the solution corresponding to the minimum χ^2 is picked out. It gives the most-likely values of the SED parameters and their uncertaintes, estimated through the covariance matrix.

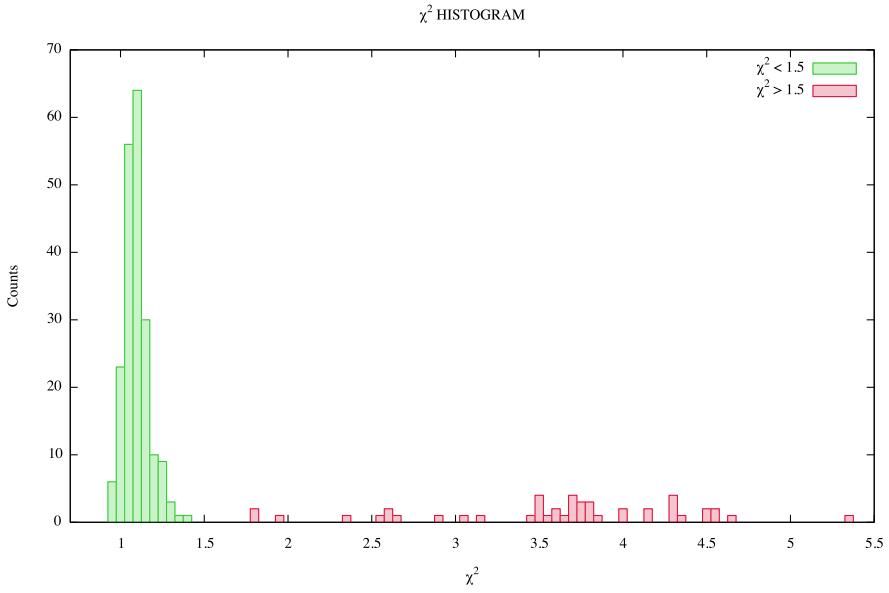

Figure 5.1: χ^2-histogram resulting from the 250 minimization for the 30-03-2011 dataset.

5.3 Results

In the following Sections the results of each SED modeling is presented. A complete explanation is given only for the 30-03-2011 dataset, whilst for the others only the results and the discussion are reported. From now on, the χ^2 is referred to the χ^2 reduced for degrees of freedom. This means that the χ^2 value resulting from the fit is divided by the degrees of freedom ν. In this case, ν is given by the number of observational data points - contained in the dataset - minus the number of the free parameters of the SED model [106]. Moreover, in literature is a common practice set $\gamma_{min} = 1$. So, the SED model results having a total number of eight free parameters.

5.3.1 30-03-2011

For this dataset I performed 250 minimizations. As a first check, I inspected the χ^2-histogram (see Figure 5.1) of the all minimizations in order to decide the χ^2-threshold, above which the solutions will be excluded. The histogram shows: (i) a high and narrow peak around 1.1; and (ii) few scattered solutions for $\chi^2 > 1.5$. The spreaded solutions characterized by a $\chi^2 > 1.5$ are excluded, since they represent unsuccesfull minimizations.
203 minimizations are characterized by a $\chi^2 < 1.5$ that corresponds to 81.2% of the total, while 47 are characterized by a $\chi^2 > 1.5$ that corresponds to 18.8%. Minimizations that results in $\chi^2 > 1.5$ are rejected since they clearly refer to quite strong local minima. Among the remaining 203 solutions, 14 further solutions are exluded when a parameter deviates more than 3σ from its mean value.[1] In fact, these solutions usually deviate strongly from physical solutions. Finally, starting from 250 minimization, 189 solution - corresponding to 75.6% of the total minimizations - fulfill the selection criteria described above and are accepted. The

[1]The mean value is calculated considering the solutions characterized by $\chi^2 < 1.5$.

χ^2 ranges between 0.97 and 1.34, with a mean value of 1.12. The statistic about the solutions quality is reported in Table 5.1.

Table 5.1: Quality of the solutions from 250 minimization processes for 30-03-2011 dataset.

Succesful minimizations ($\chi^2 < 1.5$)	203	81.2 %
Unsuccesful minimizations ($\chi^2 > 1.5$)	47	18.8 %
Excluded solutions (parameters out of 3σ)	14	5.6 %
Accepted solutions (parameters inside 3σ)	189	75.6 %

NOTES – All percentages in Col.(3) are calculated relative to the total minimization number. A further selection on acceptance will be applied later.

Considering the 189 accepted solutions, for each parameter the mean and its related error - given by the standard deviation divided by the square root of the number of minimizations - are calculated. The histograms of all parameters are shown in Figure 5.2. and the corresponding results are shown in Table 5.2. Naturally, the combination of the mean values of the parameters do not fit the data because it does not represent a solution. In fact, each minimum corresponds to a strict combination of parameters, and also a small deviation of one of them generates a completely different SED. For this reason, a mere combination of their mean values is meaningless. However, the standard deviation of their distribution can provide an estimate on how each parameter varies around the alleged minimum.

In order to test the stability of the fitting procedure, the trend of the standard deviation of the selected solutions is examinated. The stability of the fit is related to the effect of starting from different points in the space parameters on the output solution. The decrease and the stabilization of the standard deviation with the number of minimizations indicates that the minimization process is converging towards the same minimum, and that the differences between the solutions can be interpretated as due to an effective roughness of such a minimum. However, in the standard deviation trend sometimes some jumps are present. This can be due to:

(i) solutions that correspond to local minima. However this is an unlikely situation, because the solutions corresponding to local minima are usually characterized by high values of χ^2, and for this reason they are previously rejected;

(ii) degeneracies between the model parameters. If degenerations among the parameters are present, different combinations of them can produce approximately the same SED characterized by almosts the same χ^2. Such degenerate solutions may produces a jump in the standard deviation trend.

To avoid as much as possible to include degenerate solutions in the statistical analysis, all the standard deviation trends are examinated. Plots related to the physical parameter radius R, and normalization K, presents some high jumps (see Figure 5.3). It seems that the SED model is less sensitive to these parameters, since they vary up to two orders of magnitude. To avoid a contamination of spurious solutions, the selection criteria should be a bit more severe for these parameters. All solutions that vary from their mean value more than one standard deviation are rejected. In this way the less likely physical solutions are excluded.

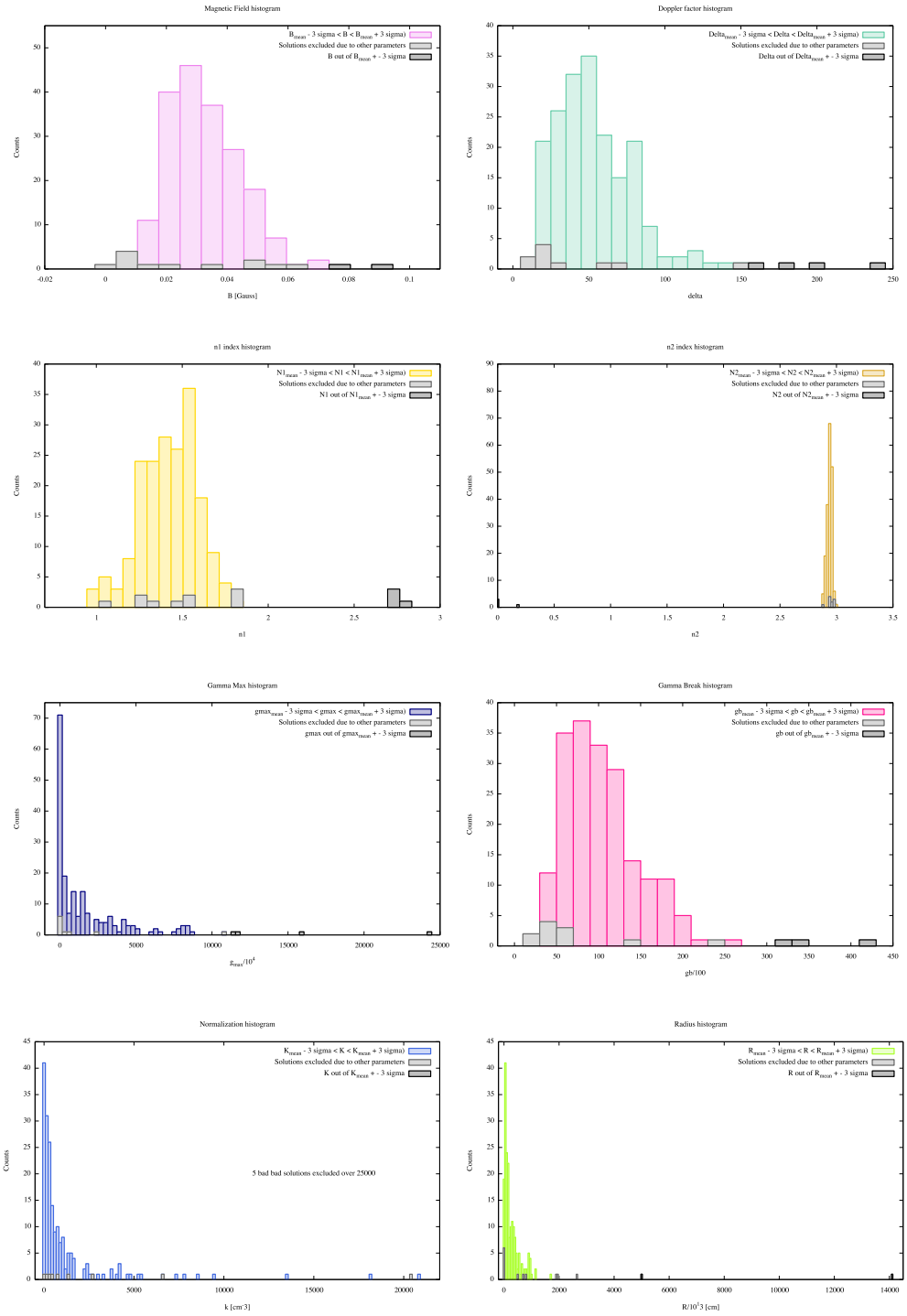

Figure 5.2: Parameter histograms of solutions charactherized by $\chi^2 < 1.5$. Coloured counts refer to the accepted solutions; black and gray to the rejected ones, i.e. to solutions where the parameter of the related plot (black), or another one (gray), deviates more than 3σ respect to its mean value.

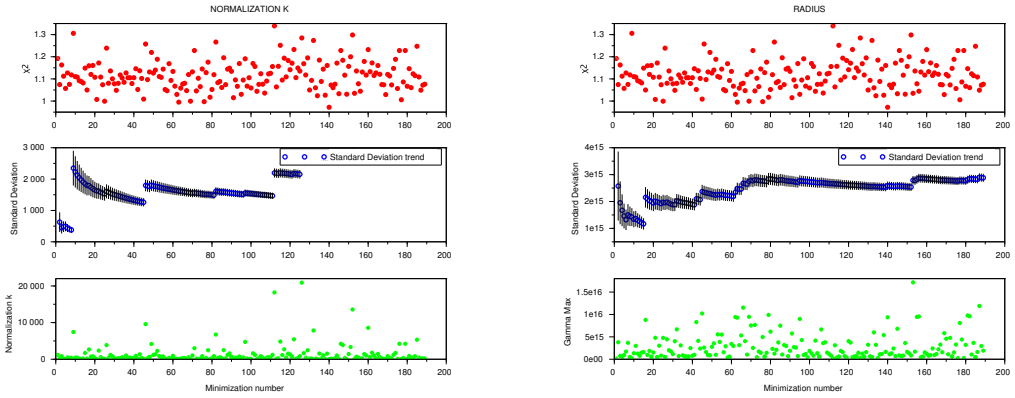

Figure 5.3: Left: Normalization K plots. Right: radius R plots. χ^2 value (top panel), the trend of the standard deviation with the number of the minimizations, and the error bars computed as the standard deviation divided by the corresponding square root of the number of minimizations (central panel), and the value of the parameter related to the plot (bottom panel).

The standard deviation trends after this further selection are shown in Figures 5.4-5.7. All of them look healty, and tend to stabilize after 40-60 minimizations.
Table 5.1, must be updated because other solutions have been excluded. The accepted solutions are 158 that corresponds to 63% of the total minimizations.

Table 5.2: Parameter values from the 158 accepted solutions for 30-03-2011 dataset.

Parameter	Mean value	σ	$\sigma/\sqrt{N}$
g_{max}	1.51×10^{7}	1.94×10^{7}	1.54×10^{6}
g_b	1.07×10^{4}	3.48×10^{3}	2.77×10^{2}
n_1	1.43	0.16	0.01
n_2	2.944	0.021	0.002
B	0.037	0.011	0.001
K	701.6	755.47	60.1
R	2.36×10^{15}	1.88×10^{15}	1.50×10^{14}
δ	57.7	20.59	1.6

NOTES – Col.(1): parameters (for definitions see 3.4.1). Col.(2): Parameters mean value, calculated from the 158 accepted solutions. Col(3): standard deviation σ of the distribution. Col(4): error related to the mean value calculated as $\sigma/\sqrt{N}$, with N the number of minimizations.

The correlations among the model parameters could affect seriously the results and the stability of the minimization process. As the model implemented in the code [76] involves many phenomenological parameters, the problem of the degeneration cannot be ruled out *a priori*. For this reason, it is worth having a quick look into the possible correlations between the parameters. The solutions are divided according to their χ^2-values in four narrow intervals: (i) $1.00 < \chi^2 < 1.05$; (ii) $1.05 < \chi^2 < 1.10$; (iii) $1.10 < \chi^2 < 1.15$; and (vi) $1.50 < \chi^2 < 1.20$. The 8 free parameter describing the SED model originate 28 possible combinations, and for each χ^2 range, all the 28 combinations are plotted. For each pair of parameters, the Spearman's rank correlation coefficient ρ_s (Sect. 5.1) is calculated. In Figure 5.8 some

Table 5.3: Spearman's rank correlation coefficient for model parameters for two different χ^2 ranges (dataset 30-03-2011).

(a) $1.05 < \chi^2 < 1.10$

	g_{max}	g_b	n_1	n_2	B	K	R	δ
g_{max}	1.00	0.58	0.49	0.74	-0.33	0.26	0.52	-0.60
g_b	-0.58	1.00	0.93	0.81	-0.89	0.54	0.98	-0.93
n_1	-0.49	-0.93	1.00	0.77	-0.91	0.77	0.90	-0.78
n_2	-0.74	-0.81	-0.77	1.00	-0.56	0.55	0.72	-0.73
B	0.33	0.89	0.91	0.56	1.00	-0.66	-0.89	0.73
K	-0.26	-0.54	-0.77	-0.55	0.66	1.00	-0.45	-0.27
R	-0.52	-0.98	-0.90	-0.72	0.89	0.45	1.00	-0.95
δ	0.60	0.93	0.78	0.73	-0.73	0.27	0.95	1.00

(b) $1.10 < \chi^2 < 1.15$

	g_{max}	g_b	n_1	n_2	B	K	R	δ
g_{max}	1.00	0.73	0.68	0.79	-0.48	0.45	0.71	-0.73
g_b	-0.73	1.00	0.96	0.85	-0.85	0.63	0.98	-0.94
n_1	-0.68	-0.96	1.00	0.80	-0.88	0.79	0.94	-0.86
n_2	-0.79	-0.85	-0.80	1.00	-0.52	0.60	0.77	-0.82
B	0.48	0.85	0.88	0.52	1.00	-0.63	-0.86	0.68
K	-0.45	-0.63	-0.79	-0.60	0.63	1.00	-0.57	-0.45
R	-0.71	-0.98	-0.94	-0.77	0.86	0.57	1.00	-0.95
δ	0.73	0.94	0.86	0.82	-0.68	0.45	0.95	1.00

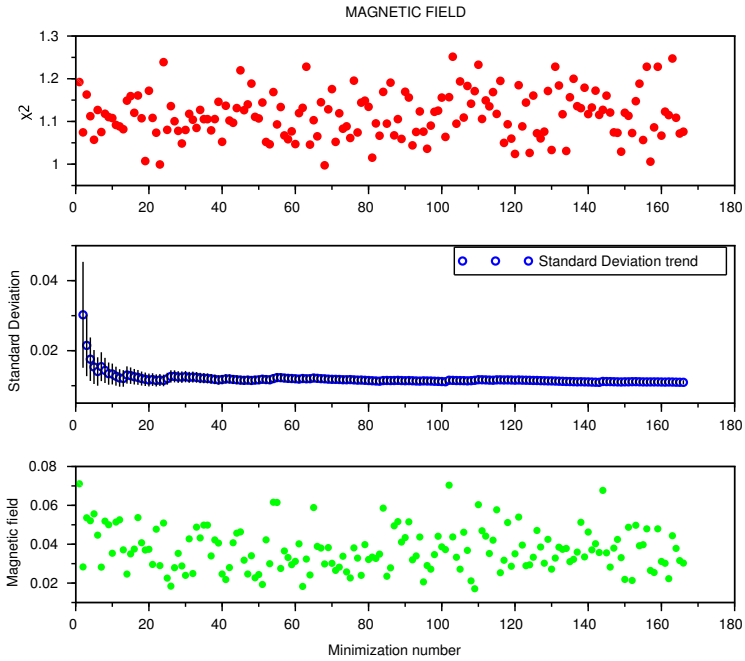

(a) Magnetic field.

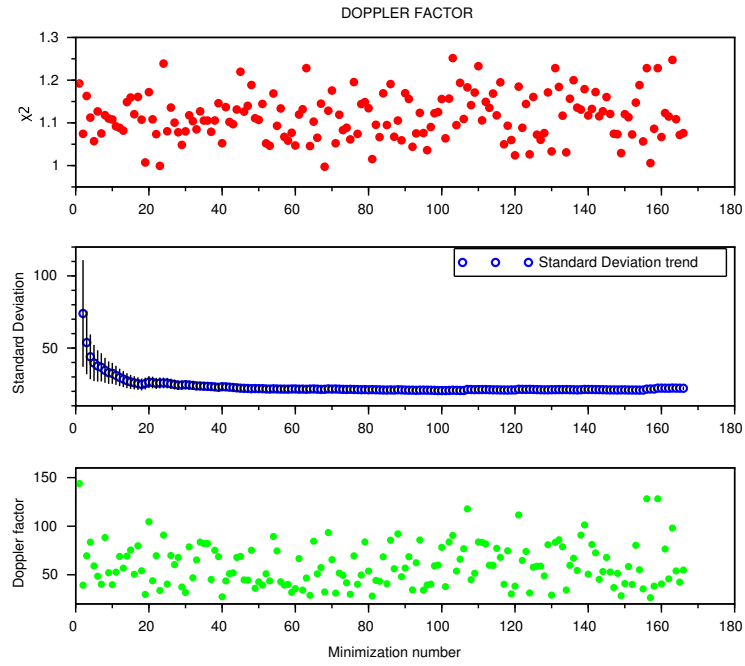

(b) Doppler factor.

Figure 5.4: For the 158 solutions are plotted: the χ^2 value (top panel), the trend of the standard deviation with the number of the minimizations, and the error bars computed as the standard deviation divided by the corresponding square root of the number of minimizations (central panel), and the value of the parameter related to the plot (bottom panel).

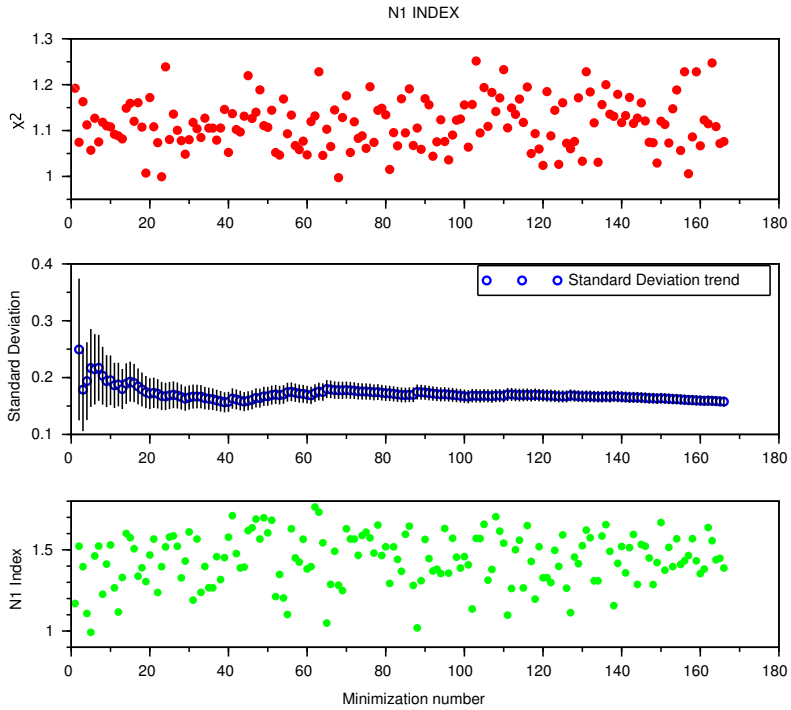

(a) First index of the double power law describing the electron energy distribution.

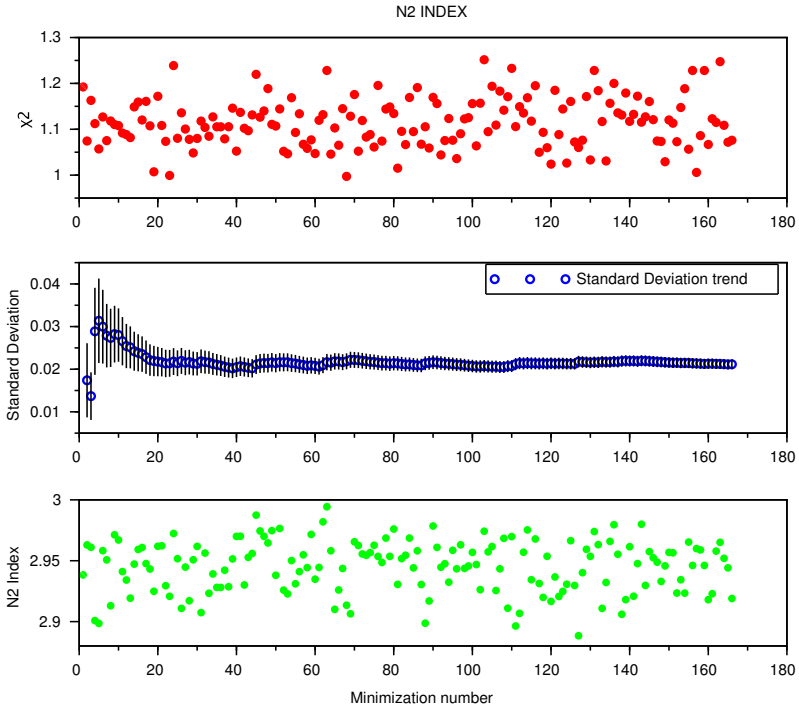

(b) Second index of the double power law describing the electron energy distribution.

Figure 5.5: Same as Figure 5.4.

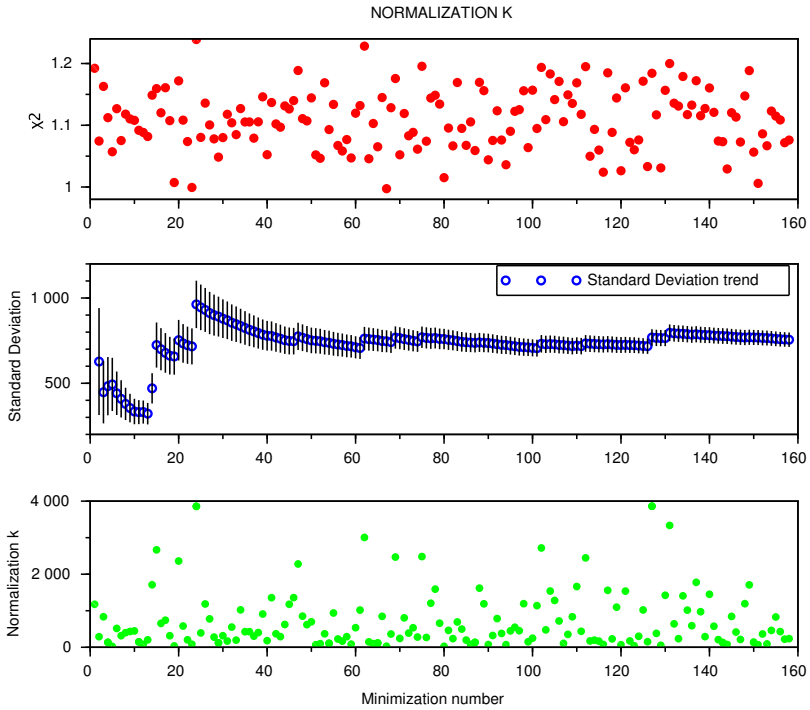

(a) Normalization

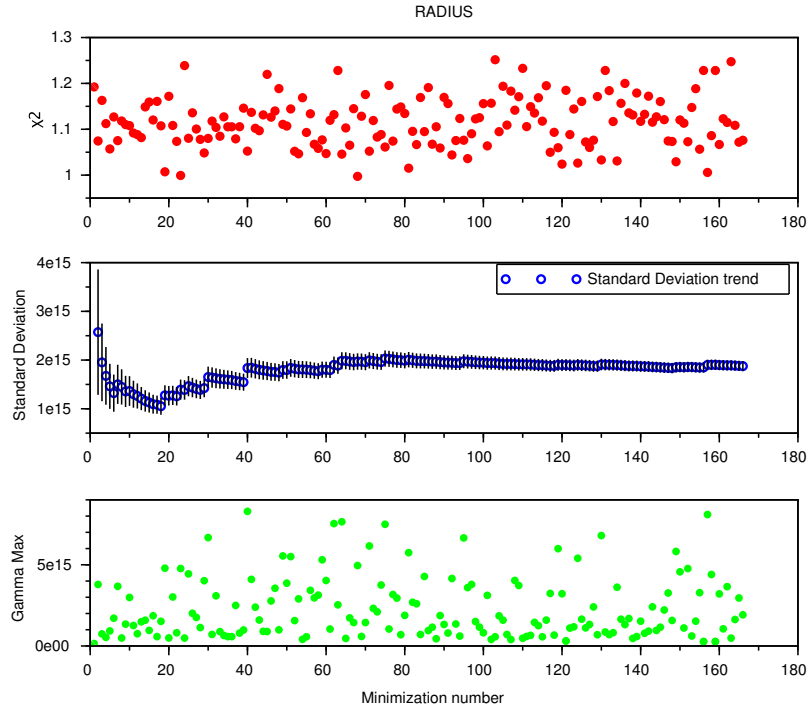

(b) Radius of the electron blob.

Figure 5.6: Same as Figure 5.4.

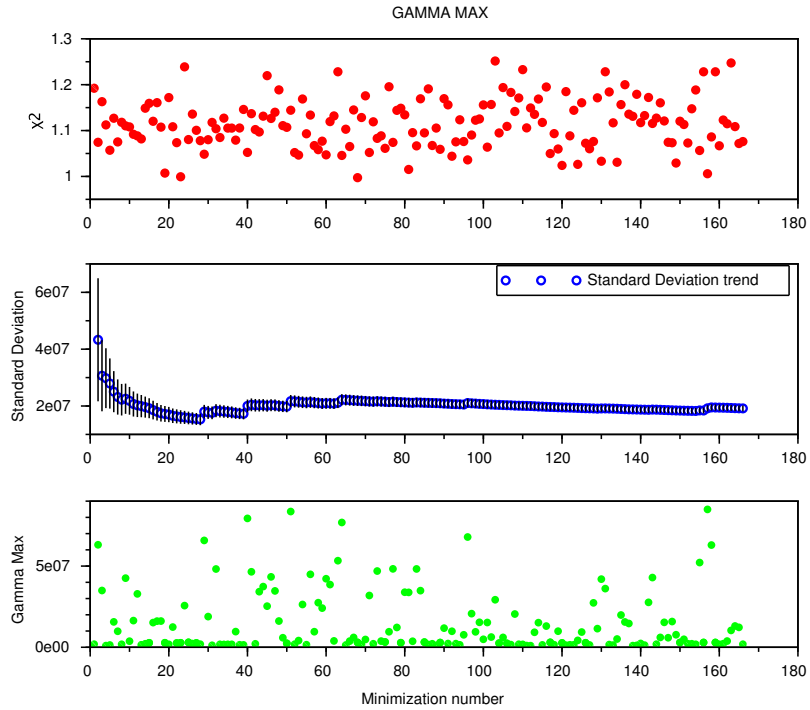

(a) Maximum Lorentz factor of the electron distribution.

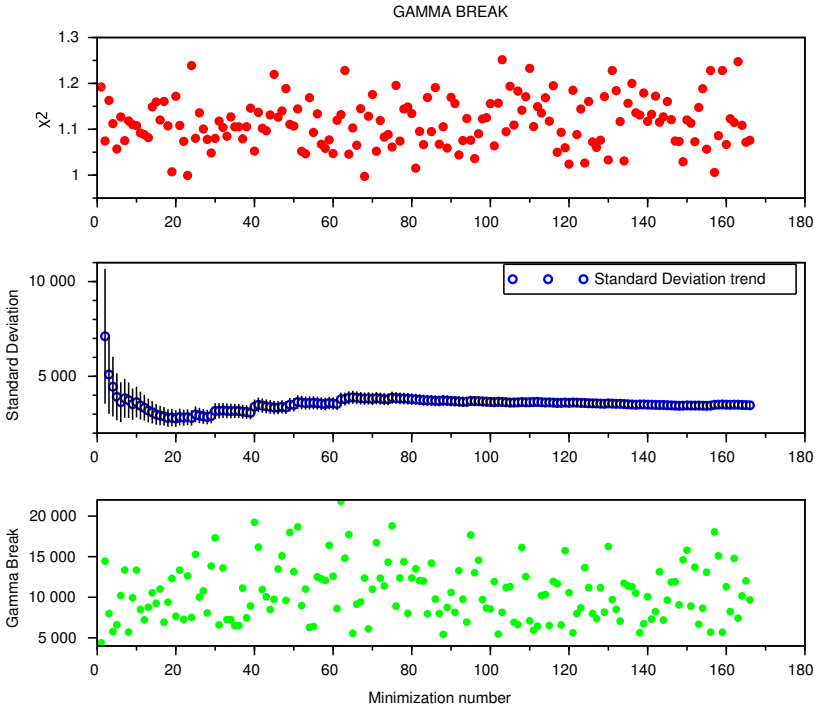

(b) Lorentz factor of the electron distribution corresponding to the change of the power law index.

Figure 5.7: Same as Figure 5.4.

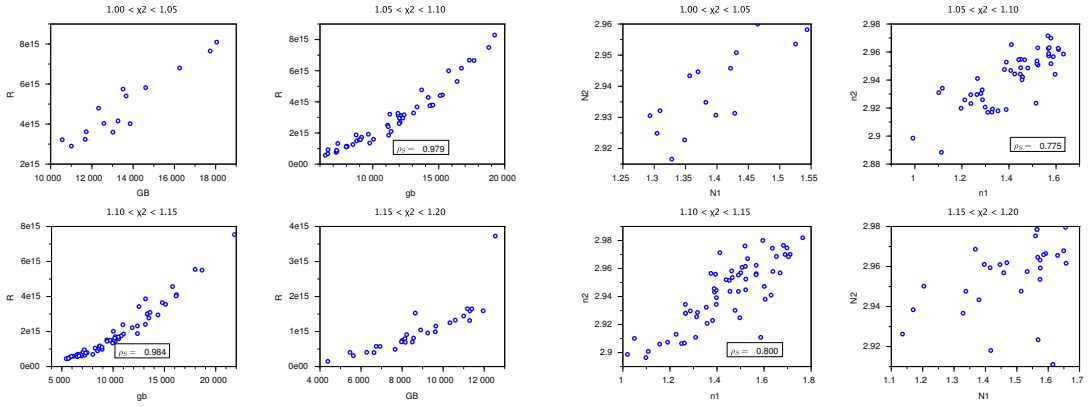

(a) Strong correlation R-γ_b

(b) Evidence of correlation n_1-n_2.

(c) Evidence of correlation B-δ.

(d) Absence of correlation K-δ

Figure 5.8: Examples of different levels of correlation between the model parameters (for parameter definition, see Sect. 3.4.1). The correlation is calculated through the Spearman's rank correlation coefficient ρ_s (Sect. 5.1), for four different narrow χ^2 ranges.

examples of strong, medium, and low correlations are provided. The strong correlations - the ones characterized by $\rho_s > 0.8$ involve mainly the phenomenological parameters. Among the physical parameters, only the couples radius R - magnetic field B, and radius R - Doppler factor δ show a strong correlation (dare eventuale interpretazione fisica).

In Figure 5.17(a) all the 158 solutions are reported. They are divided according to their χ^2 values in three intervals, ranging from 0.95 to 1.25. Such a plot underlines that the main problem consists in the lack of points in the MeV-energy range, between the synchrotron and the inverse Compton peaks. In fact, the valley between the two peaks is not well constrained, and is spreaded from $\sim 10^{20}$ to $10^{22.5}$ Hz, even for no significative differences of χ^2-values. On the contrary, the synchrotron peak is well contrained because the errors on the optical and X-ray fluxes are quite confined respect to those in the VHE band. Around the synchrotron peak all the solutions almost coincide each other. On the contrary, in the inverse Compton peak, they are much spreaded, and tend to group themselves according to their χ^2-values: the higher is the χ^2, the lower is the curvature. Between the two peaks, no particular features allow solutions with increasing χ^2-values to be distinguished. Figure 5.17(b) shows the best and the

worse solution respectively. The most likely values of the model parameters resulting from the minimization process are reported in Table 5.4. As seen in Section 3.4.3, the uncertaintes related to the parameters cannot be estimated through the covariance matrix. However, they are reported just as the formal errors of the fit, and to show that they effectively seems to be overestimated. Another method to estimate the parameters uncertaintes (discussed more deeply in Section 6) is proposed and investigated. It consists in computing the standard deviation of the distribution of each parameter, and to assign it to the parameter as its uncertainty.

Table 5.4: Best solution for 30-03-2011 dataset ($\chi^2 = 0.997$).

Parameter	Best fit value	Err_{covar}	Err_{stdev}
g_{max}	2.96×10^6	$^{+3.53}_{-1.61} \times 10^6$	1.94×10^7
g_b	1.24×10^4	$^{+6.77}_{-1.05} \times 10^4$	3.48×10^3
n_1	1.28	$^{+1.31}_{-0.65}$	0.16
n_2	2.913	$^{+0.092}_{-0.089}$	0.021
B	0.030	$^{+0.59}_{-0.028}$	0.011
K	28.07	$^{+3020.48}_{-27.80}$	755.47
R	4.95×10^{15}	$^{+1.45}_{-4.94} \times 10^{15}$	1.88×10^{15}
δ	32.3	$^{135.46}_{26.11}$	20.6

NOTES – Col.(1): parameters (for definitions see 3.4.1). Col.(2): most likely values of the model parameters resulting from the minimization process. Col(3): uncertaintes obtained from the covariance matrix. Col(4): uncertaintes obtained from the standard deviation of the parameter distribution.

5.3.2 08-05-2011

For this dataset I performed 250 minimizations. First of all, I inspected the χ^2- histogram, shown in Figure 5.9. The histogram is characterized by: (i) a high and narrow peak around 0.9; (ii) a smaller and much spreaded bump around 1.4; and (iii) few scattered solutions for $\chi^2 > 1.7$. The latter ones are immediatly excluded since they belong to unsuccessful minimizations, but those belonging to the two peaks must be trated more carefully. Probably the bump located at higher χ^2-values is due to a local minimum. In order to decide if those solutions have to be rejected, the corresponding parameters are examinated to ensure that their values are in a reasonable physical range. By inspecting the histograms of parameters (Figure 5.10), it is quite evident that most of the unhealthy solutions are automatically excluded, if those ones charachterized by a $\chi^2 > 1.1$ are not taken into account. For this reason, for the further analysis, only the solutions characterized by $\chi^2 > 1.1$ are taken into account.

After the selection, there are 190 solutions characterized by a $\chi^2 < 1.1$, corresponding to 75% of the total. The remaining 60 solutions are characterized by a $\chi^2 > 1.1$, that corresponds to 24% of the total. Among such 190 solutions, 20 further solutions are exluded when a parameter deviates more than 3σ from its mean value.[2] As for the previous case, a more strick selection for the parameters R and K is needed, and other 21 solutions Finally, starting from 250 minimization, 149 solution - corresponding to 60% of the total minimizations

[2]The mean value is calculated considering the solutions characterized by $\chi^2 < 1.1$.

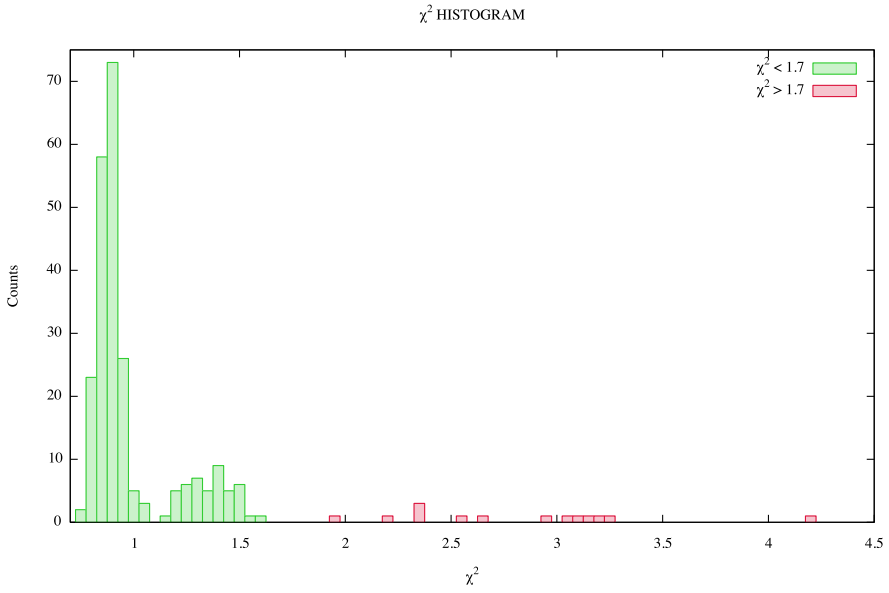

Figure 5.9: χ^2-histogram resulting from the 250 minimization for the 08-05-2011 dataset.

- fulfill the selection criteria described above and are accepted. The χ^2 ranges between 0.81 and 1.05, with a mean value of 0.90 The statistic about the solutions quality is reported in Table 5.5.

Table 5.5: Quality of the solutions from 250 minimization processes for 08-05-2011 dataset.

Succesful minimizations ($\chi^2 < 1.1$)	190	75.0 %
Unsuccesful minimizations ($\chi^2 > 1.1$)	60	24.0 %
Excluded solutions	20 + 21	8.0 % + 8.4%
Accepted solutions	149	59.6 %

NOTES – All percentages in Col.(3) are calculated relative to the total minimization number. The excluded solutions include the solutions whose parameters exceed by 3σ their mean value, and those excluded by the more severe selection on parameters R and K.

Considering the 149 accepted solutions, for each parameter the mean and its related error - given by the standard deviation divided by the square root of the number of minimizations - are calculated (see Table 5.6).

In order to test the stability of the fitting procedure, the trend of the standard deviation of the accepted solutions is examinated, as done in Section5.3.1. All the standard deviation trends look healthy, and tend to stabilize after 50-60 minimizations.

Also a study of the correlations between the parameters is carried out. The solutions are divided according to their χ^2-values in four narrow intervals: (i) $0.80 < \chi^2 < 0.85$; (ii)

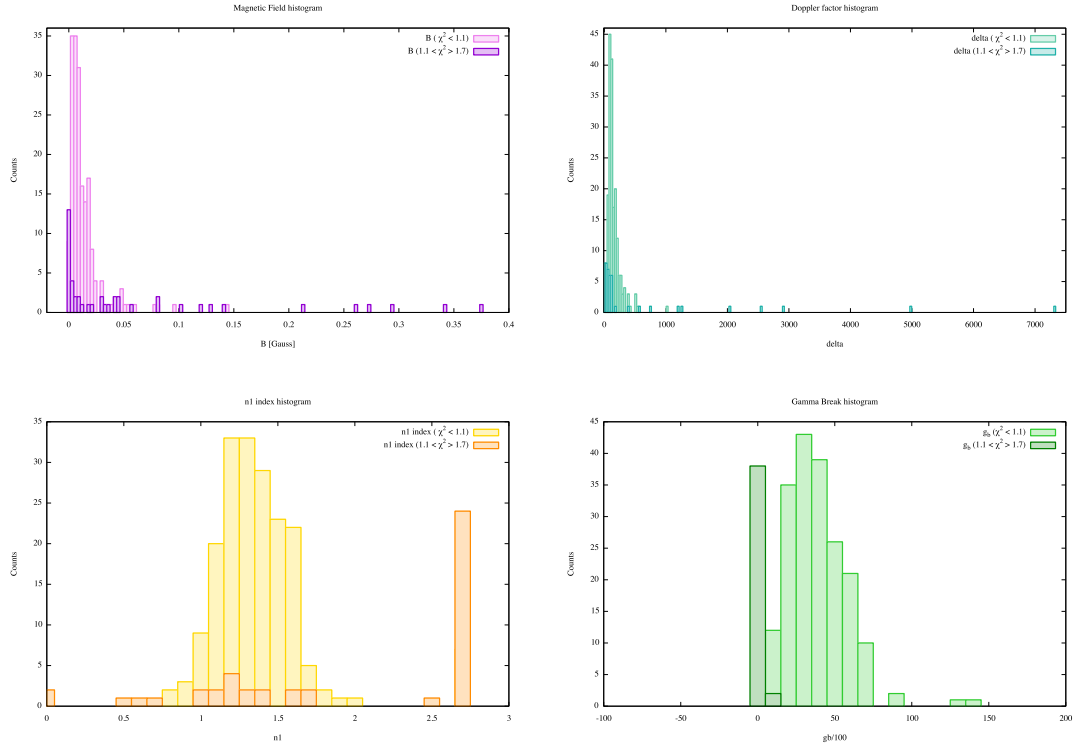

Figure 5.10: Some of the parameter histograms showing the solutions characterized by $\chi^2 < 1.1$ (light colors) and $1.1\chi^2 < 1.7$ (darker colors). (a) magnetic field; (b) Doppler factor; (c) First spectral index of the broken power low describing the electron distribution; (d) Lorentz factor corresponding to the change of index of the electron distribution.

Table 5.6: Parameter values from the 189 accepted solutions for 08-05-2011 dataset.

Parameter	Mean value	σ	$\sigma/\sqrt{N}$
g_{max}	1.67×10^{7}	1.93×10^{7}	1.48×10^{6}
g_b	4.37×10^{3}	1.37×10^{3}	1.17×10^{2}
n_1	1.39	0.17	0.01
n_2	2.787	0.02	0.001
B	0.014	0.011	0.001
K	5131.9	3640.0	915.8
R	1.32×10^{15}	9.48×10^{14}	1.01×10^{14}
δ	155.0	67.7	5.5

NOTES – Col.(1): parameters (for definitions see 3.4.1). Col.(2): Parameters mean value, calculated from the 189 accepted solutions. Col(3): standard deviation σ of the distribution. Col(4): error related to the mean value calculated as $\sigma/\sqrt{N}$, with N the number of minimizations.

$0.85 < \chi^2 < 0.90$; (iii) $0.90 < \chi^2 < 0.95$; and (vi) $0.95 < \chi^2 < 1.00$.[3] For each of the 28 possible parameters combinations and for (ii) and (iii) χ^2 (i.e. those that best underline the

[3]In the interval $1.00 < \chi^2 < 1.05$ there are only four solutions, and the Spearman correlation index has not been calculated.

correlations), the Spearman's rank coefficient ρ_s (Sect. 5.1) is calculated. The results are reported in Table 5.7. As for the previous case, the strong correlations involve mainly the phenomenological parameters. However the state of the correlations reflects those found for the prevuois case (see Table 5.3).

Table 5.7: Spearman's rank correlation coefficient for model parameters for two different χ^2 range (08-05-2011 dataset).

(a) $1.05 < \chi^2 < 1.10$

	g_{max}	g_b	n_1	n_2	B	K	R	δ
g_{max}	1.00	0.91	0.23	0.78	-0.03	-0.66	0.80	-0.87
g_b	-0.91	1.00	0.30	0.62	-0.22	-0.74	0.93	-0.96
n_1	-0.23	-0.30	1.00	-0.09	-0.73	0.30	0.49	-0.22
n_2	-0.78	-0.62	0.09	1.00	0.46	-0.47	0.38	-0.65
B	0.03	0.22	0.73	-0.46	1.00	-0.15	-0.45	0.06
K	0.66	0.74	-0.30	0.47	0.15	1.00	0.63	0.78
R	-0.80	-0.93	-0.49	-0.38	0.45	-0.63	1.00	-0.89
δ	0.87	0.96	0.22	0.65	-0.06	-0.78	0.89	1.00

(b) $1.10 < \chi^2 < 1.15$

	g_{max}	g_b	n_1	n_2	B	K	R	δ
g_{max}	1.00	0.50	0.11	0.57	-0.13	-0.41	0.47	-0.65
g_b	-0.50	1.00	0.63	0.65	-0.79	-0.31	0.96	-0.74
n_1	-0.11	-0.63	1.00	0.51	-0.86	0.49	0.69	-0.24
n_2	-0.57	-0.65	-0.51	1.00	-0.44	-0.04	0.57	-0.52
B	0.13	0.79	0.86	0.44	1.00	-0.16	-0.77	0.27
K	0.41	0.31	-0.49	0.04	0.16	1.00	0.24	0.57
R	-0.47	-0.96	-0.69	-0.57	0.77	-0.24	1.00	-0.80
δ	0.65	0.74	0.24	0.52	-0.27	-0.57	0.80	1.00

In Figure 5.18(a) all the 149 solutions are reported. They are divided according to their χ^2-value in three intervals, ranging from 0.80 to 1.05. Figure 5.18(a) shows the best and the worse solution respectively. The most likely values of the model parameters resulting from the minimization process are reported in Table 5.4.

5.3.3 14-05-2011

For this dataset I performed 250 minimizations. The χ^2- histogram in Figure 5.11 shows: (i) a high and narrow peak around 1.27; (ii) a flat distribution for $1.4 < \chi^2 < 2.5$; and (iii) few scattered solutions for $\chi^2 > 2.5$ up to 6.5. Solutions belonging to (i) and (ii) are excluded since they correspond to unsuccesfull minimizations.

After the selection, there are 134 solutions characterized by a $\chi^2 < 1.4$, corresponding to 54% of the total. The remaining 115 solutions are characterized by a $\chi^2 > 1.4$, that corresponds to 46% of the total. Among such solutions, 12 further solutions are exluded

Table 5.8: Best solution for 05-08-2011 dataset ($\chi^2 = 0.814$).

Parameter	Best fit value	Err_{covar}	Err_{stdev}
g_{max}	2.91×10^{6}	$^{+4.34}_{-1.74}\times10^{6}$	1.93×10^{7}
g_b	5.10×10^{3}	$^{+8.14}_{-3.13}\times10^{3}$	1.93×10^{3}
n_1	1.11	$^{+1.63}_{-0.66}$	0.17
n_2	2.752	$^{+0.081}_{-0.079}$	0.02
B	0.0044	$^{+0.0423}_{-0.0040}$	0.011
K	29.11	$^{+307720}_{-29.11}$	3640.0
R	2.23×10^{15}	$^{+24.33}_{-2.04}\times10^{15}$	9.48×10^{14}
δ	129.72	$^{+133.57}_{-65.81}$	67.7

NOTES – Col.(1): parameters (for definitions see 3.4.1). Col.(2): most likely values of the model parameters resulting from the minimization process. Col(3): uncertaintes obtained from the covariance matrix. Col(4): uncertaintes obtained from the standard deviation of the parameter distribution.

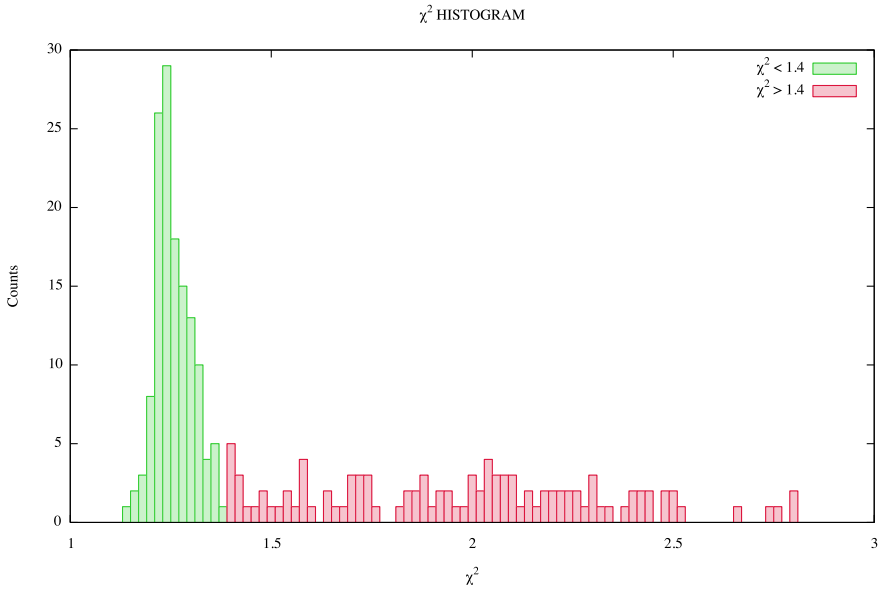

Figure 5.11: χ^2-histogram resulting from the 250 minimization for the 14-05-2011 dataset.

when a parameter deviates more than 3σ from its mean value.[4] As for the previous cases, a more strick selection for the parameters R and K is needed, and other 11 solutions Finally, starting from 250 minimization, 149 solution - corresponding to 60% of the total minimizations - fulfill the selection criteria described above and are accepted. The χ^2 ranges between 1.22 and 1.39, with a mean value of 1.27 The statistic about the solutions quality is reported in Table 5.9.

Considering the 111 accepted solutions, for each parameter the mean and its related error are calculated (see Table 5.10).

[4]The mean value is calculated considering the solutions characterized by $\chi^2 < 1.4$.

Table 5.9: Quality of the solutions from 250 minimization processes for 14-05-2011 dataset.

Succesful minimizations ($\chi^2 < 1.1$)	135	54.0 %
Unsuccesful minimizations ($\chi^2 > 1.1$)	115	46.0 %
Excluded solutions	12 + 11	12.8% + 4.4%
Accepted solutions	111	44.4%

NOTES – All percentages in Col.(3) are calculated relative to the total minimization number. The excluded solutions include the solutions whose parameters exceed by 3σ their mean value, and those excluded by the more severe selection on parameters R and K.

Table 5.10: Parameter values from the 111 accepted solutions for 14-05-2011 dataset.

Parameter	Mean value	σ	$\sigma/\sqrt{N}$
g_{max}	7.57×10^7	5.72×10^7	5.42×10^6
g_b	3.32×10^3	1.20×10^3	1.14×10^2
n_1	1.17	0.18	0.02
n_2	2.724	0.005	0.000
B	0.001	0.0006	0.000
K	1676.0	2570.1	244.7
R	5.28×10^{14}	5.22×10^{14}	4.96×10^{13}
δ	976.4	457.8	41.3

NOTES – Col.(1): parameters (for definitions see 3.4.1). Col.(2): Parameters mean value, calculated from the 111 accepted solutions. Col(3): standard deviation σ of the distribution. Col(4): error related to the mean value calculated as $\sigma/\sqrt{N}$, with N the number of minimizations.

In order to test the stability of the fitting procedure, the trend of the standard deviation of the accepted solutions is examinated, as done in Section5.3.1. All the standard deviation trends tend to stabilize after 60 minimizations. Respect to the previous cases the values of R and K appear even more spreaded. However I mantained the same selection criteria as for the analysis reported in Setions 5.3.1 and 5.3.3: no additional cuts are applied in order to make results coming from different analysis comparable to one another.

In order to verify the presence of correlation between the odel parameters, all the solutions are divided according to their χ^2-values in four narrow intervals: (i) $1.20 < \chi^2 < 1.25$; (ii) $1.25 < \chi^2 < 1.30$; (iii) $1.30 < \chi^2 < 1.35$; and (vi) $1.35 < \chi^2 < 1.40$. In this case, the correlations are evident especially for the range $1.20 < \chi^2 < 1.25$. For each of the 28 possible parameters combinations, the Spearman's rank coefficient ρ_s (Sect. 5.1) is calculated, and the results are reported in Table 5.11 for the χ^2-range that shows better the correlations ($1.20 < \chi^2 < 1.25$). The strong correlations involve mainly the phenomenological parameters, and their state reflects those found for the previous cases (see Tables **??** and **??**).

In Figure 5.19(a) all the 111 solutions are reported. They are divided according to their χ^2-value in three intervals, ranging from 1.22 to 1.39. Figure 5.19(a) shows the best and the worse solution respectively. The most likely values of the model parameters resulting from the minimization process are reported in Table 5.12.

Table 5.11: Spearman's rank correlation coefficient for model parameters for $1.20 < \chi^2 < 1.25$ range (dataset 14-05-2011).

	g_{max}	g_b	n_1	n_2	B	K	R	δ
g_{max}	1.00	0.48	0.63	-0.11	-0.44	-0.11	0.76	-0.73
g_b	-0.48	1.00	0.65	0.58	-0.67	-0.60	0.88	-0.75
n_1	-0.63	-0.65	1.00	0.23	-0.86	0.07	0.86	-0.55
n_2	0.11	-0.58	-0.23	1.00	-0.17	-0.34	0.29	-0.29
B	0.44	0.67	0.86	0.17	1.00	0.06	-0.76	0.33
K	0.11	0.60	-0.07	0.34	-0.06	1.00	0.36	0.56
R	-0.76	-0.88	-0.86	-0.29	0.76	-0.36	1.00	-0.83
δ	0.73	0.75	0.55	0.29	-0.33	-0.56	0.83	1.00

Table 5.12: Best solution for 14-05-29011 dataset ($\chi^2 = 1.193$).

Parameter	Best fit value	Err_{covar}	Err_{stdev}
g_{max}	8.56×10^6	$^{+5.09}_{-3.19}\times10^6$	5.72×10^7
g_b	2.34×10^3	$^{+10.52}_{-1.92}\times10^3$	1.20×10^3
n_1	0.68	$^{+111.16}_{-0.68}$	0.18
n_2	2.720	$^{+0.036}_{-0.0351}$	0.005
B	0.000659	$^{+0.65}_{-0.000658}$	0.0006
K	185.64	$^{+9.90443e+10}_{-185.64}$	2570.1
R	4.23×10^{13}	$^{+1.17}_{-4.21}\times10^{13}$	5.22×10^{14}
δ	2534.25	$^{+10215.5}_{-2030.52}$	457.8

NOTES – Col.(1): parameters (for definitions see 3.4.1). Col.(2): most likely values of the model parameters resulting from the minimization process. Col(3): uncertaintes obtained from the covariance matrix. Col(4): uncertaintes obtained from the standard deviation of the parameter distribution.

5.3.4 23-05-2011

For this dataset I performed 250 minimizations. The χ^2- histogram in Figure 5.12 is more complicated than the cases examinated so far. Such histogram shows: (i) a peak around 1.45; (ii) probably another two small peaks around 1.7 and 2.2; and (iii) some spreaded solutions up to $\chi^2 = 6$. The first peak is not well defined and for this reason it is quite difficult to set a χ^2-threshold. To avoid to cut too much statistic, the χ^2-threshold is set to 1.67, and only solution above this value are excluded from the analysis.

After the selection, there are 171 solutions characterized by a $\chi^2 < 1.67$, corresponding to 68.4% of the total. The remaining 79 solutions are characterized by a $\chi^2 > 1.67$, that corresponds to 31.6% of the total. Among such solutions, 18 further solutions are excluded when a parameter deviates more than 3σ from its mean value.[5] As for the previous cases, a more strict selection for the parameters R and K is needed, and other 24 solutions are rejected Finally, starting from 250 minimization, 129 solutions - corresponding to 51.6% of

[5]The mean value is calculated considering the solutions characterized by $\chi^2 < 1.67$.

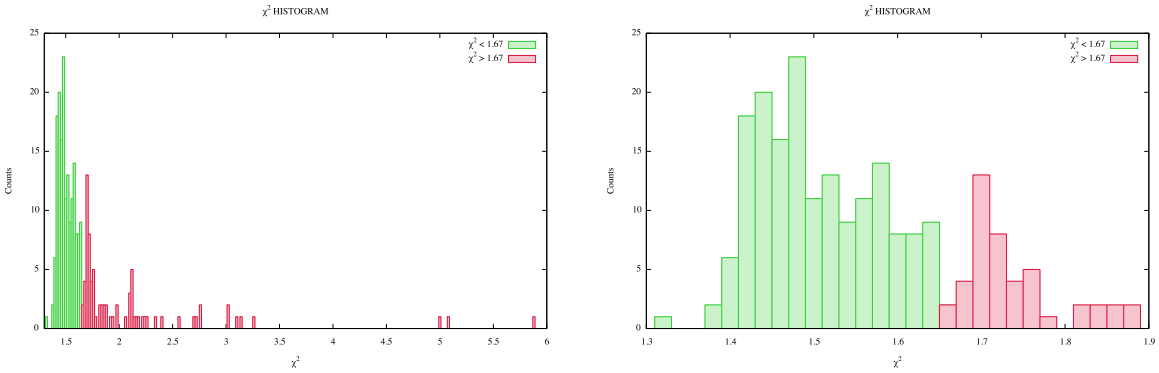

Figure 5.12: χ^2-histogram resulting from the 250 minimization for the 23-05-2011 dataset.

the total minimizations - fulfill the selection criteria described above and are accepted. The χ^2 ranges between 1.38 and 1.66, with a mean value of 1.51 The statistic about the solutions quality is reported in Table 5.13.

Table 5.13: Quality of the solutions from 250 minimization processes for 23-05-2011 dataset.

Succesful minimizations ($\chi^2 < 1.1$)	171	68.4%
Unsuccesful minimizations ($\chi^2 > 1.1$)	79	31.6%
Excluded solutions	18+ 24	7.2% + 9.6%
Accepted solutions	129	51.6%

NOTES – All percentages in Col.(3) are calculated relative to the total minimization number. The excluded solutions include the solutions whose parameters exceed by 3σ their mean value, and those excluded by the more severe selection on parameters R and K.

Considering the 129 accepted solutions, for each parameter the mean and its related error are calculated (see Table 5.14).

In order to test the stability of the fitting procedure, the trend of the standard deviation of the accepted solutions is examined, see Section 5.3.1. All the standard deviation trends tend to stabilize after 70-80 minimizations.

In order to verify the presence of correlation between the odel parameters, all the solutions are divided according to their χ^2-values in four narrow intervals: (i) $1.38 < \chi^2 < 1.45$; (ii) $1.45 < \chi^2 < 1.52$; (iii) $1.52 < \chi^2 < 1.59$; and (vi) $1.59 < \chi^2 < 1.66$. For each of the 28 possible parameters combinations, the Spearman's rank coefficient ρ_s (Sect. 5.1) is calculated, and the results are reported in Table 5.11 for the χ^2-range that shows better the correlations ($1.38 < \chi^2 < 1.45$). As for the previous cases, the strong correlations involve mainly the phenomenological parameters, and the correlations state reflects that found for the previous cases (see Tables **??**, 5.7, and 5.11).

In Figure 5.20(a) all the 129 solutions are reported. They are divided according to their

Table 5.14: Parameter values from the 129 accepted solutions for 23-05-2011 dataset.

Parameter	Mean value	σ	$\sigma/\sqrt{N}$
g_{max}	2.65×10^{7}	1.11×10^{8}	9.80×10^{6}
g_b	2.80×10^{3}	1.73×10^{3}	1.53×10^{2}
n_1	1.37	0.19	0.02
n_2	2.871	0.05	0.005
B	0.631	0.44	0.04
K	3131.1	3551.5	313.9
R	2.77×10^{15}	2.52×10^{15}	2.23×10^{14}
δ	15.7	9.2	0.8

NOTES – Col.(1): parameters (for definitions see 3.4.1). Col.(2): Parameters mean value, calculated from the 129 accepted solutions. Col(3): standard deviation σ of the distribution. Col(4): error related to the mean value calculated as $\sigma/\sqrt{N}$, with N the number of minimizations.

Table 5.15: Spearman's rank correlation coefficient for model parameters for $1.38 < \chi^2 < 1.45$ range (dataset 23-05-2011).

	g_{max}	g_b	n_1	n_2	B	K	R	δ
g_{max}	1.00	0.90	0.63	0.71	-0.33	-0.63	0.98	-0.97
g_b	-0.90	1.00	0.59	0.86	-0.16	-0.60	0.86	-0.92
n_1	-0.63	-0.59	1.00	0.56	-0.29	0.13	0.63	-0.64
n_2	-0.71	-0.86	-0.56	1.00	0.23	-0.35	0.60	-0.74
B	0.33	0.16	0.29	-0.23	1.00	0.17	-0.43	0.23
K	0.63	0.60	-0.13	0.35	-0.17	1.00	0.62	0.60
R	-0.98	-0.86	-0.63	-0.60	0.43	-0.62	1.00	-0.95
δ	0.97	0.92	0.64	0.74	-0.23	-0.60	0.95	1.00

χ^2-value in three intervals, ranging from 1.38 to 1.66. Figure 5.20(a) shows the best and the worse solution respectively. The most likely values of the model parameters resulting from the minimization process are reported in Table 5.16.

5.3.5 29-05-2011

For this dataset I performed 250 minimizations. The χ^2- histogram in Figure 5.13 shows: (i) a high and narrow peak around 1.17; (ii) a second and smaller bump around 1.3; and (iii) few scattered solutions for $2 < \chi^2 < 3$. Solutions belonging to (iii) are excluded since they correspond to unsuccesful minimizations. Those ones related to the second bump, are suspected to belong to a local minimum. To confirm this hypothesis, a check on the standard deviation trend and on the parameters values is carried out, as done in Section 5.3.2.

After the selection, there are 190 solutions characterized by a $\chi^2 < 1.27$, corresponding to 76% of the total. The remaining 60 solutions are characterized by a $\chi^2 > 1.27$, that corresponds to 24% of the total. Among such solutions, 20 further solutions are exluded when a parameter deviates more than 3σ from its mean value.[6] As for the previous cases,

[6]The mean value is calculated considering the solutions characterized by $\chi^2 < 1.27$.

Table 5.16: Best solution for 23-05-2011 dataset ($\chi^2 = 1.328$).

Parameter	Best fit value	Err_{covar}	Err_{stdev}
g_{max}	1.18×10^6	$^{+2.23}_{-0.77} \times 10^6$	1.11×10^8
g_b	3.45×10^3	$^{+7.44}_{-23.56} \times 10^3$	1.73×10^3
n_1	1.14	$^{+2.06}_{-0.73}$	0.19
n_2	2.836	$^{+0.098}_{-0.094}$	0.05
B	0.232	$^{+1.64}_{-0.20}$	0.44
K	39.2406	$^{+403590}_{-39.236}$	3551.5
R	6.06×10^{15}	$^{+77.20}_{-5.62} \times 10^{15}$	2.52×10^{15}
δ	10.52	$^{+11.77}_{-5.56}$	9.2

NOTES – Col.(1): parameters (for definitions see 3.4.1). Col.(2): most likely values of the model parameters resulting from the minimization process. Col(3): uncertaintes obtained from the covariance matrix. Col(4): uncertaintes obtained from the standard deviation of the parameter distribution.

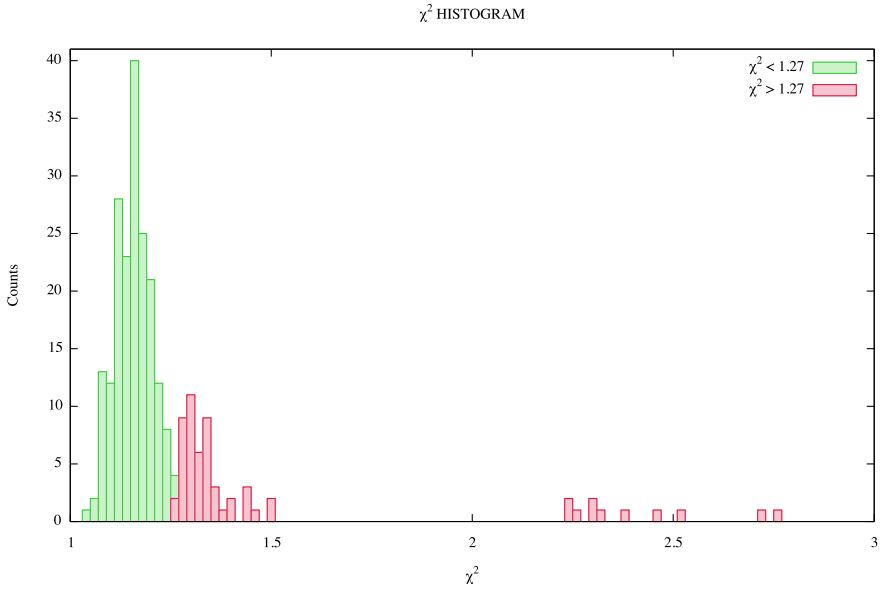

Figure 5.13: χ^2-histogram resulting from the 250 minimization for the 29-05-2011 dataset.

a more strick selection for the parameters R and K is needed, and other 10 solutions are rejected. Finally, starting from 250 minimization, 160 solutions - corresponding to 64% of the total minimizations - fulfill the selection criteria described above and are accepted. The χ^2 ranges between 1.08 and 1.26, with a mean value of 1.16. The statistic about the solutions quality is reported in Table 5.17.

Considering the 160 accepted solutions, for each parameter the mean and its related error are calculated (see Table 5.18).

In order to test the stability of the fitting procedure, the trend of the standard deviation of the accepted solutions is examinated, as done in Section5.3.1. All the standard deviation trends tend to stabilize after 80 minimizations.

Table 5.17: Quality of the solutions from 250 minimization processes for 29-05-2011 dataset.

Succesful minimizations ($\chi^2 < 1.27$)	190	76%
Unsuccesful minimizations ($\chi^2 > 1.27$)	60	24%
Excluded solutions	20 + 10	8% + 4%
Accepted solutions	160	64%

NOTES – All percentages in Col.(3) are calculated relative to the total minimization number. The excluded solutions include the solutions whose parameters exceed by 3σ their mean value, and those excluded by the more severe selection on parameters R and K.

Table 5.18: Parameter values from the 160 accepted solutions for 29-05-2011 dataset.

Parameter	Mean value	σ	$\sigma/\sqrt{N}$
g_{max}	1.36×10^{7}	1.46×10^{7}	1.16×10^{6}
g_b	1.79×10^{3}	0.680×10^{3}	53.7
n_1	1.35	0.22	0.02
n_2	2.765	0.10	0.001
B	0.044	0.025	0.002
K	6280.4	12110.9	957.4
R	1.56×10^{15}	1.26×10^{15}	9.98×10^{13}
δ	77.1	33.8	2.7

NOTES – Col.(1): parameters (for definitions see 3.4.1). Col.(2): Parameters mean value, calculated from the 160 accepted solutions. Col(3): standard deviation σ of the distribution. Col(4): error related to the mean value calculated as $\sigma/\sqrt{N}$, with N the number of minimizations.

In order to verify the presence of correlation between the other parameters, all the solutions are divided according to their χ^2-values in four narrow intervals: (i) $1.05 < \chi^2 < 1.10$; (ii) $1.10 < \chi^2 < 1.15$; (iii) $1.15 < \chi^2 < 1.20$; and (vi) $1.20 < \chi^2 < 1.27$. For each of the 28 possible parameters combinations and for the χ^2-range (ii) - where the correlations are more evident - the Spearman's rank coefficient ρ_s (Sect. 5.1) is calculated. The results are reported in Table 5.19. As for the previous case, the strong correlations involve mainly the phenomenological parameters. However the state of the correlations reflects those found for the previous cases (see Tables 5.3, 5.7, and 5.15), even if in this case their Spearman's coefficients tend to assume slightly lower values.

In Figure 5.21(a) all the 160 solutions are reported. They are divided according to their χ^2-value in three intervals, ranging from 1.08 to 1.27. Figure 5.21(a) shows the best and the worse solution respectively. The most likely values of the model parameters resulting from the minimization process are reported in Table 5.20.

5.3.6 04-06-2011

For this dataset I performed 250 minimizations. The χ^2- histogram in Figure 5.14 shows: (i) a high and narrow peak around 1.18; (ii) another one around 1.15; (iii) a smaller peak

Table 5.19: Spearman's rank correlation coefficient for model parameters for $1.10 < \chi^2 < 1.15$ range (dataset 29-05-2011).

	g_{max}	g_b	n_1	n_2	B	K	R	δ
g_{max}	1.00	0.69	0.42	0.46	-0.35	-0.42	0.78	-0.72
g_b	-0.69	1.00	0.24	0.46	-0.49	-0.77	0.87	-0.75
n_1	-0.42	-0.24	1.00	0.20	-0.56	0.33	0.53	-0.31
n_2	-0.46	-0.46	-0.20	1.00	0.22	-0.11	0.28	-0.62
B	0.35	0.49	0.56	-0.22	1.00	0.25	-0.63	0.08
K	0.42	0.77	-0.33	0.11	-0.25	1.00	0.58	0.53
R	-0.78	-0.87	-0.53	-0.28	0.63	-0.58	1.00	-0.78
δ	0.72	0.75	0.31	0.62	-0.08	-0.53	0.78	1.00

Table 5.20: Best solution for 29-05-2011 dataset ($\chi^2 = 1.078$).

Parameter	Best fit value	Err_{covar}	Err_{stdev}
g_{max}	2.01×10^6	$^{+3.49}_{-1.28}\times10^6$	1.46×10^7
g_b	1.25×10^3	$^{+2.92}_{-0.87}\times10^3$	0.680×10^3
n_1	0.72	$^{+75.4}_{-0.71}$	0.22
n_2	2.756	$^{+0.054}_{-0.053}$	0.10
B	0.08235	$^{+72.2655}_{-0.08226}$	0.025
K	161.7	$^{+2.1e+10}_{-161.737}$	12110.9
R	1.99×10^{14}	$^{+245.64}_{-1.97}\times10^{14}$	1.26×10^{15}
δ	116.4	$^{+294.5}_{-83.4}$	33.8

NOTES – Col.(1): parameters (for definitions see 3.4.1). Col.(2): most likely values of the model parameters resulting from the minimization process. Col(3): uncertaintes obtained from the covariance matrix. Col(4): uncertaintes obtained from the standard deviation of the parameter distribution.

around 1.9; and (iii) few scattered solutions for $2 < \chi^2 < 3$ and around 4. All the peaks are clearly separated from one another. Solutions related to (ii), (iii) and (iv) belong to local minima, they are quite strong in cases (ii) and (iii). Hence, all these solutions are dropped from further analysis.

After the selection, there are 113 solutions characterized by a $\chi^2 < 1.3$, corresponding to 45.2% of the total. The remaining 137 solutions are characterized by a $\chi^2 > 1.3$, that corresponds to 54.8% of the total. Among such solutions, 14 further solutions are exluded when a parameter deviates more than 3σ from its mean value.[7] As for the previous cases, a stricter selection for parameters R and K is needed, and other 18 solutions are rejected. However 4 unphysical solutions (corresponding to $n_2 = 0$ and very high values of K as shown in Figure 5.15). These solutions are exluded after a visual check of the standard deviation check.

Finally, starting from 250 minimization, only 81 solutions - corresponding to 32.4% of the total minimizations - fulfill the selection criteria described above and are accepted. The χ^2

[7]The mean value is calculated considering the solutions characterized by $\chi^2 < 1.3$.

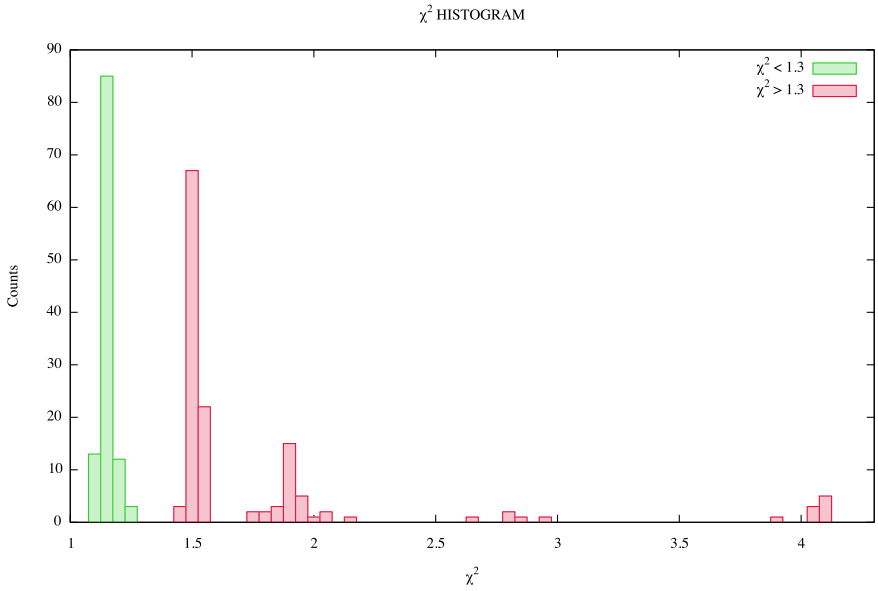

Figure 5.14: χ^2-histogram resulting from the 250 minimization for the 04-06-2011 dataset.

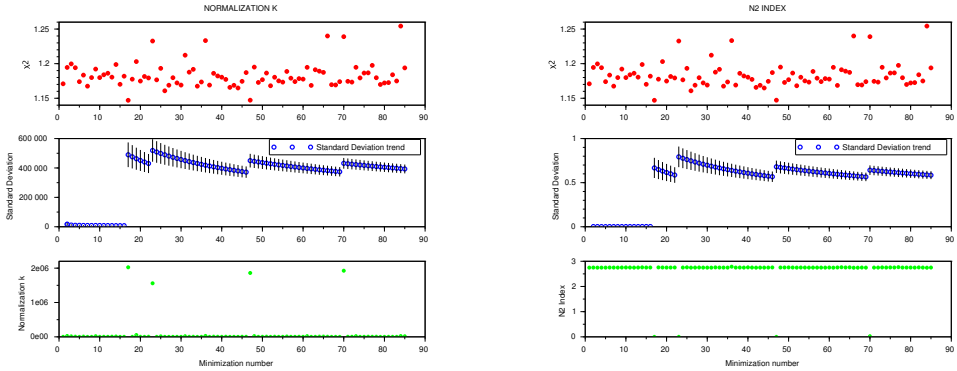

Figure 5.15: Standard deviation trend of the normalization K (left), and electron spectral index $n2$ (right). It is evident the presence of four strong outliers, even after the selections.

ranges between 1.16 and 1.25, with a mean value of 1.18. The statistic about the solutions quality is reported in Table 5.21.

Considering the 81 accepted solutions, for each parameter the mean and its related error are calculated (see Table 5.22).

In order to test the stability of the fitting procedure, the trend of the standard deviation of the accepted solutions is examinated, as done in Section5.3.1. All the standard deviation trends tend to stabilize after 50 minimizations.

In order to verify the presence of correlation between the odel parameters, all the solutions are divided according to their χ^2-values in four narrow intervals: (i) $1.16 < \chi^2 < 1.17$; (ii) $1.17 < \chi^2 < 1.18$; (iii) $1.18 < \chi^2 < 1.19$; and (vi) $1.19 < \chi^2 < 21$.[8] For each of the 28

[8]In the rangge $1.21 < \chi^2 < 1.26$ only 4 solutions are present.

Table 5.21: Quality of the solutions from 250 minimization processes for 04-06-2011 dataset.

Succesful minimizations ($\chi^2 < 1.3$)	113	45.2%
Unsuccesful minimizations ($\chi^2 > 1.3$)	137	54.8%
Excluded solutions	14 + 22	5.6% + 8.8%
Accepted solutions	81	32.4%

NOTES – All percentages in Col.(3) are calculated relative to the total minimization number. The excluded solutions include the solutions whose parameters exceed by 3σ their mean value, and those excluded by the more severe selections on parameters R and K.

Table 5.22: Parameter mean values from the 81 accepted solutions for 04-06-2011 dataset.

Parameter	Mean value	σ	$\sigma/\sqrt{N}$
g_{max}	9.46×10^5	3.19×10^5	3.54×10^4
g_b	7.27×10^2	2.88×10^2	32.0
n_1	1.37	0.21	0.02
n_2	2.752	0.005	0.001
B	0.026	0.013	0.001
K	5031.6	8538.44	948.7
R	2.45×10^{15}	2.28×10^{15}	2.54×10^{14}
δ	97.9	27.6	3.1

NOTES – Col.(1): parameters (for definitions see 3.4.1). Col.(2): Parameters mean value, calculated from the 81 accepted solutions. Col(3): standard deviation σ of the distribution. Col(4): error related to the mean value calculated as $\sigma/\sqrt{N}$, with N the number of minimizations.

possible parameters combinations and for χ^2-range (ii), the Spearman's rank coefficient ρ_s (Sect. 5.1) is calculated. The results are reported in Table 5.23. As for the previous case, the strong correlations involve mainly the phenomenological parameters. However the state of the correlations reflects those found for the previous cases (see Tables 5.3, 5.7, 5.11, 5.15, and 5.19), even characterized by lower coefficients rho_s.

In Figure 5.22(a) all the 81 solutions are reported. They are divided according to their χ^2-value in three intervals, ranging from 1.18 to 126 Figure 5.22(a) shows the best and the worse solution respectively. The most likely values of the model parameters resulting from the minimization process are reported in Table 5.24.

5.3.7 10-06-2011

For this dataset I performed 250 minimizations. The χ^2- histogram in Figure 5.16 is more difficult to interprete, because it does not present a clear peak around 1.5, but quite spreaded values, expecially on the side of larger χ^2. There are not evident features that allows to cut somewhere this not well-defined distribution, so all the solutions charachterized by $\chi^2 < 1.8$ are taken into account. Above these value, the solutions are rather thin. They are rejected, because they supposely belong to local minima located quite far away from the absolute

Table 5.23: Spearman's rank correlation coefficient for model parameters for $1.20 < \chi^2 < 1.25$ range (dataset 04-06-2011) .

	g_{max}	g_b	n_1	n_2	B	K	R	δ
g_{max}	1.00	0.57	0.64	-0.19	-0.87	-0.64	0.97	-0.75
g_b	-0.57	1.00	0.13	0.37	-0.22	-0.87	0.61	-0.76
n_1	-0.64	-0.13	1.00	0.15	-0.71	0.02	0.57	-0.43
n_2	0.19	-0.37	-0.15	1.00	0.38	0.05	-0.22	-0.06
B	0.87	0.22	0.71	-0.38	1.00	0.33	-0.78	0.45
K	0.64	0.87	-0.02	-0.05	-0.33	1.00	0.72	0.79
R	-0.97	-0.61	-0.57	0.22	0.78	-0.72	1.00	-0.84
δ	0.75	0.76	0.43	0.06	-0.45	-0.79	0.84	1.00

Table 5.24: Best solution for 04-06-2011 dataset ($\chi^2 = 1.161$).

Parameter	Best fit value	Err_{covar}	Err_{stdev}
g_{max}	6.76×10^5	$^{+3.35}_{-0.56}\times10^5$	3.19×10^5
g_b	1.06×10^3	$^{+38.60}_{-1.03}\times10^3$	2.88×10^2
n_1	0.771	$^{+5.71}_{-0.67}$	0.21
n_2	2.749	$^{+0.06}_{-0.06}$	0.005
B	0.0319	$^{+10.6645}_{-0.0318}$	0.013
K	26.61	$^{+6.15e+10}_{-26.62}$	8538.44
R	7.81×10^{14}	$^{+5796.91}_{-7.80}\times10^{14}$	$2.28\ \times10^{15}$
δ	119.2	$^{+24951.7}_{-118.67}$	27.6

NOTES – Col.(1): parameters (for definitions see 3.4.1). Col.(2): most likely values of the model parameters resulting from the minimization process. Col(3): uncertaintes obtained from the covariance matrix. Col(4): uncertaintes obtained from the standard deviation of the parameter distribution.

minimum, rather than due to its intrinsic roughness.

After the selection, there are 239 solutions characterized by a $\chi^2 < 1.8$, corresponding to 95.6% of the total. The remaining 11 solutions are characterized by a $\chi^2 > 1.8$, that corresponds to 4.4% of the total. Among such solutions, 21 further solutions are excluded when a parameter deviates more than 3σ from its mean value.[9] Contrary to the previous cases, a stricter selection - not only for R and K parameters, but also for n_1, n_2, g_{max} and B - have been applied by inspecting the parameter distribution and the standard deviation trend. After that, 45 more solutions have been rejected. However, the selection criteria described above are not strong enough to cut all the bad value of the parameters, and 9 more solutions had to be cut by hand. These special requirements could be due to a local minimum, whose solutions are characterized by a subsample of the χ^2-value of the main peak. Finally, starting from 250 minimization, 160 solutions - corresponding to 64% of the total minimizations - fulfill the selection criteria described above and are accepted. The χ^2 ranges between 1.43

[9]The mean value is calculated considering the solutions characterized by $\chi^2 < 1.8$.

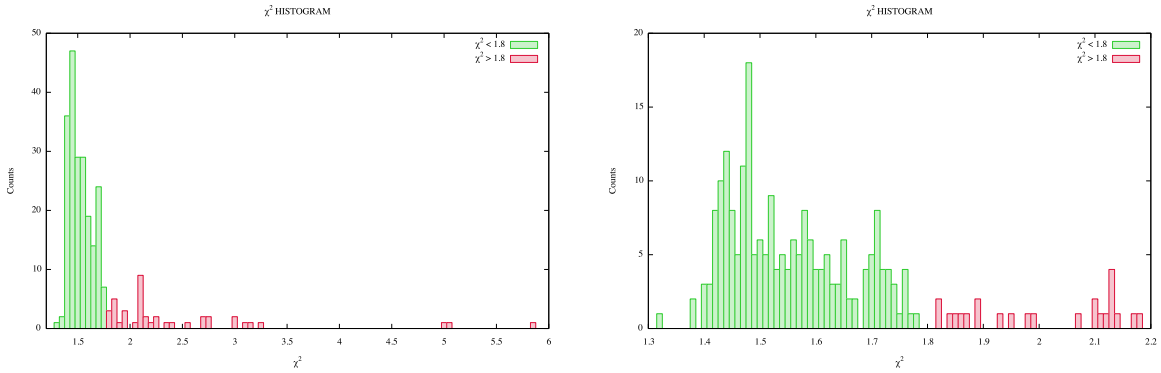

Figure 5.16: χ^2-histogram resulting from the 250 minimization for the 10-06-2011 dataset. (a) the whole histogram; (b) zoom for $1.3 < \chi^2 < 2.2$.

and 1.78, with a mean value of 1.55 The statistic about the solutions quality is reported in Table 5.25.

Table 5.25: Quality of the solutions from 250 minimization processes for 10-06-2011 dataset.

Succesful minimizations ($\chi^2 < 1.1$)	239	95.6%
Unsuccesful minimizations ($\chi^2 > 1.1$)	11	4.4%
Excluded solutions	21 + 49 + 9	8.4% + 19.6% + 3.6%
Accepted solutions	160	64%

NOTES – All percentages in Col.(3) are calculated relative to the total minimization number. The excluded solutions include the solutions whose parameters exceed by 3σ their mean value, and those excluded by the more severe selection on parameters R and K.

Considering the 160 accepted solutions, for each parameter the mean and its related error are calculated (see Table 5.26).

In order to test the stability of the fitting procedure, the trend of the standard deviation of the accepted solutions is examinated, as done in Section5.3.1. All the standard deviation trends tend to stabilize after 90-100 minimizations.

In order to verify the presence of correlation between the odel parameters, all the solutions are divided according to their χ^2-values in four narrow intervals: (i) $1.40 < \chi^2 < 1.45$; (ii) $1.45 < \chi^2 < 1.50$; (iii) $1.50 < \chi^2 < 1.55$; and (vi) $1.55 < \chi^2 < 1.60$. For each of the 28 possible parameters combinations and for χ^2-range (ii), the Spearman's rank coefficient ρ_s (Sect. 5.1) is calculated. The results are reported in Table 5.23. As for the previous case, the strong correlations involve mainly the phenomenological parameters. However the state of the correlations reflects those found for the previous cases (see Tables 5.3, 5.7, 5.11, 5.15, 5.19, and 5.23).

For this dataset, in the Fermi analysis, also an upper limit has been calculated (Section

Table 5.26: Parameter values from the 160 accepted solutions for 10-06-2011 dataset.

Parameter	Mean value	σ	$\sigma/\sqrt{N}$
g_{max}	1.01×10^{8}	3.45×10^{8}	2.73×10^{7}
g_b	6.09×10^{2}	4.95×10^{2}	39.1
n_1	1.29	0.27	0.02
n_2	2.717	0.01	0.001
B	0.106	0.10	0.007
K	10184.5	20077.3	1587.3
R	2.39×10^{15}	2.40×10^{15}	1.90×10^{14}
δ	59.0	29.9	2.4

NOTES – Col.(1): parameters (for definitions see 3.4.1). Col.(2): Parameters mean value, calculated from the 160 accepted solutions. Col(3): standard deviation σ of the distribution. Col(4): error related to the mean value calculated as $\sigma/\sqrt{N}$, with N the number of minimizations.

Table 5.27: Spearman's rank correlation coefficient for model parameters for $1.45 < \chi^2 < 1.50$ range (dataset 10-06-2011).

	g_{max}	g_b	n_1	n_2	B	K	R	δ
g_{max}	1.00	-0.27	0.42	0.13	-0.47	-0.02	0.71	-0.43
g_b	0.27	1.00	-0.30	-0.27	-0.19	-0.81	-0.05	0.18
n_1	-0.42	0.30	1.00	0.52	-0.26	0.44	0.46	-0.34
n_2	-0.13	0.27	-0.52	1.00	0.33	0.53	0.06	-0.36
B	0.47	0.19	0.26	-0.33	1.00	0.39	-0.60	-0.12
K	0.02	0.81	-0.44	-0.53	-0.39	1.00	0.23	-0.01
R	-0.71	0.05	-0.46	-0.06	0.60	-0.23	1.00	-0.70
δ	0.43	-0.18	0.34	0.36	0.12	0.01	0.70	1.00

4.3.2). Such point cannot be used during the minimization process since it is not characterized by a simmetric error. However it can be used as a constraint, once all the minimizations have been performed. In particular, all SEDs charachterized by a higher flux in correspondence of a such upper limit have been excluded. Finally, the selected solutions are 26.

In Figure 5.23(a) the 26 selected solutions are reported. They are divided according to their χ^2-value in three intervals, ranging from 1.4 to 1.8 Figure 5.23(a) shows the best and the worse solution respectively. The most likely values of the model parameters resulting from the minimization process are reported in Table 5.28.

Table 5.28: Best solution for 10-06-2011 dataset ($\chi^2 = 1.508$).

Parameter	Best fit value	Err_{covar}	Err_{stdev}
g_{max}	2.29×10^{6}	$^{+44.08}_{-2.17}\times10^{6}$	3.45×10^{8}
g_b	5.61×10^{2}	$^{+3018.75}_{-5.60}\times10^{2}$	4.95×10^{2}
n_1	0.96	$^{+29.89}_{-0.93}$	0.27
n_2	2.71	$^{+0.06}_{-0.06}$	0.01
B	0.038015	$^{+27.63}_{-0.03796}$	0.10
K	792.1	$^{+1.7e+12}_{-792.10}$	20077.3
R	3.91×10^{14}	$^{+1007.50}_{-3.89}\times10^{14}$	2.40×10^{15}
δ	141.11	$^{+19380.60}_{-140.09}$	29.9

NOTES – Col.(1): parameters (for definitions see 3.4.1). Col.(2): most likely values of the model parameters resulting from the minimization process. Col(3): uncertaintes obtained from the covariance matrix. Col(4): uncertaintes obtained from the standard deviation of the parameter distribution.

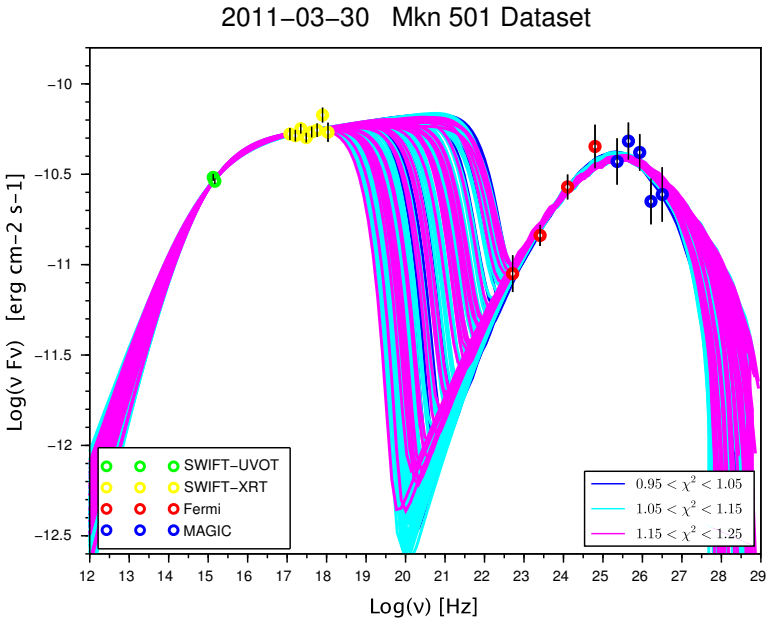

(a) 158 selected solutions, divided according to their χ^2 value: $0.95 < \chi^2 < 1.05$ (blue); $1.05 < \chi^2 < 1.15$ (cyan); $1.15 < \chi^2 < 1.25$ (magenta).

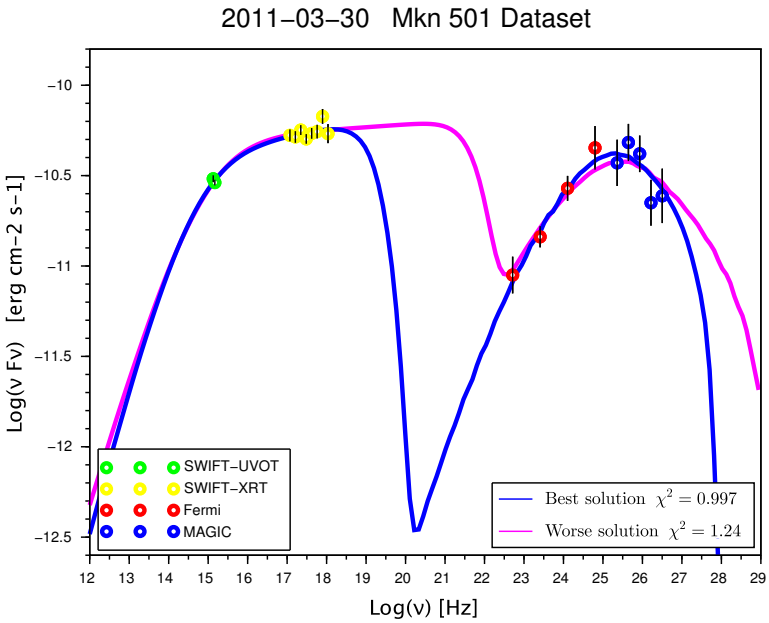

(b) Best (blue) and worse (magenta) solution, respectively.

Figure 5.17: SEDs obtained from the most likely parameters, achieved with the 158 minimizations on 30-03-2011 dataset. The best parameters are: $g_{min} = 1$, $g_{max} = 2.95 \times 10^6$, $g_b = 1.23 \times 10^3$, $n_1 = 1.28$, $n_2 = 2.91$, $B = 0.030$ G, $K = 28.06$, $R = 4.45 \times 10^{15}$ cm, $\delta = 32.34$, $z = 0.034$.

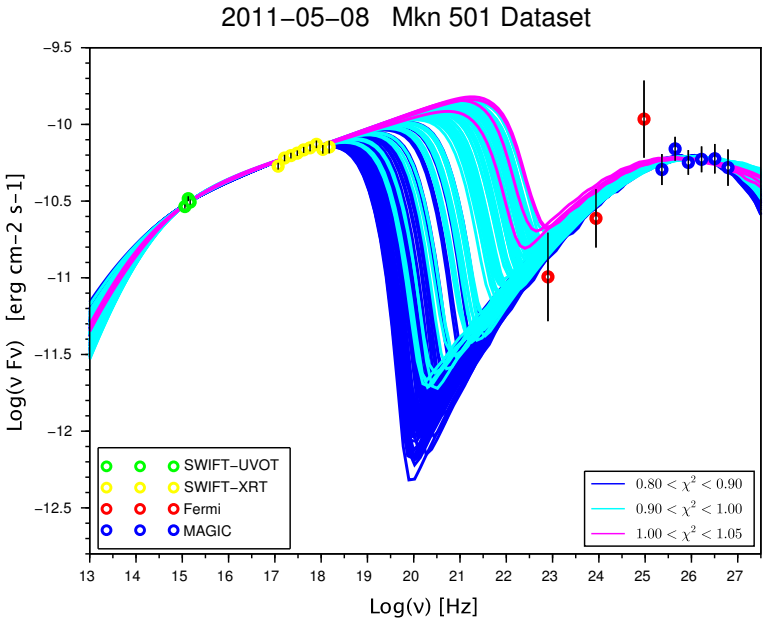

(a) 149 selected solutions, divided according to their χ^2 value: $0.80 < \chi^2 < 0.90$ (blue); $0.90 < \chi^2 < 1.00$ (cyan); $1.00 < \chi^2 < 1.05$ (magenta).

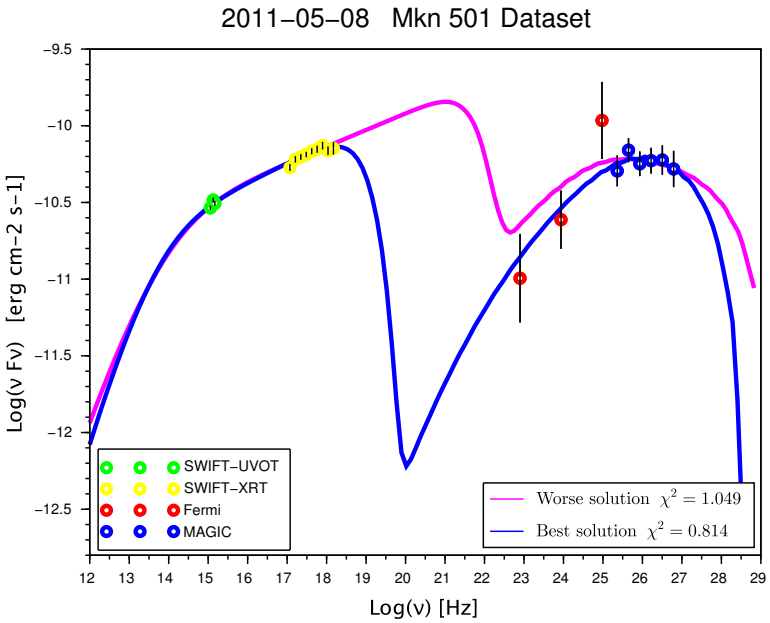

(b) Best (blue) and worse (magenta) solution, respectively.

Figure 5.18: SEDs obtained from the most likely parameters, achieved with the 149 minimizations on 08-05-2011 dataset. The best parameters are: $g_{min} = 1$, $g_{max} = 2.91 \times 10^6$, $g_b = 5.10 \times 10^3$, $n_1 = 1.11$, $n_2 = 2.75$, $B = 0.004$ G, $K = 29.11$, $R = 2.23 \times 10^{15}$ cm, $\delta = 129.7$, $z = 0.034$.

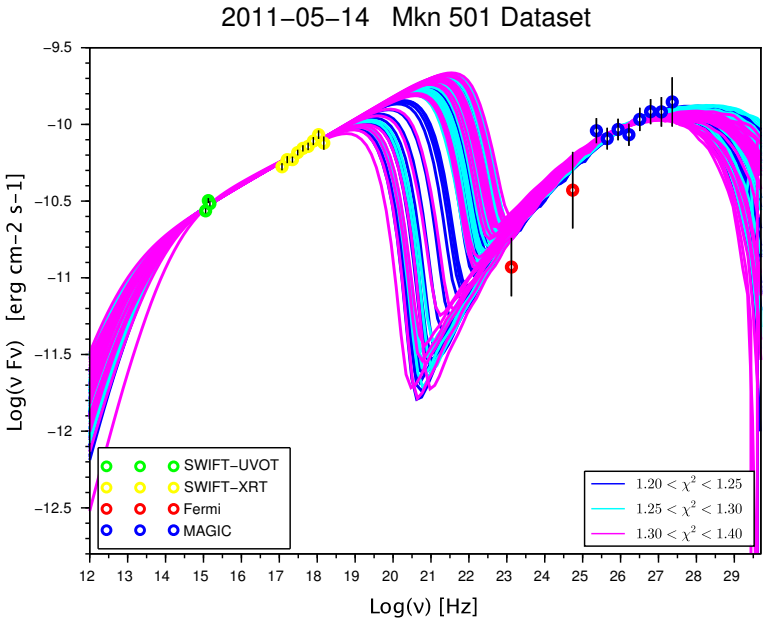

(a) 111 selected solutions, divided according to their χ^2 value: $0.95 < \chi^2 < 1.05$ (blue); $1.05 < \chi^2 < 1.15$ (cyan); $1.15 < \chi^2 < 1.25$ (magenta).

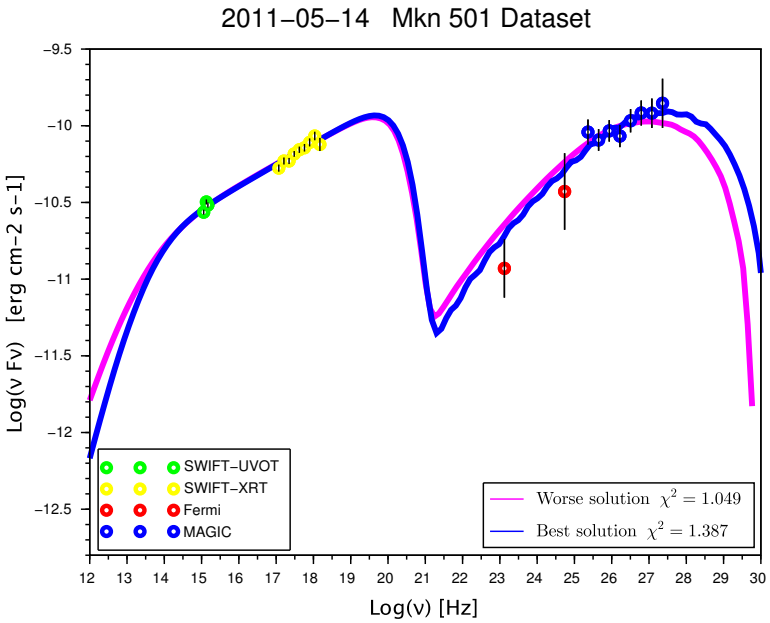

(b) Best (blue) and worse (magenta) solution, respectively.

Figure 5.19: SEDs obtained from the most likely parameters, achieved with the 111 minimizations on 14-05-2011 dataset. The best parameters are: $g_{min} = 1$, $g_{max} = 8.57 \times 10^6$, $g_b = 2.3 \times 10^3$, $n_1 = 0.69$, $n_2 = 2.72$, $B = 0.0007$ G, $K = 185.6$, $R = 4.23 \times 10^{13}$ cm, $\delta = 2534.3$, $z = 0.034$.

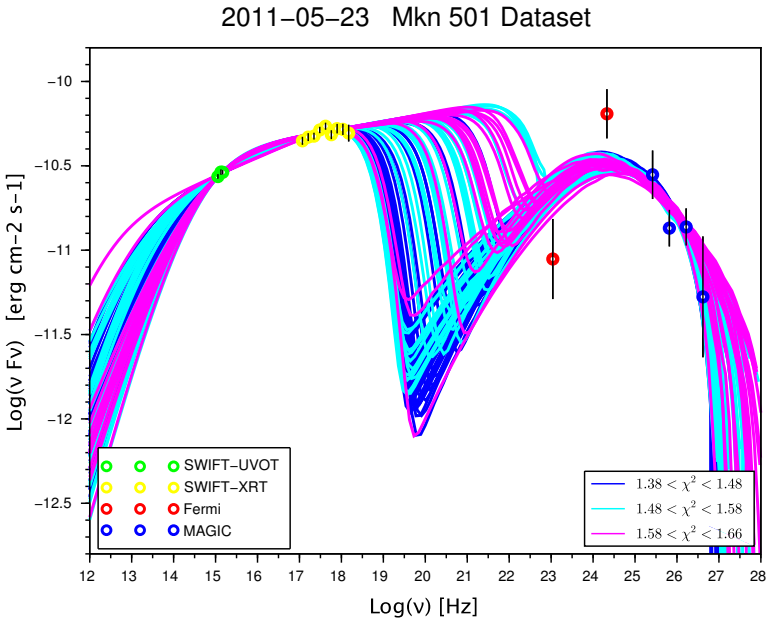

(a) 129 selected solutions, divided according to their χ^2 value: $1.38 < \chi^2 < 1.48$ (blue); $1.48 < \chi^2 < 1.58$ (cyan); $1.58 < \chi^2 < 1.66$ (magenta).

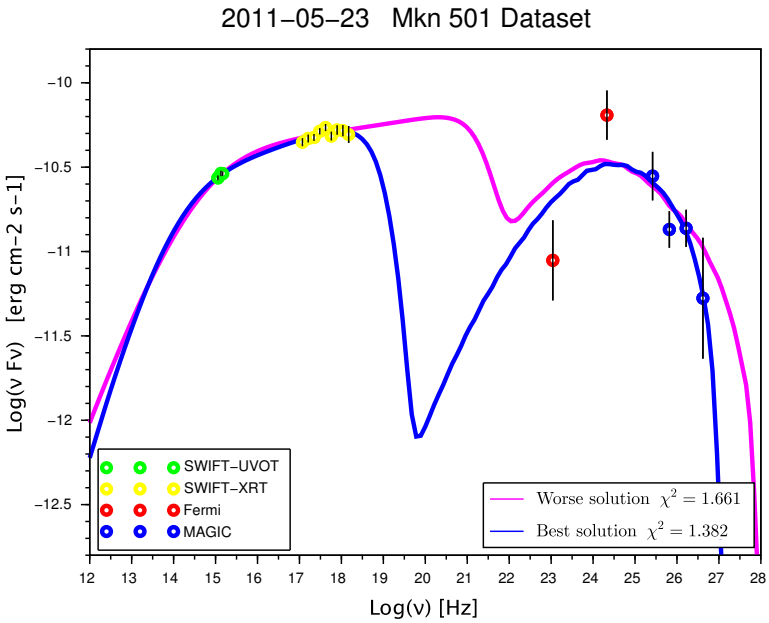

(b) Best (blue) and worse (magenta) solution, respectively.

Figure 5.20: SEDs obtained from the most likely parameters, achieved with the 129 minimizations on 23-05-2011 dataset. The best parameters are: $g_{min} = 1$, $g_{max} = 1.19 \times 10^6$, $g_b = 3.4 \times 10^2$, $n_1 = 1.14$, $n_2 = 2.84$, $B = 0.23$ G, $K = 39.24$, $R = 6.06 \times 10^{15}$ cm, $\delta = 10.52$, $z = 0.034$.

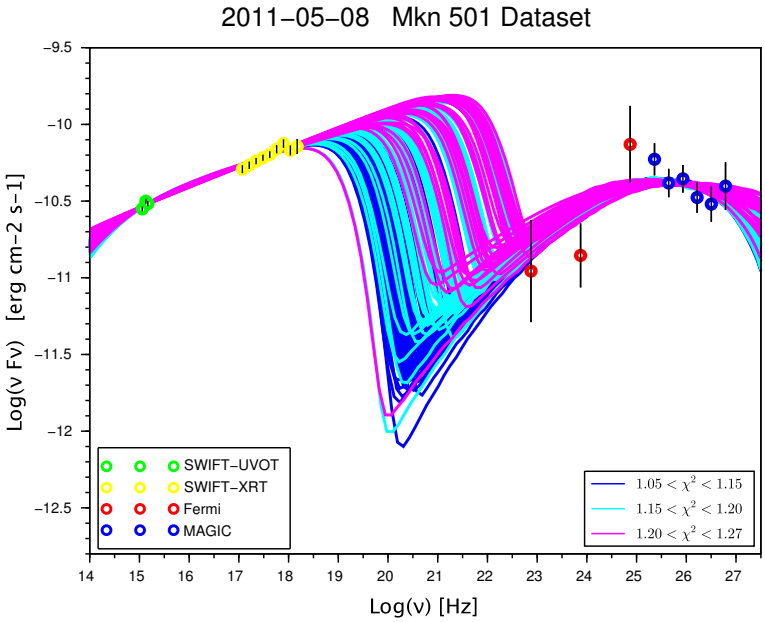

(a) 160 selected solutions, divided according to their χ^2 value: $1.05 < \chi^2 < 1.15$ (blue); $1.15 < \chi^2 < 1.20$ (cyan); $1.20 < \chi^2 < 1.27$ (magenta).

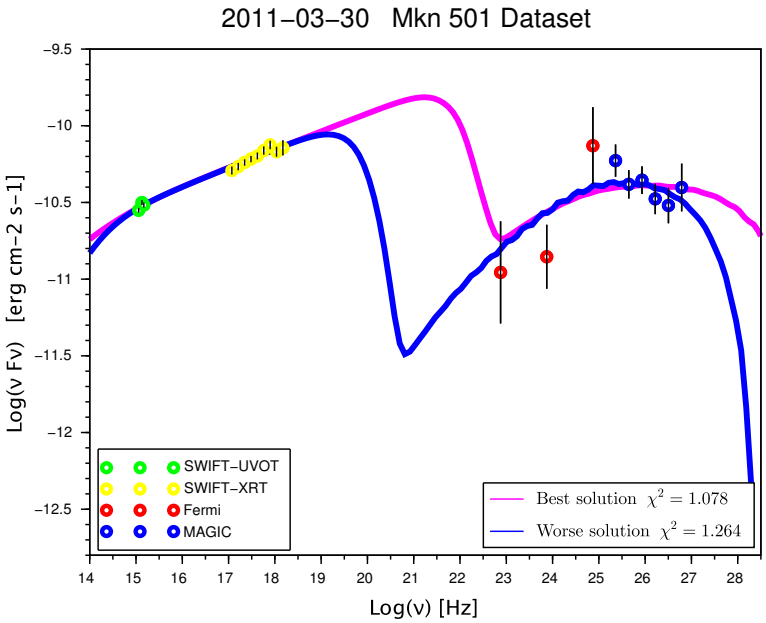

(b) Best (blue) and worse (magenta) solution, respectively.

Figure 5.21: SEDs obtained from the most likely parameters, achieved with the 160 minimizations on 29-05-2011 dataset. The best parameters are: g_{min} =, $g_{max} = 2.01 \times 10^6$, $g_b = 1.2 \times 10^3$, $n_1 = 0.72$, $n_2 = 2.76$, $B = 0.08$ G, $K = 161.74$, $R = 1.99 \times 10^{14}$ cm, $\delta = 116.37$, $z = 0.034$.

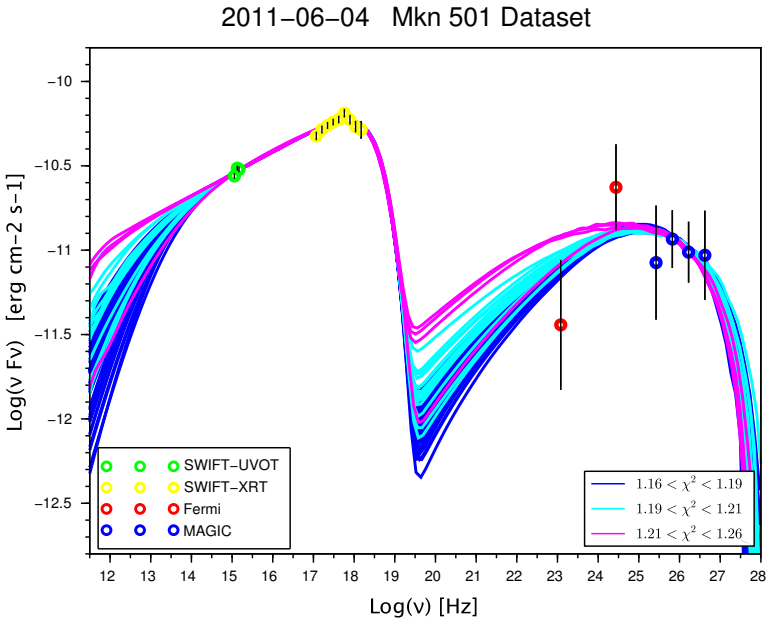

(a) 81 selected solutions, divided according to their χ^2 value: $1.16 < \chi^2 < 1.19$ (blue); $1.19 < \chi^2 < 1.21$ (cyan); $1.21 < \chi^2 < 1.26$ (magenta).

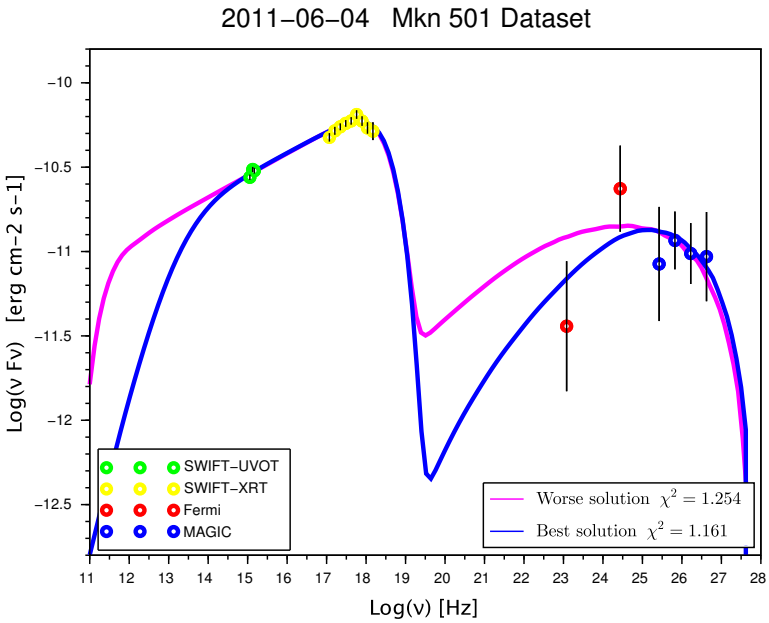

(b) Best (blue) and worse (magenta) solution, respectively.

Figure 5.22: SEDs obtained from the most likely parameters, achieved with the 81 minimizations on 04-06-2011 dataset. The best parameters are: $g_{min} = 1$, $g_{max} = 6.76 \times 10^5$, $g_b = 1.1 \times 10^3$, $n_1 = 0.77$, $n_2 = 2.75$, $B = 0.03$ G, $K = 26.6$, $R = 7.81 \times 10^{14}$, cm $\delta = 119.2$, $z = 0.034$.

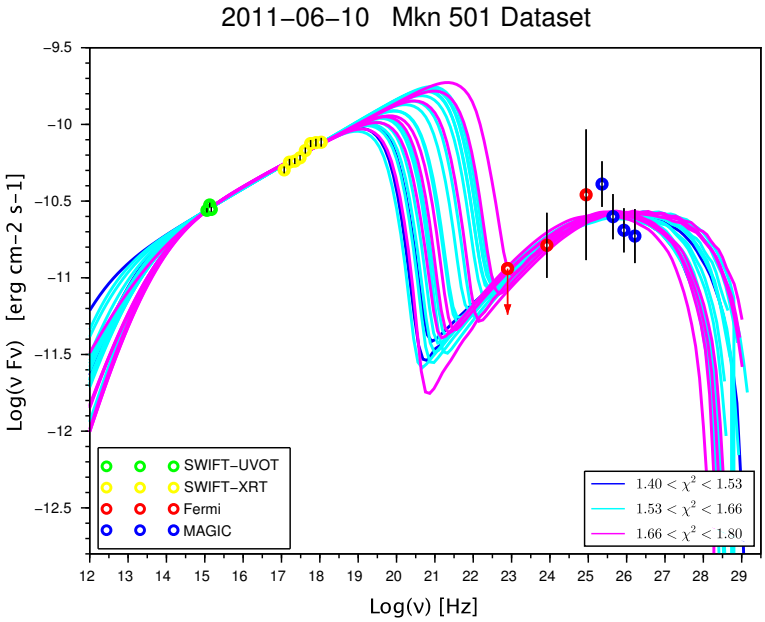

(a) 26 selected solutions, divided according to their χ^2 value: $1.40 < \chi^2 < 1.53$ (blue); $1.53 < \chi^2 < 1.53$ (cyan); $1.53 < \chi^2 < 1.80$ (magenta).

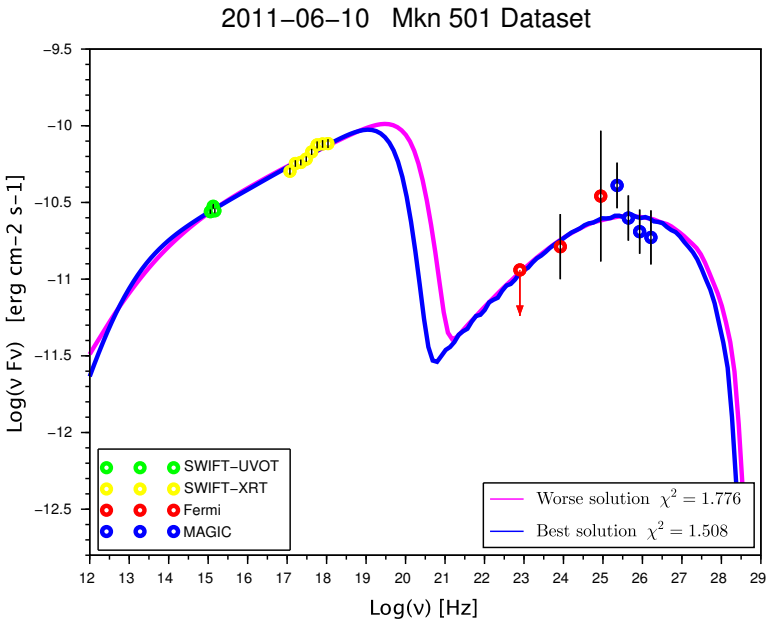

(b) Best (blue) and worse (magenta) solution, respectively.

Figure 5.23: SEDs obtained from the most likely parameters, achieved with the 26 selected solutions on 10-06-2011 dataset. The best parameters are: $g_{min} = 1$, $g_{max} = 2.28 \times 10^6$, $g_b = 5.6 \times 10^2$, $n_1 = 0.96$, $n_2 = 2.71$, $B = 0.04$ G, $K = 792.10$, $R = 3.91 \times 10^{14}$ cm, $\delta = 141.1$, $z = 0.034$.

Chapter 6

Discussion

The blazars SED modeling is a complex task, and must be performed through a non-linear least square minimization by using the one-zone synchroton-self Compton model (see Section 3.4.1). Such a model involves eight free parameters, and is currently used in literature to model the SED of several blazar, such as Mkn501. The crucial points that can make the minimization process a very challenging task are basically two: (i) the quality of the observational datasets; (ii) a complex topography of the χ^2-manifold. For what concerns (i), some considerations have to be pointed up. First of all all, data must be as simultaneous as possible, since blazars are strongly variable sources. Sometimes, the requirement of simultaneity goes to the disadvantage of the quality of data points, such as in the case of the Fermi-LAT data, where - to have more than two points with small error bars - an integration over a week is needed. To model the SED, both the sampling of the synchrotron and the inverse Compton peak are required. These two physical processes occur at two very different energy ranges, and data coming from different instruments have to be collected. This implies having data with very different error bars, depending on the characteristics of each instrument and on the different techniques in reconstructing the energy flux. So, a tipical blazar dataset contains few points (around 20), not homogeneously distributed, and characterized by different error bars. The solutions obtained from the 250 minimization for each dataset (Figures 5.17-5.23) show that SEDs are not well constrained, basically due to the lack of points in the MeV-energy range, and to the large error bars at the very high energy in the region of the inverse Compton peak. Concerning point (ii), the shape of the χ^2-manifold cannot be foreseen *a priori*. It depends mostly on the model, but also on the quality of the data. Moreover, it can not be explored with infinite resolution, and the parameters resulting from the minimization can be considered only an approximation to the searched minimum. Since the model containes many phenomenological parameters, the presence of spurious correlations among them cannot be ruled out *a priori*. Obviously, the latter, can further complicate the shape of the χ^2-manifold. This may even lead to different solutions that result in SEDs characterized by the same χ^2-value. The correlations between the model parameters are highlighted in Tables 5.3-5.27. The stronger ones have been found for the phemomenological parameters, but also some correlations between the physical ones are found: $R - \delta$ (radius - doppler factor), and $B - \delta$ (magnetic field - doppler factor).

For all these reasons, an additional statistical analysis is needed to understand the reliability of each solution. In fact, due to the presence of correlations between the parameters, it is not straightforward that the best mathematical solution - characterized by the minimum

χ^2-value - represents also the best physical one. Hence, all the parameters are analyzed and those distinguished by a value that deviates more that 3σ from their mean value are excluded. Sometimes, even after this selection, the presence of strong outliers (only for the normalization parameter K and the radius R) remains, and such solutions are rejected a posteriori. This kind of selection is justified under a particular assumption (i.e., an intrinsic roughness of the minimum of the χ^2-manifold) that will be discussed a little more forward.

Summarizing, the statystical analysis following the minimizations pointed out that the simultaneous multi-frequency data are not yet able to strongly constrain the blazars SED, especially in the region between the two peaks (since there are no instruments working in that band), and the inverse Compton one (since the systematic uncertainties are still very large). Moreover, it highlighted the presence of correlations between the parameters of the synchrotron-self Compton model [76] implemented in the code, that lead to have different SEDs charachterized by almost the same χ^2-value. Another critical ingredient included in the model is the function used to describe the electron spectral distribution. In this model, a classical broken power law with a smooth transition has been choosen. It is an approximated solution for a simplified kinetic equation of the electrons, derived in [107]. The presence of two spectral indices is purely a phenomenological choice, and it is used to describe the different slopes of the right and left sides of the synchrotron peak. However, there is still an open debate on the correct spectral law that should be used. Naturally, the presence of many phenomenological parameters - and correlations - complicates the fitting procedure. So, by removing the degeneration between the model parameters, by eliminating the phenomenological as much as possible (i.e., reducing the degree of freedom od the system), the shape of the χ^2-manifold could simplify a lot, and a smaller and cleaner parameter distribution could be achieved.

Another problem found out in the SED modeling, concerns the errors associated with the parameters. In all the cases, (see Tabels 5.4, 5.8, 5.12, 5.16, 5.20, 5.24, and 5.28) the parameter errors resulting from the covariance matrix are very large, almost of the same order of magnitude of the parameters, and sometimes even larger. One of the reason is that the standard minimization approach depends on a reliable quadratic approximation to the χ^2-surface around the minimum. In fact, significantly deviation from this assumption, implies possible overstimations (if the χ^2-manifold presents a flat shape around the minimum), or underestimations. However, as pointed out in Section 3.4.3, the uncertaintes associated to the parameters estimated through the covariance matrix are meaningful only if the error measurements of the data are normally distributed [71]. This is not exactly the case treated in this thesis, because the observational datasets collect data taken with different instruments, spreaded on several energy orderds of magnitude. This implies having data characterized by very different error bars, ranging to 3% of the fluxes in the optical band, up to more than 20% in the VHE band. The uncertaintes can be estimated through another method recurring to the confidence limits, as described in Section 3.4.3. However, in a preliminary study on the feasibility of the SED modeling by a non-linear χ^2-minimization, this approach has been already attempted in [70], by using the Ridders' method [108].

The obtained uncertaintes are very small, formally corrected, but quite unrealiable due to the complexity of the problem. These small values, make the solutions - obtained from different starting points, $\mathbf{P}_0$, in the parameter space - incompatible to one another. This also represent an underlying problem from a scientific point of view, because apparently each solution could belong to different uncorrelated local minima, and the minimization process would result $\mathbf{P}_0$-dependent.

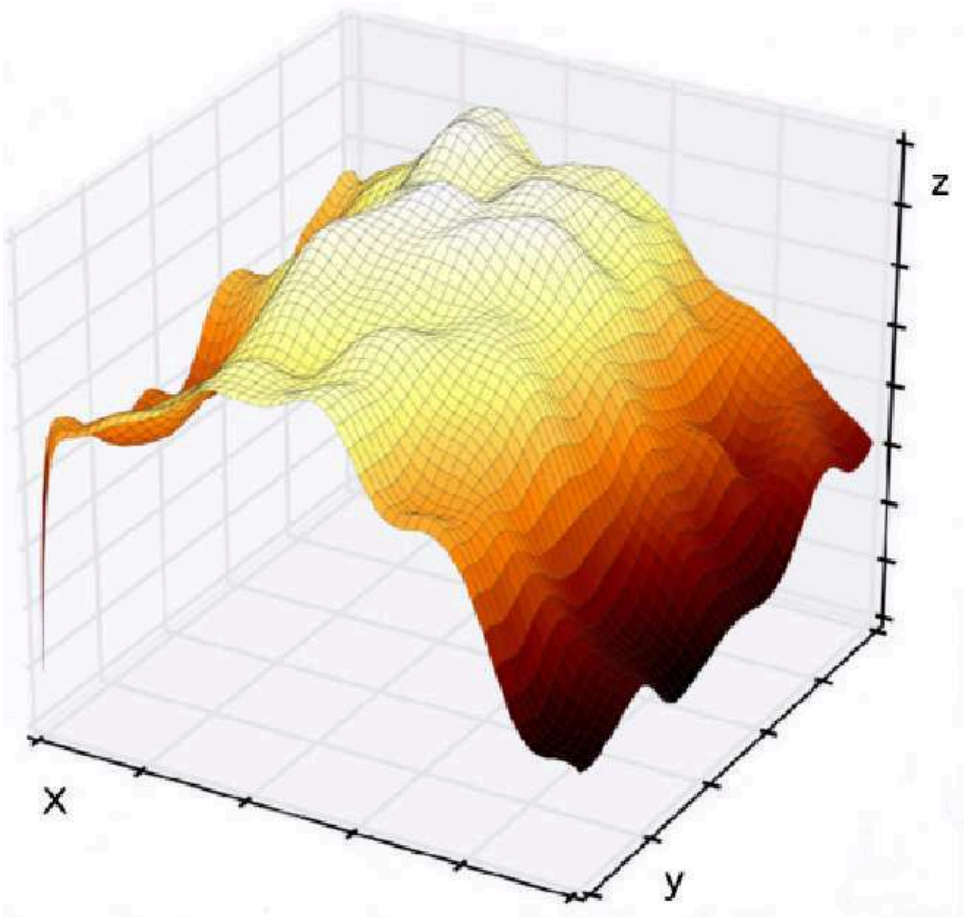

Figure 6.1: Example of rough surface in three dimensions.

In Chapter 5, through a large number of minimizations performed on different datasets, it is pointed out that the minimization algorithm converges to almost the same χ^2-value for 60-70% of the times, unless there are strong outliers. Differences in $\chi^2 \ll 1$ of around 10^{-2} are not meaningful, and in the cases treated in this thesis they are approximately $2 - 4 \times 10^{-1}$. This means that the implemented algorithm is able to approach a reasonable minimum independently from the starting point. The main aim, now, is to understand if such differences in the χ^2-values are due to an intrinsic roughness of the minimum of the χ^2-manifold or to other, deeper reasons. By considering the outcoming solutions from all the minimizations, the values of each parameter are considered as a whole. Figures 5.2 and 5.4-5.7 show that almost each parameter presents a peaked distribution and that its standard deviation trend stabilizes with increasing minimization number. If the minimization process converged to completely uncorrelated local minima, the distribution of each parameter would be rather flat and spreaded, and its standard deviation would present a chaotic trend with the minimization trials. On the contrary, all the solutions of the set are gathered around a given mean value, and this is an important indication that the fitting procedure is rather stable. So, according to the abovementioned evidences, the minimum of the χ^2 can be considered as a multidimensional surface characterized by an intrinsec roughness (a three-dimensional example of a rough surface is shown in Figure 6.1). This hypothesis would also explain why

the uncertaintes computed through the confidence limits are so small. Imagine that each solution is related to a small local minimum nested on the surface of the global one. If such small local minimum - representing a single corrugation - is small, but deep enough, the confidence level could be not so strong to jump away from it. In this way, all the solutions would seem strongly uncorrelated because their uncertaintes do not cross into one another.

Basing on all these considerations, another method to provide an estimate of the parameter uncertaintes, is proposed. Since all the solutions - characterized by a χ^2 confined in a narrow range of values - represent a good approximation of the global minimum, the standard deviation of their distribution can give an idea of the dimension of the minimum in the parameter space So, the standar deviation of each parameter, is taken as the uncertainty on the parameter itself. The results are shown in Tables 5.4-5.28. The results pointed out that: (i) the best determined parameters are the electron distribution spectral indices, n_1 and n_1, with uncertaintes ranging from 13-27% for n_1 and often $< 1\%$ for n_2; (ii) the uncertaintes related to the "break" electron Lorentz factor, g_b, - corresponding to the change of index - range from 20-50% in most of the cases; (iii) the uncertaintes on the magnetic field, B, are 30-40% in more than a half cases, while for remaining cases they are meningless; (iv) the uncertaintes on the Doppler factor are $< 30\%$ most cases, and $> 50\%$ for the remaining cases; (v) the uncertaintes on the plasma blob radius, R, are around 30% only in few cases, while are meaningless in the remaining cases; (vi) the worse determined parameters are the maximum electron Lorentz factor, g_{max}, and the electron specturm normalization parameter, K: they both show uncertaintes of over 100%. This is easily predictible by looking at their distribution and standard variation trends. These parameter, such as R, show a rather flat distribution and are spread over several orders of magnitudes. They represent the model's most critical parameters because they are not confined within a reasonable physical range.

Naturally, the minimization process can be considerably simplified if the values of some parameters are fixed *a priori*, based on other physical considerations. But this, of course, was not the case discussed in this thesis.

6.1 Outlooks

The results obtained with the non-linear χ^2 minimization, show that the SED modeling of blazar SEDs can now be attempted with a rigorous statistical approach. However, as discussed in Section 6, several features deserve to be investigated and, when possible, improved. In the following, some future works and investigations are proposed to make this approach fully stable and reliable.

1. **Adding Electron Distributions**. In Section 3.4.1 it is pointed out that the function describing the electron distribution is due to a purely phenomenological choice, assumed to describe the different slopes of the synchrotron peak. Nevertheless, adding phenomenological parameters is dangerous since these might introduce spurious correlations that lead to degenerate solutions. As explained in Section 3.4.1, the code allows one to choose among different electron distributions. All functions are still phenomenological, but some of them have fewer parameters. It is worth trying - all other things remaining equal - if the results improve or not by changing the electron distribution. However, a more correct choice (at least in a stead-state situation of the source) consists in implementing a new distibution, such as described in [109]. Here, the exact steady state electron distribution is computed taking into account also the

Coulomb, Bremsstrahlung, Compton and synchrotron losses. The contribution of these losses cannot be ignored, and with respect to a typical power-law, results in a physically motivated (as opposed to phenomenological) curved spectral density: its slope is flatter than injection at low energies where Coulomb losses dominate, as steep as injection at intermediate energies where bremsstrahlung losses dominate, and steeper than injection at higher energies where synchrotron and inverse-Compton losses dominate.

2. **Adding SED models**. Usually, to demonstrate the feasibility of a new approach, it is common sense to start from the simplest accepted rules. However, the study in this thesis pointed out that the current implementation of the one-zone synchrotron-self Compton model [76] needs to be reviewed. However, thanks to the structure of the C++ code, other SED models can be implemented and tested. One interesting model is proposed in [110]. It is a conical jet model in which the electron population evolves dynamically along the jet according to the synchrotron and inverse-Compton losses. Moreover, the synchrotron opacity is integrated along the line of sight through the jet plasma, taking into account the emission and the opacity of each region of the jet.

3. **Tests on χ^2 behaviour**. Due to the complexity of the problem and the large uncertaintes, this approach may reveal unexpected features of the χ^2-manifold that might affect convergence. For this reason, a preliminary study on the χ^2-manifold, that uses different artificial datasets differing by sampling homogeneity and density and by error bar magnitude in each energy band, should be carried out. This kind of study will permit to know *a priori* the reliability of the minimization process depending on the model and the quality of the observed data.

4. **Parameter Uncertaintes**. Once correlations among SED model parameters have been removed, or more suitable models have been implemented, the standard method of the confidence limits (see Section 3.4.3) to estimate parameter uncertaintes - in case the error measurements are not normally distributed - can be used. The confidence levels defines the space parameter region delimited by contours of constant $\Delta\chi^2$, and hence the uncertainty to associated to each parameter. The correct $\Delta\chi^2$ contours - for the desired confidence level - can be also calculated through Montecarlo simulation of synthetic datasets, according to the nature of the problem.

5. **Adding minimization methods**. Finally, also different minimization methods can be attempted. For example, in cases of data characterized by a non-normal error distribution, more robust techniques can be adopted [71]. Also other methods, computationally more expansive but very powerful - such as the genetic algorithms, can represent a viable alternative to the standard ones.

6.2 Conclusions

Blazar SED models were traditionally obtained by a heuristic approach, mainly due to severe lack of simultaneous multi-frequency data. This makes it difficult to extract significance from the results in a statistically meaningful way. It might also make challenging the comparison of results coming from different analyses. However, in the last several years simultaneous multi-frequency campaigns have been providing a broad-band coverage of source activity and many data sets are becoming available, the SED emission modeling can be attempted

with better profit. In this thesis the SED modeling of seven datasets of Mkn501 have been performed. The most likely values of the model parameters were obtained through a non-linear χ^2-minimization, using the Levenberg-Marquardt method. For each dataset, several minimizations have been repeated starting from different initial points in the space parameter, and a following statystical analysis on the outcoming solutions has been carried out. Moreover, for the first time a way to estimate the parameter uncertaintes is presented. The results obtained in this thesis show that nowadays this statistical method can be attempted in fitting blazars SEDs, even if some problematics are still opened and under investigation. However, once these difficulties will be completely overcame, this simple, but powerful approach will allow to (i) quantify if a specific model is more suitable than others for a given source; (ii) improve the models that describe the blazar SED, by finding the spurious correlations among the parameters due to purely phenomonological choices; (iii) make results coming from different analyses compatible; and (iv) carry out a statistical study on blazar properties once possible biases related to different analyses are removed.

This appraoch, although not without difficulty, is very promising for all the reasons mentioned above. So certainly, it deserves to be further developed and more deeply studied.

Bibliography

[1] De Angelis, A. & Pimenta, M.J.M.P. *Introduction to Particle and Astroparticle Physics*. Springer-Verlag Mailand, New York, NY, 2015.

[2] Longair, M.S. *High Energy Astrophysics*. Cambridge University Press, Cambridge, 2011.

[3] Greisen, K. *End to the cosmic ray spectrum?* Phys Rev Lett, vol. 16, 748–750, 1966.

[4] Zatsepin, G.T. & Kuzmin, V.A. *Upper limit of the spectrum of cosmic rays*. JETP Lett, vol. 4, 78–80, 1966. [Pisma Zh. Eksp. Teor. Fiz. 4 (1966) 114].

[5] Wagner, R. *PhD Thesis*. Phd thesis, Technische Universität München, 2006.

[6] Hoffman, C.M., Sinnis, C., Fleury, P. et al. *Gamma-ray astronomy at high energies*. Reviews of Modern Physics, vol. 71, 897–936, 1999.

[7] Blumenthal, G.R. & Gould, R.J. *Bremsstrahlung, Synchrotron Radiation, and Compton Scattering of High-Energy Electrons Traversing Dilute Gases*. Reviews of Modern Physics, vol. 42, 237–271, 1970.

[8] Hillas, A.M. *The Origin of Ultra-High-Energy Cosmic Rays*. Annual review of astronomy and astrophysics, vol. 22, 425–444, 1984.

[9] Heitler, W. *The Quantum Theory of Radiation*. The International series of monographs on physics. Clarendon Press, 1960.

[10] Coppi, P.S. & Aharonian, F.A. *Constraints on the Very High Energy Emissivity of the Universe from the Diffuse GeV Gamma-Ray Background*. Astrophysical Journal Letters, vol. 487, L9–L12, 1997.

[11] Padmanabhan, T. *Theoretical Astrophysics - Volume 3, Galaxies and Cosmology*. Cambridge University Press, Cambridge, UK, 2002.

[12] Mazin, D. & Raue, M. *New Limits on the Density of the Extragalactic Background Light from TeV Blazars*. In S. Ritz, P. Michelson & C.A. Meegan, editors, *The First GLAST Symposium*, vol. 921 of *American Institute of Physics Conference Series*, pp. 240–242. 2007.

[13] Franceschini, A., Rodighiero, G. & Vaccari, M. *Extragalactic optical-infrared background radiation, its time evolution and the cosmic photon-photon opacity*. Astronomy and Astrophysics, vol. 487, 837–852, 2008.

[14] Hauser, M.G., Arendt, R.G., Kelsall, T. et al. *The COBE Diffuse Infrared Background Experiment Search for the Cosmic Infrared Background. I. Limits and Detections.* Astrophysical Journal, vol. 508, 25–43, 1998.

[15] Madau, P. & Pozzetti, L. *Deep galaxy counts, extragalactic background light and the stellar baryon budget.* Monthly Notices of the Royal Astronomical Society, vol. 312, L9–L15, 2000.

[16] Https://magic.mpp.mpg.de.

[17] Https://www.mpi-hd.mpg.de/hfm/HESS/.

[18] Http://veritas.sao.arizona.edu.

[19] Https://portal.cta-observatory.org/Pages/Home.aspx.

[20] Https://www.auger.org.

[21] Http://argo.na.infn.it.

[22] Http://www.hawc-observatory.org.

[23] Http://www.ast.leeds.ac.uk/$\tilde{\text{f}}$s/showerimages.html.

[24] Hillas, A.M. *Cerenkov light images of EAS produced by primary gamma.* International Cosmic Ray Conference, vol. 3, 1985.

[25] Https://heasarc.gsfc.nasa.gov/docs/cgro/egret/.

[26] Pittori, C., Tavani, M. & AGILE Team. *Gamma-Ray Astrophysics with the Space Detector AGILE.* In *AAS/High Energy Astrophysics Division #8*, vol. 36 of *Bulletin of the American Astronomical Society*, p. 929. 2004.

[27] Http://fermi.gsfc.nasa.gov.

[28] Su, M., Slatyer, T.R. & Finkbeiner, D.P. *Giant Gamma-ray Bubbles from Fermi-LAT: Active Galactic Nucleus Activity or Bipolar Galactic Wind?* Astrophysical Journal, vol. 724, 1044–1082, 2010.

[29] Aharonian, F., Akhperjanian, A.G., Bazer-Bachi, A.R. et al. *Discovery of very-high-energy γ-rays from the Galactic Centre ridge.* Nature, vol. 439, 695–698, 2006.

[30] Persic, M., Rephaeli, Y. & Arieli, Y. *Very-high-energy emission from M 82.* Astronomy and Astrophysics, vol. 486, 143–149, 2008.

[31] Zubovas, K. & Nayakshin, S. *Fermi bubbles in the Milky Way: the closest AGN feedback laboratory courtesy of Sgr A*?* Monthly Notices of the Royal Astronomical Society, vol. 424, 666–683, 2012.

[32] Robson, I. *Active galactic nuclei.* Wiley-Praxis Series in Astronomy and Astrophysics, Chichester, UK, 1996.

[33] Peterson, B.M. *An Introduction to Active Galactic Nuclei.* Cambridge University Press, Cambridge, UK, 1997.

[34] de Angelis, A., Mansutti, O. & Persic, M. *Very-high energy gamma astrophysics*. Nuovo Cimento Rivista Serie, vol. 31, 187–246, 2008.

[35] Fossati, G., Maraschi, L., Celotti, A. et al. *A unifying view of the spectral energy distributions of blazars*. Monthly Notices of the Royal Astronomical Society, vol. 299, 433–448, 1998.

[36] Albert, J., Aliu, E., Anderhub, H. et al. *Upper Limit for γ-Ray Emission above 140 GeV from the Dwarf Spheroidal Galaxy Draco*. Astrophysical Journal, vol. 679, 428-431, 2008.

[37] Aliu, E., Anderhub, H., Antonelli, L.A. et al. *Upper Limits on the VHE Gamma-Ray Emission from the Willman 1 Satellite Galaxy with the Magic Telescope*. Astrophysical Journal, vol. 697, 1299–1304, 2009.

[38] Ellis, J., Feng, J.L., Ferstl, A. et al. *Prospects for detecting supersymmetric dark matter at Post-LEP benchmark points*. European Physical Journal C, vol. 24, 311–322, 2002.

[39] Paneque, D., Bloom, E. & Sanchez-Conde, M. *Study of indirect detection of Axion-Like-Particles with the Fermi-LAT instrument and Imaging Atmospheric Cherenkov Telescopes*. In *APS Meeting Abstracts*. 2009.

[40] Aleksić, J., Alvarez, E.A., Antonelli, L.A. et al. *Performance of the MAGIC stereo system obtained with Crab Nebula data*. Astroparticle Physics, vol. 35, 435–448, 2012.

[41] Cortina, J. *Status and First Results of the Magic Telescope*. Astrophysics and Space Science, vol. 297, 245–255, 2005.

[42] Doro, M. *The Commissioning and Characterization of the Calibration System of the MAGIC Telescope*. Master thesis, Università degli Studi di Padova, Universitat Autonoma de Barcelona, 2004.

[43] Paneque, D., Gebauer, H.J., Lorenz, E. et al. *A method to enhance the sensitivity of photomultipliers for Air Cherenkov Telescopes by applying a lacquer that scatters light*. Nuclear Instruments and Methods in Physics Research A, vol. 518, 619–621, 2004.

[44] Schweizer, T., Lorenz, E., Martinez, M. et al. *The optical calibration of the MAGIC telescope camera*. IEEE Transactions on Nuclear Science, vol. 49, 2497–2503, 2002.

[45] Cortina, J., Goebel, F., Schweizer, T. et al. *Technical Performance of the MAGIC Telescopes*. ArXiv e-prints, 2009.

[46] Li, T.P. & Ma, Y.Q. *Analysis methods for results in gamma-ray astronomy*. Astrophysical Journal, vol. 272, 317–324, 1983.

[47] Aleksić, J., Ansoldi, S., Antonelli, L.A. et al. *The major upgrade of the MAGIC telescopes, Part II: A performance study using observations of the Crab Nebula*. Astroparticle Physics, vol. 72, 76–94, 2016.

[48] Doro, M. *Novel Reflective Elements and Indirect Dark Matter Searches for MAGIC II and Future IACTs*. Phd thesis, Università degli Studi di Padova, 2009.

[49] Biland, A., Garczarczyk, M., Anderhub, H. et al. *The Active Mirror Control of the MAGIC Telescopes.* International Cosmic Ray Conference, vol. 3, 1353–1356, 2008.

[50] Aleksić, J., Ansoldi, S., Antonelli, L.A. et al. *The major upgrade of the MAGIC telescopes, Part I: The hardware improvements and the commissioning of the system.* Astroparticle Physics, vol. 72, 61–75, 2016.

[51] Borla Tridon, D., Goebel, F., Fink, D. et al. *Performance of the Camera of the MAGIC II Telescope.* ArXiv e-prints, 2009.

[52] Aliu, E., Anderhub, H., Antonelli, L.A. et al. *Improving the performance of the single-dish Cherenkov telescope MAGIC through the use of signal timing.* Astroparticle Physics, vol. 30, 293–305, 2009.

[53] García, J.R., Dazzi, F., Häfner, D. et al. *Status of the new Sum-Trigger system for the MAGIC telescopes.* ArXiv e-prints, 2014.

[54] López-Coto, R., Mazin, D., Paoletti, R. et al. *The Topo-trigger: A new stereo trigger for lowering the energy threshold of IACTs.* ArXiv e-prints, 2015.

[55] Tescaro, D., López-Oramas, A., Moralejo, A. et al. *The MAGIC telescopes DAQ software and the on-the-fly online analysis client.* ArXiv e-prints, 2013.

[56] Sitarek, J., Gaug, M., Mazin, D. et al. *Analysis techniques and performance of the Domino Ring Sampler version 4 based readout for the MAGIC telescopes.* Nuclear Instruments and Methods in Physics Research A, vol. 723, 109–120, 2013.

[57] Fruck, C., Gaug, M., Zanin, R. et al. *A novel LIDAR-based Atmospheric Calibration Method for Improving the Data Analysis of MAGIC.* ArXiv e-prints, 2014.

[58] Mirzoyan, R. *On the Calibration Accuracy of Light Sensors in Atmospheric Cherenkov Fluorescence and Neutrino Experiments.* International Cosmic Ray Conference, vol. 7, 265, 1997.

[59] Albert, J., Aliu, E., Anderhub, H. et al. *Implementation of the Random Forest method for the Imaging Atmospheric Cherenkov Telescope MAGIC.* Nuclear Instruments and Methods in Physics Research A, vol. 588, 424–432, 2008.

[60] Beringer, J. & et al, P.D.G. *Review of Particle Physics.* Physical Review D, vol. 86, 010001, 2012.

[61] Lafferty, G.D. & Wyatt, T.R. *Where to stick your data points : the treatment of measurements within wide bins.* Nuclear Instruments and Methods in Physics Research A, vol. 355, 541–547, 1995.

[62] Rolke, W.A., López, A.M. & Conrad, J. *Limits and confidence intervals in the presence of nuisance parameters.* Nuclear Instruments and Methods in Physics Research A, vol. 551, 493–503, 2005.

[63] Tikhonov, A.N. & Arsenin, V. *Methods of Solution of Ill-posed Problems.* Scripta series in mathematics (Winston), 1977.

[64] Schmelling, M. *The method of reduced cross-entropy A general approach to unfold probability distributions.* Nuclear Instruments and Methods in Physics Research A, vol. 340, 400–412, 1994.

[65] Bertero, M. *Linear inverse and ill-posed problems.* Advances in Electronics and Electron Physics, vol. 75, 1–120, 1989.

[66] Albert, J., Aliu, E., Anderhub, H. et al. *Unfolding of differential energy spectra in the MAGIC experiment.* Nuclear Instruments and Methods in Physics Research A, vol. 583, 494–506, 2007.

[67] Pühlhofer, G., Bolz, O., Götting, N. et al. *The technical performance of the HEGRA system of imaging air Cherenkov telescopes.* Astroparticle Physics, vol. 20, 267–291, 2003.

[68] Aleksić, J., Ansoldi, S., Antonelli, L.A. et al. *Unprecedented study of the broadband emission of Mrk 421 during flaring activity in March 2010.* Astronomy and Astrophysics, vol. 578, A22, 2015.

[69] Mankuzhiyil, N., Ansoldi, S., Persic, M. et al. *The Environment and Distribution of Emitting Electrons as a Function of Source Activity in Markarian 421.* Astrophysical Journal, vol. 733, 14, 2011.

[70] Mankuzhiyil, N., Ansoldi, S., Persic, M. et al. *Emitting Electrons and Source Activity in Markarian 501.* Astrophysical Journal, vol. 753, 154, 2012.

[71] Press, W.H., Teukolsky, S.A., Vetterling, W.T. et al. *Numerical Recipes in C++.* Cambridge University Press, New York, NY, USA, 2002.

[72] Madsen, K., Nielsen, H.B., Tingleff, O. et al. *IMM Methods for non-linear least squares problems.* Technical Report - Informatics and Mathematics Modelling, Technical University of Denmark, 2004.

[73] Bj́orck, A. *Numerical Methods for Least Squares Problems.* Siam Philadelphia, Philadelphia, PA, 1996.

[74] Levenberg, K. *A Method for the Solution of Certain Non-Linear Problems in Least Squares.* The Quarterly Journal of Applied Mathematics, vol. 2, 164–168, 1944.

[75] Marquardt, D.W. *An algorithm for least-squares estimation of nonlinear parameters.* SIAM Journal on Applied Mathematics, vol. 11, 2, 431–441, 1963.

[76] Tavecchio, F., Maraschi, L. & Ghisellini, G. *Constraints on the Physical Parameters of TeV Blazars.* Astrophysical Journal, vol. 509, 608–619, 1998.

[77] Catanese, M., Bradbury, S.M., Breslin, A.C. et al. *Multiwavelength Observations of a Flare from Markarian 501.* Astrophysical Journal Letters, vol. 487, L143–L146, 1997.

[78] Fossati, G., Buckley, J.H., Bond, I.H. et al. *Multiwavelength Observations of Markarian 421 in 2001 March: An Unprecedented View on the X-Ray/TeV Correlated Variability.* Astrophysical Journal, vol. 677, 906-925, 2008.

[79] Ghisellini, G., Maraschi, L. & Treves, A. *Inhomogeneous synchrotron-self-Compton models and the problem of relativistic beaming of BL Lac objects.* Astronomy and Astrophysics, vol. 146, 204–212, 1985.

[80] Jones, F.C. *Calculated Spectrum of Inverse-Compton-Scattered Photons.* Physical Review, vol. 167, 1159–1169, 1968.

[81] Lind, K.R. & Blandford, R.D. *Semidynamical models of radio jets - Relativistic beaming and source counts.* Astrophysical Journal, vol. 295, 358–367, 1985.

[82] Gil de Paz, A., Boissier, S., Madore, B.F. et al. *The GALEX Ultraviolet Atlas of Nearby Galaxies.* The Astrophysical Journal Supplement Series, vol. 173, 185–255, 2007.

[83] Markaryan, B.E. & Lipovetskii, V.A. *Galaxies with ultraviolet continuum V.* Astrophysics, vol. 8, 89–99, 1972.

[84] Quinn, J., Akerlof, C.W., Biller, S. et al. *Detection of Gamma Rays with $E > 300$ GeV from Markarian 501.* Astrophysical Journal Letters, vol. 456, L83, 1996.

[85] Urry, C.M. & Padovani, P. *Unified Schemes for Radio-Loud Active Galactic Nuclei.* Publications of the Astronomical Society of the Pacific, vol. 107, 803, 1995.

[86] Marscher, A.P. *The Core of a Blazar Jet.* In T.A. Rector & D.S. De Young, editors, *Extragalactic Jets: Theory and Observation from Radio to Gamma Ray*, vol. 386 of *Astronomical Society of the Pacific Conference Series*, p. 437. 2008.

[87] Maraschi, L., Ghisellini, G. & Celotti, A. *A jet model for the gamma-ray emitting blazar 3C 279.* Astrophysical Journal Letters, vol. 397, L5–L9, 1992.

[88] Sikora, M., Begelman, M.C. & Rees, M.J. *Comptonization of diffuse ambient radiation by a relativistic jet: The source of gamma rays from blazars?* Astrophysical Journal, vol. 421, 153–162, 1994.

[89] Albert, J., Aliu, E., Anderhub, H. et al. *VHE γ-Ray Observation of the Crab Nebula and its Pulsar with the MAGIC Telescope.* Astrophysical Journal, vol. 674, 1037–1055, 2008.

[90] Aharonian, F., Akhperjanian, A.G., Bazer-Bachi, A.R. et al. *Observations of the Crab nebula with HESS.* Astronomy and Astrophysics, vol. 457, 899–915, 2006.

[91] Atwood, W.B., Abdo, A.A., Ackermann, M. et al. *The Large Area Telescope on the Fermi Gamma-Ray Space Telescope Mission.* Astrophysical Journal, vol. 697, 1071–1102, 2009.

[92] Abdo, A.A., Ackermann, M., Ajello, M. et al. *Fermi/Large Area Telescope Bright Gamma-Ray Source List.* Astrophysical Journal Supplement, vol. 183, 46–66, 2009.

[93] Cash, W. *Parameter estimation in astronomy through application of the likelihood ratio.* Astrophysical Journal, vol. 228, 939–947, 1979.

[94] Mattox, J.R., Bertsch, D.L., Chiang, J. et al. *The Likelihood Analysis of EGRET Data.* Astrophysical Journal, vol. 461, 396, 1996.

[95] Atwood, W., Albert, A., Baldini, L. et al. *Pass 8: Toward the Full Realization of the Fermi-LAT Scientific Potential*. ArXiv e-prints, 2013.

[96] Acero, F., Ackermann, M., Ajello, M. et al. *Fermi Large Area Telescope Third Source Catalog*. The Astrophysical Journal Supplement Series, vol. 218, 23, 2015.

[97] Acciari, V.A., Arlen, T., Aune, T. et al. *Spectral Energy Distribution of Markarian 501: Quiescent State Versus Extreme Outburst*. Astrophysical Journal, vol. 729, 2, 2011.

[98] Abdo, A.A., Ackermann, M., Ajello, M. et al. *Insights into the High-energy γ-ray Emission of Markarian 501 from Extensive Multifrequency Observations in the Fermi Era*. Astrophysical Journal, vol. 727, 129, 2011.

[99] Gehrels, N., Chincarini, G., Giommi, P. et al. *The Swift Gamma-Ray Burst Mission*. Astrophysical Journal, vol. 611, 1005–1020, 2004.

[100] Massaro, E., Perri, M., Giommi, P. et al. *Log-parabolic spectra and particle acceleration in blazars. II. The BeppoSAX wide band X-ray spectra of Mkn 501*. Astronomy and Astrophysics, vol. 422, 103–111, 2004.

[101] Kalberla, P.M.W., Burton, W.B., Hartmann, D. et al. *The Leiden/Argentine/Bonn (LAB) Survey of Galactic HI. Final data release of the combined LDS and IAR surveys with improved stray-radiation corrections*. Astronomy and Astrophysics, vol. 440, 775–782, 2005.

[102] Poole, T.S., Breeveld, A.A., Page, M.J. et al. *Photometric calibration of the Swift ultraviolet/optical telescope*. Monthly Notices of the Royal Astronomical Society, vol. 383, 627–645, 2008.

[103] Schlafly, E.F. & Finkbeiner, D.P. *Measuring Reddening with Sloan Digital Sky Survey Stellar Spectra and Recalibrating SFD*. Astrophysical Journal, vol. 737, 103, 2011.

[104] Breeveld, A.A., Landsman, W., Holland, S.T. et al. *An Updated Ultraviolet Calibration for the Swift/UVOT*. In J.E. McEnery, J.L. Racusin & N. Gehrels, editors, *American Institute of Physics Conference Series*, vol. 1358 of *American Institute of Physics Conference Series*, pp. 373–376. 2011.

[105] Daniel, W. *Applied nonparametric statistics*. Houghton Mifflin, University of Michigan, 1978.

[106] Bevington, P.R. & Robinson, D.K. *Data reduction and error analysis for the physical sciences; 3rd ed.* McGraw-Hill, New York, NY, 2003.

[107] Inoue, S. & Takahara, F. *Electron Acceleration and Gamma-Ray Emission from Blazars*. Astrophysical Journal, vol. 463, 555, 1996.

[108] Ridder, C.J.F. *Three-point iterations derived from exponential curve fitting*. IEEE Transactions on Circuits and Systems, pp. 979–980, 1979.

[109] Rephaeli, Y. & Persic, M. *Synchrotron and Compton Spectra from a Steady-state Electron Distribution*. Astrophysical Journal, vol. 805, 111, 2015.

[110] Potter, W.J. & Cotter, G. *Synchrotron and inverse-Compton emission from blazar jets - I. A uniform conical jet model.* Monthly Notices of the Royal Astronomical Society, vol. 423, 756–765, 2012.

Acknowlegments

First of all, I want to thank my advisor Alessandro De Angelis, who led me into MAGIC and, with timely energy, smartly urged me to duly complete my work. Warm thanks go to my tutor Massimo Persic, who unfailingly followed me throughout my work also encouraging me in times of trouble. I also thank Barbara De Lotto and Stefano Ansoldi for continuously supporting me in many different ways. Finally I thank my referee Gabrjiela Zaharijas whose useful comments and suggestions helped me improving this thesis.

Very special thanks go to my family and to Michel, without whom all this would not have been possible. I thank, and will never forget, my fellow PhD students and hilarious friends, Anna, Michele, Michelino, and Carlo, for sharing this travel of a lifetime and for filling our MAGIC office with discussions, chats, and laughs. In particular, thanks Anna for sharing countless coffees and holidays in our office; thanks Michele for all those crazy Friday afternoons; thanks Michelino for your amazing childhood spirit and funny paranoia; and thanks Carlo for your unique organization spirit. A huge thanks to the new special friendships born at Roque the Los Muchachos, in the wonderful island of La Palma, and to all of my MAGIC friends. Last but not the least, a big thanks to Roberto & friends from the 89th Firefighters Brigade for unfailing discreet support.